UNIVERSITY OF BIRMINGHAM

DEVELOPMENT OF BORATE GLASS-REINFORCED HYDROXYAPATITE BIOCERAMIC POWDERS – SELECTIVE LASER SINTERING, A FEASIBILITY STUDY

by

CHRISTOS SOFTAS

A thesis submitted to the University of Birmingham for the degree of

DOCTOR OF PHILOSOPHY

School of Metallurgy and Materials

College of Engineering and Physical Sciences

University of Birmingham

April 2023

ABSTRACT

Over the past three decades, composite biomaterials comprising of hydroxyapatite (HA) as the main phase and bioactive glasses (BG) as the second phase have gained increased attention. This class of materials, glass reinforced hydroxyapatite composites (GR-HA), exhibits superior mechanical and biological performance compared to pure HA. Since the emergence of the topic in the mid-90s, mainly phosphate and silicate-based GR-HA systems were investigated. Two common issues concerning the utilisation of these glass systems are crystallisation and HA decomposition phenomena that can be deleterious both in terms of bioactivity and mechanical performance. Considerably fewer studies utilising borate-based glasses in GR-HA composites have been carried out besides their biocompatibility and enhanced thermal stability.

This work focused on the development of a novel GR-HA feedstock, resistant to crystallisation and HA dehydroxylation phenomena, utilising a borate-based glass system, $50B_2O_3$-$20SiO_2$-$20Na_2O$-$(10-x)CaO$-xLa_2O_3 ($0 \leq x \leq 2.5$). A parametric study investigating the optimal composition and processing parameters, such as glass content (0 – 10 wt.%) and sintering temperature (1200 °C – 1300 °C) was carried out; in tandem the effect of lanthanum oxide was studied, too. 10 wt.% was identified as the optimal glass loading since no thermal degradation was observed via X-ray diffraction (XRD). Additionally, enhanced densification and overall mechanical performance was recorded via microcomputed tomography (µCT), density and microhardness measurements. Small glass additions (≤ 5 wt.%) acted as heterogeneous nuclei sites or triggering points that induced limited HA dehydroxylation products, accruing for less than 27% of the total composition. The main secondary phase detected was beta tricalcium phosphate (β-TCP) that reverted to alpha tricalcium phosphate (α-TCP) with increasing temperature. No antimicrobial efficacy was detected against

S. Epidermidis or P. Aeruginosa, regardless of the glass content. No cytotoxic behaviour was recorded during SaoS-2 human osteosarcoma cell attachment studies. GR-HA specimens containing 10 wt.% of glass content exhibited enhanced cell viability compared to pure HA specimens, while similar or slightly worse biological performance was recorded for composites containing smaller additions of glass. Lastly, there are strong indications that lanthanum oxide potentially enhances the overall mechanical and biological performance of GR-HA samples. The samples containing the highest amount of lanthanum oxide content, exhibited the best performance in terms of densification, microhardness and cell culture studies.

In parallel, the utilisation of the most promising GR-HA composition was investigated as a powder feedstock during a selective laser sintering (SLS) feasibility study. The novel GR-HA feedstock containing 10 wt.% of $50B_2O_3$-$20SiO_2$-$20Na_2O$-$7.5CaO$-$2.5La_2O_3$ exhibited better processability and thermal stability compared to pure HA during SLS processing. Two different geometries were successfully printed with the glass containing powder feedstock compared to one geometry with its pure HA counterpart. Moreover, miniscule traces of secondary phases were recorded in the as-printed GR-HA specimens (< 2%), whereas significant thermal degradation was observed in the pure HA samples (~ 40% of the total composition). A post-processing heat treatment cycle was successful in partially reversing any hydroxyapatite dehydroxylation products to HA and enhanced densification.

The developed GR-HA system containing 10 wt.% of the novel borate-based glass composition, $50B_2O_3$-$20SiO_2$-$20Na_2O$-$(10-x)CaO$-xLa_2O_3 ($0 \leq x \leq 2.5$), is a promising biomaterial for tissue engineering applications. No crystallisation or HA thermal degradation were observed during heat treatment (conventional sintering or SLS processing), while the GR-HA composites exhibited enhanced biological performance compared to pure HA samples.

Στη μητέρα μου

ACKNOWELDGEMENTS

Firstly , I would like to thank my supervisor Professor Artemis Stamboulis for giving me the opportunity to work on such an interesting project. Furthermore, I would like to acknowledge the University of Birmingham and the Manufacturing Technology Centre for jointly funding this project. Last but not least, I would like to thank the JECS Trust and the European Ceramic Society, for supporting me financially during my stay at INPT in Toulouse, where I conducted the SLS experiments of this study.

The completion of my PhD studies would not have been feasible without the help and support of friends, colleagues and family members. I would like to pass on my gratitude to Dr. David Grossin and the members of staff at CIRIMAT/INPT, that made my stay in Toulouse both productive and enjoyable. I would like to acknowledge Dr. Ifty Ahmed, Dr. Towhid Islam and Dr. Benjamin Milborne for their assistance in producing the glass microspheres utilised in this work. Moreover, I would like to give my thanks to Will, Rob, Joe and every 1B20 member for creating a welcoming and fun environment for everyone. I would like to thank all the members of the Biomaterials group and more specifically Hanieh Ijakipour and Marc Bruggeman. I could never ask for a better teacher to introduce me to the microbiology and cell culture studies realm than Hanieh. Marc's scientific rigor and wittiness facilitated utterly intriguing, most usually nerd-heavy, discussions on topics I have never thought or encountered before. Besides all that, I would like to express my sincere gratitude for your camaraderie and scientific/emotional support during this journey.

Alex, I cannot express how grateful I am for your unwavering support during both the experimental and writing part of this bumpy ride. Your academic skills and knowledge should be utilised towards educating and shaping the new generation of materials scientists.

Tasos and Andreas, I hope that everyone has supporting friends like the likes of you two. Ever since I decided to start upon this fruitful journey you always had my back; the same applies to Alex, Billy, Ko and Kiki. Thank you so much!

My dearest “Manitsoi”, since the origin point of our group back in 2014, we were always there for each other through thick and thin. The best part is that this bond keeps getting stronger as the years go by and I couldn’t be more thankful about this. Afrodite, Charitini, Stella and Harry, thank you so much for your support in this trek. The same goes to the honorary members of the group: Elisa, Olivia, Andrew & Isi.

I do not think there are words to express the level of gratitude towards my mother Helen, since she has always been the cornerstone behind every success of my life. Thank you for being my role model and the inspiration towards never giving up and shooting for the stars. I cannot thank enough my brother George for always being there for me, no matter what. All our everlasting conversations on myriads of topics ranging from empathy to machine learning, have made me a better person. Thank you both from the bottom of my heart, for being in my life and supporting me in every twist and turn.

Carpe diem

This thesis incorporates work originally published in: *C. Softas, "Selective Laser Sintering of Hydroxyapatite-Based Materials for Tissue Engineering," in Additive Manufacturing in Biomedical Applications, vol. 23, ASM International, 2022, pp. 92–105* [1], where I was the sole author.

TABLE OF CONTENTS

LIST OF FIGURES

LIST OF TABLES

CHAPTER 1 – Introduction

Worldwide demand for biomedical implants nowadays is high and constantly increasing; this trend can be associated with various factors ranging from damaging sports activities to increased life expectancy and pathological issues such as osteoporosis [2]–[4]. Traditional techniques for bone reconstructive surgery often utilise bone material that is harvested either from the patients themselves (autografts) or from other donors (allografts); in both cases, there are various risks involved including implant rejection, viral or bacterial infection and inflammation. An alternative to the aforementioned methods is the use of tissue engineering scaffolds; these three-dimensional structures are designed to provide a suitable environment for bone reconstruction and share suitable characteristics both in terms of biological and mechanical properties.

Biocompatibility, bone growth promotion and cell viability are of utmost importance in such applications hence the employment of suitable biomaterials is necessary. Hydroxyapatite [$Ca_{10}(PO_4)_6(OH)_2$] (HA) is a ceramic material widely used in the biomedical sector as a bone-substitute compound due to its affinity to human bone and its ability to facilitate and promote osteogenesis. It is the main inorganic constituent (mineral phase) in the human bone and teeth, accounting for 70% of the total mass; collagen (organic phase) and water complete the composition of human hard tissue. Due to its bioactive character, hydroxyapatite has been vastly utilised in various biomedical applications regarding bone repair or tissue engineering. However, the poor mechanical properties of pure hydroxyapatite make this material incompatible for load-bearing applications. That is the main reason behind its frequent use in

Parts of this section are published as first-author and may contain replication from [1]

conjunction with different materials that enhance its mechanical properties such as alumina or zirconia [4]–[10].

Over the past three decades, composite materials comprising of HA as the main phase and bioactive glasses (BG) as the second phase have gained increased attention. This class of materials, glass reinforced hydroxyapatite composites (GR-HA), exhibits superior mechanical and biological performance compared to pure HA. BG primarily acts as a sintering aid [11]–[14], a strengthening agent within the HA matrix [12]–[14] and it also enhances the biological character of the composite [14]–[16]. It has been reported that an addition of not more than 10 wt.% of BG leads to less porosity, increased microhardness and enhanced bioactivity in the prepared samples [12], [14]–[17]. In recent years, the focus on GR-HA has shifted towards the usage of biomedical glasses containing compounds such as lanthanide oxides due to their enhanced biological and antimicrobial activity [15], [16]. Lanthanide ions (Ln^{+3}) share a close affinity with calcium ions (Ca^{+2}) in terms of ionic radii and it has been shown in previous studies that they are integrated within the HA crystal structure by replacing the latter [15], [16]. This integration is a result of the charge difference between the two ions and it has been shown to have beneficial effects in terms of biological response. Additionally, lanthanide ions display antimicrobial activity in a wide variety of bacteria, making such GR-HA systems attractive for hard tissue engineering applications since bacterial infections are quite common in bone surgery.

Besides chemical affinity, bioactivity or possible antimicrobial activity, another factor that is instrumental in the successful integration of a scaffold on the implant site is its geometrical characteristics. Pore size, architecture and interconnectivity highly affect the rate and quality of healing, vascularization among the plethora of biological processes involved in bone reconstruction [18]. Achieving the intricate geometrical features necessary for tissue

engineering scaffolds requires the utilisation of high accuracy processing techniques. In general, macropores ranging from 100 – 500 μm, high porosity greater than 50% and interconnected pore network are required for optimal results [19], [20]. Traditional manufacturing techniques fail to provide such level of detail in a reproducible and effective manner. On the contrary, additive manufacturing (AM) methods are better suited for fabricating parts of that complexity due to the high level of control on the process parameters and consistency of the printed parts [21].

The combination of AM methods with novel bioceramic feedstocks is undoubtedly a promising framework towards personalised medicine. Custom tissue engineering services, tailor-made to patient's physiology and needs, have the potential to be the paradigm shift that will revolutionise the biomedical sector. Various studies have focused on such applications utilising AM methods and HA [22], however limited work has been carried out with GR-HA feedstocks. A highly promising AM technique that fits this profile is selective laser sintering (SLS). Nevertheless, only a few investigations explored the printability of GR-HA with SLS in the past [23]–[25]. This study focused on the development of GR-HA composite powder, containing various concentrations (wt.%) of a La_2O_3-doped borosilicate glass. Additionally, the biological and antimicrobial response were assessed, in order to identify the effect of BG addition. Finally, an SLS feasibility study investigated the effect of La_2O_3-doped BG addition to the printability and physicochemical properties of the printed parts.

CHAPTER 2 – Literature review

2.1 Biomaterials

Any compound that "is designed to replace a part or a function of the human body in a safe, reliable, economic, and physiologically and aesthetically acceptable manner" can be considered a biomaterial [3]. In the case of hard tissue engineering applications (e.g., orthopaedic, dental, etc.) various types of biomaterials have been utilised in medicine: polymers, metals and ceramics [10], [26]–[29]. By definition any type of biomaterial must be able to mimic the original properties of the damaged tissue that is replacing and be at least inert in terms of physiological response [2], [10], [29]–[35]. Pure polymeric and metallic implants can efficiently perform both tasks when implanted in an affected area but are unable to actively contribute to the bone healing process [10], [27]–[29]. On the other hand, ceramic biomaterials – bioceramics – are able to facilitate and promote bone growth since they possess the highest degree of chemical affinity with natural bone [4], [28], [29]. Human hard tissue is mainly comprised of hydroxyapatite (a calcium phosphate ceramic compound), collagen and water [26]. A detailed overview of the human hard tissue composition can be found in Table 2.1.

Table 2.1: Chemical composition of bone (wt. %), reproduced from [8]

Inorganic constituents		Organic constituents	
Hydroxyapatite	60 wt.%	Collagen	20 wt.%
Water	9 wt.%	Non-collagenous proteins	3 wt.%
Carbonate	4 wt.%	Polysaccharides, lipids, cytokines	Traces
Citrate	0.9 wt.%	Primary bone cells	Traces
Na^{+}	0.7 wt.%		
Mg^{2+}	0.5 wt.%		
Cl^{-}	0.13 wt.%		
K^{+}, F^{-}, Zn^{2+}, Fe^{2+}, Cu^{2+}, Sr^{2+}, Pb^{2+}	Traces		

Parts of this section are published as first-author and may contain replication from [1]

An important characteristic of any biomaterial is biocompatibility; it is related to the interaction between living tissue and the biomaterial itself. The different types for classification of biocompatibility can be found in Table 2.2. The successful integration of any biomaterial to a damaged area is dependent not only on biocompatibility but on other traits, too. A selection of the most important properties that biomaterials should exhibit can be found in Table 2.3.

Table 2.2: Biocompatibility classification, adapted from [3], [36]

Incompatible materials	Incompatible materials can release toxic substances in the body and/or initiate antigenes formation that may lead to reactions of the immune system such as allergies, inflammation or even septic rejection.
Biocompatible materials	Biocompatible materials can release substances to the body but not in toxic concentrations and trigger analogous body responses that range from benign tissue reactions (e.g. formation of a fibrous connective tissue capsule) to weak immune reactions (formation of giant cells or phagocyts). This class of materials is also known as biotolerant.
Bioinert materials	Bioinert materials do not release any toxic substances to the human body but do not exhibit any positive interaction with living tissues, as well. Usually, a connective tissue covers the surface of these materials (contact osteogenesis).
Bioactive materials	Bioactive materials interact in a positive way with living tissue and immature cells are transformed to bone cells, a process known as differentiation. The aforementioned process leads to bone growth (bonding osteogenesis). Bioactivity is classified in two types depending on the rate of bone growth and the ability of soft tissue bonding. In the case of Class A bioactive materials, osteogenesis occurs in a rapid manner and soft tissue bonds with the implanted object. Whereas Class B bioactive materials exhibit slower rates of bone bonding/growth and are unable to bond with soft tissue. [37], [38]

Table 2.3: Properties required by biomaterials for medical applications, reproduced from [8]

Property	Function
Biocompatibility	The ability of a material to perform with an appropriate host response in a specific application.
Bioactivity	The inherent ability of a material to participate in specific biological reactions or have an effect on living tissues.
Bioactive fixation	Reactive surfaces form chemical bonding with bone, thus minimizing the fibrous capsule formation.
Biostability	The ability of a material to maintain its properties in vivo.
Crystallinity	Higher level of crystallinity prevents fast resorption (dissolution) of the bioceramic in body fluid.
Osseointegration	Direct anchorage of an implant by the formation of bony tissue around it without growth of fibrous tissue at the bone/implant interface.
Osteoconduction	Ability to provide a scaffold for the formation of new bone.
Osteoinduction	The process by which osteogenesis is induced. This term means that primitive, undifferentiated and pluripotent cells are somehow stimulated to develop into the bone-forming cell lineage.
Resorption	Gradual degradation over time to replace the biomaterial with the natural host tissue.
Wettability	The property that indicates a material's ability to attract/repel water molecules.

2.2 Hydroxyapatite

Hydroxyapatite [$Ca_{10}(PO_4)_6(OH)_2$] is a ceramic material widely used in the biomedical sector as a bone-substitute material. It is the most prominent member within the calcium phosphate group, due to its close affinity to natural bone. After all it is the main inorganic constituent (mineral phase) found in human bone and teeth along with collagen and traces of other organic substances.

Stoichiometric hydroxyapatite has a calcium to phosphorus atomic ratio of 1.67 and exhibits a monoclinic crystallographic structure ($P2_1/b$, a = 9.421 Å, b = 2a, c = 6.881 Å). However, the hexagonal phase ($P6_3/m$, a = b = 9.432 Å, c = 6.881 Å) is mostly observed in medicine and biology for two main reasons: a phase transition from monoclinic to hexagonal occurs at temperatures above 250 °C and the latter phase is more stable at room temperature than the monoclinic [8], [39].

Because of its bioactive character, hydroxyapatite has been vastly utilised in various biomedical applications regarding bone repair or tissue engineering. HA exhibits suitable chemical/corrosion resistance for such applications and it is extremely stable in terms of resorbability. In most cases it remains stable when in contact with bodily fluids or is minimally resorbed if low crystallinity HA is used. However, the poor mechanical properties of pure hydroxyapatite, attributed to high strength ionic bonds, make this material incompatible for load-bearing applications. That is the main reason behind its frequent use in conjunction with different materials that enhance its mechanical properties such as alumina, zirconia, biocompatible glasses, polymers or other calcium phosphates [4]–[9].

Tricalcium phosphate (TCP) polymorphs are frequently utilised in biomedical engineering, too. They are more resorbable than HA and exhibit a Ca/P ratio around 1.5; the most prominent phases within their group are α and β-TCP. The former can be considered a high temperature phase of β-TCP, due to a phase transformation that occurs above 1125 °C. Its resorbability is much faster than the threshold for new bone formation, hence its use in biomedical applications is limited. On the other hand, β-TCP is used much more extensively as a bone substitute material due to its suitable resorption rates in the implanted area. The resorption rate can be further optimised with the use of a biphasic calcium phosphate (BCP) compound

comprising of HA and β-TCP; it has been shown that a ratio of 20 wt.% HA – 80 wt.% β-TCP, exhibits optimal results in terms of bioactivity [8], [39].

A selection of physicochemical and mechanical properties for natural bone and calcium phosphates can be found in Table 2.4.

Table 2.4: Physicochemical and mechanical properties for natural bone and calcium phosphates [8], [27], [30]

	Young's modulus (GPa)	Tensile strength (MPa)	Compressive strength (MPa)	Fracture toughness ($MPa \cdot m^{1/2}$)	Density (Kg/m^3)
Hydroxyapatite	35 – 120	120 – 900 (dense) 2 – 100 (porous)	350 – 450	0.7 – 1.2	3.155
β-TCP	33 – 90	-	460 – 687 (dense)	-	3.067
α-TCP	-	-	-	-	2.814
Cortical bone	7 – 30	50 – 150	167 – 193	2 – 12	1.6 – 2.1
Trabecular bone	0.05 – 0.5	1.2 – 20	1.9 – 10	0.1	-

2.3 Glass

Glass is a versatile family of materials that has been utilised by mankind for millennia; archaeological findings suggest that glass objects were used since 12000 BC in Egypt [40], [41]. The etymology of the word glass can be traced back to the late-Latin term *glaseum*, which was synonymous to a shiny, durable and transparent material; vitreous, originating from *vitrum* in Latin, is another term referring to such objects, too.

The description of glass from a scientific point of view is not revolving around the lustre or transparency but focuses mainly on the intrinsic and structural properties of such materials. More specifically, the definition of glass according to standard C162 − 05 of the American Society for Testing and Materials (ASTM) is: "*an inorganic product of fusion that has cooled to a rigid condition without crystallizing*" [42]. The definition refers to the traditional route of

glass production, where inorganic oxide components, usually silicon oxide, are melted and then rapidly quenched, to create an amorphous material.

However, there are other routes of glass making that do not require either inorganic precursors or melting of any sort, such as sol-gel or vapour deposition for instance [40], [41], [43]. Hence, a broader term for defining glass can be identified utilising universal glass characteristics, indifferent to the glass formulation or synthesis technique. The absence of long-range periodicity in their atomic structure is one such trait that every known glass exhibits. Additionally, another characteristic behaviour observed in such systems is the existence of a time-dependent glass transformation behaviour. Glasses can reversibly revert from solid to liquid state and vice versa without compromising their amorphous state, if specific heating and cooling rates are observed. Thus, a more inclusive definition could be that glass is “an amorphous solid completely lacking in long range, periodic atomic structure, and exhibiting a region of glass transformation” [40].

2.3.1 Glass structure

Since glasses are amorphous with no long-range periodicity, adding the word structure next to the term glass can be considered even contradictory. However, glasses do indeed exhibit some level of “orderly” behaviour, since their atomic structure could be described as crystalline with random defects in their “lattice” in terms of atom positions, bond lengths, angles, rotations, etc. A 2D representation of the glass and crystalline atomic structure of a hypothetical compound sharing the same composition of R_2O_3, 2 cations (R) and three oxygens (O) atoms, can be seen in Figure 2.1 [41].

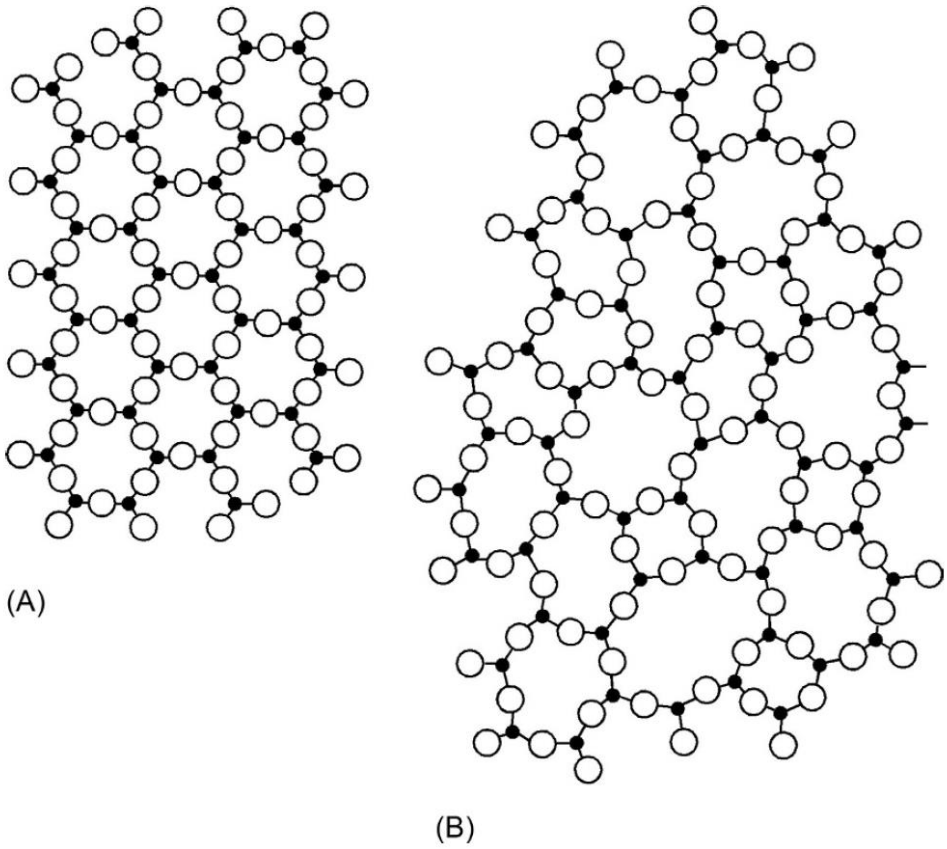

Figure 2.1: Atomic structural representation of (A) R_2O_3 crystal and (B) R_2O_3 glass, reproduced from [41].

Many scientists have tried to conceptualise the theory behind the formation of glasses. Goldschmidt in 1926 was one of the first theorists behind this, identifying a correlation between the ionic radius ratio of the cation and the oxygen ion. He suggested that glasses that could be described by the general formula of R_mO_n with a cation – oxygen ion ratio between 0.2 to 0.4, formed easier. Usually, within the proposed ionic ratio range, a cation is surrounded by four oxygen atoms forming tetrahedral building blocks. Essentially, he believed that glasses could only be formed if such tetrahedral components were present within the atomic structure. However, this was empirical and true in cases of glasses comprising of SiO_2 or GeO_2 (thus falling under the proposed ionic radius ratio rule) but not true in general. It was Zachariasen [44] in 1932 that took Goldschmidt's idea and further developed it. He suggested

that this criterium cannot be absolute for glass making since it is too limiting. A higher coordination number (i.e., additional neighboring ions within the glass structure, different angle bonds and geometry, etc.) could increase the disorder within the glass system, thus leading to glass forming. He came up with a set of rules regarding formation of glasses with a generic formula of R_mO_n that can be found in Table 2.5:

Table 2.5: Zachariasen's rules for glass formation, reproduced from [40]

Zachariasen's rules for glass formation
1. Each oxygen atom is linked to no more than two cations
2. The oxygen coordination number of the network cation is small
3. Oxygen polyhedra share only corners and not edges or faces
4. At least 3 corners of each oxygen polyhedron must be shared in order to form a 3-dimensional network

The aforementioned nomenclature, known as the Random Network Theory, is the most commonly used in describing glass structures nowadays [40]. Other theories regarding glass formation emerged soon after Zachariasen. Smekal suggested that glass forming is only attainable when the glass components bond both covalently and ionically. Pure ionic bonds cannot facilitate the formation of network structures and just covalent bonding tend to form periodic structures. Stanworth utilised Smekal' s bond theory and divided cations in three different categories, based on their electronegativity. Cations with high electronegativity were classified as network formers; such elements bond poorly ionically with oxygen anions, thus securing the formation of a network structure. Glass components that bond strongly in an ionic manner with oxygen, do not have the ability to form glasses by themselves. They are known as glass modifiers since they can only modify the network structure. Finally, elements which exhibit intermediate electronegativity and bond ionically with oxygen in a higher degree than glass formers and less than glass modifiers, are called intermediates. Those cations

cannot form glasses by themselves but can replace a network former or glass modifier if required. Similar classifications have been proposed by other scientists taking into account different criteria, such as: field strength by Dietzel, bond strength by Sun or temperature and bonding energy by Rawson [40], [41], [43].

A list of selected physical properties of glass formers, intermediates and modifiers can be found in Table 2.6.

Table 2.6: Physicochemical properties of glass formers, intermediates and modifiers [41], [43], [45]

	Ion	Electronegativity (Stanworth)	Ionic bonding of oxide (%) (Smekal)	Coordination number (Zachariasen)	Field strength - $2z/a^2$ (Dietzel)	Single bond strength (kcal) (Sun)	Single bond strength/melting point (kcal/K) (Rawson)
Glass formers	P^{5+}	2.1	39	4	4.3	88 – 111	0.104 – 0.131
	B^{3+}	2.0	42	3	3.22	119	0.164 or 0.122
	Si^{4+}	1.8	50	4	3.15	106	0.053
	Ge^{4+}	1.8	55	4	2.65	108	0.078
Intermediates	Al^{3+}	1.5	60	4	1.69	53 – 67	-
	Be^{4+}	1.5	60	4	1.51	63	-
Glass modifiers	Mg^{2+}	1.2	70	6	0.95	37	0.013
	Zn^{2+}	-	-	4	0.91	36	
	Ca^{2+}	1.0	75	8	0.69	32	0.011
	Sr^{2+}	1.0	75	8	0.58	32	-
	Pb^{2+}	-	-	6	0.53	39	-
	Ba^{2+}	0.9	80	8	0.51	33	0.015
	Li^{+}	1.0	75	4	0.45	36	-
	Na^{+}	0.9	80	6	0.35	20	-
	K^{+}	0.8	81	9	0.27	13	
	Cs^{+}	0.7	82	12	0.22	10	

2.3.2 Glass making

Glasses can be fabricated via numerous methods with the most frequent one being the melt-quenching approach [46]–[48]. The glass components, usually in powder form, are weighed according to the desired stoichiometry, are mixed thoroughly and then placed within crucibles made from heatproof materials able to withstand temperatures ≥ 1000°C, such as porcelain or platinum. Afterwards they undergo a heat treatment within a furnace until all the components are fully melted and then a rapid quenching step takes place. The glass melt is quenched either on objects with high heat dissipation capacity (e.g., stainless steel slabs) or poured in tanks filled with de-ionised water [37], [43], [46]. Such quenching techniques, usually employed during the development of simple glass systems, are able to achieve cooling rates of ~10^3 K/s [49]–[51]. However, more complex glass systems in terms of glass formation, such as metallic glasses, require higher cooling rates (~ 10^5 – 10^8 K/s) [41], [49], [50]. In such cases, more advanced techniques are utilised, such as melt spinning or laser-assisted processes [41], [49], [50]; the latter can achieve cool rates greater than 10^{12} K/s [41]. A method that has been gaining a lot of attention in recent years is the sol-gel approach. It is a wet chemistry method where glass precursors are mixed and treated in a variety of ways that leads to the creation of a 3-dimensional structure via gelation [37], [43], [46]–[48]. Main advantages of sol-gel derived glasses include enhanced homogeneity, lower processing temperatures and higher specific area compared to traditionally prepared glasses. Moreover, they exhibit higher reactivity rates, a trait linked with specific area, which could be problematic if not properly controlled. The latter along with limitations in preparing complex glass systems with this method (e.g., ternary systems including Na_2O), are the main bottlenecks hindering the wider adaptation of sol-gel glasses compared to melt-derived ones [47].

2.3.3 Bioactive glasses

Larry B. Hench, the father of bioactive glasses, was the person responsible for opening the path to what is nowadays called regenerative medicine. Before his discovery of the first bioactive glass – Bioglass – in 1969 at the University of Florida, all the biomaterials used in medicine at that point were bioinert at best. The biomaterials introduced within the body at that era were either metallic or polymeric and were either rejected or unable to bond with the injured tissue. [37], [52]

With the invention of Bioglass (or 45S5), a silicate-based glass, this changed tremendously. This type of new material had the ability of bonding with hard tissue and additionally promoting bone growth. The mechanism behind the enhanced bioactivity is attributed to the partial transformation that occurs on the surface of the Bioglass implant to hydroxycarbonate apatite (HCA) – and later to hydroxyapatite – along with the dissolution of certain ions in the affected area. More specifically, HCA has a high affinity with natural bone and interacts strongly with collagen fibrils binding the implant to the hard tissue. Additionally, dissolved calcium, silicon, phosphorus and sodium ions have the ability to stimulate osteogenic cells and kickstart the healing process. [37], [46], [52], [53]

Since the discovery of Bioglass, multiple bioactive glasses have been synthesised either comprising of similar building blocks (i.e., silicate-based) or different ones such as borate or phosphate-based glasses. Each glass family has unique characteristics in terms of biocompatibility, healing rate and applications.

2.3.3.1 Silicate glasses

Silicate-based glasses are mainly composed of SiO_2 tetrahedrons that form a 3D glass network. The most well-known member of this glass family is 45S5 which has been in use since 1969. It is based on the Na_2O-CaO-SiO_2-P_2O_5 system containing mainly SiO_2 (46 mol%), almost equal portions of Na_2O (24.4 mol%) and CaO (26.9 mol%) and a small amount of P_2O_5 (2.6 mol%) [46], [53]. This formulation has been used extensively over the past 50 years for orthopaedic reconstructive surgeries in over 1 million patients [53]. Additionally, 45S5 has been used in oral care products designed for treating hypersensitivity or as bioactive coatings in dental implants [37], [46], [48], [53], [54]. A compositional diagram of bone bonding regarding 45S5 can be found in Figure 2.2.

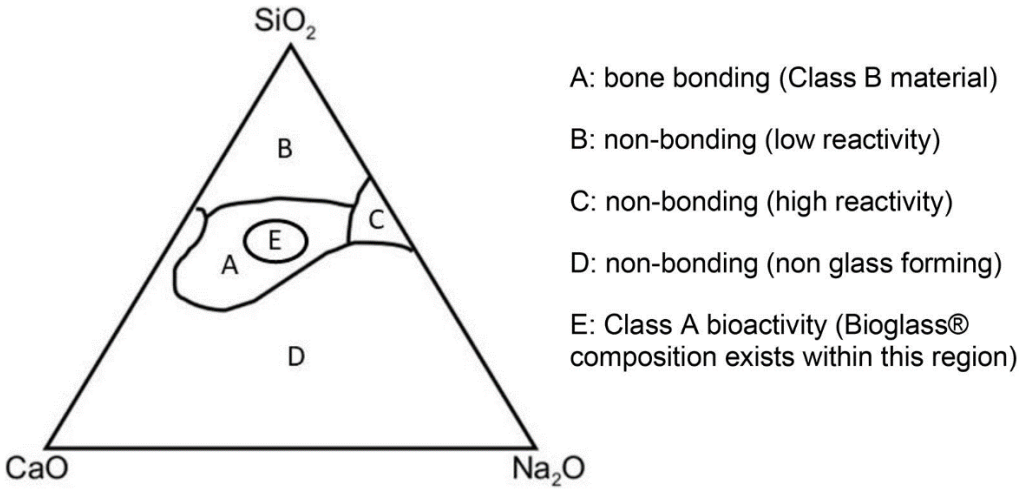

Figure 2.2: Compositional diagram for bone bonding, reproduced from [37].

Other significant members of the silicate family are the S53P4 and 13-93 compositions. Commonly tested silicate-based bioactive glasses compositions are presented in Table 2.7.

Table 2.7: Commonly tested silicate-based bioactive glasses compositions

	SiO_2 (mol%)	CaO (mol%)	Na_2O (mol%)	P_2O_5 (mol%)	K_2O (mol%)	MgO (mol%)
45S5	46	26.9	24.4	2.6	-	-
S53P4	53.8	21.8	22.7	1.7	-	-
13-93	54.6	22.1	6	1.7	7.9	7.7
Biosilicate	48.5	23.75	23.75	4	-	-
CEL2	43.8	23.6	15.0	6.9	6.1	4.6

2.3.3.2 Phosphate glasses

Phosphate glasses are P_2O_5 rich compositions and have been systematically researched since the 1980s. PO_4 tetrahedral units are the main building blocks of this family of glasses and usually do not form three-dimensional networks. The chemical durability of phosphate glasses is fairly low, due to the inherent asymmetry in the PO_4 tetrahedrons, and they tend to dissolve when in contact with body fluids; the rate of dissolution is usually controlled via doping with metal oxides. They are usually utilised either as controlled drug releasing carriers or as bioresorbable scaffolds with tailored dissolution rates promoting a more natural bone healing procedure. Lastly, phosphate glass fibers have been investigated in the fields of nerve and skeletal muscle regeneration [46], [53], [54].

2.3.3.3 Borate glasses

Borate-based bioactive glasses have been investigated widely since the early 2000s. They exhibit high levels of bioactivity and hard tissue repairing capacity, in some cases outperforming even silicate-based glasses [48], [54]. They tend to form a vastly planar “3D” glass network, due to weak binding forces in the third dimension, comprising of trigonal planar and tetrahedral units, BO_3 and BO_4 respectively. Borate glasses tend to have specific traits that

makes them suitable for wound healing applications [48], [54], [55]. More specifically, they convert faster and fully to hydroxyapatite compared to silicate glasses [46], [48], [56]. Moreover, they tolerate heat treatments without crystallising, providing a broader process windows and higher bioactivity rates [57]. Additionally, dissolved boron ions in body fluids streams promote cell proliferation and osteogenesis and prevent oxidation and inflammation. However, studies have shown that there is a threshold upon which boron concentration can become cytotoxic. This threshold has a broad range among different studies (e.g., 0.65mM [58] – 2.96 mM [59]) and is dependent upon the testing environment (i.e., in-vitro or dynamic conditions) [48].

Lastly, borate-based glasses with additions of SiO_2 (i.e., borosilicate), bridge both worlds in terms of bioactivity and crystallisation behaviour. They are more stable than both pure borate and silicate glasses and can withstand heat treatments without crystallising and/or losing their bioactive behaviour [57]. Commonly tested borate-based bioactive glasses compositions are presented in Table 2.8.

Table 2.8: Commonly tested borate-based bioactive glasses compositions

	B_2O_3 (mol%)	CaO (mol%)	Na_2O (mol%)	P_2O_5 (mol%)	K_2O (mol%)	MgO (mol%)
45B5	46.1	26.9	24.4	2.6	-	-
B53P4	53.85	21.77	22.66	1.72	-	-
13-93B	54.6	22.1	6	1.7	7.9	7.7

2.3.3.4 Doped bioactive glasses

Besides the standard building blocks of each bioactive glass that provides a function within each glass system, researchers have investigated the utilisation of additional elements within the glass structure. Upon dissolution within physiological fluids, the ionic product of those elements is able to enhance bioactivity and/or add favourable properties in terms of mechanical reinforcement and antibacterial activity, among others [30], [56], [60], [61]. A schematic representation of this process is shown in Figure 2.3.

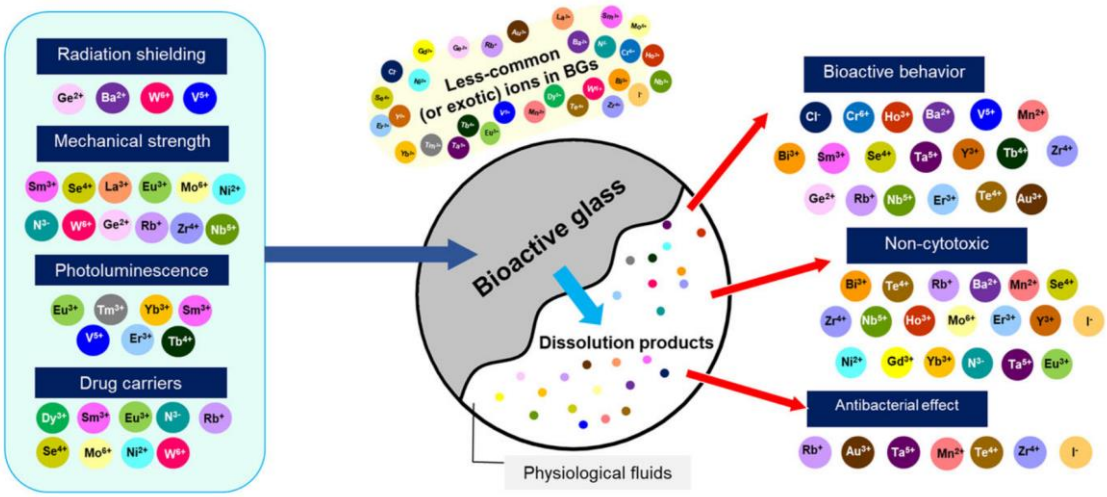

Figure 2.3: Bioactive glass doping, reproduced from [60].

"Traditional" elements utilised in this regard are gold, lithium, cobalt, calcium, copper, zinc, strontium, iron, magnesium and gallium, inter alia [56], [62]–[64]. In recent years, the addition of less common ions in bioactive glasses, and mainly rare earth elements has gained increased attention [30], [56], [60]. Utilising such elements can facilitate the addition or enhancement of physical and biological properties, such as angiogenesis, cell attachment and proliferation, antimicrobial behaviour and mechanical strengthening. Selected bioactive glasses compositions utilising rare earth elements, focusing on the doping effect and applications, are presented in Table 2.9.

Table 2.9: Selected bioactive glasses compositions utilising rare earth elements, reproduced (inc. references) from [60]

Ion	Glass composition	Application	Effect	Reference
Dysprosium (Dy)	61.2 B_2O_3–8.8 Li_2O–61.2 Dy_2O_3 (wt.%)	Drug delivery and radiation therapy	Controlling drug release	[65]
	50 SiO_2–30 CaO–10 Fe_2O_3–10 Dy_2O_3 (mol%)	Radiotherapy and hyperthermia	Radiothermal activity	[66]
Europium (Eu)	70 SiO_2–20 CaO–5 P_2O_5 with 5 Eu_2O_3 (or Tb_2O_3) (mol%)	Bone regeneration and drug delivery	Photoluminescence properties, Controlling drug release	[67]
	100 SiO_2 with 1, 2, and 3 Eu_2O_3 (mol%)	Skin and bone regeneration	Promoting osteogenesis and angiogenesis potential	[68]
	SiO_2–CaO–P_2O_5 with 5 Eu_2O_3 (mol%)	Drug delivery	Photoluminescence properties, Controlling drug release	[69]
	60 SiO_2–36 CaO–4 P_2O_5 with 0, 0.5, 1, and 2 Eu_2O_3 (mol%)	Bone regeneration	Increases cell viability	[70]
	80 SiO_2–16 CaO–4 P_2O_5 with 1, 2, and 3 Eu_2O_3 (mol%)	Cell imaging and bone regeneration	Increases apatite-forming bioactivity	[71]
	80 SiO_2–15 CaO–5 P_2O_5 with 0, 1, 2, and 5 Eu_2O_3 (mol%)	Cell imaging and bone regeneration	Increases the expression of ALP, COL1, and Runx2 genes and promoted osteogenic differentiation of BMSCs	[70]
Gadolinium (Gd), Ytterbium (Yb) and Thulium (Tm)	47.28 SiO_2–31.39 Na_2O–15.33 CaO–6 P_2O_5 with 2.5 Gd_2O_3 or Yb_2O (wt.%)	Tissue engineering	Increases glass durability, Biocompatible behaviour, Promoting proliferation and differentiation of rBMSCs cells and human exfoliated deciduous teeth (SHED)	[72]
	SiO_2–CaO–Gd_2O_3 with the Ca:Gd molar ratios 3:1 and 5:1	Bone regeneration	Promoting proliferation and differentiation of rBMSCs cells and human exfoliated deciduous teeth (SHED), Promoting newly formed bone	[73]

			and collagen deposition in rats, calvarial defect model, after 12 weeks post surgery	
	84 SiO_2–12 CaO–4 P_2O_5 with the Ca:Gd molar ration 3:1, 5:1, and 7:1	Bone regeneration	Promoting proliferation and differentiation of rBMSCs cells and human exfoliated deciduous teeth (SHED)	[74]
	47.28 SiO_2–31.39 NaO_2–15.33 CaO–6 P_2O_5 with 2.5 Gd_2O_3 or 2.5 Yb_2O_3 or 0.5 Fe_2O_3 (wt.%)	Biomedical applications	Glass network modification	[75]
	63 SiO_2–37 CaO with 0.15, 0.3 and 0.5 Tm_2O_3 and 0, 1, 2, 3 and 4 Yb_2O_3 (mol%)	Regenerative medicine or drug delivery	Decreases the average particle size, Photoluminescence properties	[76]
Holmium (Ho)	58 SiO_2–33 CaO–9 P_2O_5 with 1.25, 2.5 and 5 Ho_2O_3 (wt.%)	Brachytherapy	Promoting preosteoblast cell proliferation, Biocompatible behaviour, Bioactive behaviour	[77]
	58 SiO_2–33 CaO–9 P_2O_5 with 1.25, 2.5, 3.75, and 5 Ho_2O_3 (wt.%)	Brachytherapy	Bioactive behaviour	[78]
Lanthanum (La)	67 SiO_2–5 Na_2O–24 CaO–4 P_2O_5 with 5 La_2O_3 (or CuO) (mol%)	Tissue engineering	Increases compressive strength	[79]
	64.4 SiO_2–2.48 Na_2O–21.53 CaO–4.55P_2O_5 with 0, 1, 3 and 5 wt.% La_2O_3 (or/and CuO)	Tissue engineering	Biocompatible behaviour, Increased cell viability	[80]
	25 Na_2O–25 CaO–50 P_2O_5 with 5 and 10 La_2O_3 (mol%)	Drug delivery	Faster phosphate ionic release, Controlling drug release, Biocompatible behaviour	[81]
	58 SiO_2–38 CaO–4 P_2O_5–1 La_2O_3 (wt.%)	Bone regeneration	Biocompatible behaviour, Mechanical reinforcement	[82]
	20 Na_2O–14 CaO–66 P_2O_5 with 0, 0.1, 0.3, 0.7 and 1 La_2O_3 (mol%)	Tissue engineering	Biocompatible behaviour, Antibacterial effect against Gram positive bacteria, Mechanical reinforcement	[83]

Samarium (Sm)	45 SiO_2–24.5 Na_2O–24.5 CaO–6 P_2O_5 with 0, 1, 2, 3, and 4 Sm_2O_3 (wt.%)	Bone regeneration	Increases density, Young's modulus, bulk modulus, and shear modulus, Increases apatite-forming bioactivity	[84]
	46.1 SiO_2–24.4 Na_2O–26.9 CaO–6 P_2O_5 with 0, 0.2, and 2 Sm_2O_3 (wt.%)	Tissue engineering	Photoluminescence properties	[85]
	SiO_2–CaO–P_2O_5 with 0, 0.5, and 1 Sm_2O_3 (mol%)	Bone cancer	Increases apatite-forming bioactivity, Controlling drug release	[86]
	45.6 SiO_2–24.4 Na_2O–26.9 CaO–2.6 P_2O_5 with 0.5 Sm_2O_3 (mol%)	Biomedical applications	Photoluminescence properties	[87]
	10 Na_2O–15 CaO–65 P_2O_5–15 CaF_2 with 0, 0.5, 1, and 2 Sm_2O_3 (mol%)	Bone regeneration	Biocompatible behaviour, Improved osteoblastic cell response, Antibacterial effect against Gram positive bacteria	[15]
Terbium (Tb) and Erbium (Er)	79.5 SiO_2–15 CaO–5 P_2O_5 with 0.5 and 1 Tb_2O_3 (mol%)	Bone regeneration	Biocompatible behaviour, Increases apatite-forming bioactivity	[88]
	53 SiO_2–6 Na_2O–20 CaO–4 P_2O_5–12 K_2O–5 MgO with 1, 3, 5 Tb_2O_3 or 1, 3, 5 Er_2O_3 or 0.5, 1.5, and 2.5 with co-doping Tb_2O_3 and Er_2O_3 (wt.%)	Bioimaging	Photoluminescence properties	[89]
Yttrium (Y)	6 Na_2O–20 CaO–4 P_2O_5–12 K_2O–5 MgO–52 B_2O_3–1 Y_2O_3 (wt.%)	Tissue engineering	Promoting proliferation and migration of adipose stem cells (ASCs)	[90]
	30 Na_2O–25 CaO–45P_2O_5 with 0, 1, 3, and 5 Y_2O_3 (mol%)	Radiotherapy	Glass network modification	[91]
	62.35 SiO_2–15.85 Na_2O–(20.80–x) CaO–1.0 P_2O_5 with x = 0 and 4.68 Y_2O_3 (mol%)	Radiotherapy	Glass network modification, Controlling glass degradation	[92]
	58 SiO_2–33 CaO–9 P_2O_5 with 10 Y_2O_3 (wt.%)	Radiotherapy	Controlling glass degradation, Increased bioactivity	[93]

2.4 Glass reinforced hydroxyapatite

Pure HA has been utilised in various hard tissue engineering applications with the majority focusing on non-load bearing conditions, such as middle-ear surgery or bone defect filler material. This is because of its inherent brittleness, low impact resistance and tensile strength; on the contrary compression strength is higher than that of human hard tissue [8]. A second phase is often incorporated within the HA matrix in order to enhance its mechanical or biological behaviour or even introduce new traits (e.g., antimicrobial activity). These second phases could be other calcium phosphates (BCP) [29], [39], [94], [95], polymers [8], [96] , alumina [97], [98] , zirconia [99], [100] or bioactive glasses [11], [101], [102].

Composite materials comprising of HA and bioactive glasses have gained increased attention in the last three decades [30], [47], [60]. It has been reported that small additions of glass as a second phase (≤ 10 wt.%) can substantially enhance the mechanical and biological performance of the prepared samples compared to pure HA. More specifically, the glass phase acts as a sintering aid and allows the preparation of almost fully dense samples [11]–[14], [30], [47]. This is possible due to a liquid sintering mechanism between the melted glassy component and HA. The two phases bond strongly together, allowing faster densification between the HA particles due to a decrease in the interface energy (compared to solid state sintering) [11], [47], [103], [104]. As a consequence, GR-HA composites exhibit better mechanical properties (e.g., hardness, compression strength) in comparison to the non-glass containing specimens [11], [47], [103], [104]. Additionally, the biological behaviour is further enhanced in case of GR-HA, due to the combination of two bioactive phases and the control over the resorption rates via adjustment of the composition and amount of the glassy phase [30], [47], [60].

Phosphate, silicate and borate-based glasses have been utilised as a second phase within GR-HA composites, since the early 90's. Santos and Knowles were the pioneers in this field and the first type of glasses to be investigated were calcium phosphate glasses due to their chemical affinity to HA (or TCP). In their numerous studies [12], [13], [101], [103]–[108], they identified a significant increase in the mechanical performance of GR-HA samples containing not more than 10 wt.% of the glassy phase. More specifically, there were cases were an increase of up of up to 200% in fracture toughness and 400% in flexular strength compared to pure HA was observed [101], [105], [108]; similar trend was reported in terms of microhardness, too [107]. Oktar et al. [102] observed similar trends in terms of compressive strength and hardness and suggested that 10 wt.% is the maximum loading for phosphate-based GR-HA composites; further increase in glass content led to sintering and densification problems [102]. Lopes et al. [109] and Oktar et al. [102], in different studies, reported that high additions of phosphate glass led to phase transformations α and β-TCP, that were responsible for the decreased mechanical performance. Tancred et al. [11] observed analogous results regarding high loadings of glass and suggested that the optimum loading content should be between 5 – 10 wt.%.

Ternary and quaternary phosphate-based glasses were investigated concurrently or sequentially with the aforementioned binary compositions in GR-HA composites. Improving the chemical affinity between hard tissue and the glassy phase, led the researchers in creating more complex glass compositions, incorporating numerous elements. In particular, several ionic substituions within the HA lattice, along with the presence of trace ions or elements deeply influence the biological response in the affected area. Na_2O, MgO, CaF_2, Al_2O_3, K_2O and SiO_2 were few of the compounds used. Santos and Knowles investigated the use of glasses belonging to Na_2O–CaO–P_2O_5 and Al_2O_3–Na_2O–CaO–P_2O_5 systems and higher apatite

decomposition rates were observed, in comparison to the binary system. The increased amounts of α and β-TCP was connected to the presence of sodium and increased glass reactivity was speculated to be the underlying cause. It is worth mentioning that the mechanical performance of the ternary GR-HA system was significantly worse than the binary ones [101], [104]. Goller et al. [102], came to symmetrical conclusions in terms of sodium addition in his study with similar binary and ternary GR-HA systems. The mechanical performance of specimens containing sodium modified glass was inferior compared to the binary $CaO–P_2O_5$ system. The authors concluded that sodium rich glasses do not favour mechanical reinforcement in GR-HA composites [102]. On the contrary, in a more recent study by Kapoor and Batra [110], a similar sodium-modified phosphate glass was employed and superior mechanical properties were observed in the sodium-rich GR-HA composite; the sodium influence in phosphate systems remains unclear. It was evident that such glass systems influence the sintering process both ways. The glass probably facilitates the appearance of α or β-TCP, that induces structural changes within the HA matrix leading to lower mechanical performance [12]. However, smaller grain growth was reported in specimens containing a glass secondary phase, a microstructural feature that provides mechanical reinforcement [12]. Moreover, Georgiou et al. observed analogous trends with similar glass systems; the amount of β-TCP phase increased with increasing amounts of glass content [13]. Lastly, attempts have been made to add additional elements within the glassy phase such as Mg [103], [106], [107], [111]–[113], Al [101], [104], [114] or F [106], [107], [111]–[113], [115]–[117], in order to miminise the phase transformations and/or act as stability agents.

In the case of GR-HA systems incorporating silicate glasses, enhanced bioactivity was the main reason behind the usage of such glass systems [30], [53]. Santos et al. was the first research

group investigating the utilisation of such glass systems, in the second half of 1990s [101], [104], [114]. Bioglass 45S5 was added in quantities not exceeding 5 wt.% and the authors observed similar phase transformations as with phosphate glasses (i.e., α and β-TCP) in addition to calcium phosphate silicate ($Ca_5(PO_4)2SiO_4$); the phenomenon was more prominent with higher sintering temperatures. Additionally, higher degrees of porosity and lower mechanical performance was reported compared to phosphate GR-HA samples. The evidence suggested that the silicate induced phase transformation was partially responsible for this behaviour. Goller et al. [118] in a following study, utilised slightly higher 45S5 glass content (≤ 10 wt.%) and heat-treated the GR-HA samples in two different sintering temperatures, 1200 °C and 1300 °C. Interesting findings came out from this study, since non-linear correlations in terms of sintering temperature and glass content were observed. More specifically, microhardness decreased when the samples where heat-treated at 1300 °C, regardless of the glass content. Additionally, a glass content increase from 5 to 10 wt.% led to a decrease in microhardness, regardless of the sintering temperature. Lastly, there was an increase in compression strength for samples containing higher amounts of glass when sintered at 1200 °C, whereas this trend was reverted in the higher sintering temperature. Once again, phase transformations were responsible for the deterioration of the mechanical properties. Calcium phosphate silicate was present in samples sintered at 1200 °C, while sodium phosphate dibasic heptahydrate ($Na_2HPO_4{\cdot}7H_2O$) was observed when sintering occurred at 1300 °C. Other research groups have investigated the utilisation of 45S5, even in higher quantities (≤ 50 wt.%) [119]–[121], and came up with analogous results [101], [104], [114].

The densification of such GR-HA system is hindered by crystallisation phenomena connected to the 45S5 glass phase [53], [118], [120]. Overcoming this vulnerability led researchers to investigate either derived 45S5 compositions or similar silicate-based glass systems, usually calcium or potassium rich [122]–[125]. Belluci et al. investigated such a silicate glass system and prepared GR-HA specimens containing up to 70 wt.% of glass [119], [126]–[128]. With this new type of formulation, the research team managed to sinter the samples around 800 °C, much lower than their 45S5 counterparts. The combination of the milder heat treatment with the optimised glass composition, prevented glass crystallisation and HA decomposition while exhibiting superior mechanical and biological performance.

Additionally, to the aforementioned solutions regarding the negation of crystallisation in silicate-based GR-HA systems, borate-based or borate-rich systems exhibit this behaviour, as well [53]. B_2O_3 generally stabilises glass networks (either in silicate or phosphate glasses) in terms of thermal behaviour and it has proven to enhance the biological performance, too [129]. Ivanchenko et al. were one of the first investigating the utilisation of borosilicate glasses in GR-HA systems [130]–[133]. The research group managed to produce samples with appropriate mechanical and biological performance but had to devise optimal sintering profiles in order to negate densification complications. It was observed that the sodium borosilicate glass composition they were using, was prone to boiling and releasing water vapour/carbon oxide products that led to pore formation. Hu and Miao [17], investigated the use of 50 wt.% Pyrex, a common borosilicate glass found in labware, in GR-HA systems. Their investigation showed that the glass phase promoted densification, prevented the decomposition of HA and enhanced the microhardness performance. Following studies utilising inert borosilicate glass compositions, almost identical to commercial window glasses, have been conducted by Gunduz et al. [134], Demirkol et al. [135] and Youness et al. [136].

The composites exhibited higher degrees of sinterability and mechanical performance compared to pure HA. Studies by Abulyaziedet al. [14] and Alturki et al. [137] investigated the use of a borate-rich borosilicate glass, doped with gold and assessed the mechanical performance of the GR-HA specimens. Various glass loadings were tested, ranging from 0 to 32 wt.%, and mechanical reinforcement was reported with increasing amounts of glass.

An overview of the mechanical properties in selected GR-HA systems, can be found in Table 2.10.

Table 2.10: Mechanical properties in selected GR-HA systems

Composite	Glass (wt.%)	T_{sint} (°C)	Hardness (HV)	Compressive strength (MPa)	Young's modulus (GPa)	Fracture toughness ($MPa \cdot m^{1/2}$)	Flexural bend strength (MPa)	Reference
HA/CaO-P_2O_5	10	1200	285 ± 19	67 ± 17	-	-		[102]
HA/CaO-P_2O_5	5	1350	~500	-	-	~1	61.9 ± 7.5	[11]
HA/CaO-P_2O_5	10	1200	~300	-	-	~1.1	-	[11]
HA/CaO-P_2O_5	2.5	1300	-	-	-	1.6 ± 0.3	73 ± 13	[101]
HA/CaO-P_2O_5	5	1350	-	-	-	1.4 ± 0.2	96 ± 17	[101]
HA/CaO-P_2O_5	2.5	1300	-	-	-	1.2 ± 0.05	-	[104]
HA/CaO-P_2O_5	2.5	1250	~500	-	-	-	-	[11]
HA/Na_2O-CaO-P_2O_5	5	1300	358 ± 18	55 ± 14	-	-	-	[102]
HA/Na_2O-CaO-P_2O_5	2	1350	-		-	-	~105	[12]
HA/Na_2O-CaO-P_2O_5	2.5	1350	-	-	-	-	~140	[13]
HA/Na_2O-CaO-P_2O_5	2.5	1300	-	178.3 ± 21.9	-	-	-	[138]
HA/Na_2O-CaO-P_2O_5	10	1250	290 ± 12	67 ± 17	-	-	-	[110]
HA/Na_2O-CaO-P_2O_5	2.5	1300	-	-	-	1.1 ± 0.05	-	[104]
HA/Na_2O-CaO-P_2O_5	4	1350	500 ± 66	-	~95	1.45 ± 0.25	~115	[106], [107], [112]
HA/CaO-MgO-P_2O_5	2.5	1350	546 ± 34	-	~100	0.71 ± 0.21	~105	[106], [107], [112]

HA/CaO-MgO-P_2O_5	2.5	1350	579 ± 45	-	~100	0.68 ± 0.11	~160	[106], [107], [112]
HA/CaO-MgO-P_2O_5	2.5	1300	594 ± 35	-	~95	0.74 ± 0.15	~100	[106], [107], [112]
HA/CaO-MgO-P_2O_5	2.5	1100 (hot pressing)	693	-	117.87	1.23	88.87	[117]
HA/Na_2O-CaO-Al_2O_3-P_2O_5	2.5	1300		-	-	1.2 ± 0.06	-	[104]
HA/CaO-MgO-CaF_2-P_2O_5	4	1350	534 ± 45	-	~105	1.17 ± 0.24	~115	[106], [107], [112]
HA/CaO-MgO-CaF_2-P_2O_5	2.5	1350	555 ± 38	-	~100	0.69 ± 0.14	~115	[106], [107], [112]
HA/Na_2O- CaO-CaF_2-P_2O_5	10	1250	~295	~73	-		-	[115]
HA/45S5 (Bioglass)	2.5	1300			-	0.95 ± 0.04	-	[104]
HA/45S5 (Bioglass)	5	1200	472 ± 66	62.23 ± 20.29	-		-	[118]
HA/45S5 (Bioglass)	10	1200	383 ± 38	83.03 ± 33.95	-		-	[118]
HA/45S5 (Bioglass)	2.5	1300			-	1.7 ± 0.3	60 ± 11	[101]
HA/45S5 (Bioglass)	25	1200		131 ± 14	-	-	-	[139]
HA/Na_2O-K_2O-B_2O_3-Al_2O_3-SiO_2	50	1200	~325	-	-	-	-	[17]
HA/Na_2O-CaO-B_2O_3-Al_2O_3-P_2O_5-SiO_2	2.5	1300	411.6 ± 11.7	-	-	0.66 ± 0.04	-	[120]
HA/Na_2O-CaO-B_2O_3-Al_2O_3-P_2O_5-SiO_2	5	1350	251.5 ± 2.8	-	-	1.50 ± 0.10	-	[120]

HA/53S	30 – 50	600 – 800 (hot pressing)	-	-	-	-	~60	[140]
HA/Na_2O-K_2O-CaO-MgO-Al_2O_3-SiO_2	2.5	1200	156.4	40.61 ± 5.7	-	-	-	[141]
HA/Na_2O-K_2O-CaO-P_2O_5-SiO_2	70	818	299.1 ± 38.0	-	42.3 ± 4.8	-	-	[128]

Besides the mechanical performance improvement, GR-HA composites capitalise on the presence of the glassy phase biologically-wise, as well. The presence of elements such phosphorus, silicon, sodium or fluorine, have a positive impact on the bone healing process. Santos et al. [114] were one of the first research groups to investigate in vitro bioactivity of phosphate-based GR-HA systems in simulated body fluid solution (SBF), back in the mid-90s, and led the way for future studies [110], [125], [140]. Such tests attempt to simulate the interaction between potential biomaterials and an acellular solution mimicking the human plasma chemistry via assessing the ability to form an apatite layer on their surface while immersed [142], [143]. However, various researchers have expressed their concerns for such bioactivity tests, ever since their introduction. One of their main friction points was the fact that there are various processes/interactions between cells, proteins and human plasma that are not accounted for, hence making this test unrealistic to the true biological environment [144]. Additionally, there are cases (e.g., β-TCP) where biomaterials interact to a certain extent with bone tissue upon implantation but do not always showcase such a biological response (i.e., forming of an apatite layer) [145], [146]. Lastly, fast dissolution rates might provide a false-positive result in terms of bioactivity compared to similar or even more bioactive compounds exhibiting slower dissolution rates. A typical example is pure HA that compared to bioactive glasses or BCP, is much more stable and “fails” to form an apatite layer as fast as the latter [146]. Apart from all the resorption related properties, the SBF test is agnostic to intrinsic biocompatibility parameters related to surface characteristics (e.g., wettability, free energy charge, topography, etc.) [111], [147], [148]. That is the reason many researchers shifted towards more representative frameworks, such as in vitro osteoblast cell line assays [15], [113], [138], [149]–[153] or animal in vivo tests [154], [155].

The biocompatibility of GR-HA samples containing 2.5 wt.% of various ternary phosphate-based glasses was assessed in a study by Kalita et al. [138]. Osteoblast cell culture studies revealed no cytotoxic effects and a subset of the tested composites showed increased biocompatibility compared to pure HA. The aforementioned subset contained sodium within their glassy phase, an element linked with cell growth. Ferraz et al. [151]–[153] and Afonso et al. [156], arrived in analogous results during independent studies investigating the biocompatibility of GR-HA samples containing ternary and quaternary phosphate-based glass compositions, respectively. Similar studies have been conducted with fluorine rich phosphate-based GR-HA systems, since the fluorine presence is a well-established biological enhancing agent. Lopes et al. [157] conducted in vivo push out studies with such GR-HA samples and quantitively assessed the bonding strength between the host tissue and the implant. The composites containing up to 4 wt.% of a ternary phosphate glass doped with CaF_2, exhibited higher degrees of osteoconductivity compared to pure HA. Additionally, enhanced bone bonding ability was reported for the composites, too. A great amount of work has been carried out with a commercial GR-HA system, called Bonelike, containing 4 wt.% of quaternary phosphate glass system, enriched with both fluorine and sodium. Superior mechanical and biological performance over HA have been documented in various studies, both in vitro and in vivo [158]–[160]. Such behaviour can be attributed to the optimised phase composition profile of the compound, an optimal ratio between stable (HA) and resorbed phases (TCP) [113], [157], [160], [161].

Multiple studies were focused on investigating the biological effect induced by silicate-based glass systems in GR-HA samples. After all, such glass compositions were initially utilised in this framework, primarily for their well-established bioactivity [162]–[166]. In conjunction with the latter, silicate-based glasses have been reported to exhibit antimicrobial activity [167], [168]

while having an active role in promoting angiogenesis and neovascularization [169]–[171]. Santos et al. [114] in the mid-90s investigated the in vitro bioactivity of a GR-HA system containing 2.5 wt.% 45S5 glass. The silicate-based GR-HA samples showed higher degrees of dissolution and surface apatite formation, compared to pure HA and phosphate-based GR-HA system. It is worth mentioning that since this work, analogous results have been reported in various studies investigating similar silicate-based, mainly melt-derived, glasses [17], [119], [126], [128], [139], [172], [173]. Demirkiran et al. [139], [172] investigated the use of 45S5 glass either as a sintering aid or a secondary glassy phase, with varying glass loadings. In the first case, small quantities of 45S5 glass was introduced in GR-HA specimens (< 5 wt.%) and HA decomposition to β-TCP was reported. The authors speculated that the small amount of glass behaves as a heterogeneous nucleus site or a triggering point that promotes the β-TCP phase transformation. Increasing the glass content (> 5wt.%) resulted in different phase transformations, unrelated to HA decomposition but heavily connected to the glass components; calcium phosphate silicate and sodium calcium phosphate phases were reported this time. Both GR-HA specimens outperformed pure HA samples during an apatite formation test and a primary rat bone marrow stromal cells study; the composites containing lower glass loadings, exhibited inferior biological response than the glass-rich samples. Bellucci et al. [122]–[124] investigated the usage of a novel silicate-based glass composition, resistant to crystallisation, and carried out biocompatibility studies containing GR-HA with various glass loadings. Optimised GR-HA compositions (> 20 wt.%) and sintering profiles (~800°C) were employed, in order to prevent glass crystallisation, an event linked to reduced mechanical and biological performance. GR-HA specimens containing the novel silicate compositions, outperformed composites with the same amount of 45S5 glass, a golden standard in the biomaterials industry, in terms of bioactivity and cell culture response.

In recent years, a lot of effort has been focused on the utilisation of sol-gel silicate glasses in GR-HA systems. These types of glasses showcase high porosity and smaller particle size, portraying higher dissolution and apatite formation rates compared to traditionally manufactured melt-derived glasses. Due to their increased reactivity, tailored utilisation strategies are employed when used in GR-HA systems, in order to prevent phase transformations or inappropriate resorption rates [174]–[177]. Padilla et al. [174] investigated the biocompatibility of GR-HA specimens containing a sol-gel prepared 55S glass. The composites contained either 5 wt.% or 20 wt.% of this ternary silicate-based glass composition. GR-HA specimens showed higher biocompatibility rates compared to pure HA or the glassy phase on its own, revealing a synergistic role between the two phases. Analogous results were reported by Ragel et al. [178], in their study investigating the use of a different sol-gel silicate glass (i.e., 77S). SBF immersion tests showed increased bioactivity for the GR-HA composite samples compared to either phase tested individually.

Considerably fewer studies utilising borate-based glasses in GR-HA composites have been carried out, compared to either phosphate or silicate counterparts. Since the emergence of the topic of strengthening HA with a glass phase in the mid-90s, it was mostly solely phosphate and silicate glasses used. One of reasons behind this, could potentially be cytotoxicity usually associated with boron ions. Various studies have investigated this phenomenon and concluded that concentrations above a certain range can be cytotoxic (0.65mM [58] – 2.96 mM [59]). However, this concept is not validated in every case and test environments. Higher concentrations of boron ions have been reported to be not cytotoxic in dynamic conditions during in vivo studies [47], [137], [138]. Pinchuk et al. [179] investigated the solubility of GR-HA specimens containing biogenic or synthetic HA with high loadings (~ 50 wt.%) of a novel borosilicate glass. Suitable dissolution rates for hard tissue engineering applications were

reported in both cases; the GR-HA samples containing synthetic HA, could potentially be used as drug carriers due to their higher solubility, as per the authors' suggestion. Moreover, Youness et al. [136] investigated the biocompatibility of GR-HA samples containing high quantities of inert borosilicate glass (60 – 90 wt.%), either pure or doped with selenium. Both sets of GR-HA specimens exhibited suitable bioactivity during SBF immersion tests, while the selenium doped samples outperformed their non-doped counterparts. Lastly, Abulyaziedet al. [14] and Alturki et al. [137] investigated the use of a borate-rich borosilicate glass, doped with gold and assessed the bioactivity of the fabricated GR-HA specimens; multiple glass loadings were tested in each study, 0 – 20 wt.% [14] in one case and 0 – 32 wt.% in the other [137]. Increased bioactivity was reported in either case with increasing amounts of glass content during SBF immersion studies.

There have been attempts by various research groups, to further enhance the biological response of GR-HA systems by adding active ingredients within the glassy phase. The extra elements or compounds enhance the bioactive character even further, introduce antimicrobial activity or act as targeted therapeutic agents. Ionic substitutions within the HA matrix have been shown to stabilise against phase transformations and/or further enhance the bioactive behaviour of the composite. Elements containing similar electronegativity and ionic radius with calcium cations, are able to substitute them within the HA unit cell. Mg [103], [106], [107], [111]–[113], Al [101], [104], [114] or F [106], [107], [111]–[113], [115]–[117] are some of the elements "traditionally" employed for such applications. In recent years, rare earth elements have gained increased attention for usage in GR-HA, due to their ability to actively contribute in the bone healing process and the introduction of antimicrobial activity in certain cases [15], [16], [180]. Coelho et al. [16] utilised a novel phosphate glass system, doped with cerium and lanthanum, and investigated the biocompatibility of GR-HA specimens

containing 2.5 wt.% glass loadings. Increased cell adhesion and viability were reported for both lanthanide-containing GR-HA samples compared to pure HA specimens, during in vitro osteoblast cell culture studies. Morais et al. [15], in a similar study utilising samarium as an active ingredient, investigated the biocompatibility and the antimicrobial activity of GR-HA samples with a glass loading ranging from 0 – 2.5 wt.%. Composite samples containing the active lanthanide phase, outperformed their samarium-free counterparts during osteoblast cell culture studies. Additionally, samarium-doped composites exhibited antimicrobial activity towards Gram positive bacteria (Staphylococcus aureus & Staphylococcus epidermidis) but not against Gram negative (Pseudomonas aeruginosa), during a bacterial adhesion study. The same group investigated the use of a cerium in a similar study [180], with GR-HA samples containing 0 – 5 wt.% glass content. Similar results were reported in terms of biocompatibility during osteoblast cell culture studies; cerium-doped specimens outperformed pure HA and cerium-free GR-HA samples. In terms of antimicrobial behaviour, the authors reported analogous results with their previous study since the cerium-doped GR-HA specimens were only effective against Gram positive bacteria.

2.5 Additive manufacturing

The combination of modern manufacturing methods with novel bioceramic feedstocks is undoubtedly a promising framework towards personalised medicine. Custom regenerative tissue engineering services, tailor-made to a patient's needs, have the potential to be the paradigm shift in shaping the biomedical sector of the future. Generally, bone tissue related surgeries require the adaptation of pre-fabricated implants agnostic to the skeletal morphology of each patient. This approach can be troublesome for clinicians since each patient shares different skeletal characteristics. Additive Manufacturing (AM) techniques can undoubtedly aid towards this direction since a custom implant can be precisely fabricated to meet each patient's requirements, in an ad hoc manner. Such a process mainly comprises of four steps:

1) 3D scan of the affected area to acquire the geometry of the damaged part.
2) Analysis of the scanned area and digitisation of the implant to be fabricated.
    i. Digitising the part to be printed is a multi-step process. Initially, a digital file is created that holds all the information regarding the geometrical features of the part; .STL or .3MF, are typical formats. Subsequently, this file is further processed in slicer software where all the printing parameters are set (e.g., layer height, printing speed, etc.). Finally, a .gcode file is produced and uploaded to the printing platform.
3) Production of the tailor-made hard tissue specimen via AM methods.
4) Implantation of the AM fabricated implant.

A schematic approach showcasing the aforementioned process can be found in Figure 2.4 [181].

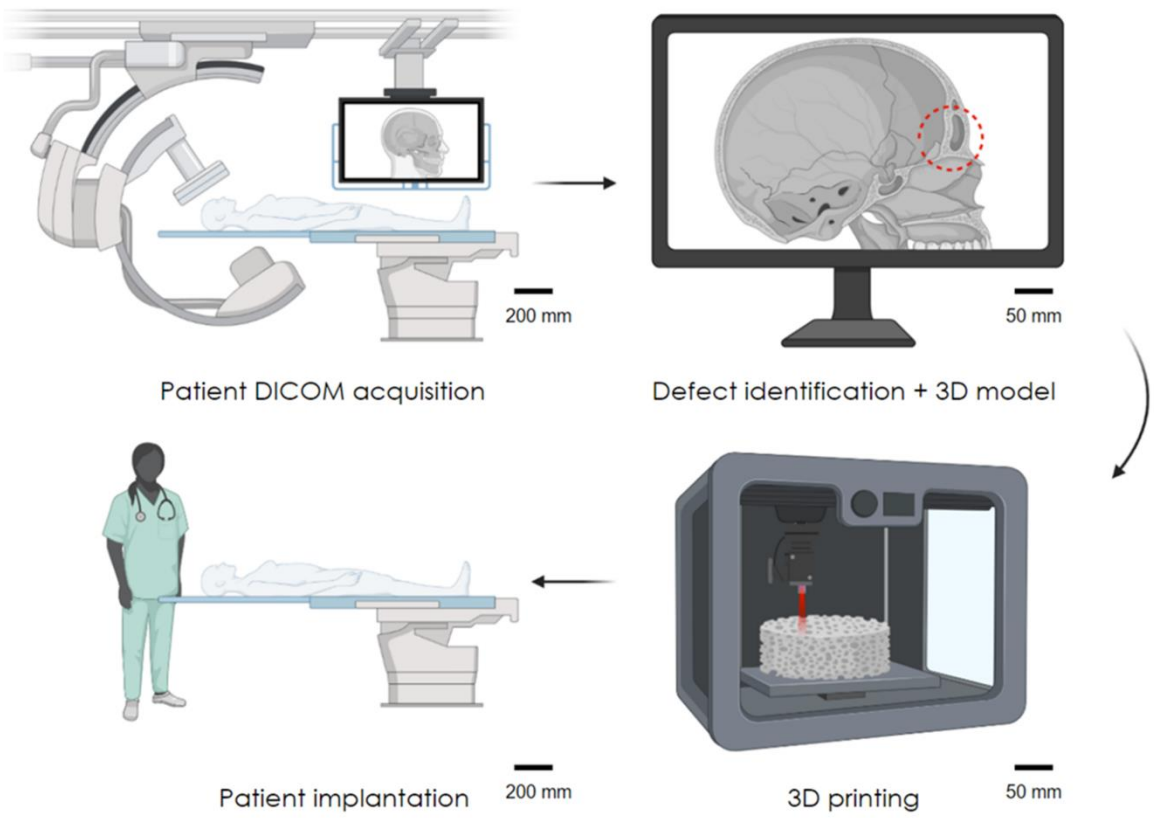

Figure 2.4: The process of personalised medicine with the use of Additive Manufacturing, reproduced from [181].

Additive manufacturing is a relatively new material processing route and it was initially commercially introduced with “Stereolithography” (SLA) by Chuck Hull, in the mid-80s [182]. Back then, polymeric prototypes of any sort, frequently required an engineering team, a design team, a machine shop and finally an injection moulder. If a revision was required, the whole process needed to start from scratch. With this invention, the same result was achieved much faster, at a fraction of the human resources required. An industrial unit equipped with a UV source would selectively fuse a photocurable resin in a layer-by-layer fashion, until the 3D prototype was developed. In recent years, additional families of AM methods have been introduced and the technology as a whole has matured enough to go beyond rapid prototyping purposes. Polymeric, metallic or ceramic production parts are currently realised in such manner.

The latest classification of all the different AM techniques, according to ISO/ASTM 52900, is presented in Figure 2.5 [183].

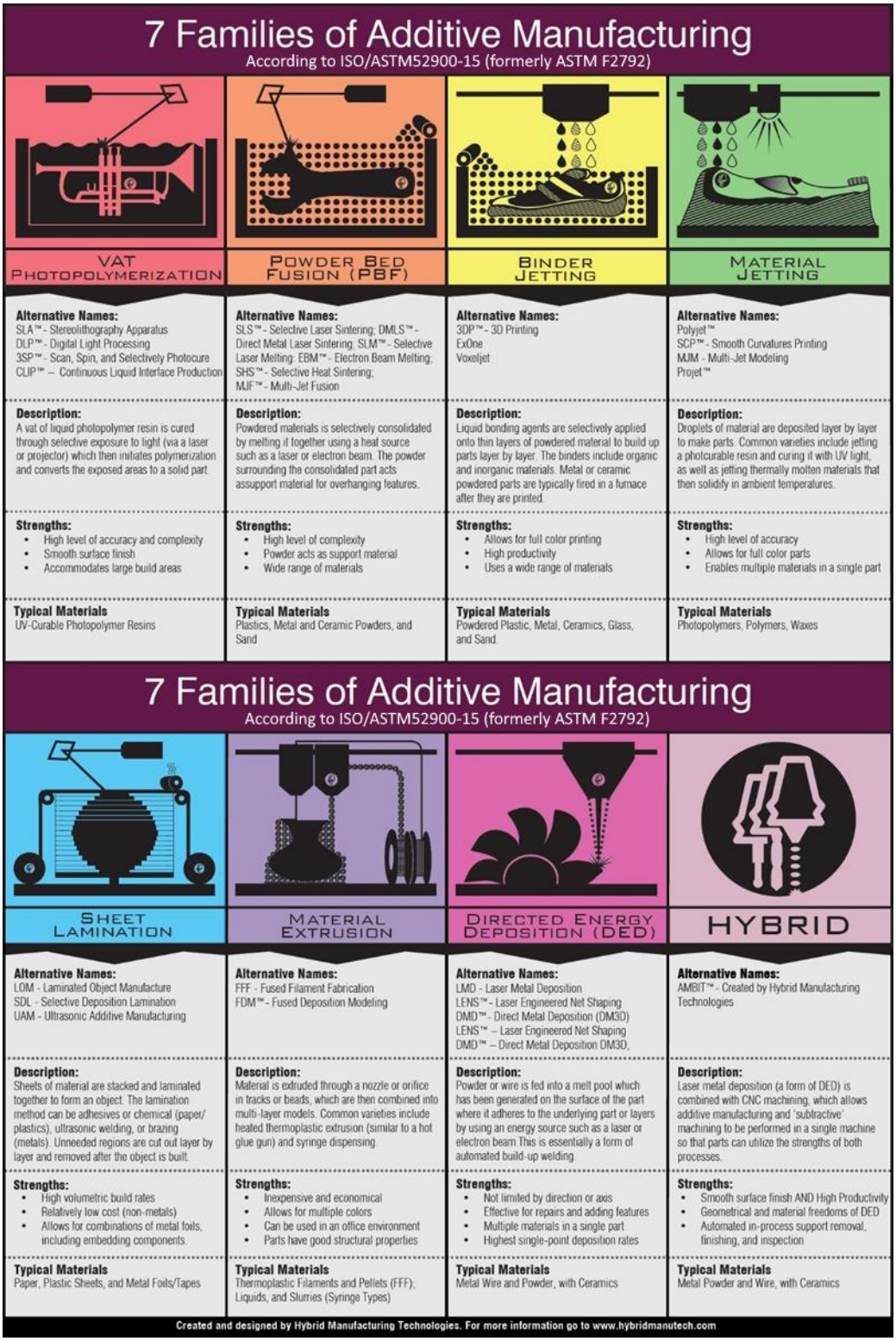

Figure 2.5: Classification of the AM techniques according to ISO/ASTM 52900 [183].

The diffusion of AM techniques within the biomedical sector has been relatively slow, compared to the rapid advancements in available printing platforms. The main reason behind this lag could be attributed to the scrutinous, but required, procedures surrounding medical applications and the lack of standardisation up to a certain extent. However, in recent years multiple steps forward have been taken towards this goal, as it can be seen in Table 1 at Bose et al. [184]. More specifically, since the early 2000s, various bone tissue engineering studies investigated the usage of AM techniques, such as: fused filament fabrication (FFF), stereolithography (SLA), direct ink writing (DIW) and selective laser sintering (SLS). Calcium phosphates, polymers and bioactive glasses were some of the materials covered in those studies. However, limited work has been carried out with GR-HA feedstocks [21]. A highly promising AM technique that fits this profile is selective laser sintering, where even less work has been conducted so far regarding the printability of GR-HA with SLS.

2.5.1 Selective laser sintering

2.5.1.1 Process overview

Selective laser sintering was developed in the 1980s, at the University of Texas by Carl R. Deckard and Joseph J. Beaman [18], [21], [185]–[187]. The technology was further developed by DTM, with the Rapidsteel process [188], [189], which was later acquired by 3D systems [21], [190]. SLS is a powder bed fusion AM technology in which a high power laser irradiates the powder bed and sinters the powder feedstock creating the geometric 2D pattern on every layer. The specifications of each layer and the printing process in general are included in the input file uploaded to the printer (i.e., .gcode file), as previously discussed. By the time the scanning of a layer is complete, the printing platform lowers to the desired layer thickness and a roller or a doctor blade introduces a fresh layer of untreated powder so the laser irradiation can start once again. The aforementioned process is repeated in a layer-by-layer fashion until

the desired 3D geometry is achieved; the unirradiated powder acts as supporting structure to the printed part, therefore no printed supports are required for this method. Lastly, any unbound powder is removed via a de-powdering process as soon as the printing is finished [191]–[198]. A schematic representation of the SLS process is shown in Figure 2.6 [199].

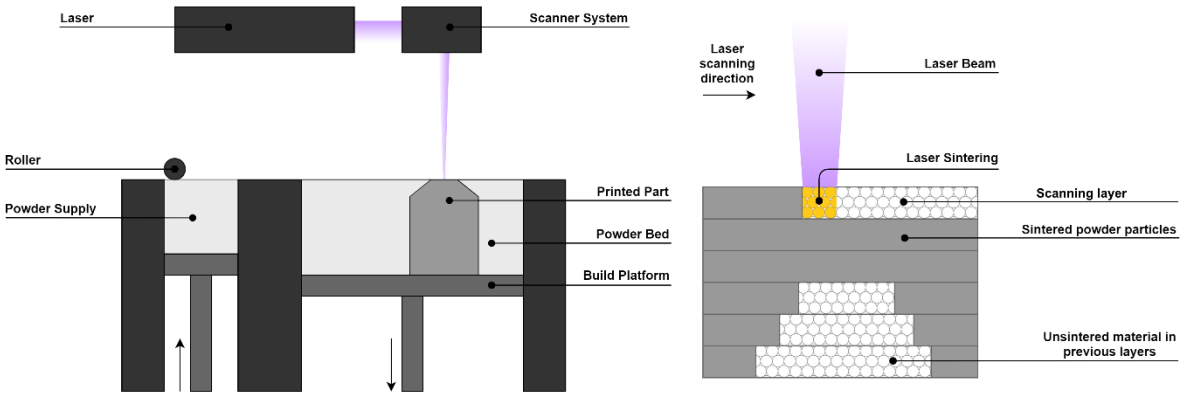

Figure 2.6: Schematic representation of the SLS process [199].

SLS can either be a single-step or a multi-step AM process. In the first case no post-processing is required for producing a part with the intended properties (e.g. mechanical properties, roughness, porosity, etc.), whereas extra processing steps are required in the case of the latter [200], [201]. Conventional sintering, hot/cold isostatic pressing and ceramic infiltration are the most common post-processing steps that the irradiated part (green body) undergoes post printing [191]–[198].

Thermal shock is a common issue during SLS processing due to the large thermal gradients realised on the printing bed during printing [202]–[204]. Extreme heating and cooling rates can have adverse effects (e.g., shrinkage, porosity, cracking, etc.) on the final properties of the printed part [202]–[204]. Various mitigation strategies are employed in order to minimise this phenomenon, with the most common being the use of a preheated powder bed/chamber [203]. Radiant and conductive heat transfer methods (or both) are used to heat the powder

bed to a suitable temperature [205]–[208]. The heating temperature depends on the powder feedstock but it is usually set just below its melting point. This applies to semi-crystalline polymers, metals and ceramics; in the case of amorphous polymers, the temperature is set just below their glass transition temperature [191], [209], [210]. As soon as the selected temperature is achieved, the SLS process proceeds normally with the scanning laser source irradiating the powder bed according to the part's specifications/geometry. Other mitigation strategies include the utilisation of slow cooling rates before the printed part is removed from the printing chamber. High cooling rates may induce similar adverse effects as previously described, including warping, cracking and shrinkage [203].

There are two approaches for producing parts with SLS:

In the first approach, often called direct SLS (dSLS) [186], [191], [198], [211], the feedstock is deposited on the work area either as dry powder or in slurry form; in both cases no binding agents are used. The densification of the part is achieved mainly through a solid state diffusion mechanism [21], [186], [205] and this justifies the popularity of this method with low-melting polymers and metals [186].

Processing ceramics via the dSLS approach can be challenging mainly due to the high temperatures required by the inherent refractory nature of the powder feedstock and the limited thermal shock resistance [186]. Minimising the thermal gradient during SLS processing is often achieved by the use of a preheated powder bed [193], [212], [213], as previously discussed. This has been achieved with the usage of defocused laser sources that heat the printing area just below the powder feedstock's melting point in the past [212], [214]. Other common issues with ceramic dSLS printed parts are high porosity or dimensional inaccuracies;

fast laser scanning can lead to low density parts while multiple scanning attempts can introduce geometrical irregularities [191].

The second approach is commonly used for high melting temperature materials, such as metals and ceramics; this method is usually referred to as indirect SLS (iSLS) and the feedstock deposition is similar to dSLS [186], [191], [198], [211], [215]. The fundamental difference between dSLS and iSLS is the incorporation of a low melting binding agent within the powder feedstock. The required geometry for a printed part is achieved via melting the binding agents that act as bonding elements between the primary powder particles. Common binding agents utilised in iSLS are organic compounds with a low melting temperature, but inorganic substances with similar thermal characteristics are used, as well. The most frequently used organic binders are thermoplastics (e.g. polyetheretherketone (PEEK), polycaprolactone (PCL)), thermosetting polymers, waxes (e.g. carnauba wax) and acids (e.g. stearic acid, etc.) [186], [198]. Moreover, low melting glasses and metal oxides have been used in the past as inorganic binding agents [25], [216], [217]. In the case of iSLS printed parts, the mitigation strategy of the preheated powder bed previously described is applicable, too. However, in this case the powder bed temperature is selected in regard to the binder's melting point rather than the powder feedstock component exhibiting a higher melting point [186], [191], [203].

This approach is highly advantageous compared to dSLS since the aforementioned substances require lower temperatures to be partially or fully melted and are more resilient to thermal shocks [186], [218]. The resulting green body is a composite material, comprising of the primary powder and the binder. In the case of organic binders, a debinding step is required before any further post-processing; the printed parts undergo a heat treatment that removes any traces of the binders. However, the use of large quantities of binding agents can lead to

significant shrinkage during the final post-processing step (i.e., sintering) [219]. Additionally, total binder removal can be problematic in large printed parts, leading to crack and porosity formation, unless appropriate measures are in place (e.g., slow debinding rates, integration of ventilation openings in the part's geometry) [187], [201], [220]. On the other hand, inorganic binders cannot be removed in such a way; they remain within the final product and form new phases with the primary material. Furthermore, they can act as sintering aids [17], [47], promoting the densification of the final product, and can provide additional functionality to the printed part (e.g., enhanced biological and antimicrobial properties [56]).

2.5.1.2 Process window

There are a number of parameters that influence the overall quality of ceramic parts manufactured by SLS such as the laser-powder interaction, the powder feedstock properties, the position and orientation of the part on the building platform and slicing parameters. More specifically, every material/composition has a different process window that can only be identified via experimentation. Laser wavelength, power, scanning speed and hatch distance heavily impact the quality of the printed parts and their values vary depending on the powder feedstock [21], [192], [194], [195], [221]–[224].

A schematic overview of the SLS process in a single layer is shown in Figure 2.7.

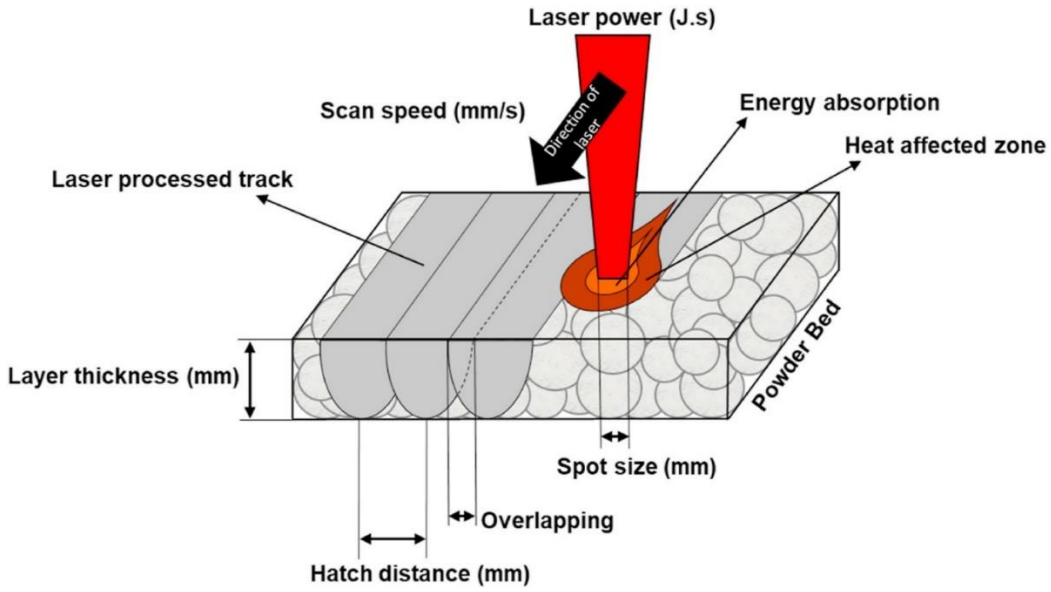

Figure 2.7: Schematic overview of the SLS process in a single layer [187].

The main parameters that influence the final properties of an SLS printed part can be found in Table 2.11.

Table 2.11: SLS printing parameters [1]

	Parameter	Description	References
Powder feedstock	Particle geometry Particle size distribution	Spherical particles with a particle size distribution that ranges from 10 - 150 µm, provide better packing density, homogeneity and flowability to the powder feedstock, parameters that are crucial for achieving optimal results.	[5], [20], [224]–[230], [21], [191]–[196], [215]
Laser Characteristics	Power	The power of the laser source in each print varies depending on the nature and the characteristics of the powder feedstock as well as the SLS approach used (dSLS or iSLS); typical power values span from tens to hundreds of watts. It highly affects the density of the printed part, in conjunction with the scanning speed.	[186], [197], [229]–[232]
	Wavelength	Energy absorbance is an important factor during the scanning process. Nd:YAG and fiber sources that operate at 1.06 µm are better suited for metals whereas CO_2 laser sources (10.6 µm) provide excellent energy coupling with ceramics and polymers. Absorbance enhancers (e.g., graphite) can be added to the powder feedstock to boost the energy absorption. (This topic is further discussed in sub-section 6.2)	[221], [225], [230], [231], [233]–[235]
Scanning parameters	Scan speed	The pace at which the laser source irradiates the scanning area per pass; it is usually measured in mm/s and typical values vary from 10 - 6000 mm/s. It affects the final properties of printed part as lower scan speeds can lead to increased densification and vice versa.	[191], [195], [218], [221], [230], [232]
	Hatch distance	The spacing between two scan lines highly affects the density of the printed part as well as the production speed; synonyms for this parameter are hatch space, hatch spacing and scan spacing. Overlapping avoidance can be achieved via selecting a hatch distance value equal or greater to the laser spot size.	[191], [194], [230], [232]

Energy deposition	Energy density	Energy density (e) is a product of the scanning speed (v), laser power (P) and laser spot size (s) (or hatch distance) and provides a metric regarding the applied energy per unit area. It is usually measured in J/mm^2 and can be calculated through the following formula: $$e = \frac{P}{v * s}$$ It is a very useful metric for identifying the optimum process window since it relates crucial printing parameters together. However, energy density should not be the sole design parameter during SLS printing optimisation studies. The energy density metric is agnostic to important process parameters, such as powder feedstock characteristics (e.g., absorbance, thermal conductivity, flow behaviour, etc.), environmental conditions (e.g., pre-heated powder bed, etc.) or process variables (e.g., melt pool dynamics). Therefore, a holistic approach capable of describing both the printing parameters and the laser-powder interaction needs to be followed during SLS studies.	[186], [192], [193], [195], [221], [230], [231], [236]

2.5.2 Selective laser sintering of hydroxyapatite

The coupling of hydroxyapatite and selective laser sintering is an effective approach in producing porous structures for bone tissue scaffolds applications; patient tailored medical devices can be printed with high dimensional accuracy (e.g., interconnected porous network with features ranging from 100 – 400 μm) and enhanced biocompatibility [191], [237]. Processing hydroxyapatite via SLS, either directly or indirectly, presents some limitations, mainly due to its refractory character and its limited thermal shock resistance. It is often combined with polymeric or inorganic binders, either as a filler or as the main material in scaffold-guided tissue engineering applications. Glass and low-melting ceramic substances are the usual inorganic binders used alongside hydroxyapatite, whereas polyvinyl alcohol (PVA), polyetheretherketone, polyethylene (PE), polylactid acid (PLA), poly(lactic-co-glycolic acid) (PLGA) and polycaprolactone are their polymeric counterparts [25], [191], [194], [216], [217], [221], [222], [224], [237], [238] .

2.5.2.1 Direct selective laser sintering of hydroxyapatite

Additively manufacturing HA via dSLS is a challenging approach due to the limited thermal shock resistance and the inherent refractory nature of the material. High energy densities are required and mitigation strategies for minimizing the temperature gradients during processing need to be employed.

Shuai et al. conducted a feasibility study on fabricating nano hydroxyapatite (nHA) scaffolds via dSLS [239]; an in-house developed CO_2 laser system was utilised and rectangular porous scaffolds were printed. The specimens exhibited fair geometrical accuracy and no chemical degradation was reported when the optimal printing parameters were in use. Shuai et al. investigated in a similar approach the feasibility of processing a biphasic calcium phosphate

(BCP) powder feedstock, comprising of HA and beta tricalcium phosphate (β-TCP) via dSLS [95]. The porous printed scaffolds with a TCP ratio of 30 wt.% showed great dimensional accuracy and mechanical properties comparable to cortical bone; fully dense microstructure was further confirmed via SEM analysis. Moreover, MG63 cell culture studies showed increased adhesion and proliferation performance on the BCP scaffolds compared to pure HA.

An extension to the feasibility study in 2011 [239] was conducted by Shuai et al. [237], investigating the process optimization of fabricating nHA tissue engineering scaffolds via dSLS. Multiple samples were prepared with varying energy densities, ranging from 2 – 5 J/mm^2, and an optimum process window was identified. The printed specimens prepared with an energy density of 4 J/mm^2 exhibited fully dense microstructure, enhanced mechanical properties and no chemical degradation due to dehydroxylation; 4 GPa and 1.28 MPa were the reported values for Vickers hardness and fracture toughness, respectively. Moreover, the printed parts showed good biological activity since bone-like apatite crystals appeared on the surface of the parts after immersion in simulated body fluid (SBF).

Feng et al. investigated the fabrication of nHA tissue scaffolds through a novel two-step sintering (NTSS) method [9]. Rectangular scaffolds were printed via SLS (see Figure 2.8) and were subsequently subjected to optimized heat treatment profiles in various temperatures; 1100 °C was reported to be the optimum temperature since any further increase resulted in chemical degradation (i.e., dehydroxylation and phase transformation phenomena), poorer mechanical and biological properties. The specimens exhibited great dimensional accuracy, suitable mechanical properties and dense microstructure; 97.6%, 18.68 MPa and 245.79 MPa were the values reported for relative density, compressive strength and stiffness, respectively.

Lastly, good cell adhesion, cell proliferation (MG63 cell culture study) and bone growth promotion were reported (apatite formation, SBF immersion).

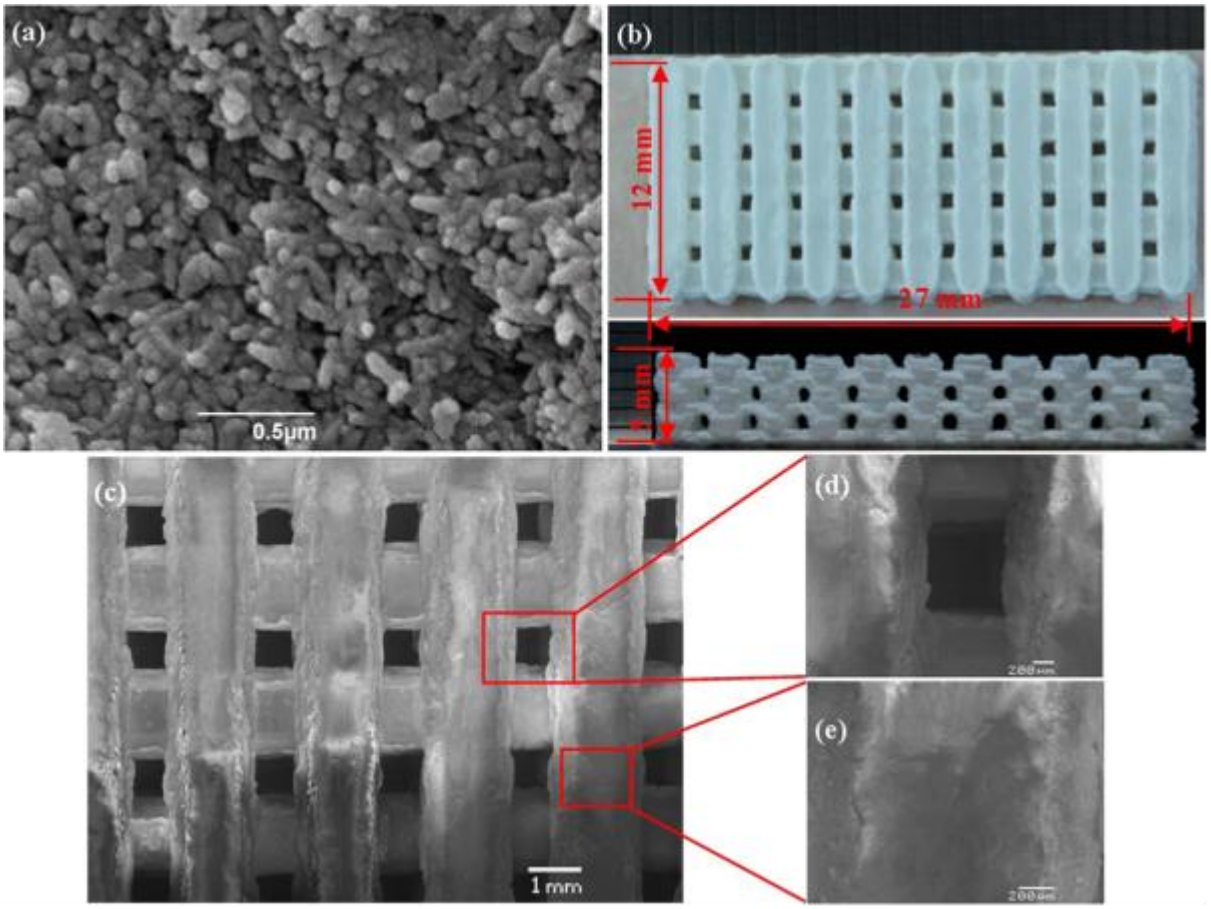

Figure 2.8: a) SEM image of the nHA powder, b) Optical image of the printed scaffold and c)-e) SEM images of the printed scaffold, reproduced from [9].

Navarrete-Segado et al. [240] investigated the processability of hydroxyapatite and chlorapatite during SLS processing. An addition of up to 10 wt.% of graphite powder in each feedstock was found to be necessary since energy absorbance was minimal for the precursor powders at 1070 nm. A process window study, investigating the processability of short circular samples, revealed that chlorapatite was more versatile compared to hydroxyapatite, since the latter exhibited a significantly narrower process window. Furthermore, chlorapatite exhibited better performance in terms of thermal stability since no dehydroxylation was observed in the

as-printed specimens. In the case of hydroxyapatite, extensive thermal degradation was recorded with secondary phases, tetracalcium phosphate and α-TCP, accruing for more than 50% of the total composition of the SLS-printed samples.

Furthermore, the fabrication of more complex designs utilising the HA powder feedstock was investigated and a suitable printing profile was identified (30 W, 25 mm/s). The printed specimens exhibited fair dimensional accuracy and an interconnected porous structure that was mainly attributed to balling phenomena during printing. Last but not least, the printability of tall cylindrical specimens with a printing profile optimised for maximum yield (36 W, 75 mm/s) was assessed. The printed specimens exhibited fair dimensional accuracy compared to the CAD geometry (3% and 12% difference in height and diameter, respectively), however they suffered from significant brittleness. Thermal degradation similarly to the process window study was reported. However, the research team identified that the phase transformations can be partially reverted via a heat treatment cycle. Lastly, post-processing had a positive effect in terms of compression strength (increase from 0.010 MPa to 0.049 MPa) and densification in addition to the removal of any trapped graphite powder in the samples via pyrolysis.

2.5.2.2 Indirect selective laser sintering of hydroxyapatite

Few attempts have been reported for producing HA/glass parts via SLS; the main hindering reasons include high temperature processing and difficulty in fabrication of multi-layer components. Lorrison et al. investigated the feasibility of processing HA and an in-house synthesized, bioresorbable phosphate glass (P_2O_5·CaO·Na_2O) via SLS [24], [25]. This biphasic, physically blended powder feedstock was chosen for maximizing the process window; the intention behind the glass addition was to enhance the biological properties of the printed

parts while acting as an inorganic binding agent for the HA particles. A glass loading ratio of 10 vol.% was selected via a printing process optimization study and both monolayer and multilayer specimens were printed. Fragility was reported for both types of specimens and curling was a major issue for the multilayer printed parts, too. Morphological analysis by SEM showed that the glass particles melted, forming pockets filled with glass, rather than wetting the HA particles.

Liu investigated the fabrication of HA scaffolds via a slurry iSLS approach, utilising colloidal silica and an inorganic dispersing agent (STPP – sodium tripolyphosphate) [216]; the main components of the slurry feedstock were biocompatible while the latter was bioinert. A thorough process optimization study was carried out and a slurry with a weight ratio of 36.5:62.5:1 wt.% (HA:Silica:STPP) was chosen. Rectangular porous scaffolds were fabricated that exhibited good dimensional accuracy and structural integrity. The printed specimens underwent heat treatment for further solidification; the post processing analysis showed that 1200 °C for 2 hours was the optimum overall setting. It was reported that an increase in temperature by 100 °C was beneficial towards further solidification but negatively impacted the formation of the microporous network required for cell growth; any further temperature increase led to material degradation due to HA dehydroxylation. A significant increase in density, compressive strength and bending strength was reported for the printed specimens compared to the green body. Furthermore, microstructural analysis by SEM and surface roughness tests showed suitable microporosity (~ 25 μm) for cell adhesion and growth on the surface of the specimens; the latter was further validated by an MG63 cell culture study.

Duan et al. investigated the feasibility of processing nHA via SLS with the addition of a triphasic low melting compound, comprising of CaO-Al_2O_3-SiO_2 (CAS) [217]; the latter was utilised for

promoting both densification through liquid phase sintering and bioactivity via Si ion interactions. 3 wt.% CAS ratio was found to be optimal since any further addition of CAS to the powder feedstock had a negative impact on the overall properties of the fabricated samples. The composite specimens exhibited superior mechanical properties compared to pure nHA; the increased performance was attributed to the achieved fully dense microstructure. 22.22 MPa, 1.68 MPa/$m^{-1/2}$ and 4.47 GPa were the reported values for compression strength, fracture toughness and Vickers hardness, respectively. Furthermore, the samples showed excellent biocompatibility during an MG63 cell study; cell adhesion and proliferation were reported. Lastly, the specimens exhibited bone growth promotion during SBF immersion tests.

Zeng et al. fabricated biphasic calcium phosphate tissue engineering scaffolds via a polymeric sacrificial binder route [241]; the powder feedstock was a physical blend of HA, β-TCP and a medical grade, low-melting epoxy resin (ER). An optimization study was carried out to determine the optimal weight ratios for the ternary system; 70/30 wt.% was chosen as the optimal HA/β-TCP ratio, based on a previous study by Shuai et al. [95], and 50/50 wt.% BCP/ER ratio exhibited the best overall performance. Cylindrical porous scaffolds were fabricated and heat-treated at 1100 °C for a duration of 4 hours to remove any trace of the epoxy resin. The specimens exhibited great dimensional accuracy, high specific surface area and suitable mechanical properties; 80.8%, 133.25 KPa, 4.38 MPa were the values reported for average porosity, compressive strength and elastic modulus, respectively. Furthermore, excellent biocompatibility both in vitro and in vivo was reported; the specimens induced osteogenic response, too.

CHAPTER 3 – Aims and objectives

The aim of the present study is to develop a novel GR-HA powder feedstock suitable for tissue engineering applications. The composite powder feedstock should be resistant to crystallisation and HA degradation while enhancing the overall mechanical and biological performance. Additionally, processing the developed GR-HA powder feedstock via selective laser sintering should be feasible.

A silicate-based glass could not fit this role, since this family of glasses is prone to crystallisation [53], [118], [120] unless tailored compositions and sintering profiles are employed [119], [126]–[128]. Additionally, GR-HA containing a phosphate-based glass secondary phase would not be ideal candidates. They are similarly vulnerable to crystallisation phenomena, unless appropriate measures are in place (e.g., glass loading ≤ 10 wt.%, sintering temperatures ≤ 1300 °C) that partially mitigate the adverse effects [11], [102], [103], [106], [109], [113].

Taking into account all of the above, a borosilicate glass is an ideal candidate for the proposed GR-HA system. Borosilicate glasses have been employed successfully in such systems, exhibiting superior mechanical [17], [131], [132], [134], [135] and biological [14], [136], [137], [179] performance, compared to pure HA specimens. Additionally, their tolerance in crystallisation is well established [57] and such systems have started to gain increased attention only in recent years. Furthermore, lanthanide-doping in such systems has not been investigated adding to the novelty of the work. Lanthanum oxide in particular is a great fit, since when utilised in GR-HA systems it provided both mechanical strengthening and superior biological properties [16], [83], [180]. Lastly, the few SLS studies carried out utilising a GR-HA

feedstock, investigated the use of HA blended with a phosphate-based glass without exploring any powder optimisation routes [24], [25].

In the present study, the glass system $50B_2O_3$-$20SiO_2$-$20Na_2O$-(10-x)CaO-xLa_2O_3 is expected to provide mechanical and biological enhancement when employed within GR-HA specimens, without exhibiting any crystallisation phenomena upon sintering. Furthermore, the introduction of La_2O_3 within the glassy phase, is envisaged to provide further reinforcement in terms of mechanical and biological properties. Lastly, powder feedstocks comprising of HA and the novel glass system are expected to perform better in terms of SLS printability compared to pure HA, due to their increased thermal stability.

The objectives of the present study are:

1. Investigate the mechanical and biological performance of a GR-HA system containing $50B_2O_3$-$20SiO_2$-$20Na_2O$-(10-x)CaO-xLa_2O_3, as a secondary glassy phase.
    1.1. Investigate whether the composite samples are susceptible to crystallisation or HA decomposition phenomena during sintering.
    1.2. Investigate whether the glass phase acts as a sintering aid and enhances densification.
        1.2.1. Identify the glass loading threshold upon which the densification process occurs.
    1.3. Examine whether the glass phase enhances the mechanical performance of the composite samples.
    1.4. Investigate whether the composite specimens exhibit any antimicrobial efficacy against bacteria commonly found in tissue engineering applications.
    1.5. Examine the biocompatibility of the composite samples.

1.6. Investigate the role of La_2O_3 content in terms of mechanical and biological performance.

2. Investigate the feasibility of utilising the novel GR-HA powder feedstock in SLS studies.

2.1. Examine whether the glass content affects SLS processability.

2.2. Investigate whether the composite powder feedstock is susceptible to crystallisation or HA decomposition phenomena during SLS processing.

2.3. Investigate whether the glass phase acts as a sintering aid and enhances densification.

CHAPTER 4 – Materials and methods

4.1 Glass making

The molar compositions of the synthesised glasses investigated in this study, can be found in Table 4.1.

Table 4.1: Molar compositions of the synthesised glasses

	B_2O_3 (mol%)	SiO_2 (mol%)	Na_2O (mol%)	CaO (mol%)	La_2O_3 (mol%)
BG0	50	20	20	10	-
BG1.25	50	20	20	8.75	1.25
BG2.5	50	20	20	7.5	2.5
BG3	50	20	20	7	3
BG4	50	20	20	6	4
BG5	50	20	20	5	5

Stoichiometric quantities of boric acid (H_3BO_3, Sigma, ≥ 99.5%), sodium carbonate (Na_2CO_3, Sigma-Aldrich, ≥ 99.0%), silicon dioxide (SiO_2, Riedel-de Haën, ≥ 99.0%), calcium carbonate ($CaCO_3$, Fluka, ≥ 99.3%) and lanthanum oxide (La_2O_3, Sigma-Aldrich, ≥ 99.99%) were prepared as per Table 4.1, taking into account the required gravimetric factors for each composition [40]. The glass components were mixed thoroughly for 2 hours, using a 3D shaker mixer (Turbula® mixer, WAB-GROUP, Switzerland) and then the mixture was poured in a disposable porcelain crucible. The crucible was placed in a furnace (BRF16/5-2416CG, Elite Thermal Systems Ltd, UK) and heated to 1000 °C for 2 hours, with a heating rate of 10 °C/min. Subsequently, the contents of the crucible were rapidly quenched in a metallic container filled with 5L of deionised water. The glass frit was collected, dried, milled under dry conditions and then sieved to a granule size of d ≤ 45 μm. An overview of the glass making process is presented in Figure 4.1.

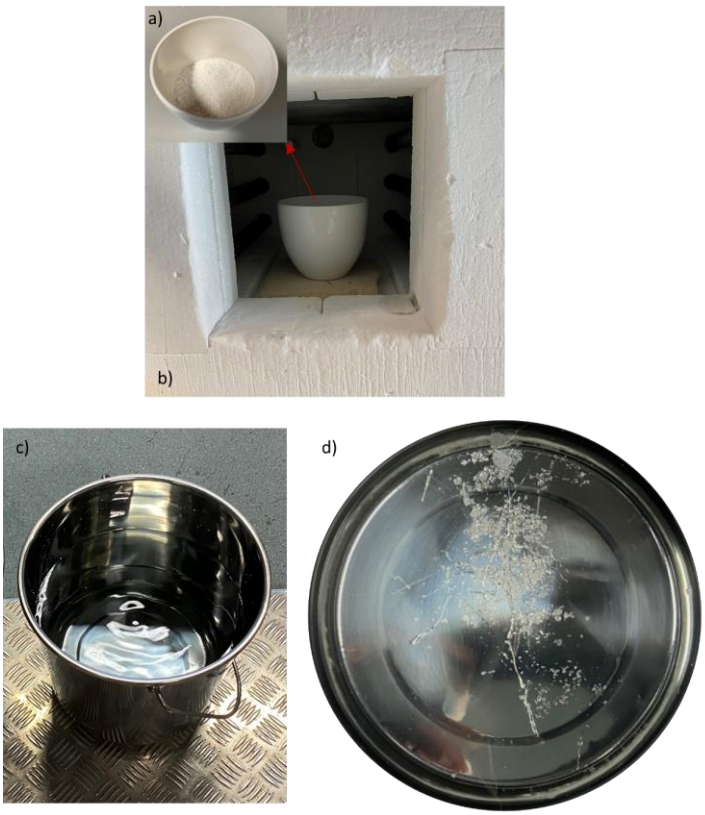

Figure 4.1: Overview of the glass making process. a) Powder reagents in porcelain crucible, b) Porcelain crucible placed within the furnace, c) Quenching tank filled with deionised water and d) Glass frit.

Glass compositions BG3 and BG4 were translucent (partly-crystallised) while BG5 was fully crystallised. None of the aforementioned glasses will be discussed further in the thesis.

4.2 Glass reinforced hydroxyapatite sample preparation

Analytical grade hydroxyapatite powder (Urodelia, ≥ 99.9%) alongside fixed proportions of the synthesided glass were used for preparing all the samples. More specifically, 2.5, 5.0 and 10.0 wt.% of BG0, BG1.25 and BG2.5 glass was blended with HA and mixed for 30 minutes, using a 3D shaker mixer (Turbula® mixer, WAB-GROUP, Switzerland), as per Table 4.2. Cylindrical specimens with a diameter of 13 mm were prepared via uniaxial pressing, utilising an evacuable die (GS03000, Specac Ltd., UK) and a hydraulic press. Each sample contained 0.75 g of powder that was mixed with 10 wt.% ethanol and then 1.1T of force was applied for 45 seconds.

Table 4.2: GR-HA compositions

	HA (wt.%)	BG (wt.%)
HA2.5BG0	97.5	2.5
HA5BG0	95	5
HA10BG0	90	10
HA2.5BG1.25	97.5	2.5
HA5BG1.25	95	5
HA10BG1.25	90	10
HA2.5BG2.5	97.5	2.5
HA5BG2.5	95	5
HA10BG2.5	90	10

Subsequently, the samples were placed on alumina boats and sintered (BRF16/5-2416CG, Elite Thermal Systems Ltd, UK) at three different sintering temperatures – 1200 °C, 1250 °C and 1300 °C. The heating rate was 4 °C/min, the dwell time was 1 hour and the samples were allowed to cool down naturally within the furnace. An overview of the sample making process is presented in Figure 4.2.

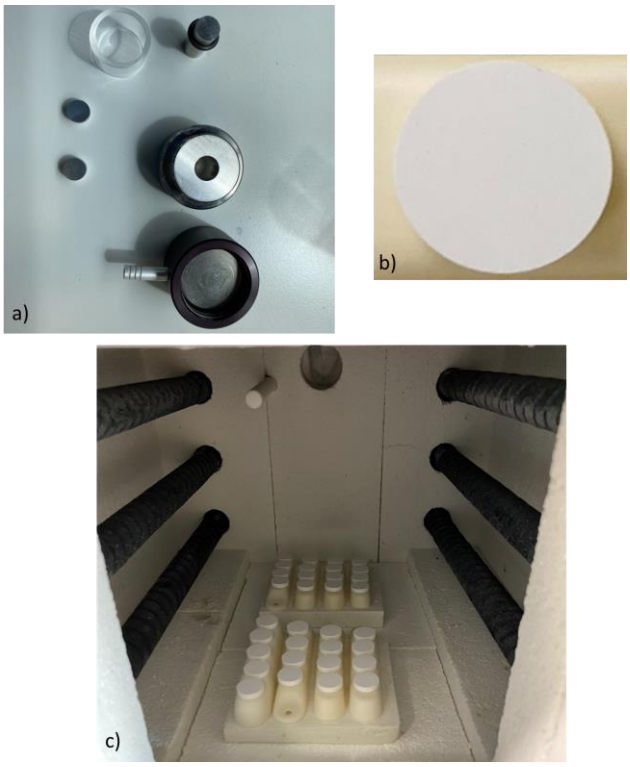

Figure 4.2: Sample preparation. a) Evacuable die, b) Pressed sample, c) Samples placed within the furnace prior to sintering.

The mass of each sample was measured pre and post sintering using a digital scale (Pioneer PA64, OHAUS, USA) to assess weight loss during sintering. The radius and height of each sample was measured with a digital calliper (IAN275222, Powerfix Profi) to assess the shrinkage during sintering.

4.3 Sample polishing

Samples were initially cold mounted in clear resin (EpoFix, Struers, Denmark) and then grounded and polished (Labopol-5/Laboforce-3, Struers, Denmark) as per the steps described in Table 4.3.

Table 4.3: Sample polishing protocol

	Grounding/Polishing disc	Duration (min)	Force (N)	RPM	Lubricant/Polishing agent
1	Struers MD-220	5	30	50	Water
2	Struers MD-1200	7	30	50	Water
3	Struers MD-2000	7	30	50	Water
4	Struers MD-Pan	10	20	50	Diamond solution, 9 µm
5	Struers MD-Dac	10	20	50	Diamond solution, 6 µm
6	Struers MD-Nap	10	20	50	Diamond solution, 3 µm
7	Struers MD-Chem	15	20	50	Diamond solution, 1 µm

4.4 Scanning electron microscopy (SEM)/Energy dispersive X-ray spectrometry (EDS)

The morphological characteristics of samples were qualitatively examined using scanning electron microscopy (6060, JEOL, Japan) at a forward voltage of 20 kV, a working distance of 10 mm and a spot size of 50. The samples were mounted on aluminium stubs before being gold coated (SC 500, Emscope Engineering Ltd, UK); copper conductive tape was applied in certain cases of poor connection between the sample and the sample holder. Compositional analysis was conducted in samples previously etched in 10 vol.% hydrofluoric acid, using an energy dispersing X-ray detector (INCA 300, Oxford Instruments, UK) at a forward voltage of 20 KV, a working distance of 10 mm and a spot size of 50.

4.5 Grain size analysis

The mean grain size was estimated in accordance with ASTM E112 standard utilising the planimetric method on SEM images. The samples were etched in 10 vol.% hydrofluoric acid for 1 minute.

4.6 X-ray diffraction (XRD)

Phase identification analysis was conducted with a Bruker D8 Advance Diffractometer (Bruker, UK) using Ni-filtered, Cu Ka radiation with a forward voltage of 40 kV and a current of 40 mA. 10° to 60° was the 2θ range that was covered during data collection, with a step size of 0.02° and dwell time of 1 sec. Phase identification was carried out using the software DIFFRAC.EVA (Bruker, UK). Rietveld analysis was carried out using GSAS-II software in order to identify phase compositions and lattice parameters. The initial phase .cif files were downloaded from the Crystallography Open Database (http://www.crystallography.net). The parameters refined in each run were five and more specifically: histogram scale, unit cell, phase fraction, crystallite size and microstrain.

4.7 Particle size analysis

Particle size distribution for both HA and BG powders was carried out using a laser diffraction system (Mastersizer MS 3000, Malvern Panalytical, UK). The powders were dispersed in dry conditions at 0.1 bar of pressure though a venturi channel. Additionally, the particles were morphologically analysed via SEM.

4.8 Micro computed tomography (μCT)

The internal structure of solid samples (e.g., porosity) was assessed via micro computed tomography (Scyscan 2211, Bruker, USA), utilising X-rays at a forward voltage of 95 kV, a working current of 110 μA and 14 μm of voxel size/resolution. The system was equipped with

a 3MP flat panel X-ray CMOS sensor and the samples were secured on top of a 20 mm cylindrical sample holder via double sided tape. In the case of multiple samples being examined simultaneously, polymeric 3D printed separators were inserted in between each sample, as per Figure 4.3. CTVOX and CTAN software (Bruker, USA) were used for image reconstruction.

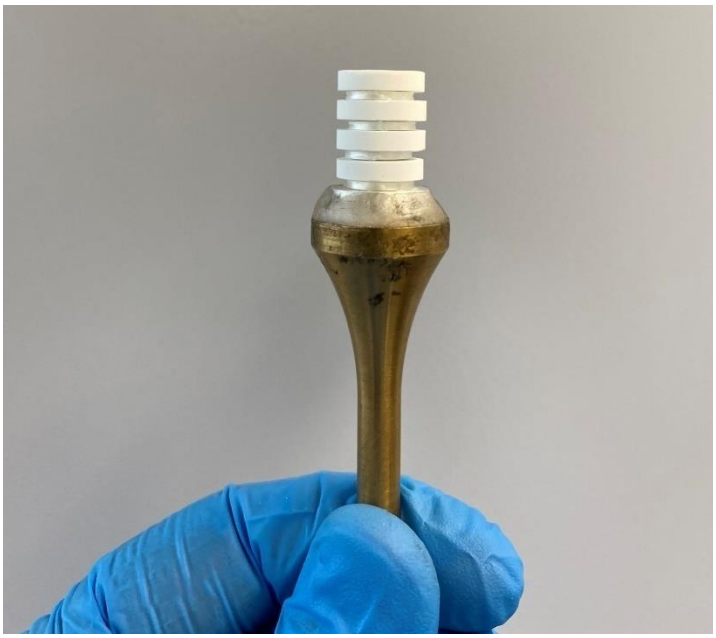

Figure 4.3: µCT sample holder.

4.9 Microhardness

Vickers microhardness measurements (VH1202, Buehler Wilson, USA) were carried out in order to assess the mechanical performance of the fabricated specimens. Polished test samples were subjected to a 5x5 indentation matrix, at a load of 3N for a duration of 10 seconds/indent. Three samples were tested for each different experimental point (e.g., composition) and an average microhardness value was calculated. The indenting diamond head was pyramid shaped with opposite faces in an angle of 136°. The indentation diagonal was measured using an optical microscope (Axioskop 2, Zeiss, Germany) and ImageJ software.

Microhardness was calculated using the following equation:

$$H_v = 1.854 \times \frac{P}{D^2}$$

where P stands for the indentation load (kgf) and D the measured diagonal (mm). Microhardness was only measured for samples sintered at 1300 °C, due to high porosity present at samples sintered below this temperature.

4.10 Density

The densities of solid samples during this study were assessed via the Archimedes principle [242], a gravimetric volume displacement technique. The mass of the samples was recorded in grams both in air (m_{air}) and while submerged in deionised water (m_{water}), at room temperature using a density determination kit (Mettler Toledo, Switzerland). The density (ρ) was calculated using the following constants and formula:

$$Water\ density\ at\ 20\ °C: \rho_{water} = 0.9982\ {}^{g}/_{cm^3}$$

$$Air\ density: \rho_{air} = 0.0012\ {}^{g}/_{cm^3}$$

$$\rho = \frac{m_{air}}{m_{air} - m_{water}} \times (\rho_{water} - \rho_{air}) + \rho_{air}$$

Additionally, helium gas pycnometry measurements were carried out for powder specimens (AccuPyc II 1340, Micromeritics, USA). In this method a known amount of powder (~ 0.25 g) is inserted within a sealed chamber of known dimensions (~ 1 cm^3). Helium gas fills the sample chamber and upon equilibrium, the chamber's pressure is recorded. Subsequently, the sample chamber is evacuated to a connected expansion chamber of known dimensions and the pressure is measured again. Upon equilibrium the system is flushed and the process is

repeated 10 times. Finally, the density of the sample is calculated using the following equation:

$$\rho_{sample} = \frac{m_{sample}}{V_{sample}} = \frac{m_{sample}}{V_{sample\_chamber} - \frac{V_{expansion\_chamber}}{\frac{P_{sample\_chamber}}{P_{expansion\_chamber}} - 1}}$$

4.11 Thermal analysis

Differential scanning calorimetry (DSC) was employed in Chapter 5, in order to assess the thermal behaviour of the synthesised powder feedstocks.

More specifically, DSC measurements (Stanton Redcroft DSC1500, Rheometric Scientific, UK) for every synthesised glass powder was carried out and glass transition temperature (T_g) was calculated with the use of Mettler Toledo's StarE software. 10 mg of each powder was tested in platinum crucibles, over a temperature range between 25 °C and 1300 °C, a heating rate of 10 °C/min and an inert (nitrogen) atmosphere. (The DSC measurements were conducted by Dr. Saroash Shahid at the Queen Mary University of London.)

4.12 Cell culture studies

Biocompatibility behaviour studies were carried out using a human osteoblast cell line in order to assess the cell attachment and viability on the fabricated samples.

Saos-2 cells were cultured in McCoy's 5A media supplemented with 10 vol.% fetal bovine serum (FBS), 5 vol.% mixture of penicillin/streptomycin antibiotics and 5 vol.% L-Glutamine. They were seeded on T25 flasks (ThermoFisher Scientific, USA) and stored within a 5% CO_2 humidified incubator, at 37 °C until they reached 70 – 90% confluency. Prior to cell harvesting with Trypsin and centrifugation, the cells were washed with phosphate buffered saline (PBS). Subsequently the cells were resuspended in culture media and counted using Trypan blue and

a hemocytometer. 1 mL of culture media containing 10^5 cells was seeded on top of each sample in 24-well plates; the samples prior to seeding were sterilised via autoclaving. The cells were cultured for 1, 4 and 7 days and the cell medium was changed every 2 days.

Cell viability/proliferation was assessed at days 1, 4 and 7, using the MTT assay. MTT is a colorimetric technique that measures the metabolic activity of viable cells through the reduction of 3-(4, 5-dimethylthiazol-2-yl)-2,5-diphenyltetrazolium bromide to purple formazan crystals. Prior to adding the MTT reagent, the medium was removed from each well and each sample was transferred to new 24-well plates to ensure that MTT would react only with the cells adhered on the surface of the samples. 20 μL of MTT (CyQUANT™, ThermoFisher Scientific, USA) were placed on the surface of each sample. Subsequently 1 mL of unsupplemented media (Dulbecco's Modified Eagle Medium – DMEM) was added to each well and the plates were incubated for 3 h within a 5% CO_2 humidified incubator, at 37 °C. Post incubation the media containing the MTT was discarded and 0.5 mL of dimethyl sulfoxide (DMSO) was added in each well. The plates were agitated on a plate shaker and the formazan crystals were thoroughly mixed in DMSO via pipetting. 300 μL of the supernatant from each well was transferred to a new 24-well plate and OD readings were taken at 570 nm using an Elisa microplate reader (ELx800, BioTek, USA).

Additionally, the cells were fixed on the surface of the samples using glutaraldehyde (2.5 vol.% in sodium cacodylate buffer), a series of dehydration cycles using various concentrations of ethanol in water (40 – 100 vol.%) and a final evaporation step with hexamethyldisilizane. Subsequently, the samples were gold coated (SC 500, Emscope Engineering Ltd, UK) and observed under SEM to assess the degree of attachment and proliferation.

4.13 Antimicrobial studies

Antimicrobial studies with Gram positive and Gram negative bacteria were carried out in order to assess the antimicrobial character of the fabricated specimens.

Staphylococcus epidermidis (Gram positive) and Pseudomonas aeruginosa (Gram negative) were cultured on Mueller–Hinton agar and incubated for 24 hours in a 5% CO_2 humidified incubator, at 37 °C. One single colony was suspended in 5 mL of Mueller–Hinton broth and incubated for 12 hours within a shaking incubator at 37 °C and 100 rpm. A bacterial suspension in Mueller–Hinton broth with an OD_{600} = 0.1 (7305 UV/Visible Spectrophotometer, Jenway, UK) was prepared. 1 mL of liquid culture, containing approximately $10^7 – 10^8$ colony-forming units (CFU), was seeded on top of each sample in 24-well plates; the samples prior to seeding were sterilised via autoclaving. The bacterial culture was incubated for 4 hours in 5% CO_2 humidified incubator, at 37 °C.

Bacteria viability was assessed after 4 hours of incubation, using the MTT assay. MTT is a colorimetric technique that measures the metabolic activity of viable bacteria through the reduction of 3-(4, 5-dimethylthiazol-2-yl)-2,5-diphenyltetrazolium bromide to purple formazan crystals. Prior to adding the MTT reagent, the liquid culture was removed from each well and each sample was transferred to new 24-well plates to ensure that MTT would react only with the bacteria adhered on the surface of the samples. 20 µL of MTT (CyQUANT™, ThermoFisher Scientific, USA) were placed on the surface of each sample. Subsequently 1 ml of Mueller–Hinton broth was added to each well and the plates were incubated for 3 h within a 5% CO_2 humidified incubator, at 37 °C. Post incubation the Mueller–Hinton broth containing the MTT was discarded and 0.5 mL of DMSO was added in each well. The plates were agitated on a plate shaker and the formazan crystals were thoroughly mixed in DMSO via pipetting.

300 μL of the supernatant from each well was transferred to a new 24-well plate and OD readings were taken at 570 nm using an Elisa microplate reader (ELx800, BioTek, USA).

4.14 Ultraviolet – Visible (UV-Vis) spectroscopy

Absorbance powder measurements used in the SLS experiments presented in Chapter 6 was carried out using a UV-Vis spectrophotometer (AGILENT® Cary 5000 UV/Visible/NIR) equipped with a 110 mm integration sphere accessory. The system was calibrated with specimens of known absorbances over the range of 900 – 1100 nm with a step size of 1 nm and 0.5 seconds of integration time. The measurements were conducted over dry conditions, where a thin powder layer (~ 3 mm) was placed within the sample holder in each run.

4.15 Flow rate – Angle of repose – Compressibility index/Hausner ratio

Powder flow characteristics were assessed with three different methods, as described at European Pharmacopeia "2.9.36. POWDER FLOW", for all the powders involved in the SLS studies in Chapter 6. More specifically:

- Flow rate: The rate at which a given amount of powder passes through a container (e.g., cylinder, funnel) is measured at the closest of a tenth of a second. Higher rates are characteristic of free flowable powders and vice versa. There is no general scale of flowability for such measurements and comparing results between studies is difficult. Method used:
    - 100 g of powder were placed within a glass funnel with a diameter of 15.5 cm, height of 13.5 cm and orifice opening of 3.2 cm. The end of the funnel was blocked until the experiment commenced and the amount of time required for the powder to pass through the orifice was recorded.

- Angle of repose: The angle of the powder pile formed when a given amount of powder passes through a container (e.g., cylinder, funnel) relative to the horizontal plane, is related to the flowability of the tested powder. Due to slight differences on equipment specifications used in measuring the angle of repose, some variation can be found between different studies. However, the generally accepted classification for this type of measurement was introduced by Carr [243] and can be found in Table 4.4.

  Method used:

  - 100 g of powder were placed within a glass funnel with a diameter of 15.5 cm, height of 13.5 cm and orifice opening of 3.2 cm. The end of the funnel was blocked until the experiment commenced, a photograph of the powder pile was taken from a fixed point each time and the angle of repose was measured utilising the image analysis software ImageJ.

- Compressibility index/Hausner ratio: The bulk and tapped volume of a powder is used to measure the compressibility index and the Hausner ratio. Those powder flow behaviour metrics are widely used in recent years due to their simplicity and speed. A known amount of powder is placed within a volumetric cylinder and the unsettled apparent volume is recorded (V_0). Subsequently, the cylinder is tapped until no change in the powder volume can be observed and the final tapped volume is recorded (V_f). The generally accepted classification for both measurements was introduced by Carr [243] can be found in Table 4.4.

Method used:

- 100 g of powder were placed within a glass 250 mL volumetric cylinder and V_0 was recorder. The cylinder was subsequently secured on a Tap Density Tester (PT-TD1, Pharma Test Apparatebau GmbH) that was programmed to tap the cylinder at a drop height of 3 mm, for 250 times or until no change could be observed at the final tapped volume. At the end of each run V_f was recorded and the compressibility index and Hausner ratio were calculated using the following equations:

$$Compressibility\ index = 100\ \times \frac{V_0}{V_f}$$

$$Hausner\ ratio = \frac{V_0}{V_f}$$

Table 4.4: Flowability metrics classification [243]

Flow character	Angle of repose (°)	Compressibility index (%)	Hausner ratio
Excellent	25 – 30	1 – 10	1.00 – 1.11
Good	31 – 35	11 – 15	1.12 – 1.18
Fair	36 – 40	16 – 20	1.19 – 1.25
Passable	41 – 45	21 – 25	1.26 – 1.34
Poor	46 – 55	26 – 31	1.35 – 1.45
Very poor	56 – 65	32 – 37	1.46 – 1.59
Very, very poor	> 66	> 38	> 1.60

4.16 SLS experiments

Spheroidised HA (300.08.2, Urodelia, France) was tested either autonomously (HA) or blended with 10 wt.% of the novel glass containing 2.5 mol% of La_2O_3 (HA10BG). The glass powder synthesised as previously described in section 4.1, crushed and classified via manual sieving between 45 – 75 μm. To ensure flowability of the powder feedstock, the glass powder was spheroidised by the means of flame spheroidisation. This process also known as plasma melting or combustion flame spraying is based on a melting – surface tension mechanism. The powder is fed to a flame torch through a hopper feeder; various gaseous mixtures are used in order to fuel the flame such as propane/oxygen, natural gas/air and acetylene/oxygen [228], [244]–[250]; an overview of the process is presented in Figure 4.4. In the case of the novel glass system an MK 74 torch system (Metallisation Ltd, UK) was utilised with an oxyacetylene ratio of 2.5:2.5 while the microspheres were quenched/collected in air. (The glass spheroidisation was conducted by collaborators at the University of Nottingham – Dr. Ifty Ahmed, Dr. Md Towhidul Islam and Dr. Benjamin Milborne. The glass microspheres were sent back to the University of Birmingham for characterisation and processing.) Additionally, 10 wt.% of graphite (TIMREX® KS 44, Imerys, France) was introduced in both powder feedstocks in order to enhance the laser absorbance. Each powder feedstock was weighted accordingly, poured within a mixing jar and mechanically blended with the use of a 3D shaker mixer (Turbula® mixer, WAB-GROUP, Switzerland) for 1 hour.

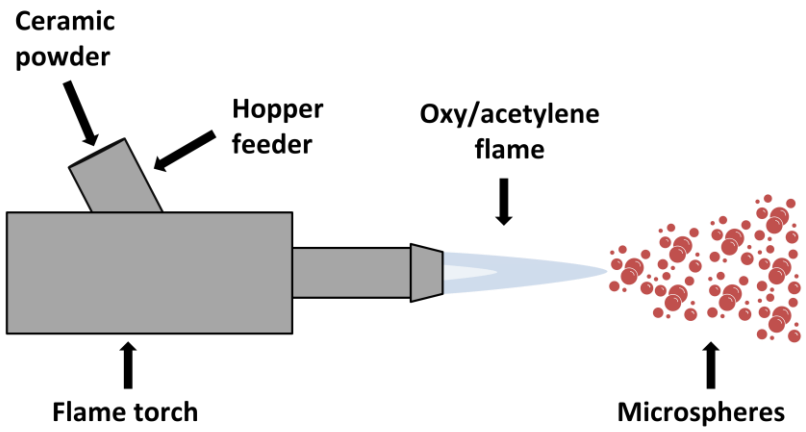

Figure 4.4: Flame spheroidisation process overview.

A DMP 200 Pro X (Phoenix Systems, France) SLS printing platform was used for producing the test samples. (The powder loading, SLS operation and depowdering was conducted by Mr. Vincent Baylac, member of technical staff at CIRIMAT/INPT) This SLS system is equipped with a 300W fiber laser source operating at 1070 nm. The laser beam passes through a collimator (15 mm output spot, $1/e^2$ method), a scanner head, and a flat field F-Theta lens (420 mm focus length). The resulting beam diameter after the final step is 38.1 µm (focal spot). The powder is spread with the use of a 110 mm roller, rotating at a speed of approximately 4 revolutions per seconds; this system is responsible for smoothing and compacting the powder, too. The scraper system in place ensures a flat printing surface and is responsible for carrying each layer's powder from the feeding piston to the sintering piston. Any untreated powder during the process is recovered at the collecting tank, minimising potential waste since the collected powder is suitable for recycling. An overview of the main components found in the DMP 200 Pro X system can be found in Figure 4.5 .

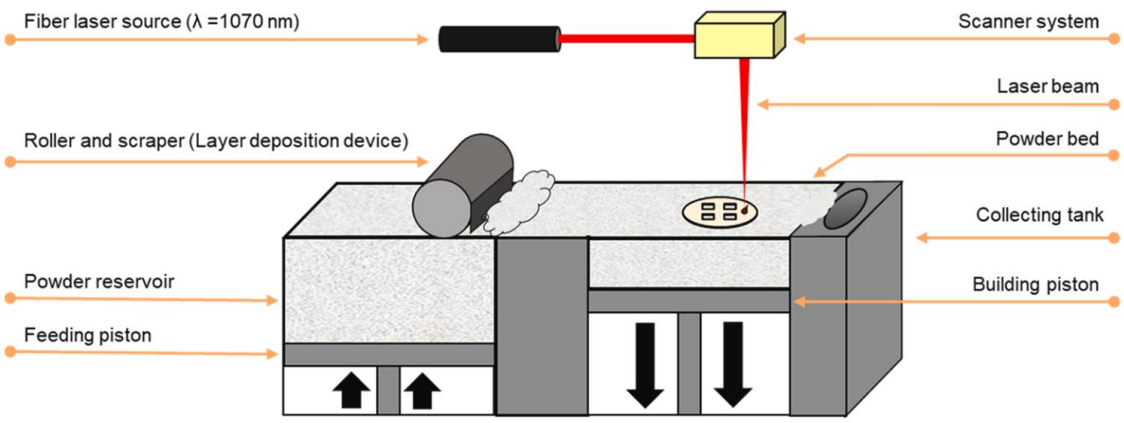

Figure 4.5: Schematic illustration of the printing chamber of Phoenix Systems DMP 200 Pro X, reproduced from [240].

The SLS experiments were conducted in ambient temperature conditions. Titanium disc substrates coated with HA (Projection Plasma Système, France) were used in order to improve attachment of the first printed layers to the build plate. The discs measured 10 cm in diameter and the HA coating was 2 mm in height. Three different geometries were selected as test samples for both powder feedstocks; short cylinders (13 mm (D) x 4 mm (H)), tall cylinders (10 mm (D) x 17 mm (H)) and a cylindrical scaffold (20 mm (D) x 17 mm (H)). The layout of the printing bed can be seen on Figure 4.6.

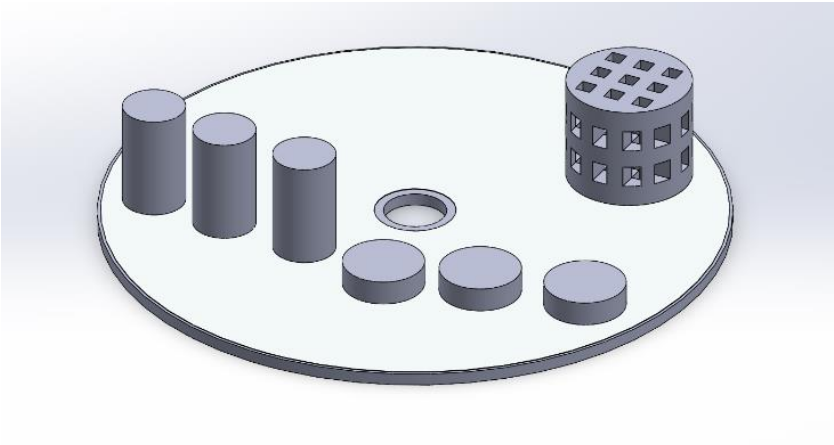

Figure 4.6: Samples layout on the printing bed.

SolidWorks CAD software (Dassault Systèmes SE, France) was used in order to design the 3D geometries of the printed parts and DMP ProX Manufacturing software (Phoenix Systems, France) was used in order to slice the model. The printing parameters used for both powder feedstocks can be found in Table 4.5:

Table 4.5: Printing parameters used during the SLS feasibility study

Printing parameter	Setting
Laser power	36W
Scanning speed	75 mm/s
Spot size	38.1 µm
Layer height	0.10 mm
Powder bed compression	300%
Atmosphere	Air
Hatching distance	0.05 mm
Scanning strategy	Zig-Zag (5 passes + orientation change)
Printing substrate	HA-coated TA6V discs

This printing profile was based on a previous study by Navarrete-Segado et al. [240], that utilised the same SLS printing platform and HA powder feedstock. Conducting an individual process window study would pose a risk towards the realisation of the SLS feasibility study, due to time constraints and limitations in accessing SLS facilities.

A Keyence VHX 2000 digital microscope was used for capturing stereoscopic images of the printed samples during the SLS feasibility study.

CHAPTER 5 – Development and characterisation of the GR-HA system

The first part of this chapter covers the physicochemical characterisation of HA and BG powders in terms of particle size, morphology and elemental analysis. In addition, the physical properties of all the tested BG glasses were assessed, too. The second part of this chapter is focusing on the characterisation of the developed specimens, providing a comparison between pure HA and GR-HA samples. The effect of glass and/or lanthanum content is assessed in terms of physical properties, phase identification, sinterability, mechanical and biological performance.

5.1 Powders characterisation

Particle size distribution results along with SEM images showcasing the morphology of the HA powder used for the preparation of HA and GR-HA samples, can be found in Figure 5.1. The particles are of irregular shape and exhibit an average diameter (D_{50}) of 17.8 μm. All the BG powders, regardless of their La_2O_3 content, exhibited the same irregular particle morphology and a similar particle size distribution (D_{50} ≈ 23.0 μm). Particle size distribution results along with SEM images showcasing the morphology of the BG powders used for the preparation of GR-HA samples, can be found in Figure 5.2.

The EDX analysis for HA is presented in Figure 5.3. Only the following elements were identified through the EDX analysis: calcium (Ca), phosphorus (P) and oxygen (O), as expected. Moreover, the calcium to phosphorus ratio (Ca/P) was determined to be 1.71, a similar value to stoichiometric HA (i.e., 1.67). In the case of BG powders, the EDX analysis presented in Figure 5.4, showed that no impurities were present within any of the glass compositions. Only the following elements were identified: sodium (Na), silicon (Si), calcium (Ca), oxygen (O) and lanthanum (La), as expected. Additionally, the atomic percentage values reported for La_2O_3

show good correlation with the nominal molar percentage values for each glass (i.e., 1.25 and 2.5 mol%). (The peak at ~2.25 keV was omitted from the EDX analysis since it corresponds to the gold coating that was applied to each sample)

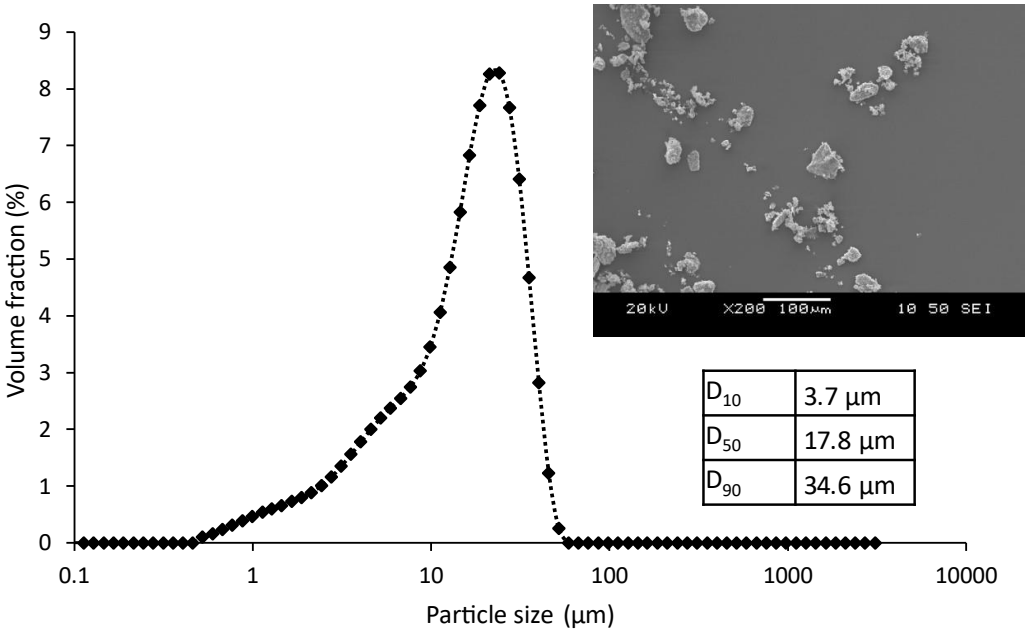

Figure 5.1: Particle size distribution and morphology of HA powder.

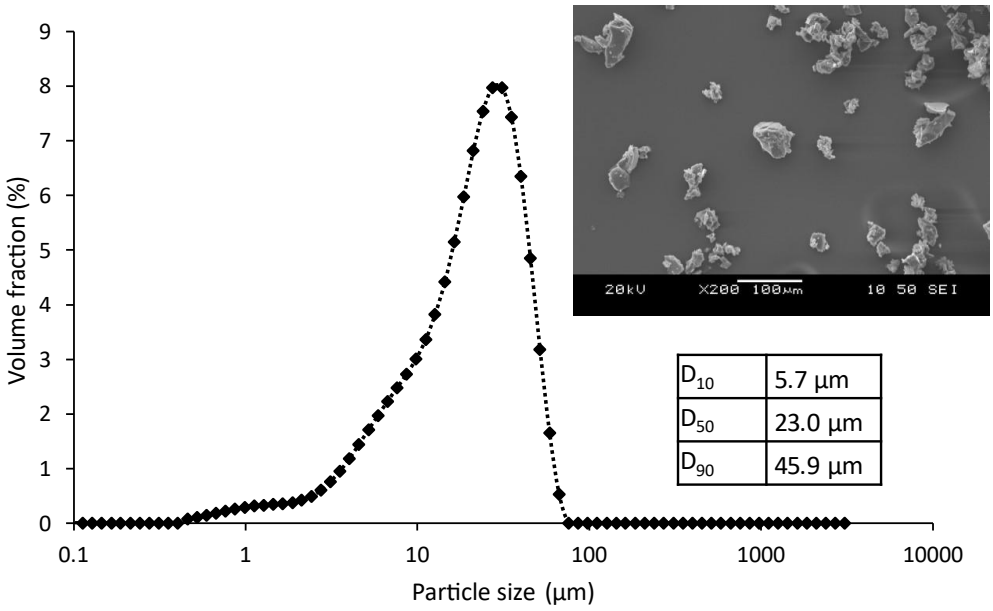

Figure 5.2: Particle size distribution and morphology of BG powders (BG0 is presented as an example).

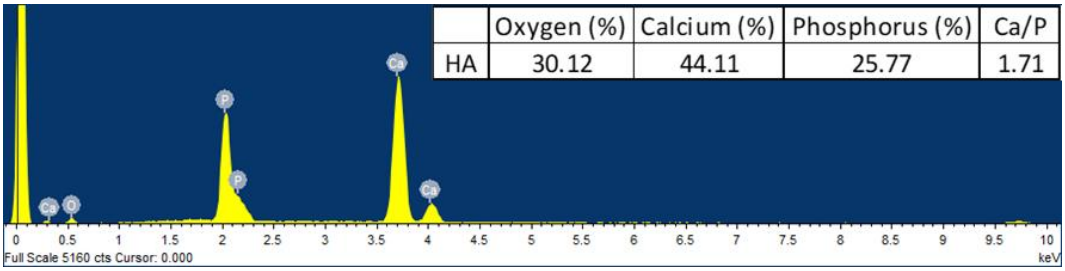

	Oxygen (%)	Calcium (%)	Phosphorus (%)	Ca/P
HA	30.12	44.11	25.77	1.71

Figure 5.3: EDX results for HA powder.

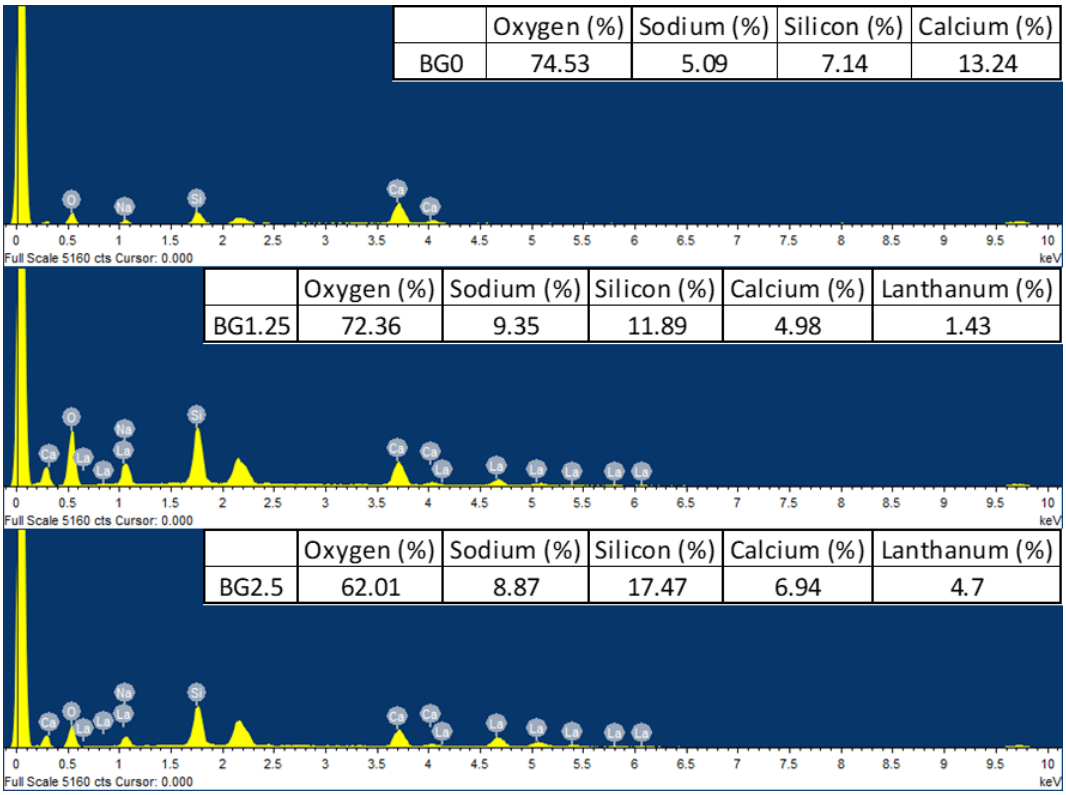

	Oxygen (%)	Sodium (%)	Silicon (%)	Calcium (%)
BG0	74.53	5.09	7.14	13.24

	Oxygen (%)	Sodium (%)	Silicon (%)	Calcium (%)	Lanthanum (%)
BG1.25	72.36	9.35	11.89	4.98	1.43

	Oxygen (%)	Sodium (%)	Silicon (%)	Calcium (%)	Lanthanum (%)
BG2.5	62.01	8.87	17.47	6.94	4.7

Figure 5.4: EDX results for BG powders.

The physical properties of the different BG glasses and can be found in Table 5.1.

Table 5.1: Physical properties of BG glasses

	BG0	BG1.25	BG2.5
Density (g/cm^3)	2.400	2.489	2.589
Molecular weight (g/mol)	64.835	68.207	71.578
Molar volume (cm^3/mol)	27.019	27.403	27.644
N_{La} (ions x 10^{22} /cm^3) [251]	-	2.747	5.446
Inter nuclear distance r_i (Å) [251]	-	3.314	2.638
Polaron radius r_p (Å) [251]	-	1.336	1.063
Field strength (cm^{-2}) [251]	-	3.20E+17	5.04E+17
Glass transition temperature - T_g (°C)	540	546	552
Oxygen packing density (cm^3/mol) [252]	2.200	2.225	2.250
Average boron - boron distance (Å) [253]	3.553	3.570	3.581

An increase in density and molar volume is observed with increasing lanthanum content. This can be mainly attributed to the addition of La_2O_3 which exhibits approximately 6 times higher molecular weight compared to CaO. Moreover, the increase in density is reflected in the decrease in the ion – ion spacing (r_i) with increasing La^{3+} concentration (N_{La}). An increase in field strength is also observed with increasing lanthanum content (i.e., decrease in polaron radius). Increased field strength is associated with thermal stability, which can be directly correlated with the higher T_g values recorded with increasing lanthanum content. Lastly, the increase in the average boron – boron distance is directly related to the presence of La^{+3}, which exhibit a slightly larger ionic radius [254] than calcium, resulting in the expansion of the glass structure. Analogous results have been reported in previous studies where La_2O_3 was incorporated within similar glass systems [255], [256].

5.2 Phase identification – XRD study

GR-HA systems have been studied for the best part of the last 30 years. A common issue with silicate and phosphate-based systems is crystallisation during sintering and the introduction of new phases. Hence, phase identification experiments were carried out to investigate the crystallisation kinetics of the developed borosilicate GR-HA system.

Figure 5.5 shows the X-ray diffractograms for all the synthesised glasses containing 0, 1.25 and 2.5 mol% of La_2O_3. No diffraction peaks are observed for any of the BG compositions, regardless of their lanthanum content, confirming their amorphous nature.

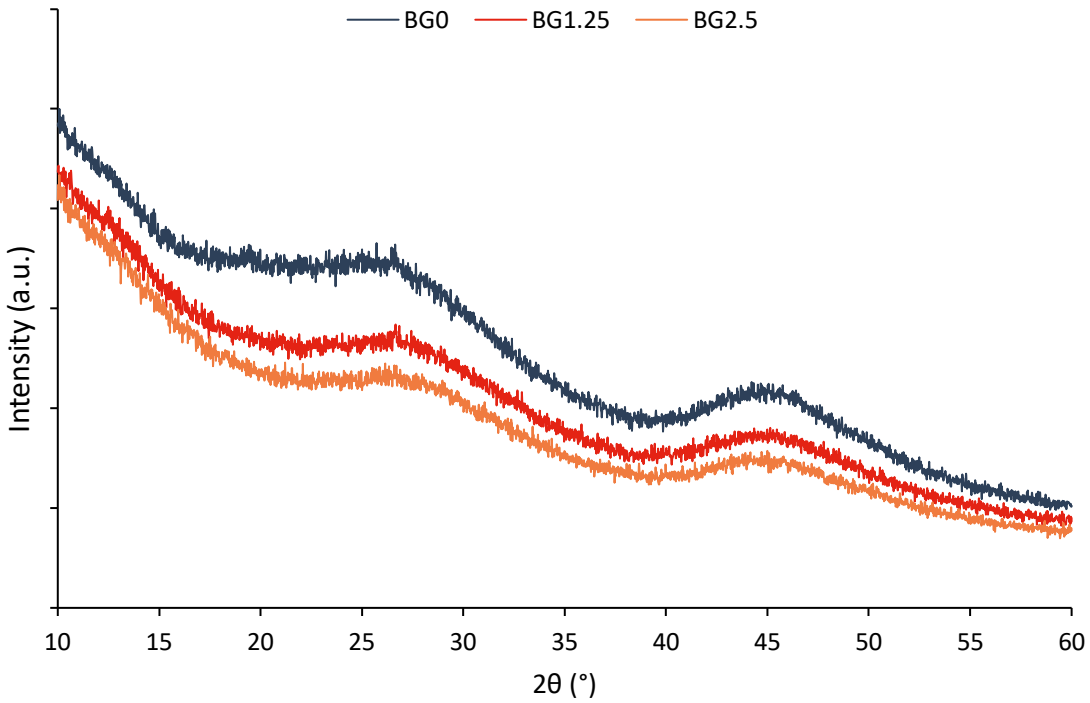

Figure 5.5: X-ray diffractograms of BG glasses.

Figure 5.6 portrays the X-ray diffractograms of HA powder before any heat treatment and then after sintering at 1200 °C, 1250 °C and 1300 °C. No phase transformations occurred during heat treatment and all the diffraction peaks correspond to stoichiometric HA, as per JCPDS 00 009 0432.

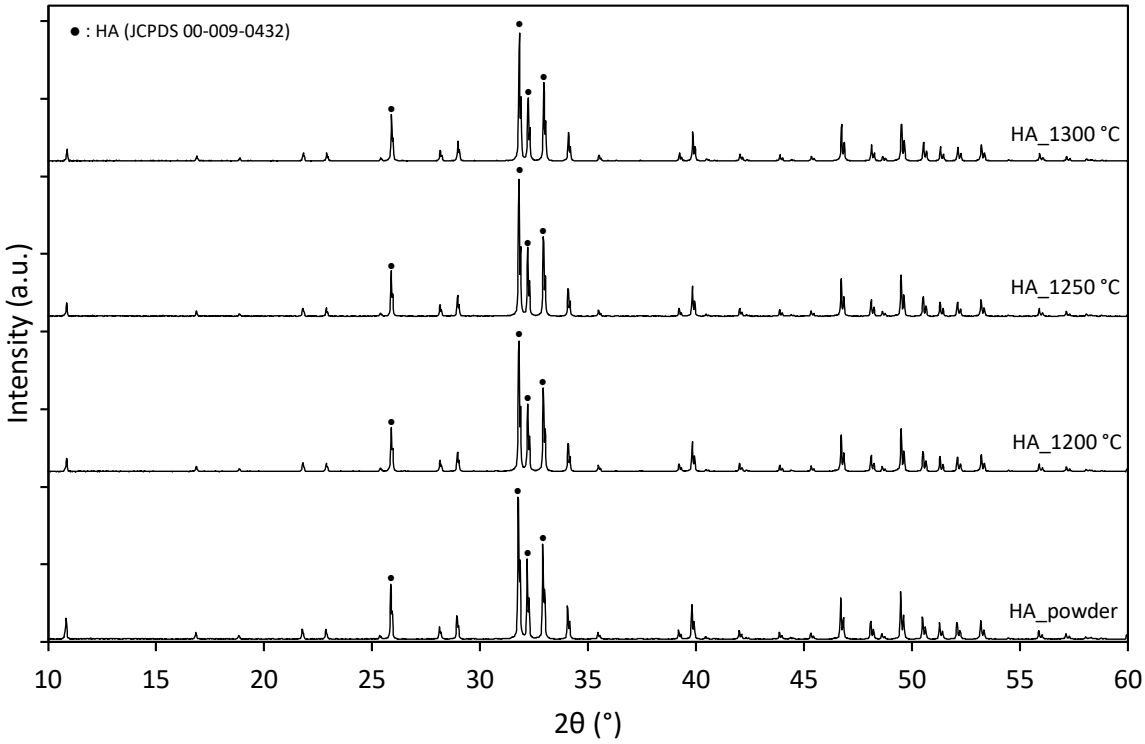

Figure 5.6: X-ray diffractograms of non-sintered and sintered HA samples at different sintering temperatures.

The fact that HA samples did not exhibit any other calcium phosphate phases even at the highest sintering temperature is an indication of the powder's stoichiometry. Stoichiometric HA (i.e., Ca/P=1.67) is relatively stable at temperatures up to 1250 °C, especially when no rapid quenching is employed at the end of the sintering cycle, as per this case. It is worth mentioning that phase transformations do take place during sintering, mainly oxyapatite and TCP are formed, however these are reversible during cooling under an adequate water partial pressure. In the case of non-stoichiometric apatites, phase transformations are more

prominent and irreversible. The thermal degradation products vary based on the Ca/P ratio and include β-TCP, β-calcium pyrophosphate, stoichiometric HA and CaO [8], [257].

Figure 5.7, Figure 5.8, Figure 5.9 show the diffractograms of the composite samples containing BG0, BG1.25 and BG2.5, respectively. Small additions of glass (≤ 5 wt.%) tend to induce phase transformations in every sintering temperature. More specifically, β-TCP is present in every composite employing glass content between 2.5 – 5.0 wt.%, while α-TCP is found primarily in glasses containing 5.0 wt.% of glass. On the other hand, GR-HA samples containing 10.0 wt.% of glass show the best performance in terms of thermal stability, throughout the sintering temperature range. No phase transformations are observed besides the occurrence of miniscule quantities of β-TCP found in the sample containing the highest lanthanum content and sintered at 1300 °C. Furthermore, lanthanum addition does not seem to affect the HA decomposition phenomena. Lastly, phase transformations are more prominent in higher sintering temperatures for the majority of the GR-HA specimens, as expected.

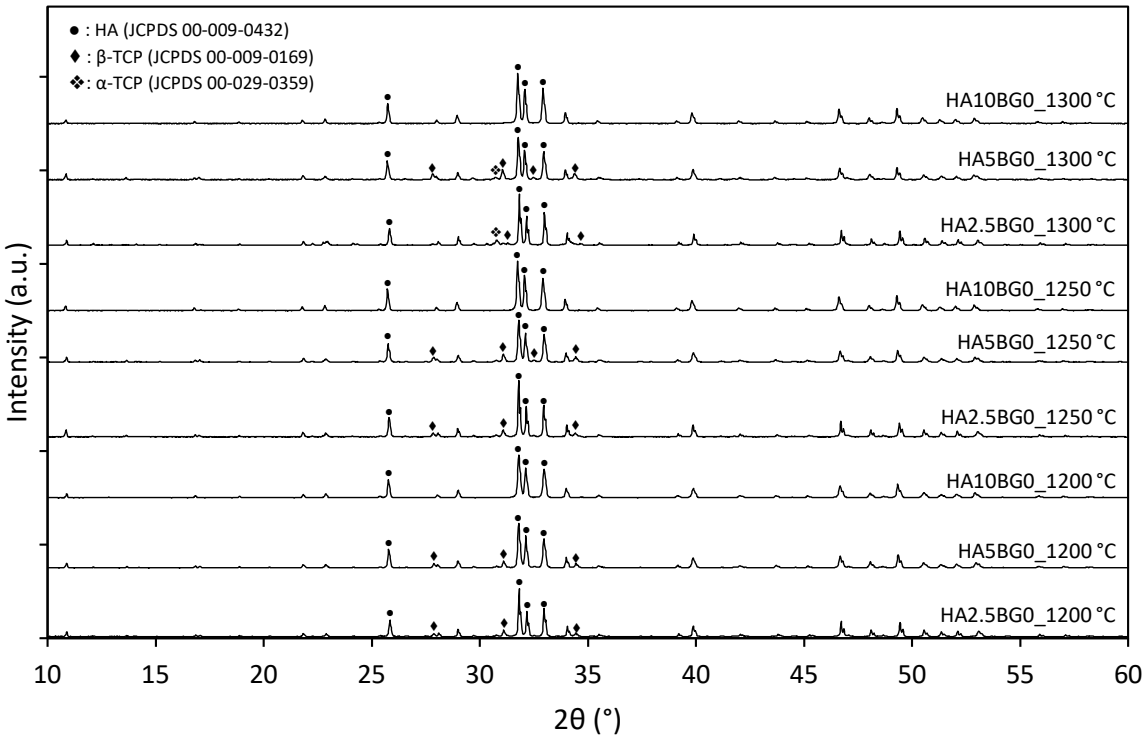

Figure 5.7: X-ray diffractograms of sintered GR-HA specimens containing BG0.

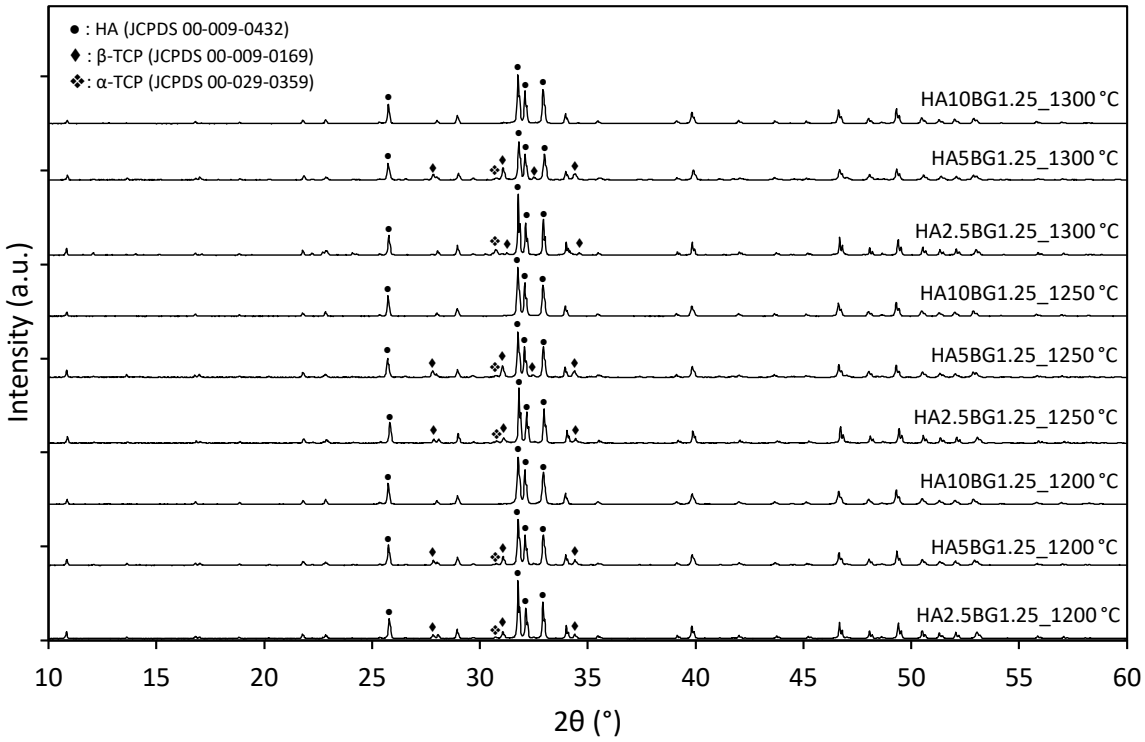

Figure 5.8: X-ray diffractograms of sintered GR-HA specimens containing BG1.25.

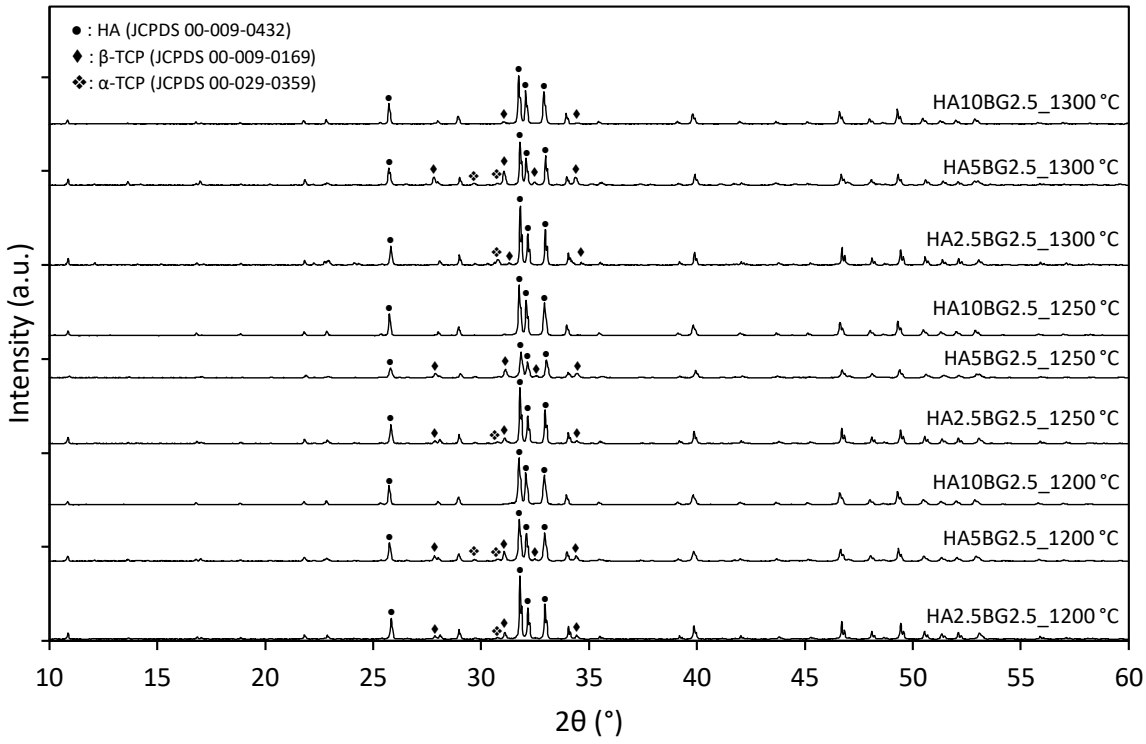

Figure 5.9: X-ray diffractograms of sintered GR-HA specimens containing BG2.5.

In previous GR-HA studies employing silicate, phosphate or borosilicate-based glasses, phase transformations were reported and the glass presence was identified as the underlying cause. Those phase transformations are mainly connected to HA decomposition, mainly β-TCP that transforms to α-TCP at higher sintering temperatures, but can be glass composition dependent, such as: calcium phosphate silicate in silicate-based systems [101], [104], [114]. Moreover, the reactivity of the glass, which is responsible for the presence of the aforementioned phases, increases with increasing sintering temperature.

In the case of the studied borosilicate GR-HA system, it is evident that similar trends are partially present in terms of phase transformations. Specimens containing up to 5 wt.% of glass content exhibit increased reactivity with increasing temperature. The main phase recorded is β-TCP that reverts to α-TCP at higher sintering temperatures. The presence of

small quantities of β-TCP is not necessarily harmful in terms of bioactivity, since its solubility and dissolution rate can be favourable in biomedical systems [8], [111], [257]. However, the higher dissolution rates of α-TCP could prove to be problematic, as described in Chapter 2. When the glass content increases to 10 wt.%. this trend is completely reversed. Thermal degradation is negated in samples containing the highest amount of glass and no phase transformations are present, besides miniscule traces of β-TCP found in HA10BG2.5 sintered at 1300 °C.

In order to quantify the phase presence within the studied GR-HA system, Rietveld analysis was carried out. The results for all the GR-HA specimens, including phase analysis and unit cell related values, can be found in Table 5.2.

Table 5.2: Rietveld analysis results of HA and GR-HA specimens

Description	Sintering temperature (°C)	a (Å)	b (Å)	c (Å)	Volume (Å^3)	%HA	%β-TCP	%α-TCP
HA	1200	9.41583	9.41583	6.879805	528.231	100%	0%	0%
HA	1250	9.422141	9.422141	6.883087	529.192	100%	0%	0%
HA	1300	9.410572	9.410572	6.8798	527.641	100%	0%	0%
HA2.5BG0	1200	9.414956	9.414956	6.889078	528.845	95%	5%	0%
HA5BG0	1200	9.403274	9.403274	6.893292	527.856	96%	4%	0%
HA10BG0	1200	9.416542	9.416542	6.906814	530.385	100%	0%	0%
HA2.5BG0	1250	9.409682	9.409682	6.892378	528.506	92%	8%	0%
HA5BG0	1250	9.413236	9.413236	6.909271	530.201	93%	7%	0%
HA10BG0	1250	9.403516	9.403516	6.883239	527.113	100%	0%	0%
HA2.5BG0	1300	9.439892	9.439892	6.90755	533.076	92%	3%	4%
HA5BG0	1300	9.444526	9.444526	6.915736	534.231	73%	21%	6%
HA10BG0	1300	9.406182	9.406182	6.891042	528.01	100%	0%	0%
HA2.5BG1.25	1200	9.420367	9.420367	6.89809	530.146	95%	4%	1%
HA5BG1.25	1200	9.413367	9.413367	6.892158	528.903	89%	9%	2%
HA10BG1.25	1200	9.419714	9.419714	6.896603	529.958	100%	0%	0%
HA2.5BG1.25	1250	9.418589	9.418589	6.888652	529.22	95%	4%	1%
HA5BG1.25	1250	9.401353	9.401353	6.888031	527.238	76%	20%	5%
HA10BG1.25	1250	9.412133	9.412133	6.886351	528.319	100%	0%	0%
HA2.5BG1.25	1300	9.44743	9.44743	6.900291	533.366	93%	2%	5%
HA5BG1.25	1300	9.404974	9.404974	6.899386	528.514	82%	16%	2%
HA10BG1.25	1300	9.410772	9.410772	6.888092	528.299	100%	0%	0%

HA2.5BG2.5	1200	9.413219	9.413219	6.887856	528.556	95%	4%	1%
HA5BG2.5	1200	9.39357	9.39357	6.888951	526.435	85%	12%	3%
HA10BG2.5	1200	9.411806	9.411806	6.893232	528.81	100%	0%	0%
HA2.5BG2.5	1250	9.400662	9.400662	6.897917	527.917	93%	5%	2%
HA5BG2.5	1250	9.390693	9.390693	6.909702	527.698	90%	9%	1%
HA10BG2.5	1250	9.395847	9.395847	6.887458	526.576	100%	0%	0%
HA2.5BG2.5	1300	9.400336	9.400336	6.892773	527.487	95%	0%	5%
HA5BG2.5	1300	9.402717	9.402717	6.893749	527.828	73%	24%	3%
HA10BG2.5	1300	9.413793	9.413793	6.890293	528.807	98%	2%	0%

From the phase analysis results presented in Table 5.2, it is evident that sintering did not negatively affect pure HA in terms of thermal degradation; HA was the sole phase present throughout the sintering range. GR-HA composites containing glass loading of 5 wt.%, regardless of their lanthanum content, are the most susceptible within the test range to phase transformation phenomena. β-TCP is present in every sample even in the lowest sintering temperature. As the heat treatment intensifies the amount of β-TCP increases, complimented by small portions of α-TCP, as expected. Up to 1250 °C, the amount of β-TCP and α-TCP are comparable to samples containing both 2.5 and 5.0 wt.% of glass content. However, as the sintering temperatures rise, GR-HA samples containing 2.5 wt.% of glass do not exhibit phase transformations as intensely as their 5.0 wt.% counterparts. Last but not least, GR-HA composites containing 10 wt.% of glass loading, do not exhibit any HA degradation phenomena. The sole case where small traces of β-TCP (i.e., 2%) can be found, was with the specimen containing the highest loading of La_2O_3, when sintered at 1300 °C.

In general, it can be concluded that specimens containing 5 wt.% of glass or less, regardless of the lanthanum loading and the sintering temperature, exhibit the highest amount of phase transformation phenomena. Small glass additions act as heterogeneous nuclei sites or triggering points that promote the β-TCP phase transformation, which in higher sintering temperatures degrades partially to α-TCP. Analogous results with similar glass loadings have been reported by Lopes et al. [106] and Demirkiran et al. [139], [172]. Moreover, GR-HA specimens containing the highest glass loading do not induce any phase transformation phenomena; the high amount of glass potentially shields HA from thermal degradation.

Phase analysis results per La_2O_3 loading (including pure HA for reference) can be found in Figure 5.10.

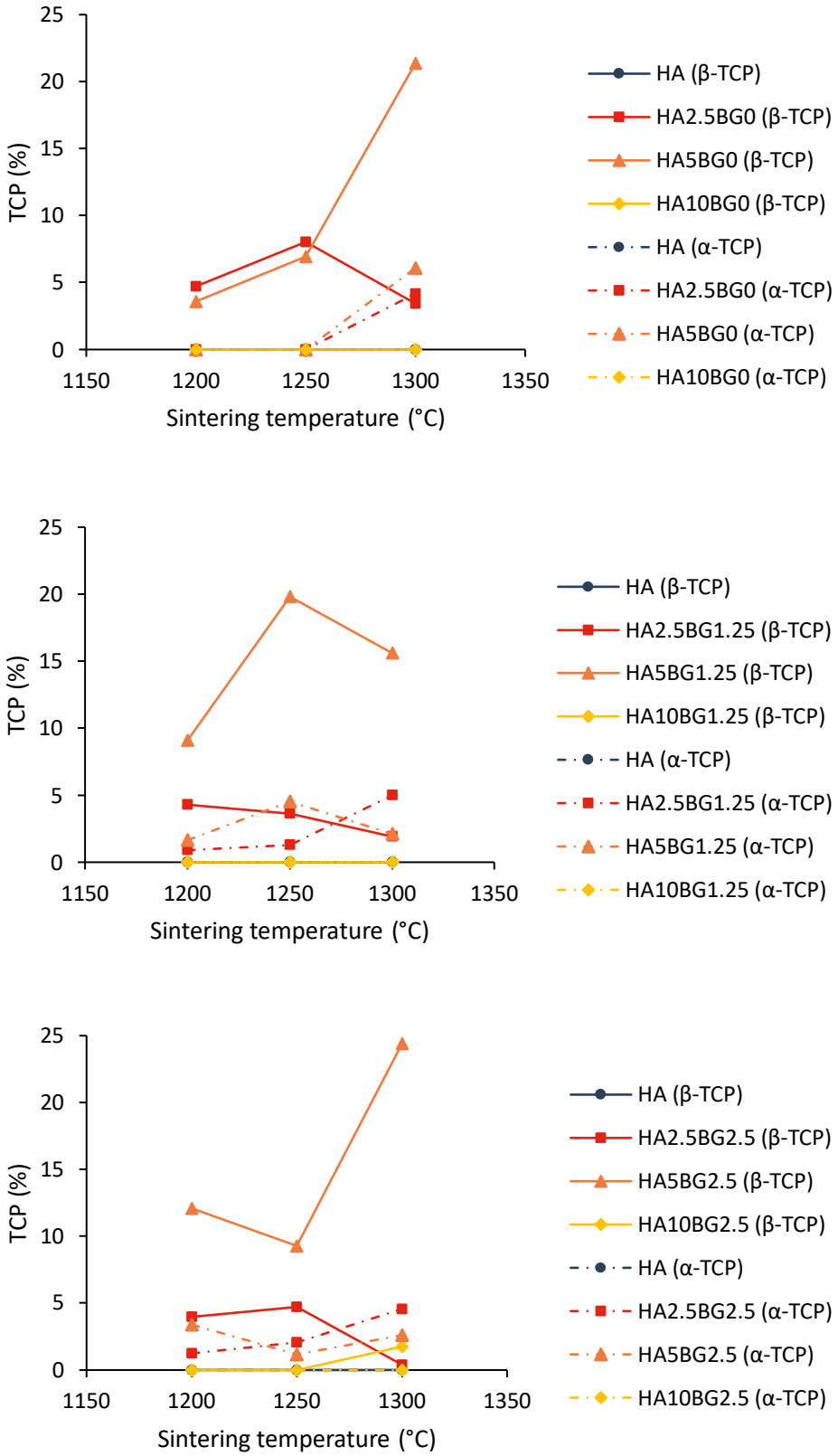

Figure 5.10: α-TCP and β-TCP phase fraction present in GR-HA specimens per La_2O_3 loading (including pure HA for reference).

Variation of the a-axis, c-axis and unit cell volume parameters per La_2O_3 loading (including pure HA for reference) can be found in Figure 5.11.

The a-axis parameter of pure HA's unit cell tends to increase with sintering temperature up to 1250 °C and then decreases slightly at the highest sintering temperature. A similar trend is observed for the c-axis parameter and the unit cell volume. Similar results have been reported in studies by Tancred et al. [11] and Lopes et al. [103], [109].

The a-axis in GR-HA composites containing ≤ 5 wt.% glass loading, regardless of their lanthanum content or sintering temperature, generally shrinks compared to pure HA. This trend is reversed only in the case of HA2.5BG0, HA5BG0 and HA2.5BG1.25 sintered at 1300 °C. This can be attributed to the glass reactivity that in small amounts acts as a triggering point that promotes thermal degradation. After all, the majority of the HA decomposition observed were in GR-HA composites containing ≤ 5 wt.% glass loading. Moreover, as the lanthanum content increases in these composites, this phenomenon attenuates. This could be an indication that lanthanum oxide could potentially play a role in stabilising this phenomenon. A decrease in the length of the a-axis of samples containing 10 wt.% of glass is observed for composites sintered up to 1250 °C compared to pure HA, regardless of their lanthanum content. However, as the sintering temperature rises to 1300 °C, a gradual stretch of the a-axis occurs as the lanthanum content increases. Since no phase transformations were observed for this subset of tested samples (i.e., influencing the expansion) this could be an indication of ion exchange within the lattice. La ions exhibit a larger ionic radius than Ca ions [254], hence such a replacement could justify the a-axis expansion.

The c-axis in GR-HA composites generally expands regardless of the sintering temperature, glass and/or lanthanum content. The composites exhibiting the lowest c-axis expansion are the ones containing 10 wt.%, followed by the ones with 2.5 wt.% and 5 wt.%. Small glass additions (≤ 5 wt.%) tend to act as heterogeneous nuclei sites or triggering points that promote thermal degradation. This can be attributed to chemical reactions taking place within the lattice between hydroxyl groups and specific glass components. Calcium carbonate, a glass precursor within this glass system, is known for inducing such distortions in GR-HA systems. Lopes et al. [13], [14] in similar studies employing a phosphate glass that used calcium carbonate as a precursor, confirmed the presence of carbonate groups at hydroxyl sites via FTIR measurements. The carbonate groups occupy a larger space compared to hydroxyl groups hence the lattice needs to expand in order to accommodate their presence. They concluded that small quantities of carbonate groups are dissolved during glass making and then are "redeployed" when the glass is used as a reinforcing aid in the GR-HA samples. Sodium carbonate is used as a glass precursor in the studied glass system potentially augmenting this effect. Therefore, the underlying cause behind this instability can be attributed to the aforementioned chemical imbalance mechanism. Moreover, it is worth mentioning that it was only this subset within the test group (i.e., GR-HA containing ≤ 5 wt.% glass loading) that exhibited thermal degradation, as discussed earlier.

Similar trends were observed regarding the unit cell volume of GR-HA specimens per the observations for the a-axis values. In general, composites containing ≤ 5 wt.% of glass loading, exhibited a smaller unit cell compared to HA, regardless of their lanthanum content or sintering temperature. Once again HA2.5BG0, HA5BG0 and HA2.5BG1.25 sintered at 1300 °C, did not conform with general trend for the same reasons described earlier. A decrease in the lattice volume of samples containing 10 wt.% of glass compared to pure HA is observed for

composites sintered up to 1250 °C, regardless of their lanthanum content. However, as the sintering temperatures rises at 1300 °C, the unit cell expands and a gradual increase is observed with increasing lanthanum content. This expansion cannot be attributed to any phase transformation phenomena since none were observed for this subset of tested samples. Therefore, the increase in unit cell volume could be justified by the replacement of Ca with La ions, since the latter exhibit a larger ionic radius [254].

Analogous results were presented in the literature in similar studies by Tancred et al. [120] and Lopes et al. [103], [109]. In the study by Lopes et al. [109], the research team observed similar glass reactivity in a GR-HA system employing a binary phosphate-based glass which included calcium carbonate as a precursor. With increasing sintering temperature, the a-axis shrunk while the c-axis expanded compared to pure HA, when glass loadings of 2.5 and 4 wt.% were used. HA decomposition was reported in either case, more prominent with increasing glass content. Symmetrical results were reported in a following study utilising 4 wt.% of a similar phosphate-based glass [103], where a-axis shrinkage, c-axis expansion and thermal degradation were recorded once again. In a study by Tancred et al. [120] investigating the use of silicate-based glass this time, the lattice parameters of the GR-HA composites exhibited the same behaviour, as previously described.

It can be concluded that the studied glass system exhibit similar behaviour in terms of HA decomposition phenomena when ≤ 5 wt.% of glass content is present within GR-HA specimens. However, it is worth mentioning that these thermal degradation phenomena are quite limited since the maximum HA to TCP conversion recorded was 27%. Furthermore, in the case of GR-HA composites employing 10 wt.% of glass content, no thermal degradation is observed which indicates that the glass presence mitigates HA decomposition. This can be

attributed to even heat distribution while sintering and in the glass system's resilience to undergo crystallisation phenomena. Lastly, there are strong indications that lanthanum ions replace calcium ions within HA's lattice, exhibiting stabilising behaviour in terms of thermal degradation. It was only in the case of the GR-HA specimen containing the highest amount of glass and lanthanum content, sintered at the highest sintering temperature, that miniscule HA decomposition (i.e., 2%) was observed.

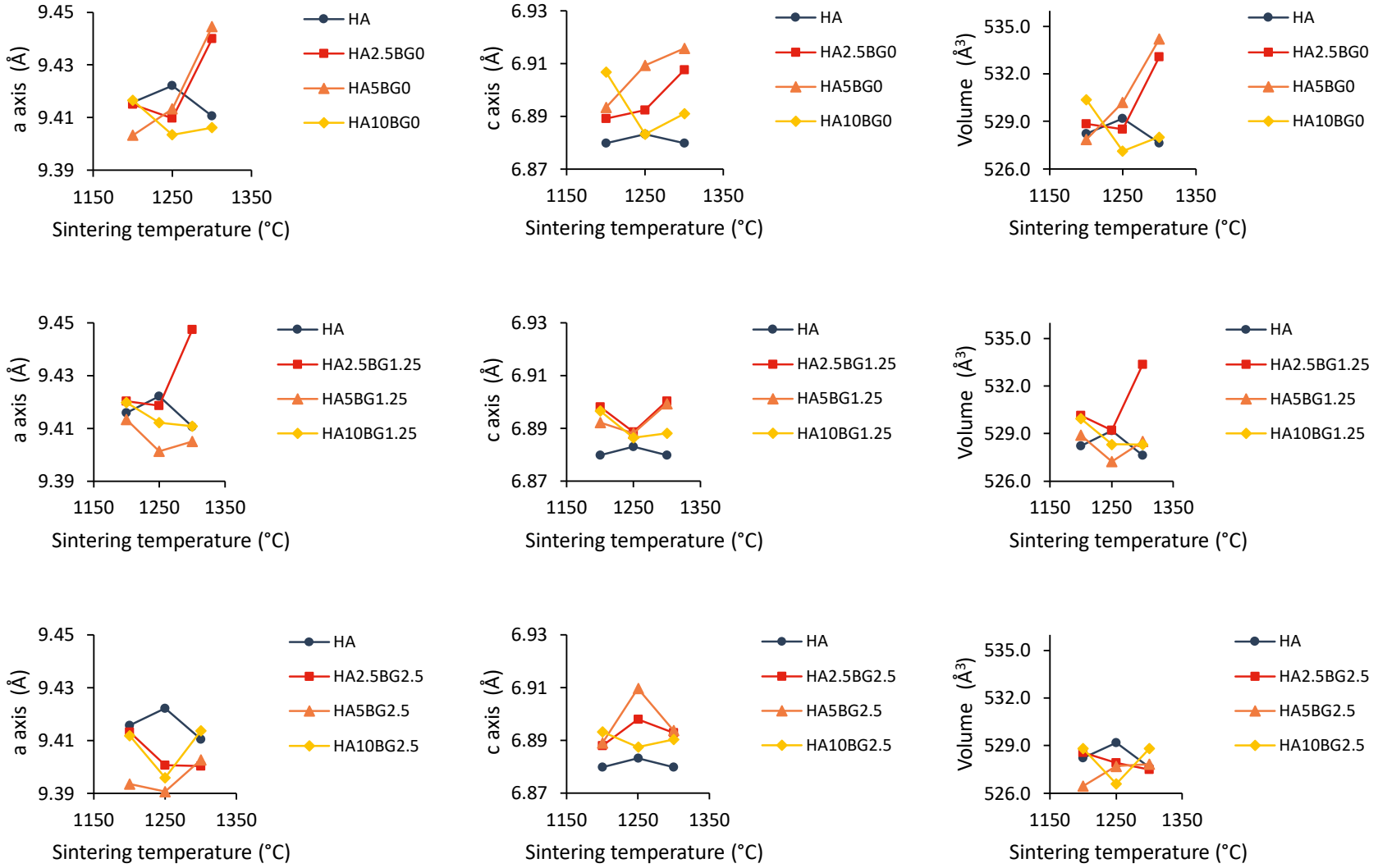

Figure 5.11: Unit cell lattice parameters of the GR-HA specimens per La_2O_3 loading (including pure HA for reference).

5.3 Mass loss during sintering

Mass measurements before and after sintering were carried out in order to investigate the sintering behaviour of the developed GR-HA system. The average pre and post sintering mass and average mass loss for all the tested samples can be found in Table 5.3.

Table 5.3: Average pre-sintering, post-sintering mass measurements and mass loss during sintering

Description	Sintering temperature (°C)	(Pre-sintering) Average mass ± STD (gr)	(Post-sintering) Average mass ± STD (gr)	Average mass loss (%)
HA	1200	0.741 ± 0.003	0.740 ± 0.002	0.16%
HA	1250	0.738 ± 0.011	0.738 ± 0.011	0.11%
HA	1300	0.750 ± 0.018	0.740 ± 0.006	1.34%
HA2.5BG0	1200	0.739 ± 0.012	0.731 ± 0.011	1.09%
HA5BG0	1200	0.745 ± 0.003	0.732 ± 0.003	1.67%
HA10BG0	1200	0.744 ± 0.003	0.723 ± 0.002	2.79%
HA2.5BG0	1250	0.744 ± 0.004	0.736 ± 0.004	1.13%
HA5BG0	1250	0.743 ± 0.002	0.73 ± 0.002	1.80%
HA10BG0	1250	0.741 ± 0.004	0.72 ± 0.005	2.87%
HA2.5BG0	1300	0.745 ± 0.002	0.736 ± 0.002	1.14%
HA5BG0	1300	0.741 ± 0.004	0.726 ± 0.003	1.96%
HA10BG0	1300	0.744 ± 0.003	0.720 ± 0.003	3.25%
HA2.5BG1.25	1200	0.738 ± 0.011	0.731 ± 0.011	1.00%
HA5BG1.25	1200	0.741 ± 0.005	0.729 ± 0.004	1.64%
HA10BG1.25	1200	0.743 ± 0.003	0.724 ± 0.003	2.48%
HA2.5BG1.25	1250	0.742 ± 0.003	0.733 ± 0.003	1.12%
HA5BG1.25	1250	0.737 ± 0.017	0.724 ± 0.017	1.72%
HA10BG1.25	1250	0.740 ± 0.005	0.721 ± 0.005	2.61%
HA2.5BG1.25	1300	0.739 ± 0.006	0.731 ± 0.006	1.07%
HA5BG1.25	1300	0.741 ± 0.002	0.728 ± 0.002	1.78%
HA10BG1.25	1300	0.739 ± 0.005	0.718 ± 0.004	2.86%
HA2.5BG2.5	1200	0.743 ± 0.006	0.735 ± 0.006	1.02%
HA5BG2.5	1200	0.740 ± 0.003	0.728 ± 0.003	1.63%
HA10BG2.5	1200	0.744 ± 0.003	0.725 ± 0.004	2.53%
HA2.5BG2.5	1250	0.744 ± 0.002	0.736 ± 0.002	1.02%
HA5BG2.5	1250	0.739 ± 0.005	0.725 ± 0.008	1.90%
HA10BG2.5	1250	0.741 ± 0.004	0.72 ± 0.004	2.84%
HA2.5BG2.5	1300	0.737 ± 0.010	0.729 ± 0.010	1.08%
HA5BG2.5	1300	0.738 ± 0.007	0.725 ± 0.006	1.76%
HA10BG2.5	1300	0.739 ± 0.006	0.717 ± 0.006	2.99%

Mass loss results per La_2O_3 loading (including pure HA for reference) can be found in Figure 5.12.

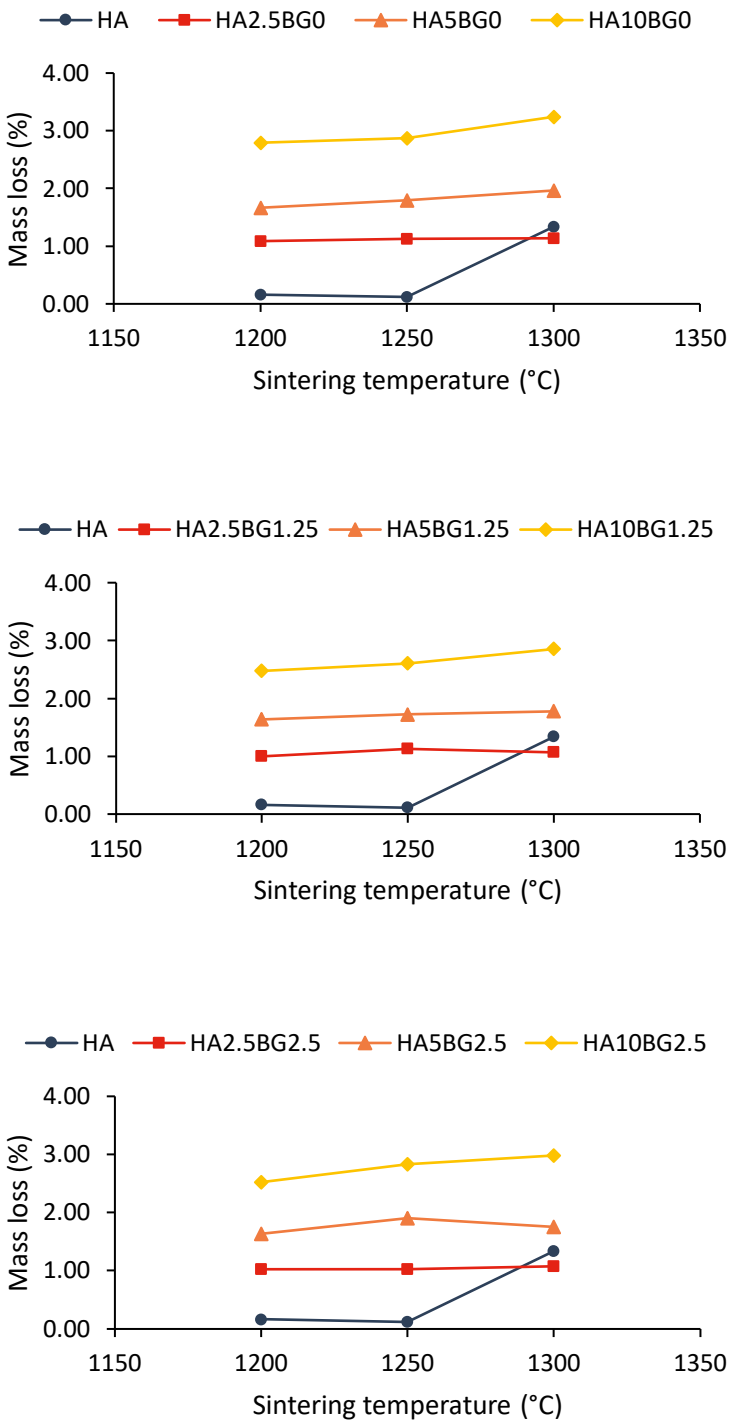

Figure 5.12: Mass loss during sintering of the GR-HA specimens per La_2O_3 loading (including pure HA for reference).

Pure HA samples exhibit no mass loss during sintering up to 1250 °C, and then a mass loss of 1.34% is recorded. In general, GR-HA samples exhibit increasing mass loss with increasing glass content, regardless of the La_2O_3 content and the sintering temperature. In particular, composite samples containing 2.5 wt.% of glass loading, experience a mass loss between 1.00 – 1.12 %. The samples containing double the amount of glass (i.e., 5 wt.%) exhibit a mass loss between 1.63 – 1.96 %. Finally, the samples containing the highest amount of glass, lose between 2.48 – 3.25 % of their mass during sintering.

Dehydroxylation could be the underlying cause regarding the mass loss observed for pure HA at 1300 °C besides the fact the fact that no secondary phases were observed for this specimen in the phase identification analysis. Miniscule quantities of decomposition products (e.g., β-TCP), most probably below the XRD instrument's detection limit, is a probable cause. (The detection limit in powder XRD measurements is dependent on various parameters, such as: sample preparation or background noise, and ranges between 1 – 2% [258]–[261]) Mass loss observed in GR-HA samples is probably linked to the glass addition. Increasing mass loss is observed with increasing glass content regardless of the sintering temperature and/or La_2O_3 content, as described earlier. This behaviour could potentially be linked to unreacted glass components that were released during sintering (e.g., CO_2 gas bubbles). Analogous results have been reported by Ivachenko when he studied a similar GR-HA system and identified pores that were linked to "*the removal of carbon oxides and water vapors resulting from glass charge decomposition and glass boiling*" [130].

This assumption is further validated by the SEM images taken for both pure HA and GR-HA composite samples, as it can be seen in Figure 5.13. Pure HA exhibits a large number of small pores. In contrast, the number of smaller pores seen on the surface of GR-HA specimens, is lower compared to pure HA and decreasing linearly with increasing glass content. In tandem, larger pores are observed with increasing glass content, which could indicate a potential escape route for gaseous components (e.g., water or CO_2). Therefore, it is safe to assume that there is a high possibility that unreacted glass components could be present in every BG composition tested. Additionally, this gradual elimination of smaller pores with increasing glass content is a strong indication of the glass' action as a sintering aid. The glass presence seems to positively influence the consolidation of GR-HA composites since larger consolidated areas are observed with increasing glass content. The increased liquid glass content present in those samples aids the sintering process by reducing the interfacial energy between particles and facilitating a faster atomic diffusion, compared to pure HA. This is achieved via a liquid sintering mechanism, as it has been reported for various GR-HA systems in the past [11], [47], [103], [104].

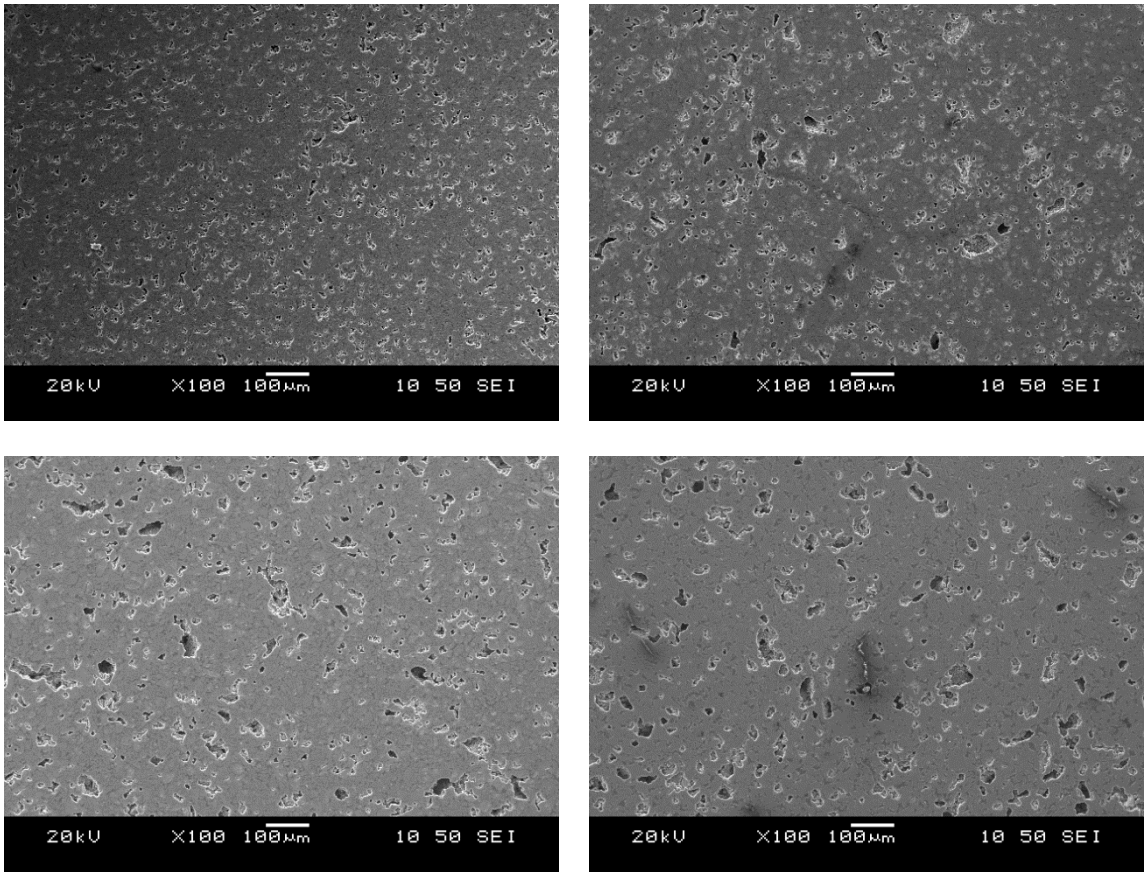

Figure 5.13: SEM images of the surface of HA (upper left), HA2.5BG0 (upper right), HA5BG0 (lower left) and HA10BG0 (lower right) sintered at 1300 °C.

5.4 Linear shrinkage

Linear shrinkage provides a useful metric describing the sinterability of ceramics; higher linear shrinkage values can be associated with increased densification/sintering capability. A linear shrinkage investigation was carried out in order to assess the effect of glass addition and sintering temperature in the developed GR-HA system. The average diameter, height and linear shrinkage of all the tested samples, can be found in Table 5.4.

Table 5.4: Average diameter, height and linear shrinkage results of pure HA and GR-HA specimens

Description	Sintering temperature (°C)	Average diameter ± STD (mm)	Average height ± STD (mm)	Linear shrinkage (%)
Non-sintered sample	-	13.02 ± 0.00	2.87 ± 0.00	0.00%
HA	1200	12.69 ± 0.00	2.77 ± 0.01	2.51%
HA	1250	12.46 ± 0.02	2.72 ± 0.02	4.33%
HA	1300	12.27 ± 0.02	2.69 ± 0.01	5.76%
HA2.5BG0	1200	12.91 ± 0.01	2.85 ± 0.01	0.82%
HA5BG0	1200	13.02 ± 0.00	2.88 ± 0.01	0.03%
HA10BG0	1200	12.54 ± 0.02	2.81 ± 0.01	3.71%
HA2.5BG0	1250	12.73 ± 0.02	2.78 ± 0.01	2.20%
HA5BG0	1250	12.92 ± 0.01	2.88 ± 0.01	0.77%
HA10BG0	1250	12.14 ± 0.02	2.75 ± 0.01	6.73%
HA2.5BG0	1300	12.55 ± 0.01	2.75 ± 0.00	3.61%
HA5BG0	1300	12.79 ± 0.01	2.83 ± 0.01	1.79%
HA10BG0	1300	11.87 ± 0.13	2.67 ± 0.03	8.80%
HA2.5BG1.25	1200	12.90 ± 0.01	2.83 ± 0.01	0.95%
HA5BG1.25	1200	12.99 ± 0.01	2.87 ± 0.02	0.23%
HA10BG1.25	1200	12.58 ± 0.05	2.78 ± 0.02	3.41%
HA2.5BG1.25	1250	12.72 ± 0.00	2.79 ± 0.02	2.28%
HA5BG1.25	1250	12.92 ± 0.01	2.82 ± 0.11	0.79%
HA10BG1.25	1250	12.15 ± 0.05	2.72 ± 0.00	6.71%
HA2.5BG1.25	1300	12.55 ± 0.01	2.78 ± 0.03	3.58%
HA5BG1.25	1300	12.78 ± 0.01	2.83 ± 0.01	1.82%
HA10BG1.25	1300	11.88 ± 0.13	2.64 ± 0.04	8.74%
HA2.5BG2.5	1200	12.91 ± 0.01	2.87 ± 0.03	0.84%
HA5BG2.5	1200	12.99 ± 0.01	2.91 ± 0.01	0.23%
HA10BG2.5	1200	12.68 ± 0.01	2.79 ± 0.01	2.64%
HA2.5BG2.5	1250	12.71 ± 0.01	2.81 ± 0.01	2.41%
HA5BG2.5	1250	12.90 ± 0.01	2.82 ± 0.02	0.92%
HA10BG2.5	1250	12.38 ± 0.04	2.77 ± 0.00	4.89%
HA2.5BG2.5	1300	12.55 ± 0.00	2.77 ± 0.03	3.58%
HA5BG2.5	1300	12.77 ± 0.00	2.8 ± 0.01	1.95%
HA10BG2.5	1300	12.06 ± 0.09	2.69 ± 0.02	7.37%

Linear shrinkage results per La_2O_3 loading (including pure HA for reference) are presented found in Figure 5.14.

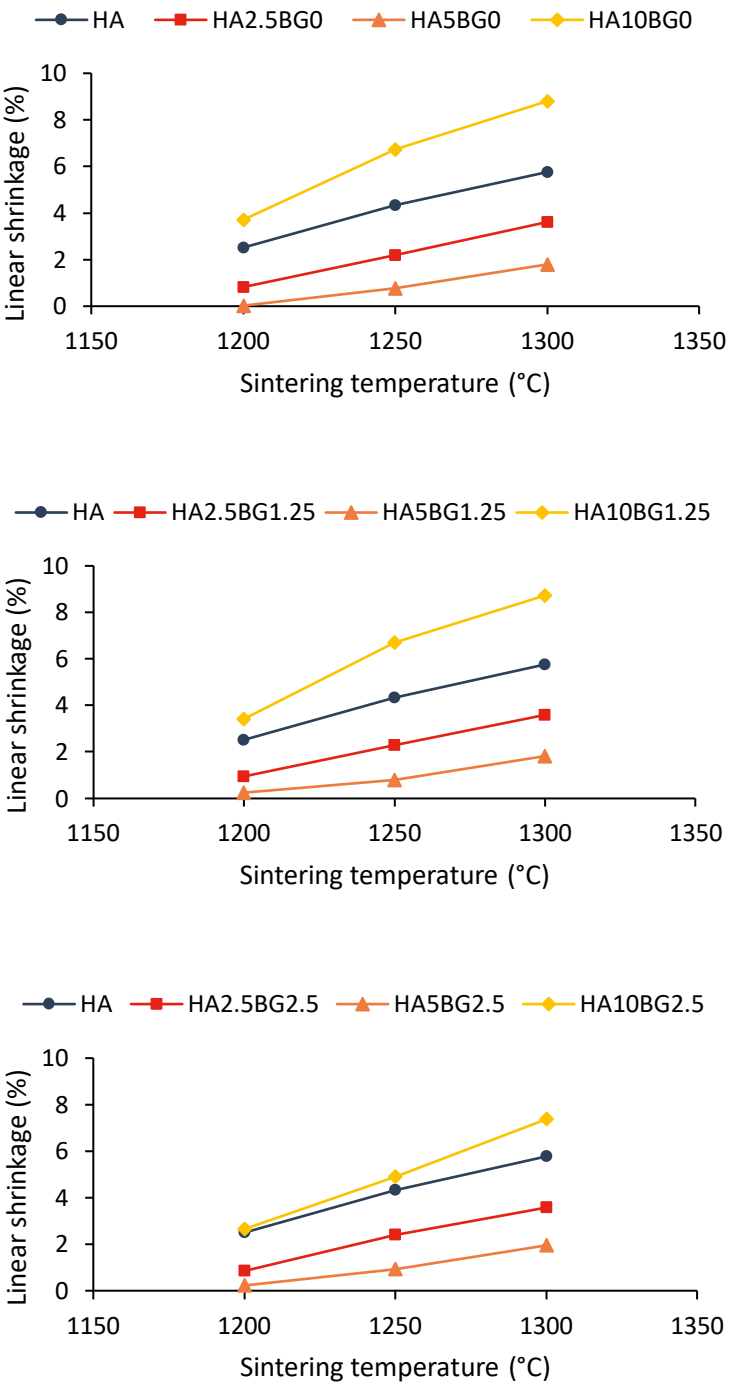

Figure 5.14: Linear shrinkage of the GR-HA specimens per La_2O_3 loading (including pure HA for reference).

Linear shrinkage is increasing with sintering temperature for all samples as expected when sintering ceramics. GR-HA samples containing ≤ 5 wt.% of glass loading, exhibit lower linear shrinkage compared to pure HA, regardless of the lanthanum loading. This finding directly

correlates with the results shown earlier in the XRD analysis, where these samples exhibited phase transformation phenomena during sintering. The presence of α and β-TCP, HA dehydroxylation products, induce a volume increase that hinders linear shrinkage [12]. GR-HA samples containing 5 wt.% of glass loading exhibited the lowest linear shrinkage within the test group followed by the composites containing 2.5 wt.% of glass content. This is directly related with the presence of secondary phases due to thermal degradation (i.e., α and β-TCP).

GR-HA containing the highest amount of glass loading exhibit the highest linear shrinkage within the test group, regardless of the lanthanum content. Generally, these samples did not exhibit any phase transformation phenomena and exhibit higher linear shrinkage compared to pure HA. Additionally, a gradual decrease in linear shrinkage is observed for GR-HA samples containing 10 wt.% of glass loading with increasing lanthanum content, when sintered at the highest temperature. This correlates directly to the finding presented earlier, where small traces of β-TCP (i.e., 2%) were found in HA10BG2.5 sintered at 1300 °C.

Analogous results were reported by Knowles et al. [12], where lower linear shrinkages were reported for GR-HA composites exhibiting thermal degradation phenomena.

5.5 Density and porosity

An apparent density investigation was carried out in order to assess the effect of glass presence within GR-HA specimens during sintering. Apparent density per La_2O_3 loading (including pure HA for reference) can be found in Figure 5.15. The average mass, diameter, height, volume and apparent density of all the tested samples, can be found in Table 5.5.

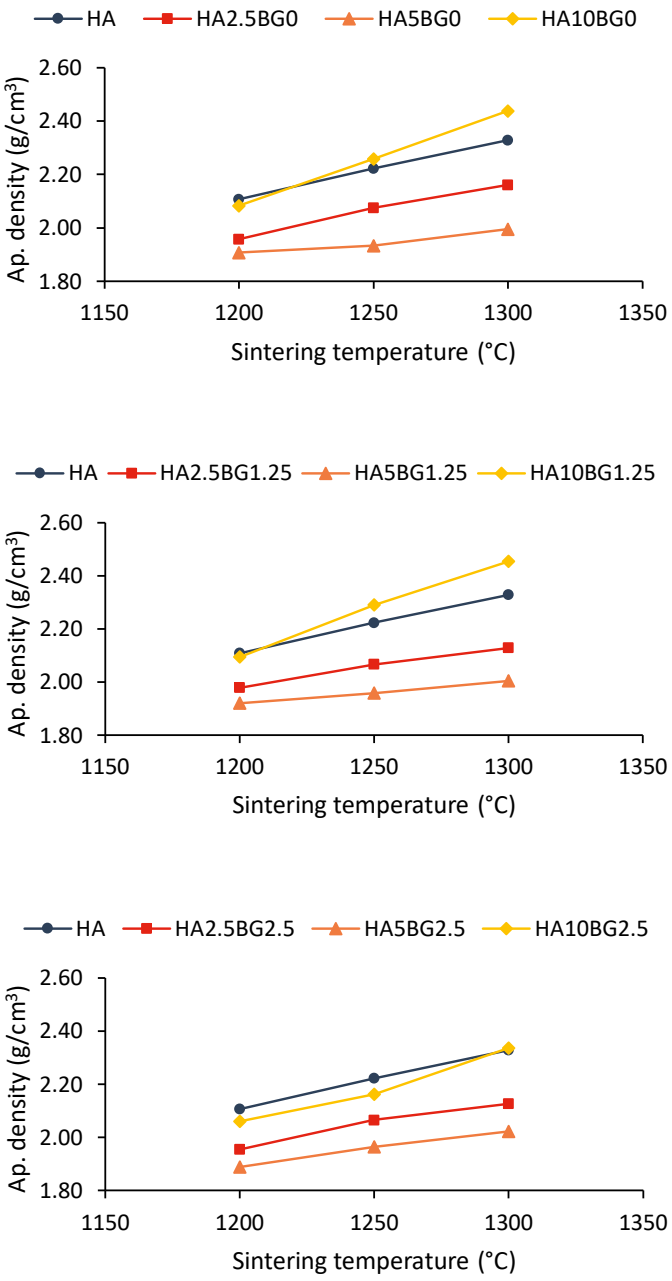

Figure 5.15: Apparent density of the GR-HA specimens per La_2O_3 loading (including pure HA for reference).

Table 5.5: Average mass, diameter, height, volume and apparent density results of HA and GR-HA specimens

Description	Sintering temperature (°C)	Average mass ± STD (g)	Average diameter ± STD (mm)	Average height ± STD (mm)	Average volume (mm^3)	Apparent density (g/cm^3)
HA	1200	0.74 ± 0.01	12.69 ± 0.01	2.77 ± 0.01	350.95	2.11
HA	1250	0.74 ± 0.01	12.46 ± 0.02	2.72 ± 0.02	331.89	2.22
HA	1300	0.74 ± 0.01	12.27 ± 0.02	2.69 ± 0.01	317.68	2.33
HA2.5BG0	1200	0.73 ± 0.01	12.91 ± 0.01	2.85 ± 0.01	373.70	1.96
HA5BG0	1200	0.73 ± 0.00	13.02 ± 0.01	2.88 ± 0.01	383.69	1.91
HA10BG0	1200	0.72 ± 0.00	12.54 ± 0.02	2.81 ± 0.01	347.28	2.08
HA2.5BG0	1250	0.74 ± 0.01	12.73 ± 0.02	2.78 ± 0.01	354.44	2.08
HA5BG0	1250	0.73 ± 0.01	12.92 ± 0.01	2.88 ± 0.01	377.58	1.93
HA10BG0	1250	0.72 ± 0.01	12.14 ± 0.02	2.75 ± 0.01	318.88	2.26
HA2.5BG0	1300	0.74 ± 0.01	12.55 ± 0.01	2.75 ± 0.01	340.59	2.16
HA5BG0	1300	0.73 ± 0.01	12.79 ± 0.01	2.83 ± 0.01	363.83	2.00
HA10BG0	1300	0.72 ± 0.01	11.87 ± 0.13	2.67 ± 0.03	295.22	2.44
HA2.5BG1.25	1200	0.73 ± 0.01	12.9 ± 0.01	2.83 ± 0.01	369.25	1.98
HA5BG1.25	1200	0.73 ± 0.01	12.99 ± 0.01	2.87 ± 0.02	379.91	1.92
HA10BG1.25	1200	0.72 ± 0.01	12.58 ± 0.05	2.78 ± 0.02	345.77	2.09
HA2.5BG1.25	1250	0.73 ± 0.01	12.72 ± 0.01	2.79 ± 0.02	355.15	2.07
HA5BG1.25	1250	0.72 ± 0.02	12.92 ± 0.01	2.82 ± 0.11	369.90	1.96
HA10BG1.25	1250	0.72 ± 0.01	12.15 ± 0.05	2.72 ± 0.01	314.80	2.29
HA2.5BG1.25	1300	0.73 ± 0.01	12.55 ± 0.01	2.78 ± 0.03	343.66	2.13
HA5BG1.25	1300	0.73 ± 0.01	12.78 ± 0.01	2.83 ± 0.01	363.22	2.00
HA10BG1.25	1300	0.72 ± 0.01	11.88 ± 0.13	2.64 ± 0.04	292.76	2.45
HA2.5BG2.5	1200	0.73 ± 0.01	12.91 ± 0.01	2.87 ± 0.03	376.14	1.95

HA5BG2.5	1200	0.73 ± 0.01	12.99 ± 0.01	2.91 ± 0.01	385.22	1.89
HA10BG2.5	1200	0.73 ± 0.01	12.68 ± 0.01	2.79 ± 0.01	352.09	2.06
HA2.5BG2.5	1250	0.74 ± 0.01	12.71 ± 0.01	2.81 ± 0.01	356.34	2.07
HA5BG2.5	1250	0.73 ± 0.01	12.90 ± 0.01	2.82 ± 0.02	369.00	1.97
HA10BG2.5	1250	0.72 ± 0.01	12.38 ± 0.04	2.77 ± 0.01	333.21	2.16
HA2.5BG2.5	1300	0.73 ± 0.01	12.55 ± 0.01	2.77 ± 0.03	342.84	2.13
HA5BG2.5	1300	0.72 ± 0.01	12.77 ± 0.01	2.8 ± 0.01	358.43	2.02
HA10BG2.5	1300	0.72 ± 0.01	12.06 ± 0.09	2.69 ± 0.02	307.00	2.34

Apparent density is increasing with sintering temperature for all samples as expected when sintering ceramics. GR-HA samples containing ≤ 5 wt.% of glass loading, exhibit lower apparent density compared to pure HA, regardless of the lanthanum loading and sintering temperature. The volume increase recorded in these samples, a by-product of the thermal degradation phenomena described earlier, hindered the sintering process in general. This drove the volume of the fired samples in higher values compared to pure HA, leading to lower apparent density values.

GR-HA specimens containing the highest amount of glass loading, generally exhibit the highest apparent density within the test group. This can be attributed to the presence of glass as a sintering aid. It essentially acts as a hindering agent for thermal degradation phenomena that can lead to volume expansion and facilitates even heat distribution during sintering. It is only in the case of samples containing the highest loading of La_2O_3, where the apparent density is almost equal or lower to pure HA. In tandem, a gradual decrease in apparent density with increasing lanthanum content is observed. Both those findings could not be linked to presence of HA decomposition by-products that lead to volume increase. On the contrary, it can be attributed to the expansion of the HA unit cell volume due to the infiltration of lanthanum ions within the lattice.

In order to investigate the densification effect of the glass presence within the GR-HA specimens, density measurements utilising the Archimedes' method were carried out. The average density, and porosity of all the tested samples, can be found in Table 5.6. Average density and porosity per La_2O_3 loading (including pure HA for reference) can be found in Figure 5.16.

Table 5.6: Average density and porosity of HA and GR-HA specimens

Description	Sintering temperature (°C)	Average density ± STD (g/cm^3)	Porosity (%)
HA	1200	2.76 ± 0.05	11.87%
HA	1250	2.81 ± 0.15	10.33%
HA	1300	2.85 ± 0.03	9.15%
HA2.5BG0	1200	2.64 ± 0.07	15.31%
HA5BG0	1200	2.68 ± 0.02	13.37%
HA10BG0	1200	2.66 ± 0.02	13.14%
HA2.5BG0	1250	2.74 ± 0.03	11.94%
HA5BG0	1250	2.72 ± 0.01	12.28%
HA10BG0	1250	2.69 ± 0.07	12.00%
HA2.5BG0	1300	2.71 ± 0.04	12.83%
HA5BG0	1300	2.72 ± 0.01	12.02%
HA10BG0	1300	2.68 ± 0.01	12.27%
HA2.5BG1.25	1200	2.69 ± 0.06	13.77%
HA5BG1.25	1200	2.68 ± 0.01	13.42%
HA10BG1.25	1200	2.68 ± 0.02	12.58%
HA2.5BG1.25	1250	2.65 ± 0.05	14.81%
HA5BG1.25	1250	2.67 ± 0.02	13.86%
HA10BG1.25	1250	2.64 ± 0.07	13.92%
HA2.5BG1.25	1300	2.71 ± 0.07	12.93%
HA5BG1.25	1300	2.67 ± 0.06	13.72%
HA10BG1.25	1300	2.70 ± 0.02	12.04%
HA2.5BG2.5	1200	2.73 ± 0.01	12.40%
HA5BG2.5	1200	2.61 ± 0.13	15.84%
HA10BG2.5	1200	2.66 ± 0.05	13.62%
HA2.5BG2.5	1250	2.74 ± 0.03	12.26%
HA5BG2.5	1250	2.68 ± 0.04	13.68%
HA10BG2.5	1250	2.72 ± 0.01	11.61%
HA2.5BG2.5	1300	2.75 ± 0.03	11.79%
HA5BG2.5	1300	2.71 ± 0.03	12.85%
HA10BG2.5	1300	2.73 ± 0.02	11.37%

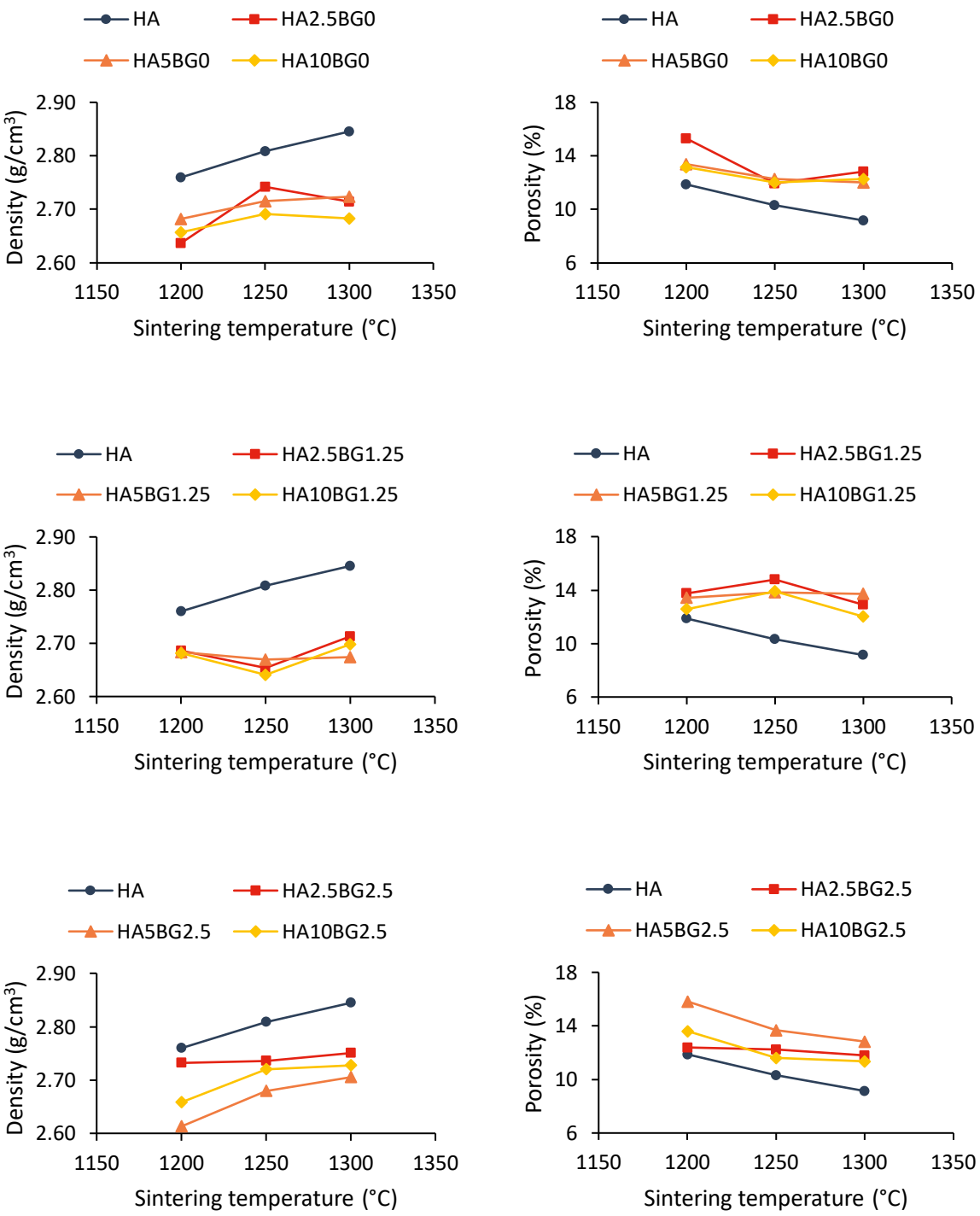

Figure 5.16: Average density and porosity of GR-HA specimens per La_2O_3 loading (including pure HA for reference).

Average density for both pure HA and GR-HA specimens is generally increasing with sintering temperature, as expected. Pure HA samples exhibit higher density values compared to GR-HA regardless of the glass or lanthanum content. This can be partially attributed to the lighter glass content replacing HA within the GR-HA matrix. Additionally, mass loss during sintering, as previously shown in sub-section 5.3, is another factor that could have potentially influenced the density values of the GR-HA specimens.

Porosity for both pure HA and GR-HA specimens is decreasing with increasing sintering temperature, as expected. Pure HA samples exhibit lower porosity compared to GR-HA specimens containing up to 5 wt.% of glass content; the trend is reversed with GR-HA samples containing the highest glass loading (i.e., 10 wt.%). These results directly correlate with the findings shown earlier in sub-section 5.4 regarding linear shrinkage, where lower values were recorded for GR-HA specimens containing ≤ 5 wt.% of glass content. Densification is inhibited in this subset of the tested samples, due to the dehydroxylation phenomena (i.e., volume increase). On the contrary, GR-HA samples containing the highest amount of glass content, exhibited lower degrees of porosity which can be attributed to better densification. This is an indicator of the glass performance as a sintering aid.

5.6 Grain size

In this section average grain size for all the tested samples was investigated in order to understand the influence of the glass presence in the microstructure of the GR-HA specimens. Average grain size of all the tested samples, can be found in Table 5.7. Average grain size per La_2O_3 loading (including pure HA for reference) can be found in Figure 5.17.

Table 5.7: Average grain size values of HA and GR-HA samples

Description	Sintering temperature (°C)	Average grain size (μm)
HA	1200	4.50 ± 0.50
HA	1250	4.53 ± 0.50
HA	1300	6.03 ± 0.50
HA2.5BG0	1200	4.12 ± 0.50
HA5BG0	1200	4.31 ± 0.50
HA10BG0	1200	4.04 ± 0.50
HA2.5BG0	1250	3.97 ± 0.50
HA5BG0	1250	4.07 ± 0.50
HA10BG0	1250	3.87 ± 0.50
HA2.5BG0	1300	3.52 ± 0.50
HA5BG0	1300	3.71 ± 0.50
HA10BG0	1300	3.98 ± 0.50
HA2.5BG1.25	1200	4.04 ± 0.50
HA5BG1.25	1200	3.71 ± 0.50
HA10BG1.25	1200	3.68 ± 0.50
HA2.5BG1.25	1250	3.86 ± 0.50
HA5BG1.25	1250	3.88 ± 0.50
HA10BG1.25	1250	4.10 ± 0.50
HA2.5BG1.25	1300	3.88 ± 0.50
HA5BG1.25	1300	4.32 ± 0.50
HA10BG1.25	1300	3.29 ± 0.50
HA2.5BG2.5	1200	3.73 ± 0.50
HA5BG2.5	1200	3.75 ± 0.50
HA10BG2.5	1200	3.46 ± 0.50
HA2.5BG2.5	1250	3.54 ± 0.50
HA5BG2.5	1250	3.45 ± 0.50
HA10BG2.5	1250	3.65 ± 0.50
HA2.5BG2.5	1300	3.24 ± 0.50
HA5BG2.5	1300	3.34 ± 0.50
HA10BG2.5	1300	3.29 ± 0.50

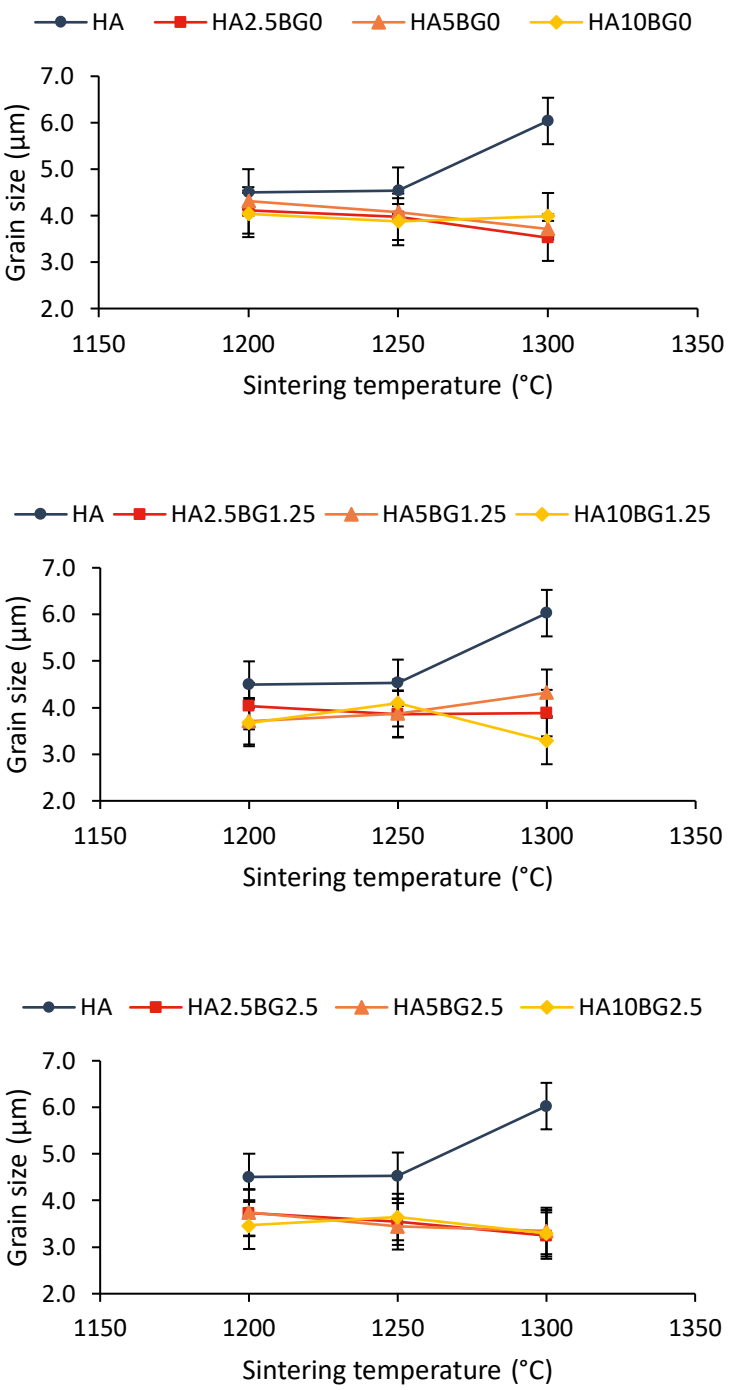

Figure 5.17: Grain size of GR-HA specimens per La_2O_3 loading (including pure HA for reference).

In pure HA samples, average grain size increases with increasing temperature, ranging from 4.50 – 6.03 μm. GR-HA composites regardless of their glass and/or lanthanum content, exhibit similar average grain size values throughout the sintering range temperature. This result suggests that the glass presence within GR-HA composites, inhibits grain growth. This is less evident at sintering temperatures between 1200 – 1250 °C, since the grain size values recorded for GR-HA specimens although smaller than pure HA, are still within the error range. The trend is much more visible at the highest sintering temperature, where pure HA samples exhibit an average grain size value of 6.03 μm and the highest value recorded throughout the GR-HA test range is 4.32 μm (i.e., HA5BG1.25). The smaller grain size recorded for the GR-HA composite samples compared to pure HA samples, is an indicator of mechanical performance enhancement. This result is favourable for the intended purpose (i.e., tissue engineering), considering the limitations of pure HA in load-bearing applications [8], [97].

Analogous results were reported by Santos et al. [104], Knowles et al. [12] where the glass constituent has been linked with grain growth inhibition. On the contrary, there were various studies that reported higher average grain size values for GR-HA specimens compared to pure HA [101], [106], [117]. In either case, the mechanism behind the ability to inhibit or promote grain growth is not clear. Grain growth is mainly associated with the glass composition and reactivity (i.e., induce of secondary phases) [101], [106], [117] while grain inhibition is associated to the presence of the liquid phase [12], [104] and the stability of HA during sintering [12].

5.7 Densification - µCT study

In order to investigate the densification of GR-HA specimens and the ability of the glass to act as a densification agent, µCT studies were carried out. The results from the µCT study regarding the densification of the sintered samples at 1300 °C can be found in Figure 5.18. The graph is divided into three sections – upper left, upper right & bottom – one per La_2O_3 content, 0, 1.25 and 2.5 mol% La_2O_3, respectively. Each section is further divided into four sub-sections where the identifier of each sample can be found in the upper right corner (e.g., HA). In the lower left corner, the X-Y cross section of each sample is depicted. The X-Z and Z-Y cross sections of all the samples per the same lanthanum content (e.g., 0 mol% La_2O_3) are depicted in the upper right and the lower left corner of each sub-section, respectively. The samples are stacked with increasing glass content, starting from pure HA at the bottom and progressing to the GR-HA specimen containing 10 wt.% of glass at the top.

GR-HA samples containing less than 5 wt.% of glass loading, regardless of the La_2O_3 content, exhibit lower densification compared to pure HA. On the contrary, the composite specimens containing the highest amount of glass, showcase the highest densification overall within the test group (including pure HA). The increased liquid glass content present in those samples aids the sintering process by reducing the interfacial energy between particles and facilitating a faster atomic diffusion, compared to pure HA. This can be directly correlated to the linear shrinkage and porosity results, shown earlier.

A brief study containing only composite samples employing BG2.5 was carried out in order to investigate the threshold upon which densification becomes more prominent. GR-HA containing glass loadings between 6 – 9 wt.% were prepared and tested under the same conditions as per the original study. The results from the aforementioned densification study can be found in Figure 5.19. The graph is divided into four sections – upper left, upper right, lower left & lower right – one per La_2O_3 content, 6, 7, 8 and 9 wt.% of glass content, respectively. Each section is further divided into four sub-sections where the identifier of each sample can be found in the upper right corner (e.g., HA). In the lower left corner, the X-Y cross section of each sample is depicted. The X-Z and Z-Y cross sections of all the samples are depicted in the upper right and the lower left corner of each sub-section, respectively. The samples are stacked with increasing glass content, starting from HA6BG2.5 at the bottom and progressing to HA9BG2.5 at the top.

Densification seems to be increasing proportionally with increasing glass content, confirming that glass acts as a sintering aid. There is no radical densification observed for samples containing up to 7 wt.% of glass content. However, X-ray penetration reduces significantly as the glass content reached 8 wt.% and densification becomes more prominent. As the glass content increases at the final stage (i.e, HA9BG2.5), a similar densification pattern as for HA10BG2.5 is observed. To conclude, 8 wt.% of glass loading seems to be the threshold upon which the glass starts acting as an effective densification agent.

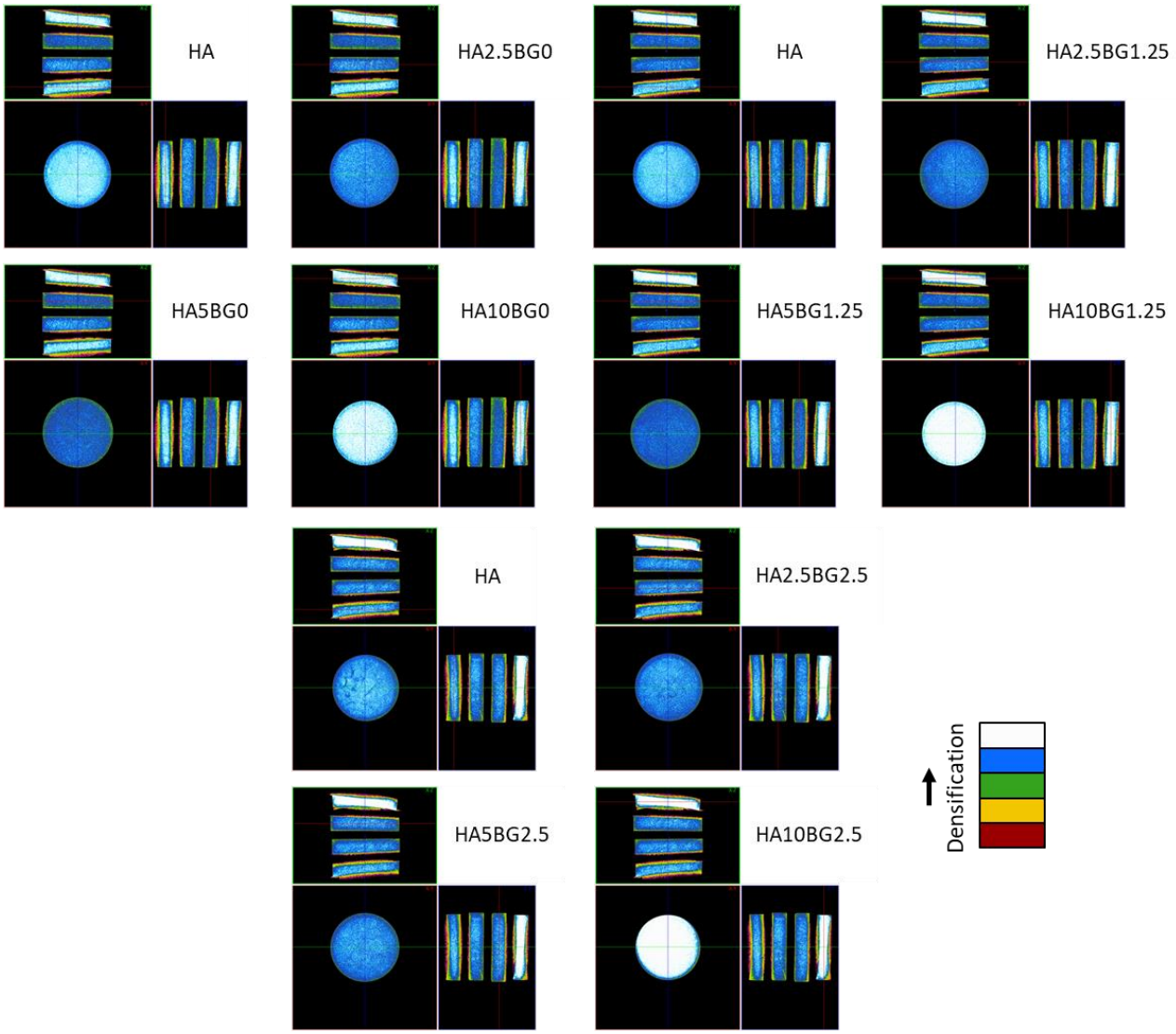

Figure 5.18: µCT images of the cross sections of pure HA and GR-HA specimens.

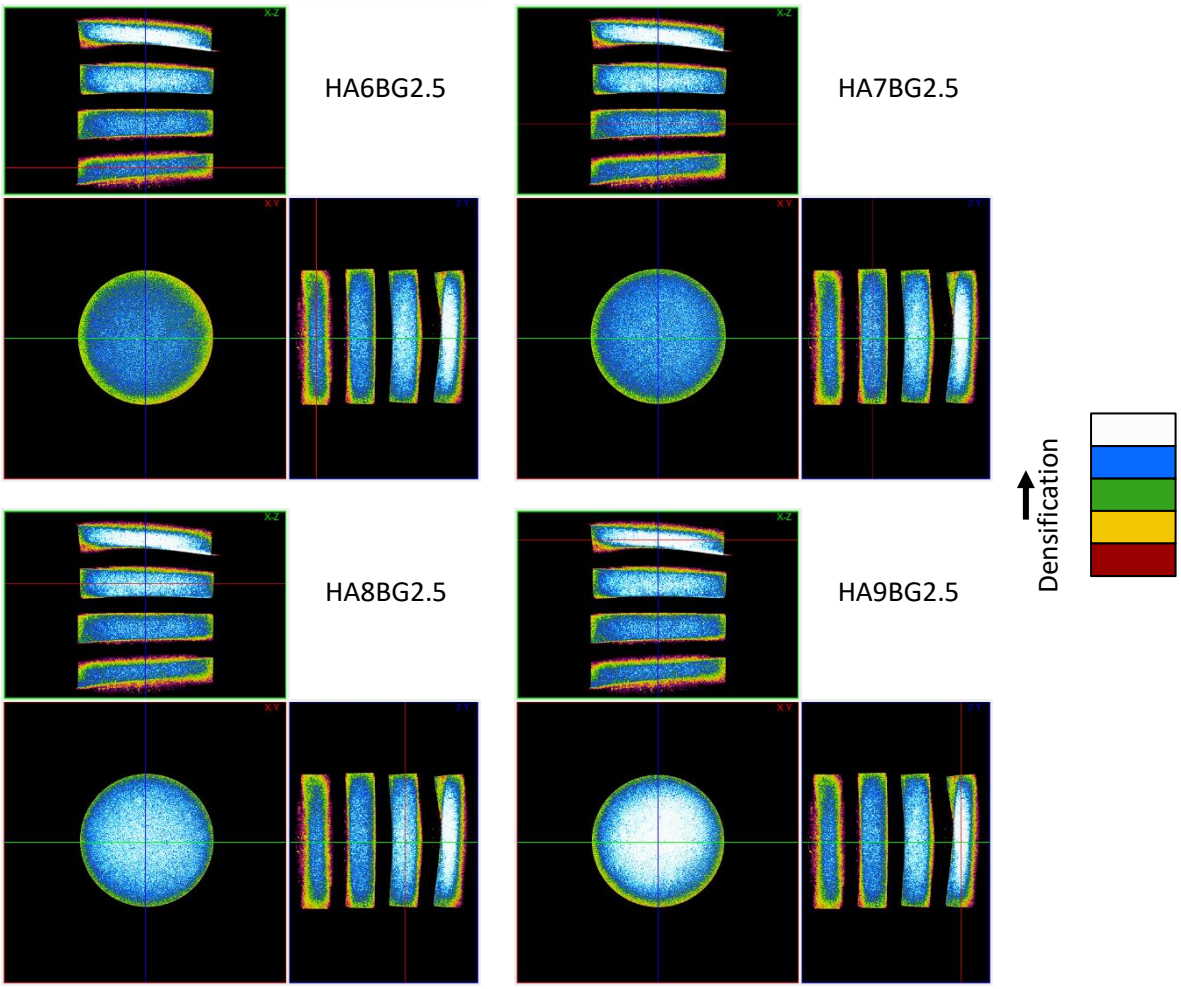

Figure 5.19: µCT images of the cross sections of the GR-HA specimens during the densification study.

5.8 Mechanical performance – Microhardness

In this section microhardness measurements were carried out in order to investigate the glass effect on strengthening the GR-HA samples. Average microhardness of all the tested samples, can be found in Table 5.8. Microhardness per La_2O_3 loading (including pure HA for reference) can be found in Figure 5.20.

Table 5.8: Microhardness values of HA and GR-HA samples

Description	Microhardness ± STD (HV0.3)
HA	122.31 ± 12.26
HA2.5BG0	87.25 ± 15.61
HA5BG0	84.73 ± 14.84
HA10BG0	134.25 ± 32.46
HA2.5BG1.25	104.06 ± 16.42
HA5BG1.25	70.89 ± 9.90
HA10BG1.25	155.36 ± 46.66
HA2.5BG2.5	92.42 ± 14.76
HA5BG2.5	82.98 ± 13.51
HA10BG2.5	160.40 ± 43.02

GR-HA composites containing ≤ 5 wt.% of glass loading, regardless of their La_2O_3 content, exhibit lower microhardness values compared to pure HA. This trend reverses with GR-HA containing 10 wt.% of glass content since higher microhardness values are observed compared to pure HA. Additionally, an increasing trend in microhardness is observed within this test group (i.e., 10 wt.% of glass content) with increasing lanthanum content. More specifically, an increase of 9.7%, 27.0% and 31.1% is recorded for HA10BG0, HA10BG1.25 and HA10BG2.5 compared to pure HA, respectively.

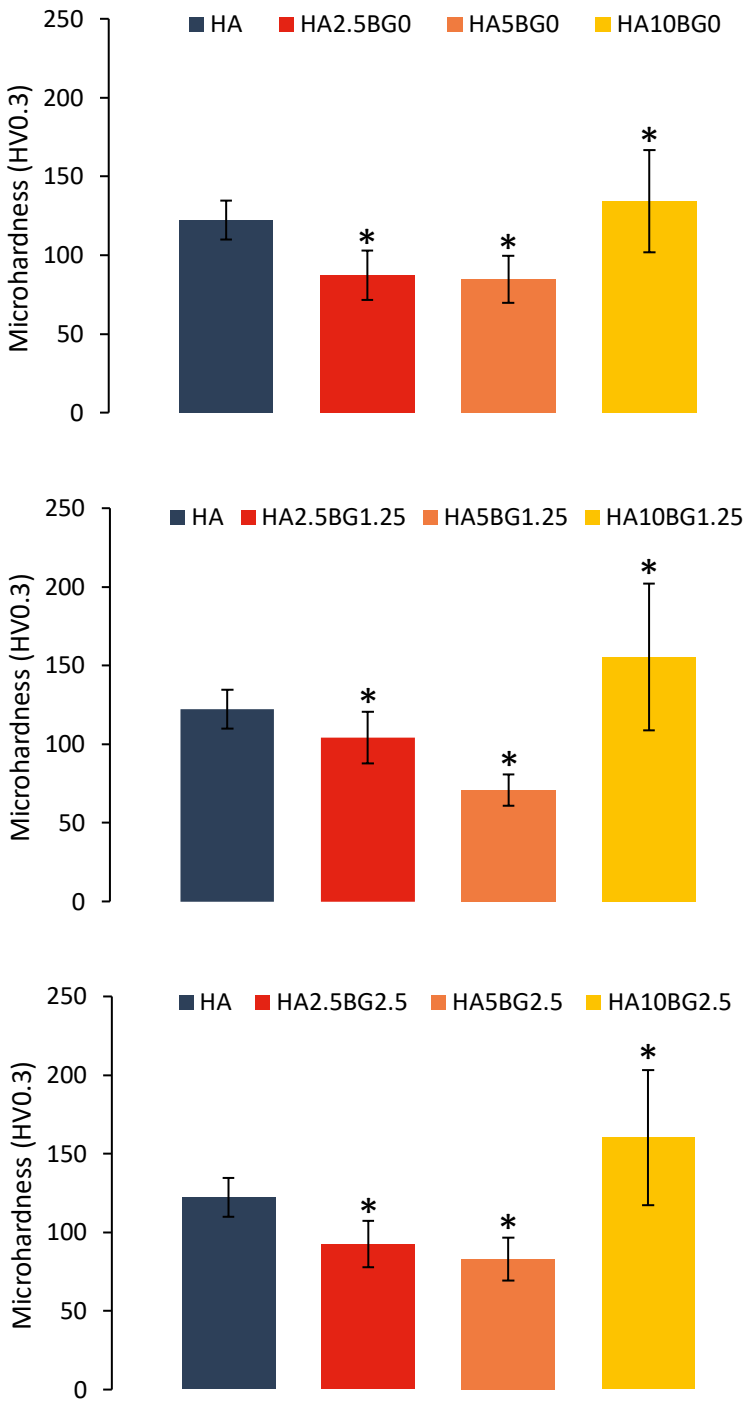

Figure 5.20: Microhardness values of GR-HA specimens per La_2O_3 loading (including pure HA for reference). (The asterisk (*) indicates significant difference (P<0.05) between HA and the tested GR-HA specimens.)

The decrease in microhardness for samples containing ≤ 5 wt.% of glass content, can be attributed to decreased densification due to the thermal degradation phenomena, reported previously. Additionally, the higher values of microhardness in samples containing 10 wt.% of glass content compared to pure HA, is a direct result of the glass' function as a liquid sintering aid.

One of the main mechanisms behind the enhancement in microhardness is the elimination of porosity [102], [107]. As seen previously, at sub-sections 5.3, 5.5 and 5.7, the densification of the samples containing less than 5 wt.% of glass content was always lower compared to pure HA. Only GR-HA specimens containing the highest amount of glass loading exhibited better densification performance. An additional microstructural feature besides porosity that can influence hardness at a lesser extent, is the presence of β-TCP. The presence of the latter in calcium phosphate ceramics has been linked with microhardness enhancement in the literature [107], [262]. However, its contribution comes into effect only when minimal porosities are observed since densification is the main driving force behind mechanical reinforcement. That is the case with the GR-HA specimens containing less than 5 wt.% of glass content. Besides the presence of substantial quantities of β-TCP present in those samples, it was the increased porosity that hindered the microhardness enhancement. Additionally, La_2O_3 has been linked as a mechanical performance enhancer in the literature [60], [79], [263]. Lastly, the incorporation of La ions within the HA matrix is known aid towards densification [264]. Therefore, it is plausible that the increase in microhardness with increasing La_2O_3 content in GR-HA composites containing 10 wt.% of glass content, can be jointly attributed to the presence of La_2O_3.

Analogous results have been reported in similar studies investigating GR-HA systems by various research groups. More specifically, Oktar et al. [102] reported increased hardness for GR-HA samples containing 10 wt.% of a binary phosphate-based glass, compared to pure HA and composites containing 5 wt.% of glass content. Lopes et al. [107] in a similar study investigating GR-HA systems employing ≤ 4 wt.% of ternary and quaternary phosphate-based glasses, identified a correlation between the glass presence and increased hardness values. The GR-HA samples exhibited higher densification rates compared to pure HA and in some cases the presence of β-TCP enhanced this effect, as well. On the contrary, Tancred et al. [120] did not identify a link between glass content and improved microhardness. This study investigated the use of a silicate-based glass system and every GR-HA composite was inferior in terms of hardness compared to pure HA specimens. The deterioration in mechanical strengthening was attributed to the glass reactivity that hindered sintering (i.e., high porosity) and induced thermal degradation.

5.9 Antimicrobial studies

To investigate the antimicrobial efficacy of the developed GR-HA system, bacteria attachment studies were carried out. Two different bacteria were used, S. Epidermidis and P. Aeruginosa, in order to assess the effectiveness for both Gram positive (S. Epidermidis) and Gram negative (P. Aeruginosa) candidates.

5.9.1 S. Epidermidis

The S. Epidermidis attachment study results for HA and GR-HA specimens can be found in Figure 5.21. In general, no inhibition of S. Epidermidis attachment on the surface of GR-HA specimens is observed throughout the test group, regardless of the glass or La_2O_3 content. The absorbance at 570 nm is directly related to the bacteria viability on the surface of the tested samples. Therefore, it can be concluded that the developed GR-HA system did not exhibit any efficacy against Gram positive bacteria; the bacteria population was not inhibited compared to pure HA which at this study acts as the control group. This result directly correlates with the literature on the subject since neither non-doped borosilicate glasses (e.g., Ag_2O, CuO, etc.) [48] nor La_2O_3 [60] have been shown to exhibit antimicrobial activity.

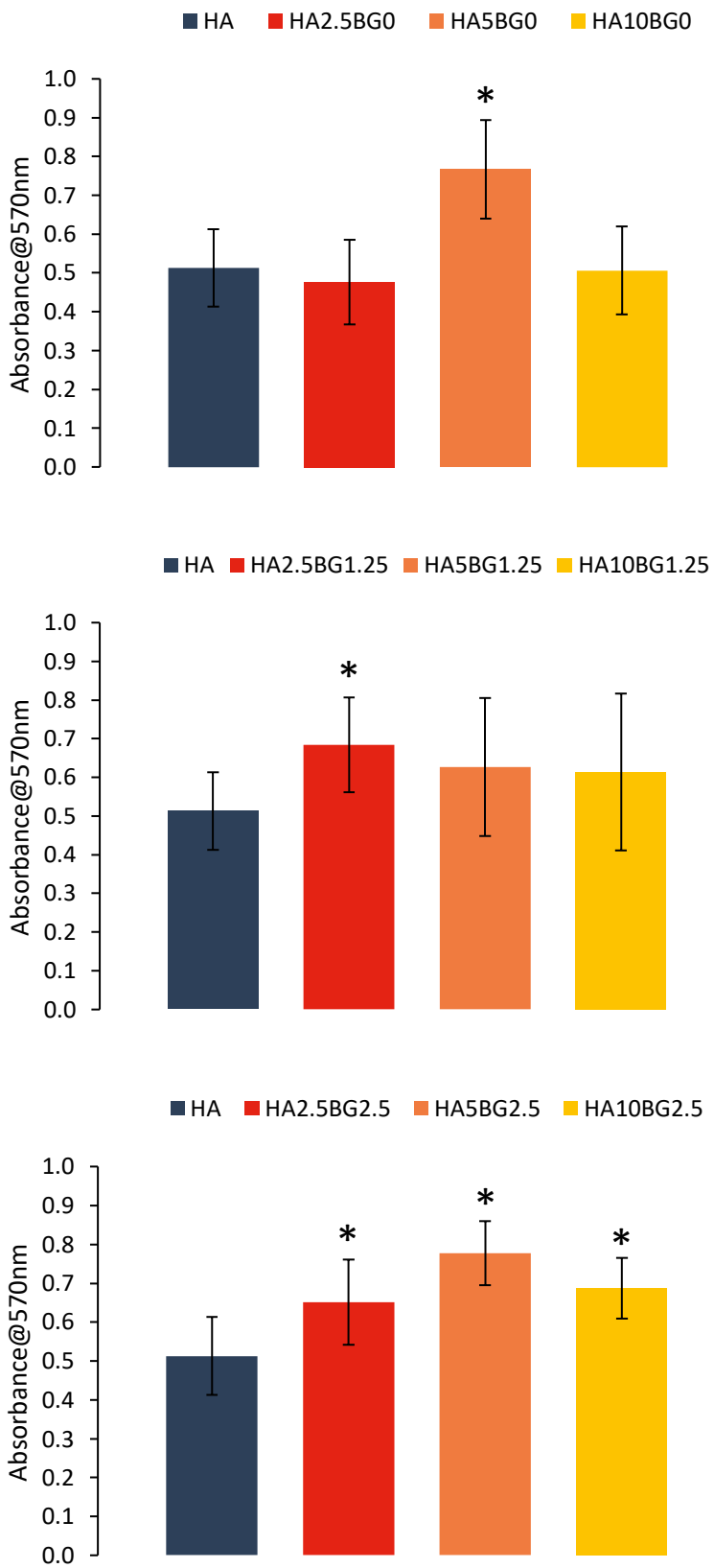

Figure 5.21: S. Epidermidis viability on the surface of the GR-HA specimens per La_2O_3 loading (including pure HA for reference). (The asterisk (*) indicates significant difference (P<0.05) between HA and the tested GR-HA specimens.)

5.9.2 P. Aeruginosa

The P. Aeruginosa attachment study results for HA and GR-HA specimens can be found in Figure 5.22. In general, no inhibition of P. Aeruginosa attachment on the surface of GR-HA specimens is observed throughout the test group, regardless of the glass or La_2O_3 content. The absorbance at 570 nm is directly related to the bacteria viability on the surface of the tested samples. Therefore, it can be concluded that the developed GR-HA system did not exhibit any efficacy against Gram negative bacteria; the bacteria population increased in numbers compared to pure HA, which at this study acts as the control group. Hence, the developed GR-HA system did not exhibit any efficacy against Gram negative bacteria. This result directly correlates with the literature on the subject since neither non-doped borosilicate glasses (e.g., Ag_2O, CuO, etc.) [48] nor La_2O_3 [60] have been shown to exhibit antimicrobial activity.

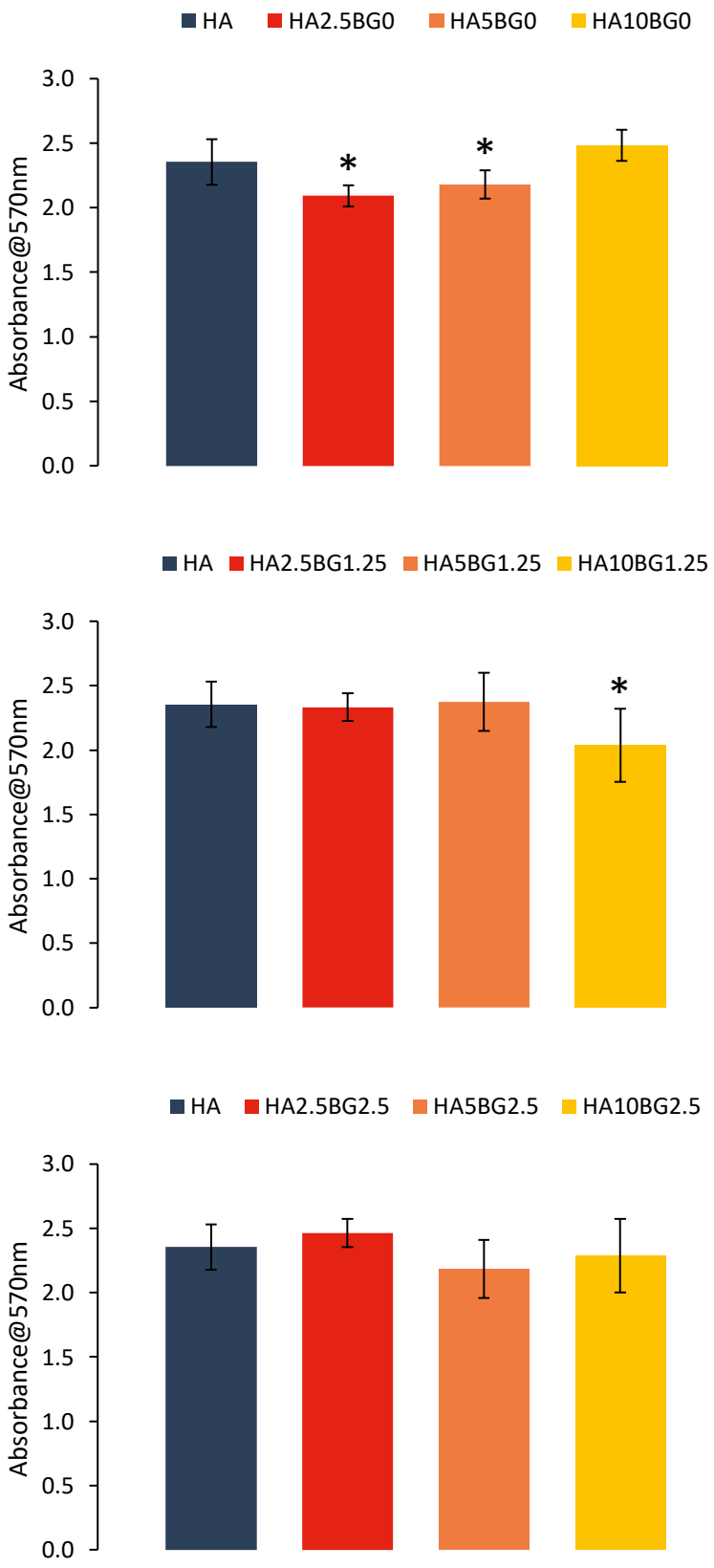

Figure 5.22: P. Aeruginosa viability on the surface of the GR-HA specimens per La_2O_3 loading (including pure HA for reference). (The asterisk (*) indicates significant difference (P<0.05) between HA and the tested GR-HA specimens.)

5.10 SaoS-2 cell culture study

In order to assess the biocompatibility and/or cytotoxicity of the developed GR-HA system, SaoS-2 cell attachment studies were carried out for three different incubation periods; day 1, 4 and 7. Pure HA was used as the control group of this study and the cell viability was measured using the MTT protocol.

The results from the MTT biocompatibility in vitro study regarding HA and GR-HA specimens containing BG0, for days 1,4 and 7 are presented in Figure 5.23.

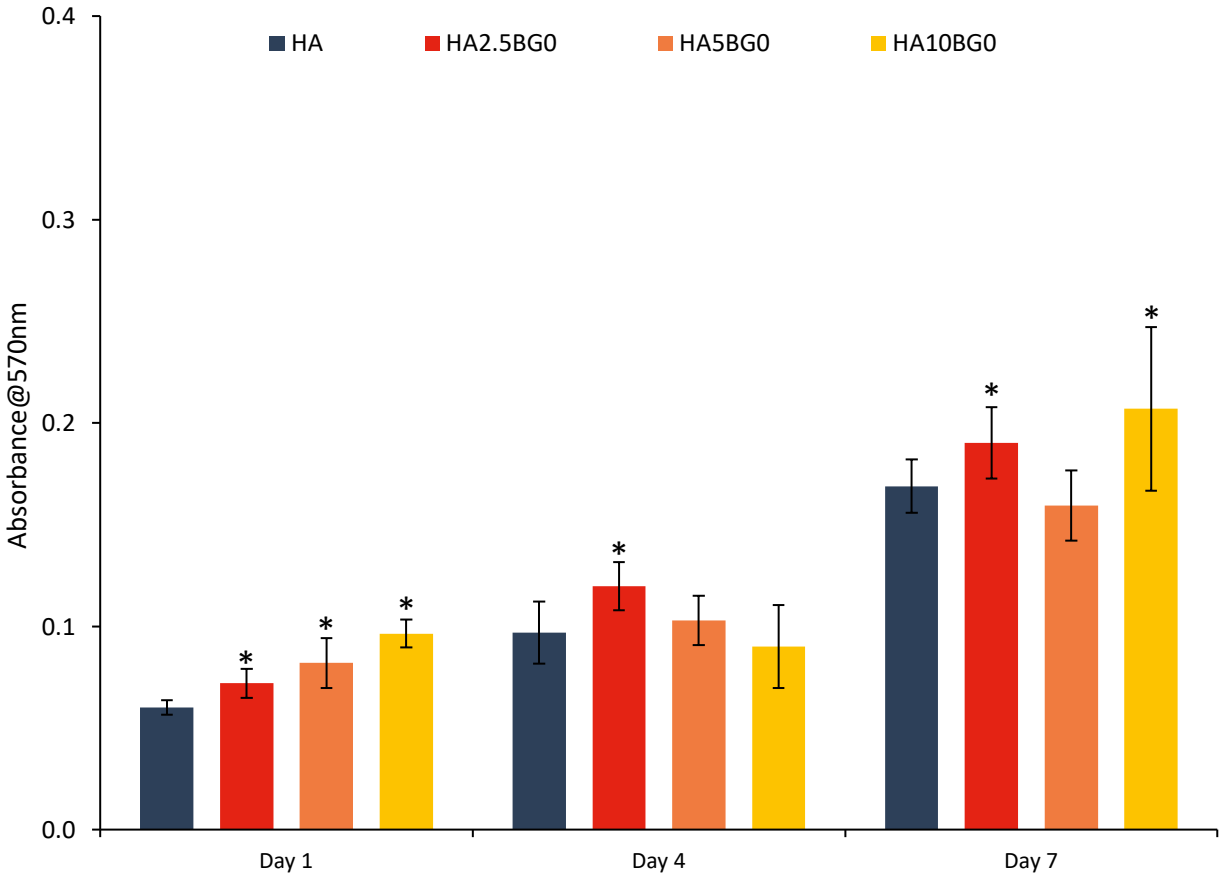

Figure 5.23: MTT results for HA and GR-HA containing BG0. (The asterisk (*) indicates significant difference (P<0.05) between HA and the tested GR-HA specimens.)

During the first day of incubation there is gradual increase of SaoS-2 cell viability with increasing amount of glass and all GR-HA specimens outperform pure HA samples. This trend is reversed in day 4 with HA2.5BG0 exhibiting the highest cell viability that gradually decreases with increasing amount of glass content. Only HA2.5BG0 and HA5BG0 perform better than HA, while HA10BG0 exhibits the lowest cell viability within the test group. In the final day of incubation, HA10BG0 is the sample exhibiting the highest cell viability, surpassing GR-HA specimens containing smaller glass loadings and pure HA samples. It is worth mentioning that HA5BG0 is the only specimen within the day 7 test group, that shows a slight decline in cell viability compared to pure HA. The reason behind this trend could be associated with the increased amounts of TCP present in these specimens. In general, TCP exhibits higher dissolution rates than HA, effectively decreasing the available surface area that could be utilised for cell attachment and proliferation [95].

SEM images portraying the SaoS-2 cell morphology and attachment on the surface of pure HA and GR-HA specimens are presented in Figure 5.24, Figure 5.25, Figure 5.26 for day 1, 4 and 7, respectively.

On the first day of incubation the cells attached to pure HA specimens exhibit a round morphology with limited filopodia extensions. With increasing glass content up to 5 wt.%, cells exhibit similar morphology but more developed filopodia extensions. In the case of HA10BG0, cell morphology shifts to flatter and more elongated shapes across the surface of the samples.

On day 4, SaoS-2 cell population increased for all samples compared to day 1. The cells attached to pure HA samples still exhibit round geometries but the level of filopodia development is increased compared to day 1. HA2.5BG0 and HA10BG0 showcase a high number of attached cells of elongated and flattened geometry, creating an extensive network

of interconnecting cells, throughout the specimen's surface. In the case of HA5BG0, a small amount of round cells can be seen, similar to the performance recorded on day 1.

On the last day of incubation, all samples exhibit higher degrees of cell viability compared to days 1 and 4. In the case of pure HA, SaoS-2 cells attached on the surface exhibit a much flatter and elongated morphology compared to the previous days. Moreover, the cell morphology that attached on the surface of HA2.5BG0 was similar to the one observed for HA, but the number of cells was greater. Similar morphology and behaviour as per days 1 and 4, is observed for cells attached on HA5BG0. Lastly, the SaoS-2 cells on the surface of HA10BG0, exhibit flattened and elongated fusiform structures.

HA

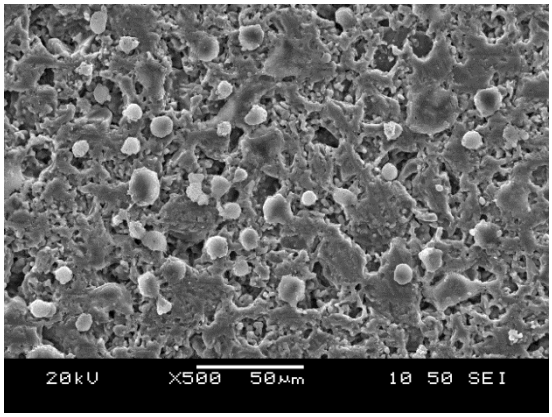

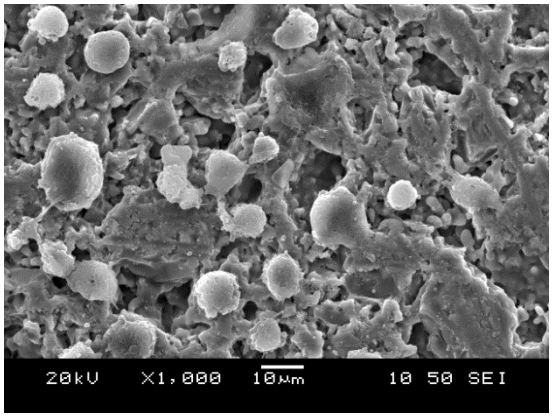

HA2.5BG0

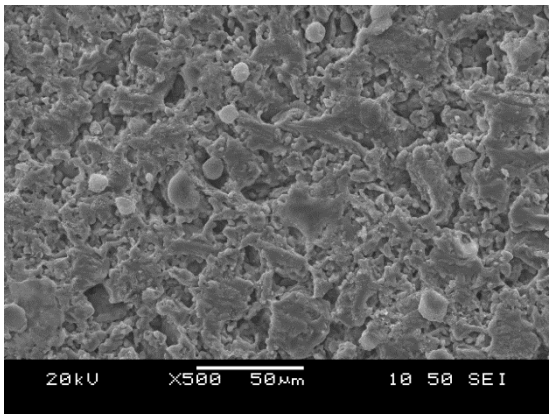

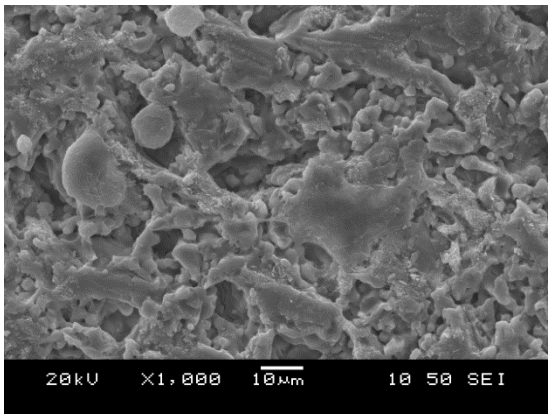

HA5BG0

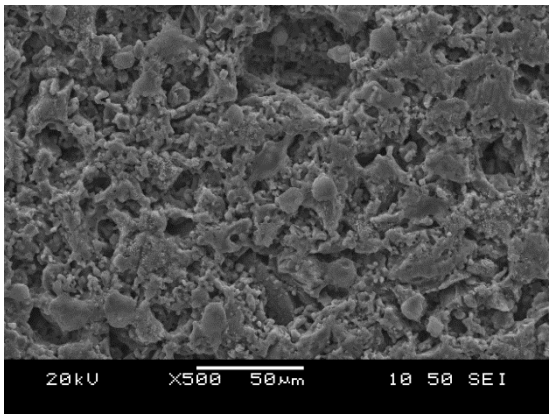

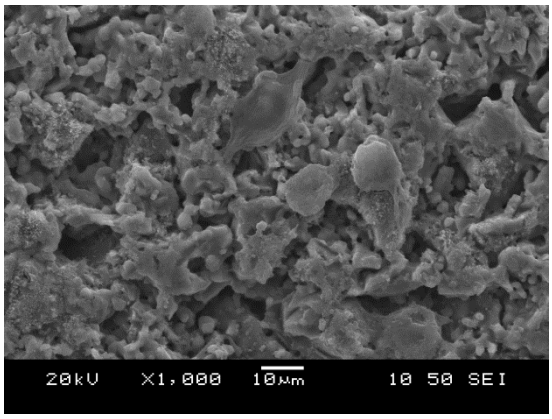

HA10BG0

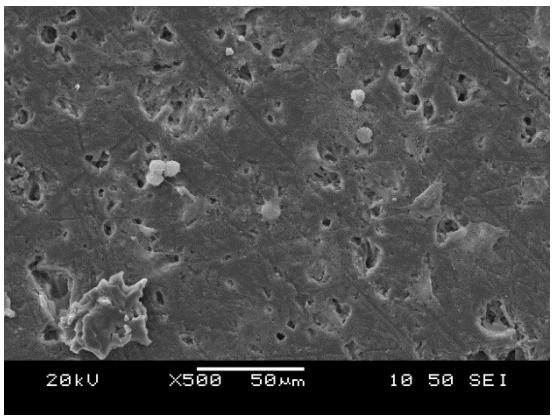

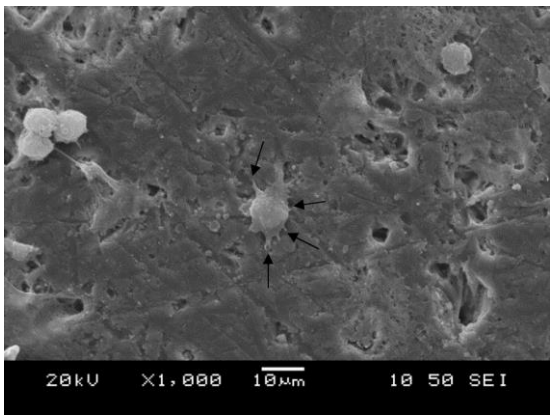

Figure 5.24: HA and GR -HA samples containing BG0, fixed cells Day 1 (filopodia extensions are highlighted with arrows, as an example).

HA

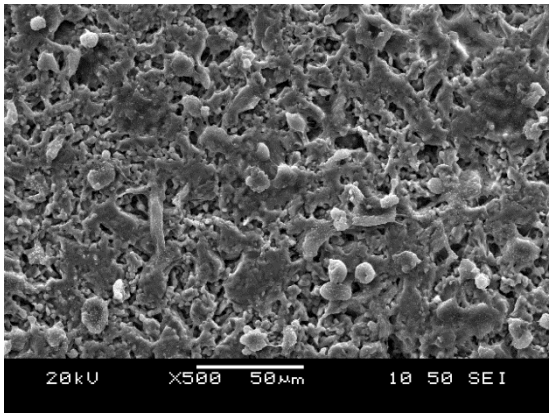

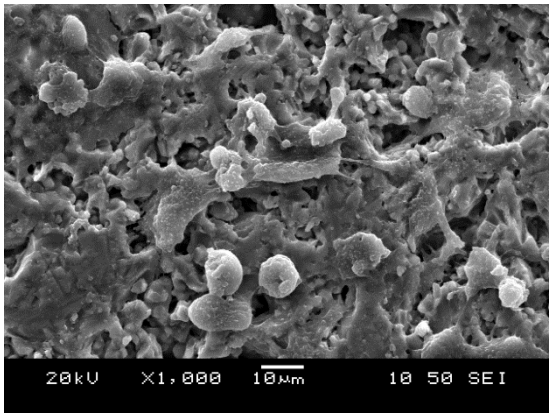

HA2.5BG0

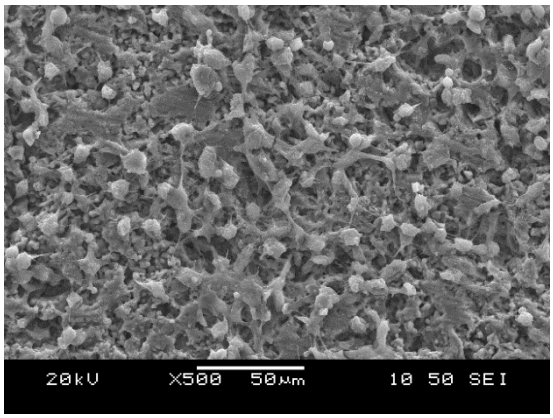

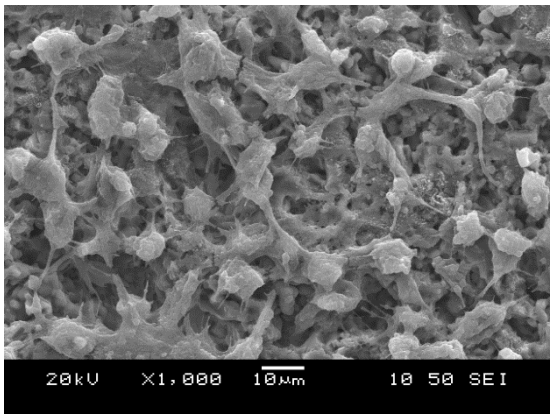

HA5BG0

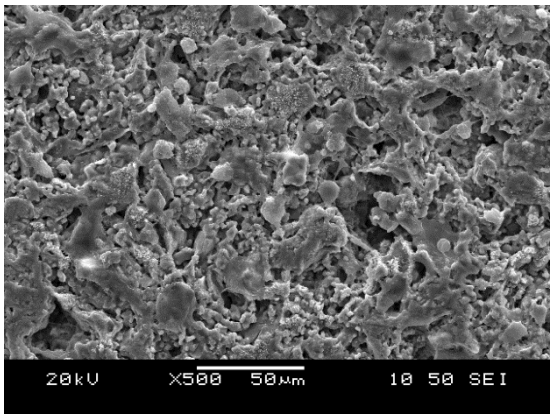

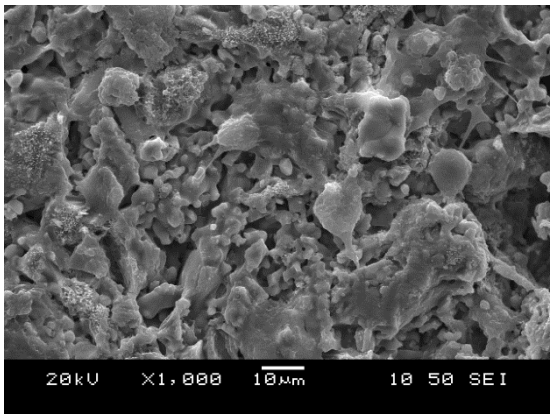

HA10BG0

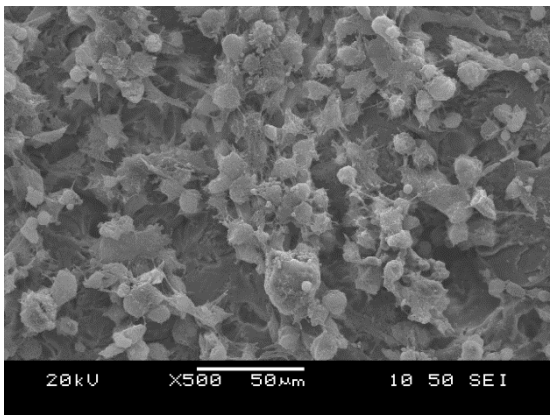

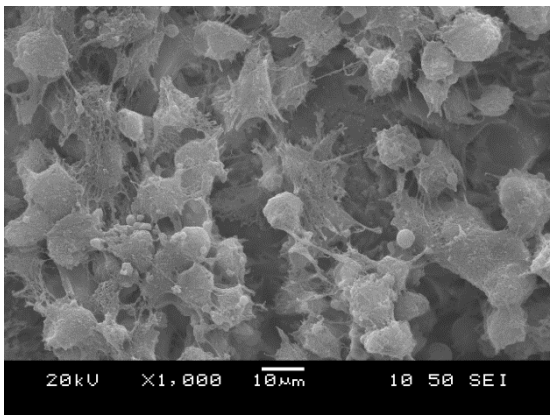

Figure 5.25: HA and GR-HA samples containing BG0, fixed cells Day 4.

HA

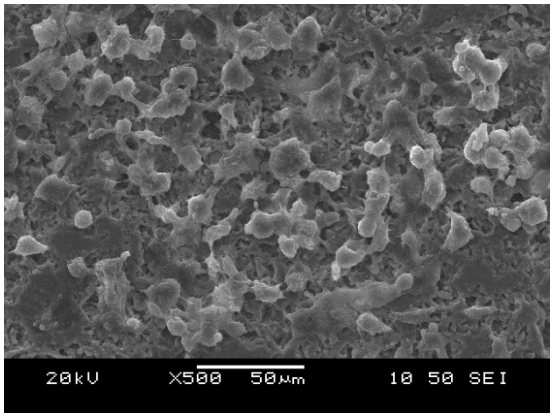

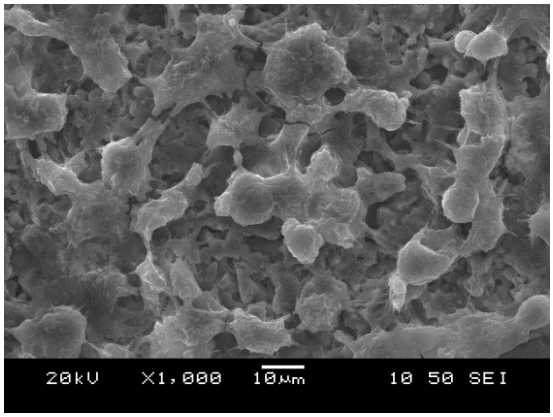

HA2.5BG0

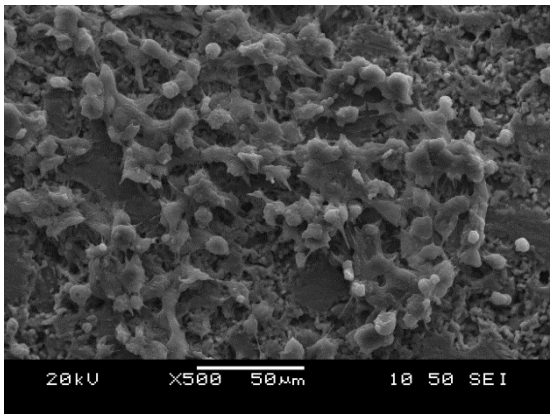

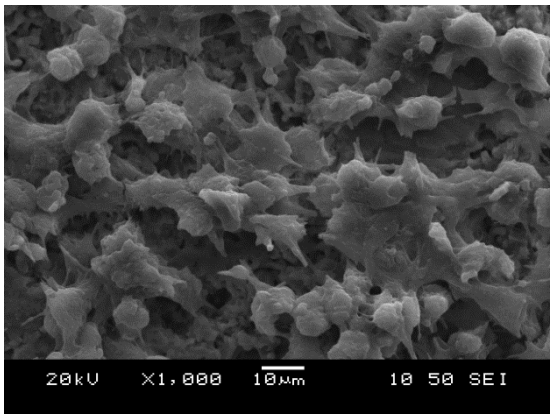

HA5BG0

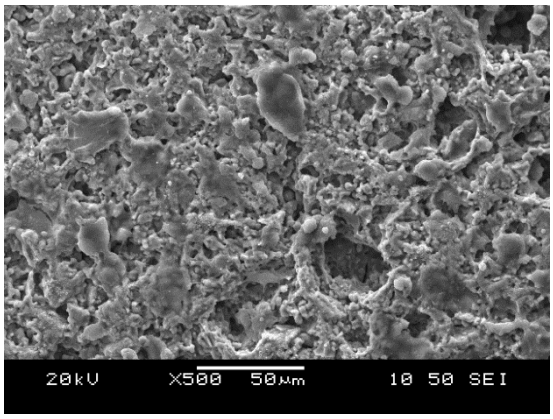

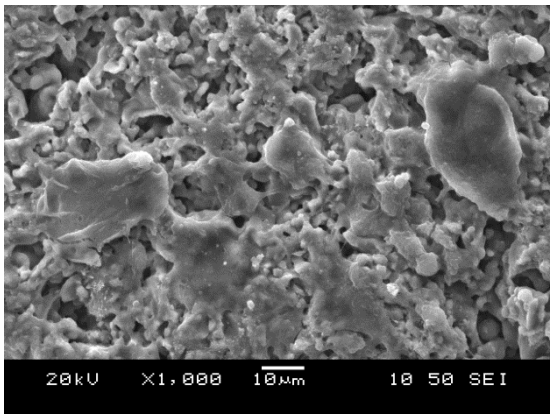

HA10BG0

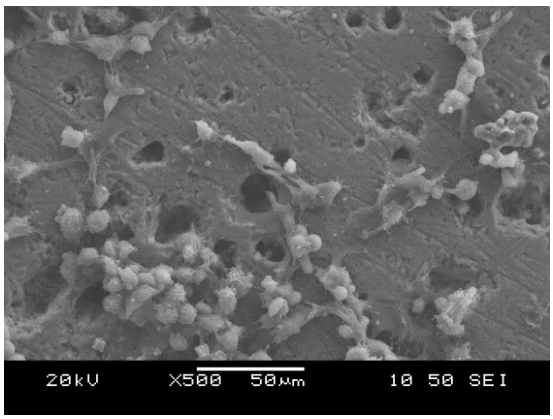

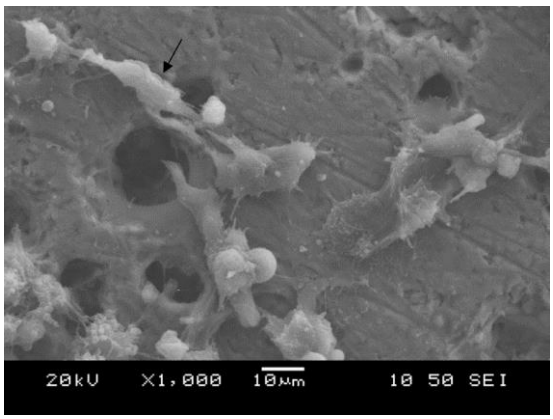

Figure 5.26: HA and GR-HA samples containing BG0, fixed cells Day 7 (a cell exhibiting fusiform geometry is highlighted with the arrow, as an example).

The results from the MTT biocompatibility in vitro study regarding HA and GR-HA specimens containing BG1.25, for days 1, 4 and 7 are presented in Figure 5.27.

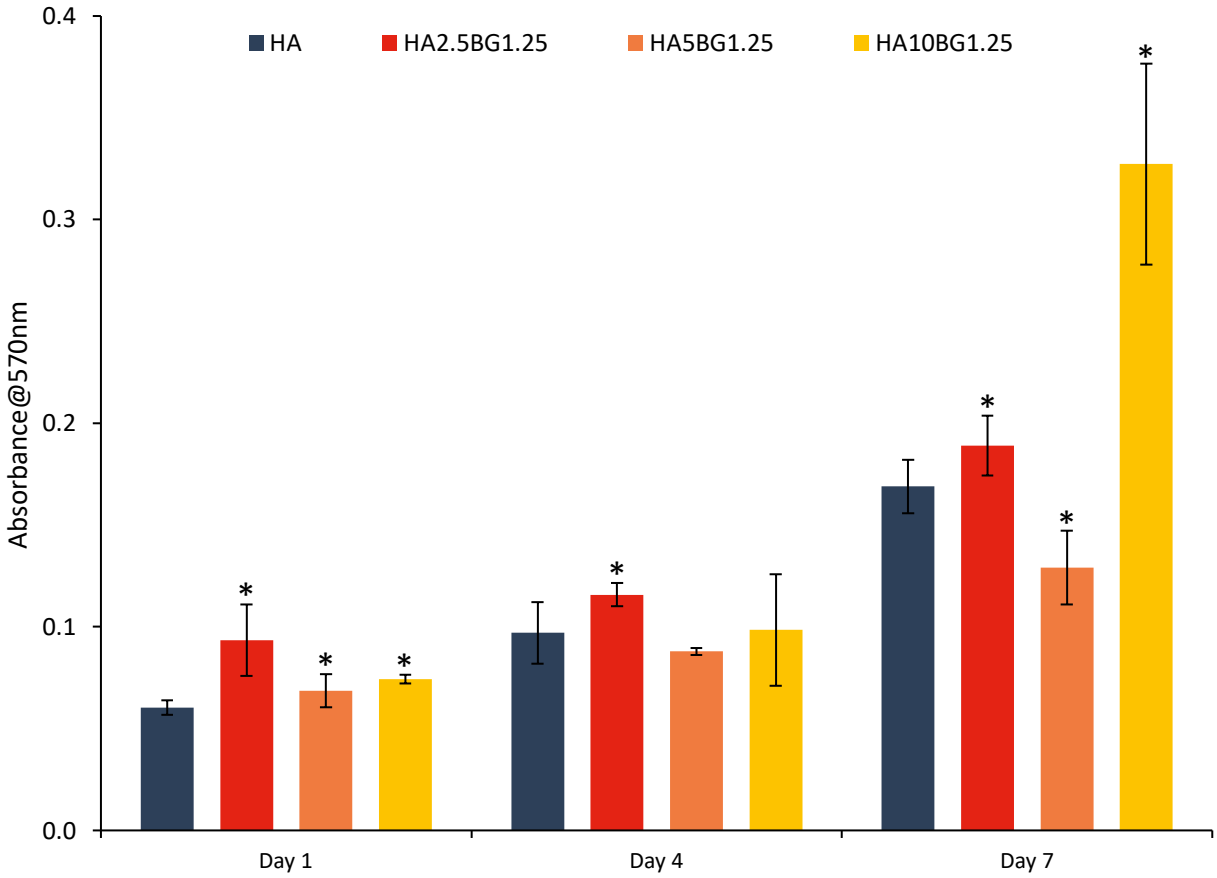

Figure 5.27: MTT results for HA and GR-HA containing BG1.25. (The asterisk (*) indicates significant difference (P<0.05) between HA and the tested GR-HA specimens.

During the first day of incubation all GR-HA samples exhibit similar or higher cell viability compared to pure HA. HA2.5BG1.25 shows the highest degree of cell viability, with HA10BG1.25 and HA5BG1.25 following it. This trend is ongoing during day 4, with HA2.5BG1.25 exhibiting the highest cell viability compared to all the specimens within the test group. HA10BG1.25 shows similar cell viability to pure HA whereas HA5BG1.25 exhibits a slightly lower viability rate. In the final day of incubation, HA10BG1.25 is the sample portraying the highest cell viability, surpassing both GR-HA specimens containing smaller glass loadings and pure HA samples. It is worth mentioning that HA5BG1.25 is the only specimen within the day 7 test group, that shows a decline in cell viability compared to pure HA. The reason behind this trend could be associated with the increased amounts of TCP present in these specimens, as previously described.

SEM images portraying the SaoS-2 cell morphology and attachment on the surface of pure HA and GR-HA specimens are presented in Figure 5.28, Figure 5.29, Figure 5.30 for day 1, 4 and 7, respectively.

On the first day of incubation the cells attached to pure HA specimens exhibit a round morphology with limited filopodia extensions. With increasing glass content up to 5 wt.%, cells exhibit similar morphology, while the ones attached to HA2.5BG1.25 tend to showcase slightly flatter patterns. In the case of HA10BG1.25, cell morphology shifts to flatter and more elongated shapes across the surface of the samples.

On day 4, SaoS-2 cell population increased for all samples compared to day 1. The cells attached to pure HA samples still exhibit round geometries but the level of filopodia development is increased compared to day 1. HA2.5BG1.25 and HA10BG1.25 showcase a high number of attached cells. In the case of the former the cells exhibit a combination of round

and fusiform shapes, with highly developed filopodia extensions. An array of elongated and flattened SaoS-2 cells can be seen across the surface of the HA10BG1.25 samples. A small number of round cells can be observed on the surface of HA5BG1.25, similar to day 1.

On the last day of incubation, all samples exhibit higher degrees of cell viability compared to days 1 and 4. In the case of pure HA, SaoS-2 cells attached on the surface exhibit a much flatter and elongated morphology compared to the previous days. Moreover, the cell morphology on the surface of HA2.5BG1.25 is much flatter and elongated compared to day 4. Similar morphology and behaviour as per days 1 and 4 are observed for cells attached on HA5BG1.25; small number of round cells with undeveloped filopodia can be seen across the surface of the specimens. Lastly, there are large areas covered by a big population of SaoS-2 cells on the surface of HA10BG1.25. They grow in multiple layers, with cells at the bottom exhibiting a flattened and elongated geometry; cells in higher levels portray a combination of round and fusiform shapes.

HA

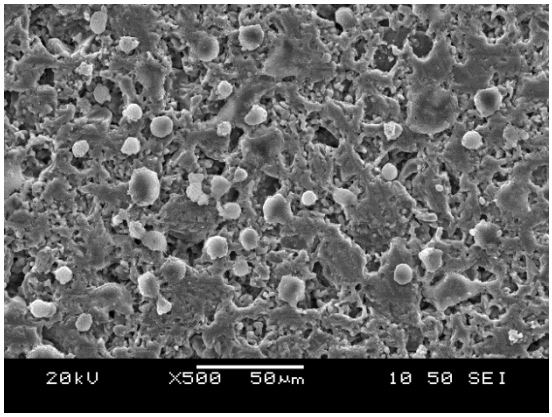

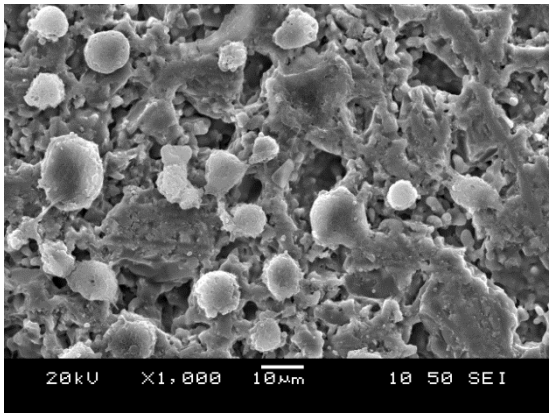

HA2.5BG1.25

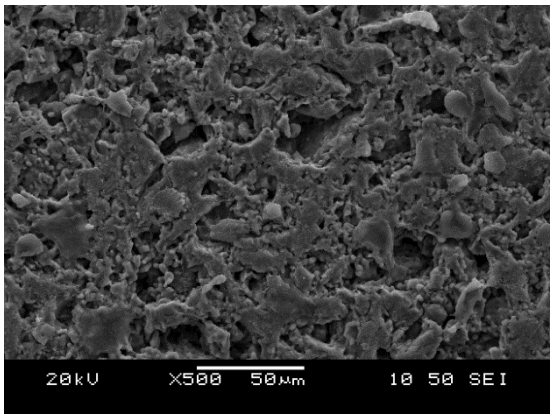

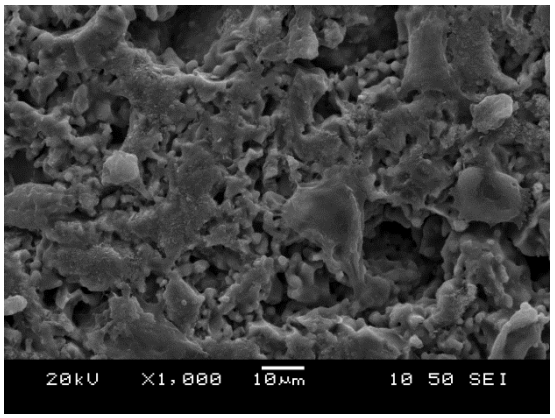

HA5BG1.25

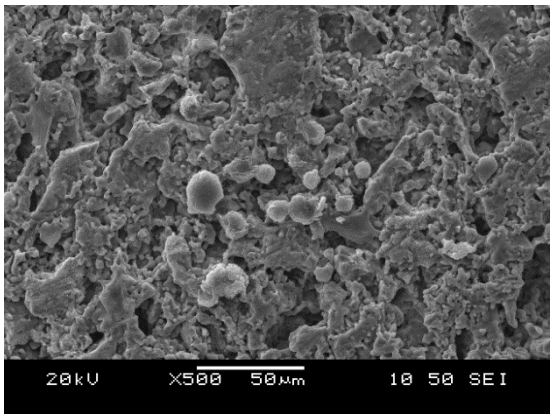

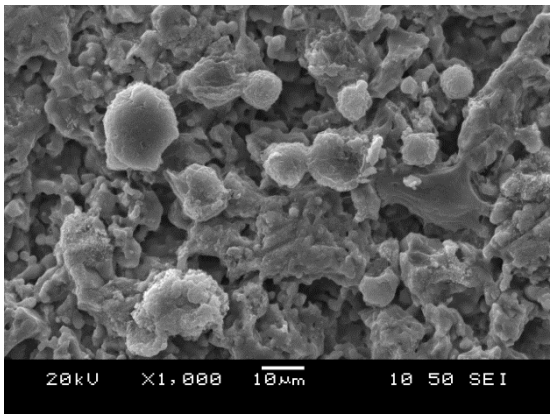

HA10BG1.25

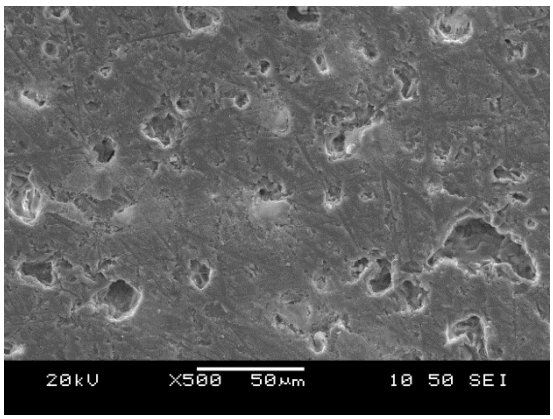

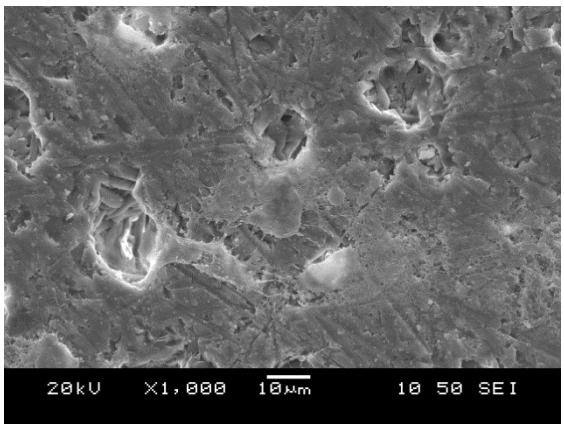

Figure 5.28: HA and GR-HA samples containing BG1.25, fixed cells Day 1.

HA

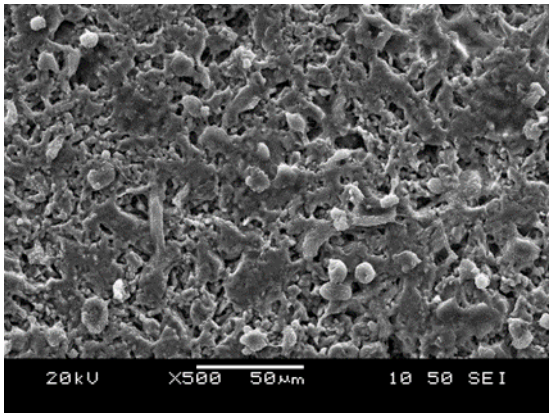

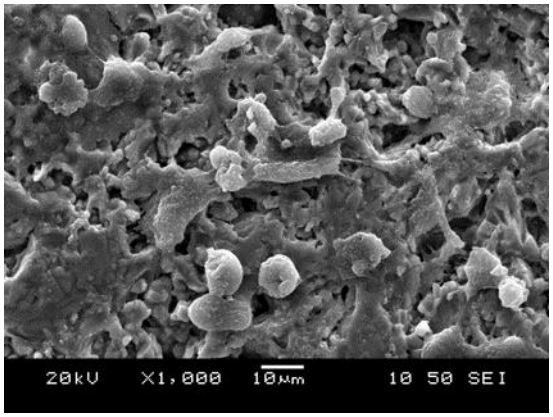

HA2.5BG1.25

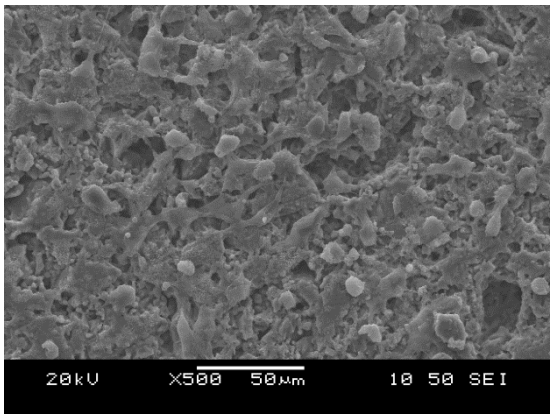

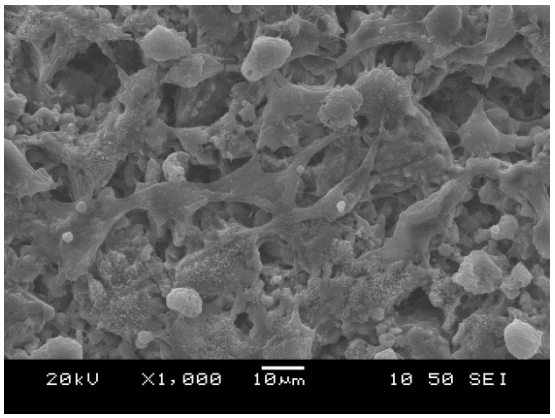

HA5BG1.25

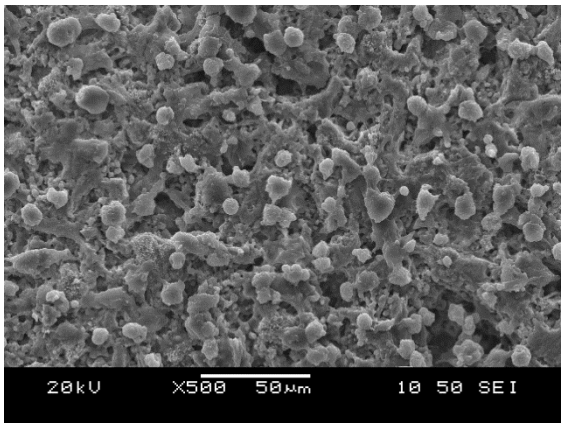

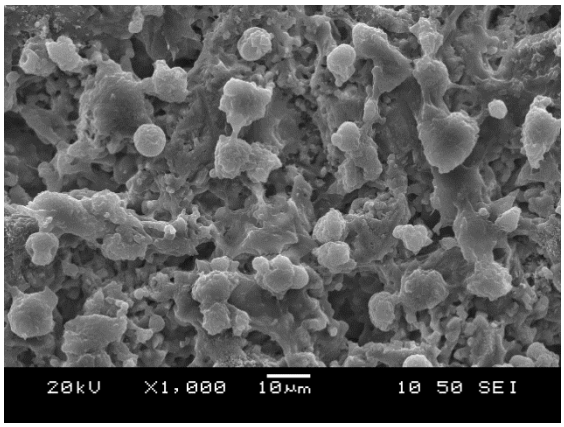

HA10BG1.25

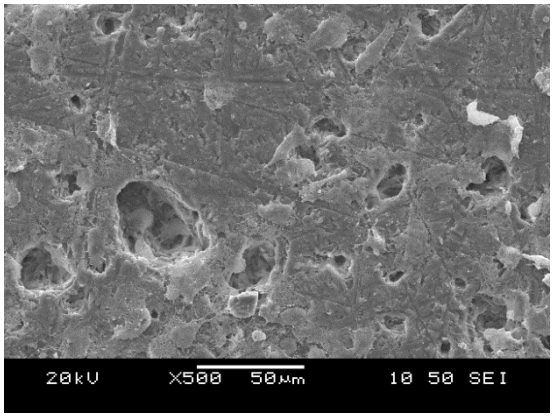

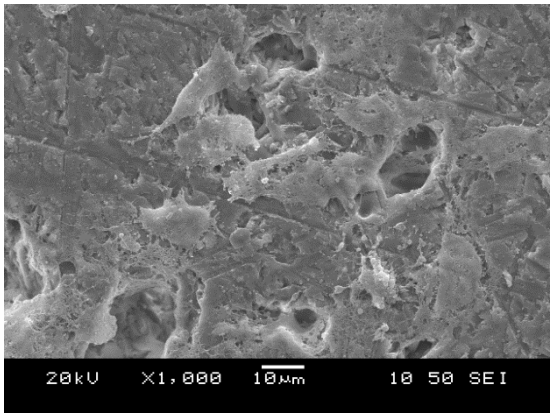

Figure 5.29: HA and GR-HA samples containing BG1.25, fixed cells Day 4.

HA

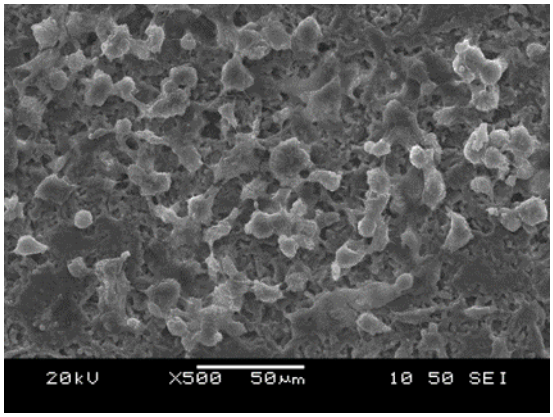

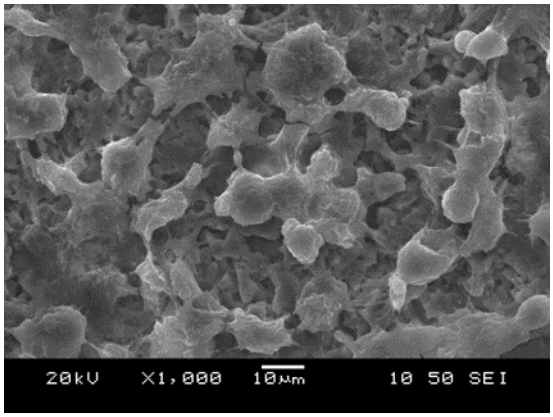

HA2.5BG1.25

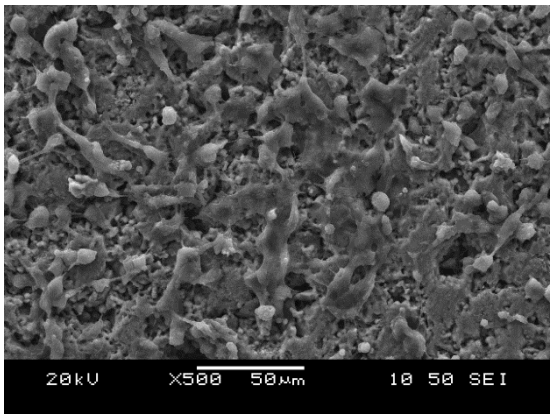

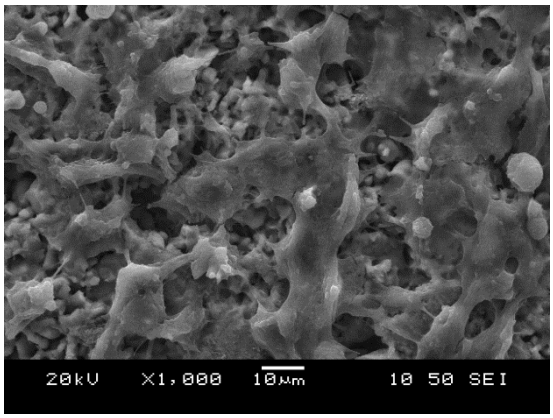

HA5BG1.25

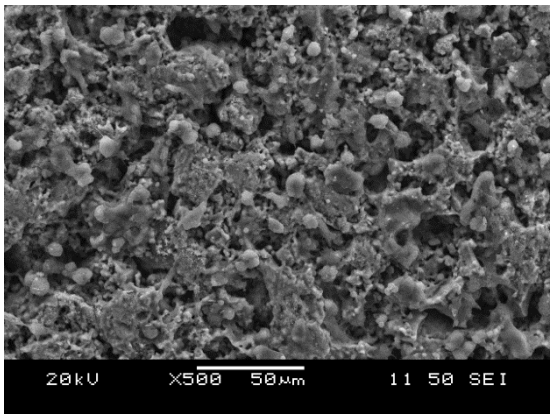

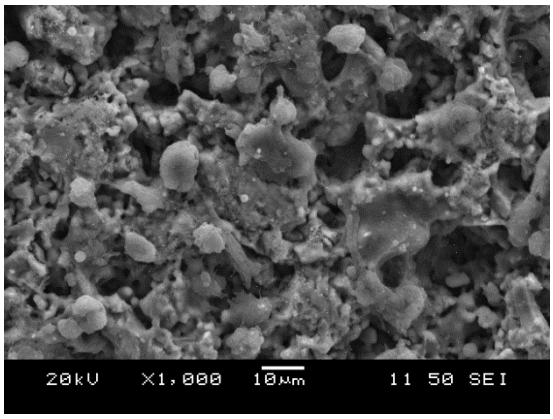

HA10BG1.25

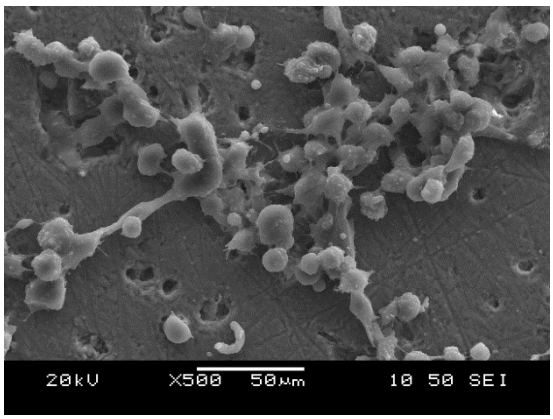

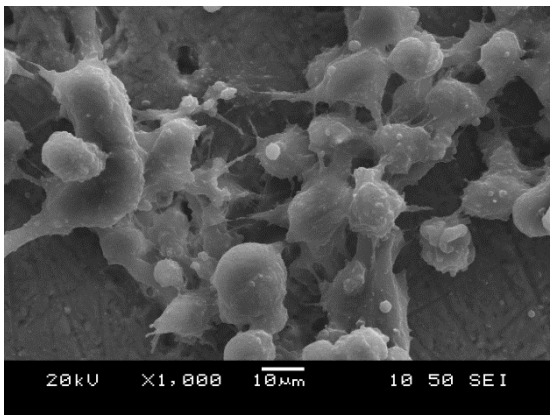

Figure 5.30: HA and GR-HA samples containing BG1.25, fixed cells Day 7.

The results from the MTT biocompatibility in vitro study regarding HA and GR-HA specimens containing BG2.5, for days 1, 4 and 7 are presented in Figure 5.31.

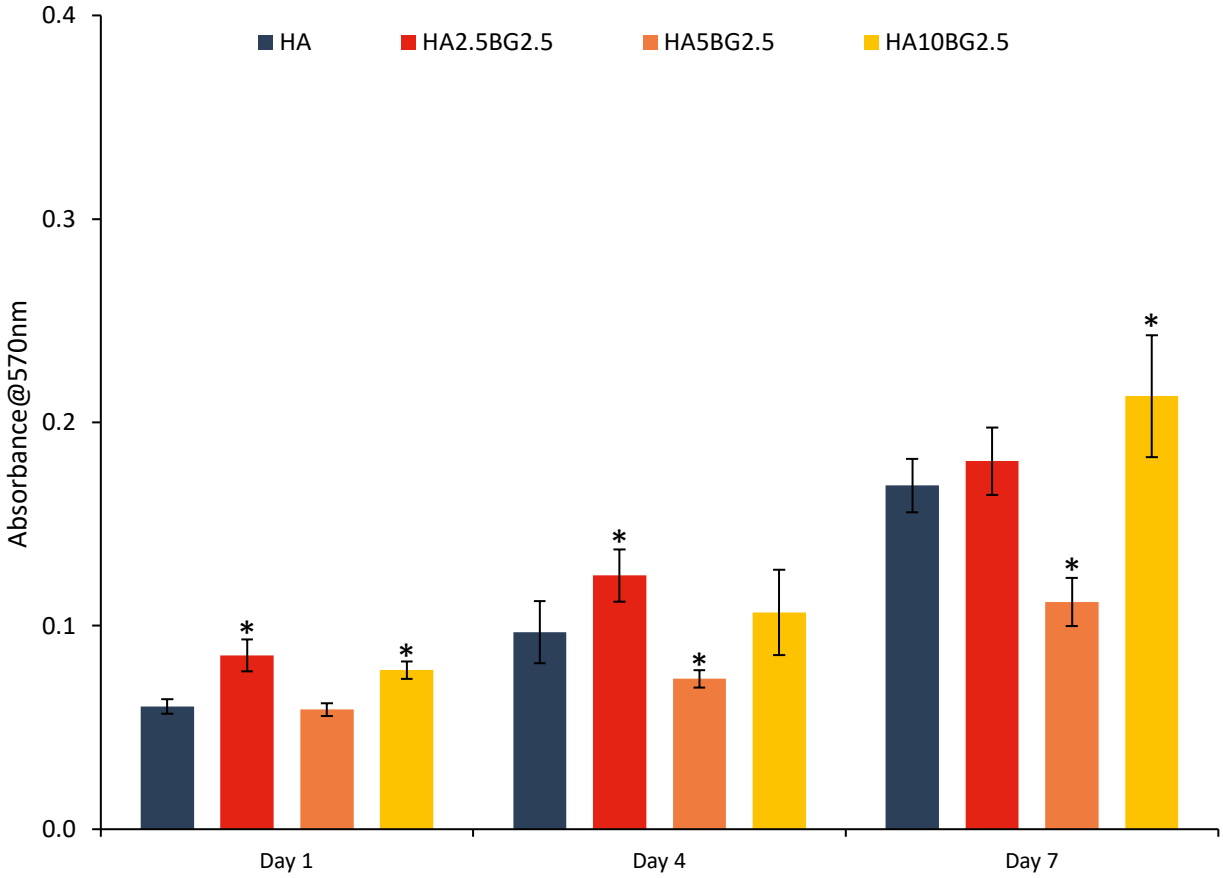

Figure 5.31: MTT results for HA and GR-HA containing BG2.5. (The asterisk (*) indicates significant difference (P<0.05) between HA and the tested GR-HA specimens.)

During the first day of incubation all GR-HA samples exhibit similar or higher cell viability compared to pure HA. HA2.5BG2.5 shows the highest degree of cell viability, with HA10BG2.5 and HA5BG2.5 following it. This trend is ongoing during day 4, with HA2.5BG2.5 exhibiting the highest cell viability compared to all the specimens within the test group. HA10BG2.5 shows similar cell viability to pure HA whereas HA5BG2.5 exhibits a lower viability rate. In the final day of incubation, HA10BG2.5 is the sample portraying the highest cell viability, surpassing both GR-HA specimens containing smaller glass loadings and pure HA samples. It is worth mentioning that HA5BG2.5 is the only specimen within the day 7 test group, that shows a significant decline in cell viability compared to pure HA. The reason behind this trend could be associated with the increased amounts of TCP present in these specimens, as previously stated.

SEM images portraying the SaoS-2 cell morphology and attachment on the surface of pure HA and GR-HA specimens are presented in Figure 5.32, Figure 5.33, Figure 5.34 for day 1, 4 and 7, respectively.

On the first day of incubation the cells attached to pure HA specimens exhibit a round morphology with limited filopodia extensions. With increasing glass content up to 5 wt.%, cells exhibit similar morphology, with the ones attached to HA2.5BG2.5 specimens showcasing slightly flatter patterns and filopodia attachments. In the case of HA10BG2.5, cell morphology shifts to flatter and more elongated shapes across the surface of the samples.

On day 4, SaoS-2 cell population increased for all samples compared to day 1. The cells attached to pure HA samples still exhibit round geometries but the level of filopodia development is increased compared to day 1. HA2.5BG2.5 and HA10BG2.5 showcase a high number of attached cells. In general, fusiform and flattened shaped cells occupy the surface

of the specimens, while round ones are observed stacking on top of the former. An array of elongated and flattened SaoS-2 cells, along with spindle-like cells can be seen across the surface of the HA10BG2.5 samples. Flattened and fusiform cells are observed on the surface of HA2.5BG2.5, too. A small number of round cells with further developed filopodia can be observed on the surface of HA5BG2.5, similar to day 1.

In the last day of incubation, all samples exhibit higher degrees of cell viability compared to days 1 and 4. In the case of pure HA, SaoS-2 cells attached on the surface exhibit a much flatter and elongated morphology compared to the previous days. Moreover, the cell morphology that attached on the surface of HA2.5BG2.5 is much flatter and elongated compared to day 4. Similar morphology and behaviour as per days 1 and 4, is observed for cells attached on HA5BG2.5; small number of round cells with undeveloped filopodia can be seen across the surface of the specimens. Lastly, there are large areas covered by a big population of SaoS-2 cells on the surface of HA10BG2.5. They exhibit an extensive network of attachment filopodia connected to the substrate while other areas showcase limited cell confluency, too.

HA

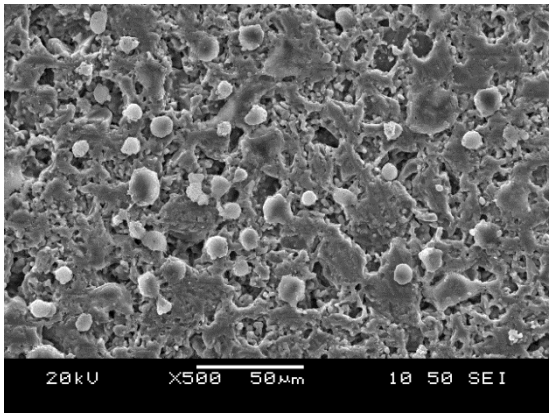

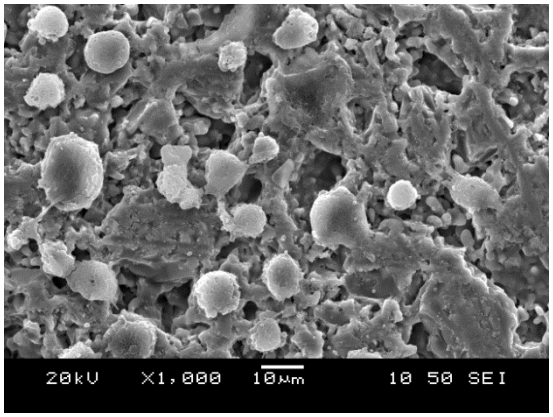

HA2.5BG2.5

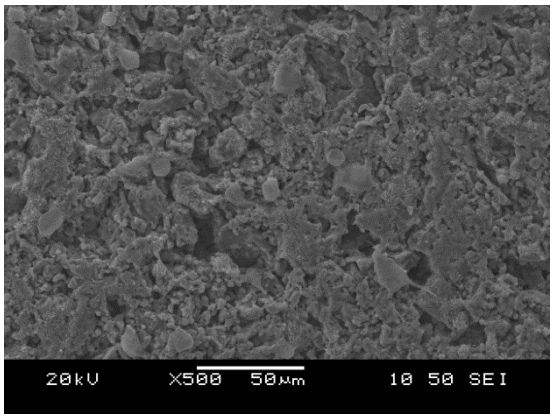

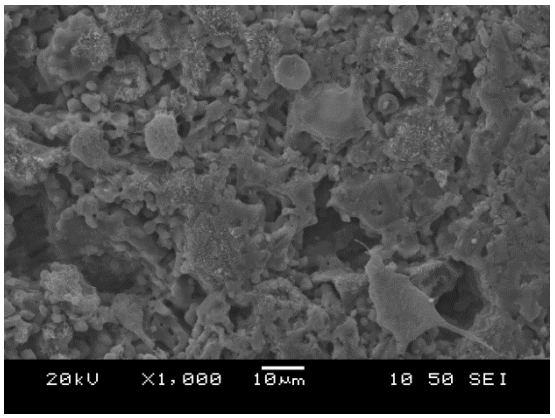

HA5BG2.5

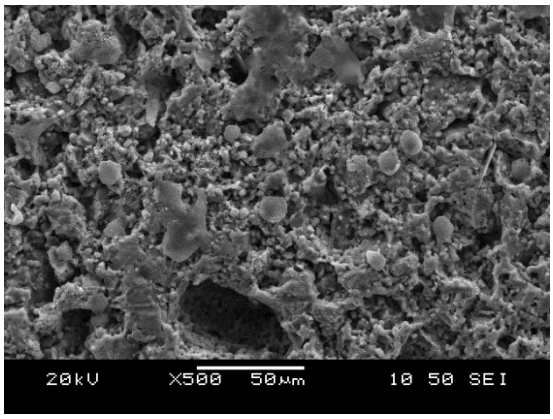

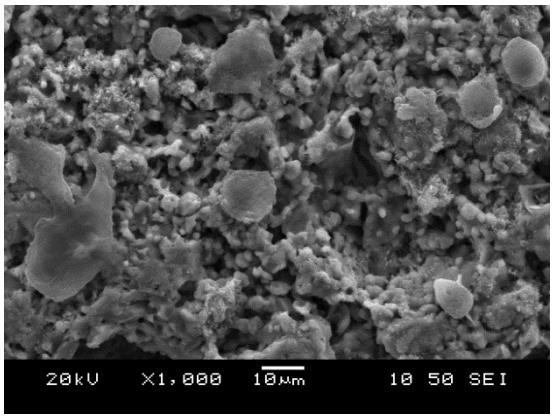

HA10BG2.5

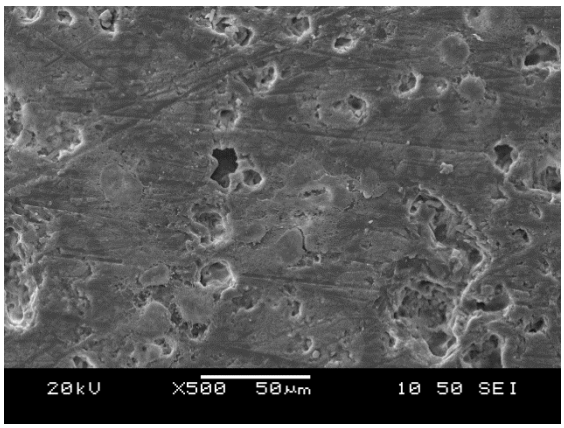

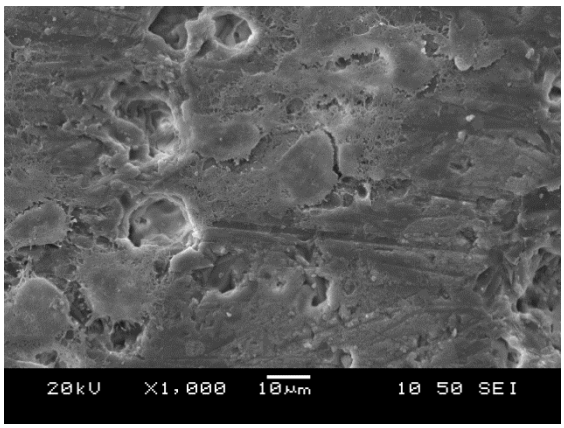

Figure 5.32: HA and GR-HA samples containing BG2.5, fixed cells Day 1.

HA

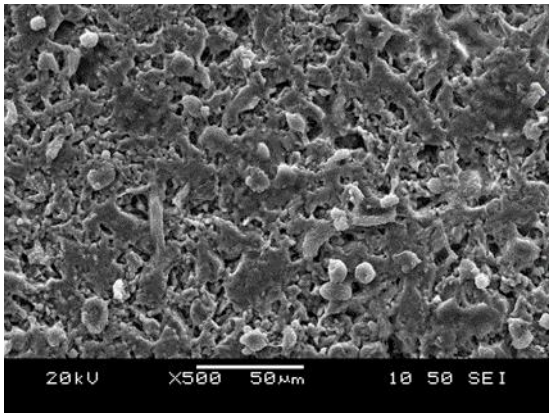

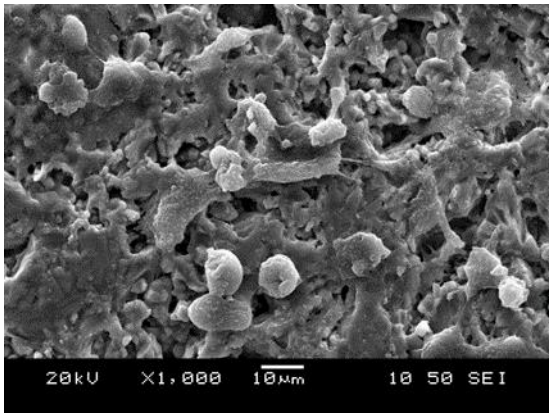

HA2.5BG2.5

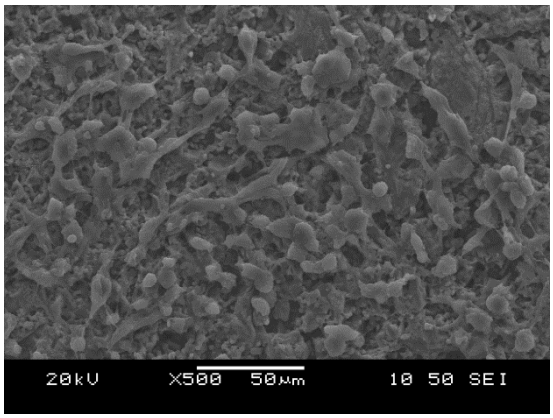

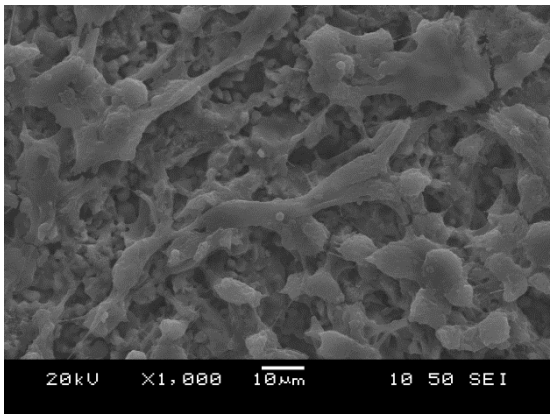

HA5BG2.5

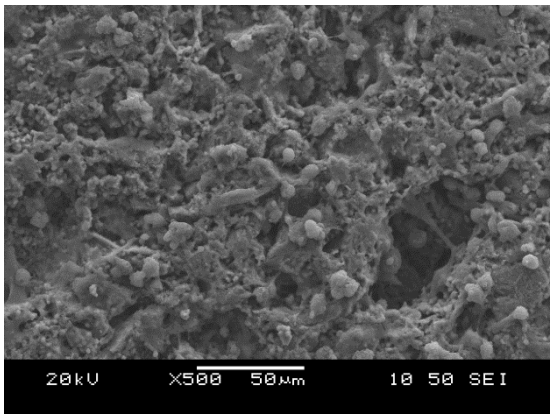

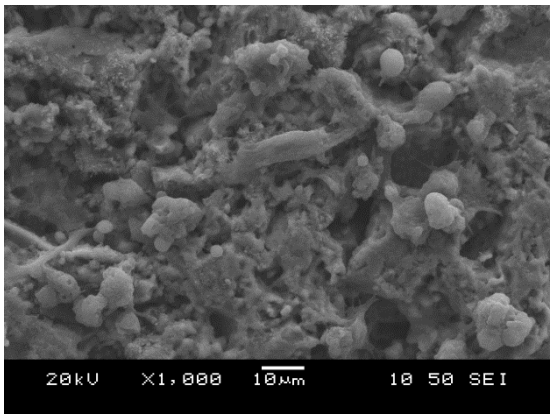

HA10BG2.5

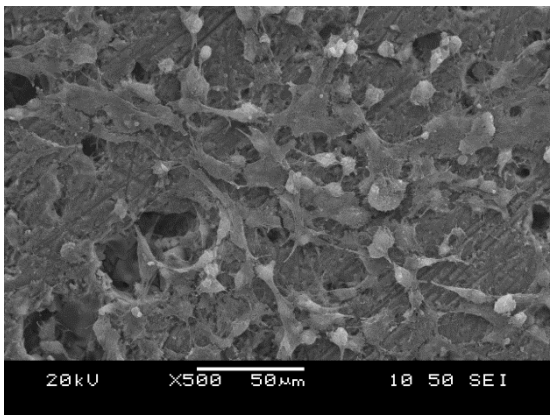

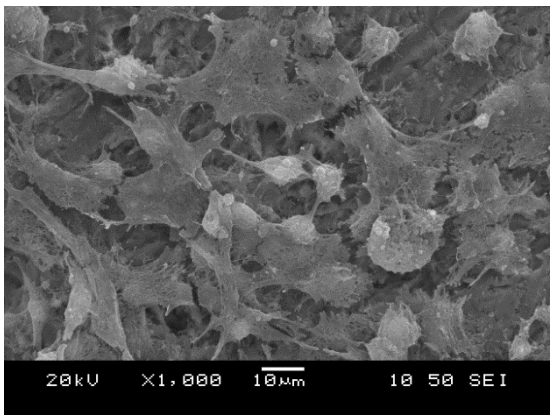

Figure 5.33: HA and GR-HA samples containing BG2.5, fixed cells Day 4.

HA

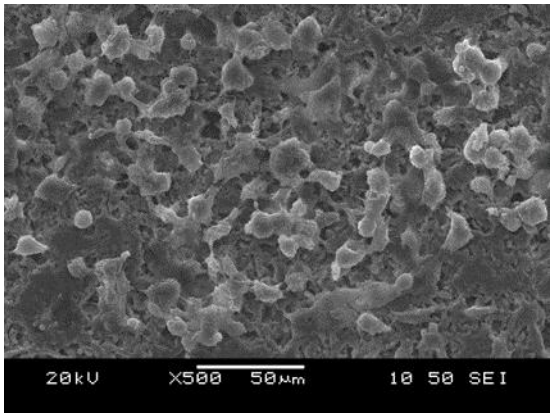

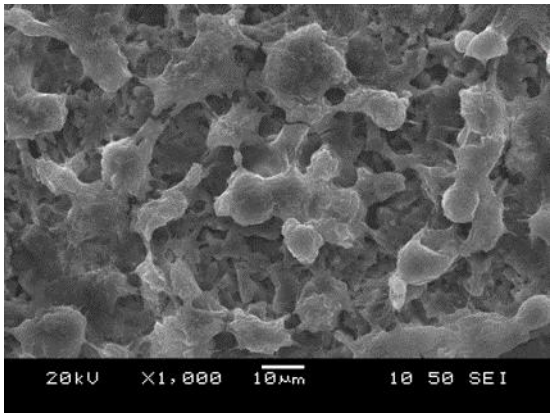

HA2.5BG2.5

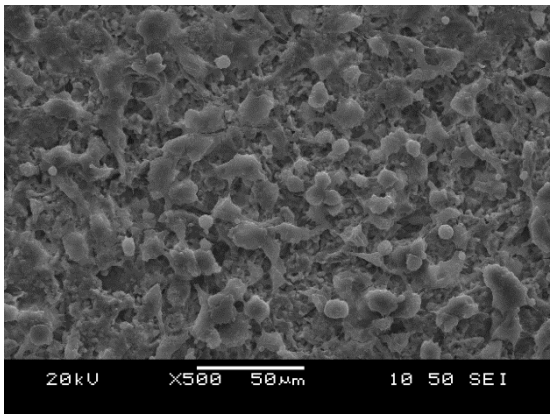

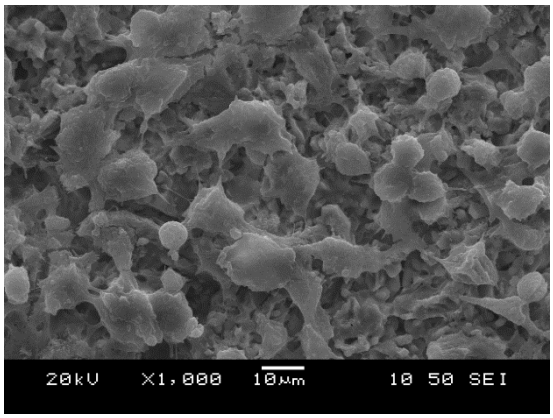

HA5BG2.5

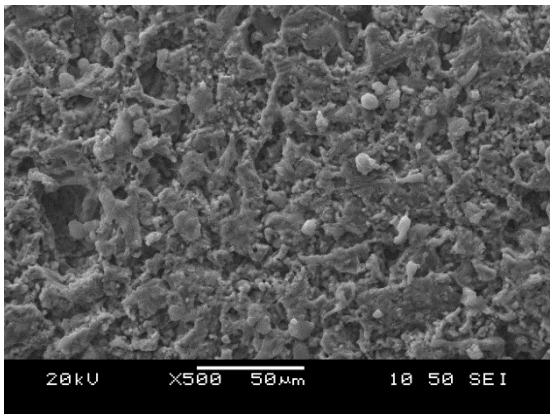

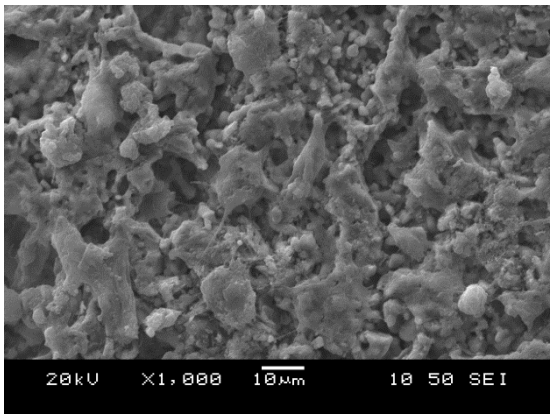

HA10BG2.5

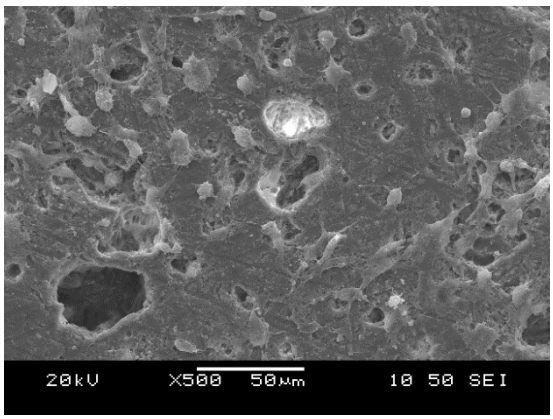

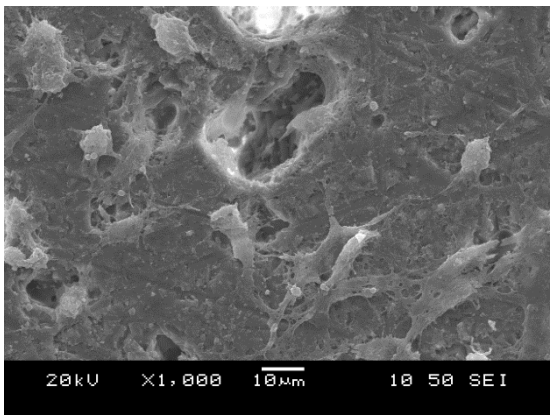

Figure 5.34: HA and GR-HA samples containing BG2.5, fixed cells Day 7.

To conclude, none of the GR-HA specimens regardless of their La_2O_3 exhibited cytotoxic behaviour. The inhibition of cell viability in samples containing 5 wt.% of glass loading, can be attributed to the increased dissolution rates associated with the TCP phases present in those specimens. In general, GR-HA samples loaded with 2.5 wt.% of glass loading, exhibited similar or slightly increased cell viability on days 1 and 4 compared to pure HA and GR-HA samples loaded with 10 wt.% of glass, regardless of the lanthanum content. The trend is reversed on day 7, where the latter portray higher cell viability rates compared to pure HA and composites containing 2.5 wt.% of glass loading. This increase in cell viability can be attributed to the presence of the glass within the composites, since the MTT results are statistically significant in every such case (i.e., 10 wt.% of glass loading, regardless of the lanthanum content) compared to the results for pure HA. More specifically, there is an increase in cell viability by 22.5%, 93.5% and 26.0% for samples HA10BG0, HA10BG1.25 and HA10BG2.5 compared to pure HA, respectively. Additionally, the cell morphology in those samples is always flattened and elongated covering large areas of the substrate, indicating reduced cell stress.

CHAPTER 6 – SLS feasibility study

This chapter focuses on the investigation regarding the processability of the novel powder feedstock via SLS. The coupling of hydroxyapatite and selective laser sintering is potentially capable of producing the intricate geometries required for tissue engineering applications. However, processing hydroxyapatite via SLS, either directly or indirectly, presents some limitations, mainly due to its refractory character and its limited thermal shock resistance. In this feasibility study, BG2.5 (hereafter called BG) was the only glass composition chosen to be tested since it exhibited better mechanical and biological performance compared to the other two glass compositions (i.e., BG0 and BG1.25). Two different powder feedstocks were tested in the feasibility study. More specifically, one consisting solely of a commercial spray-dried, spheroidised HA powder and the second one comprising of the aforementioned HA powder blended with 10 wt.% of BG (HA10BG). This specific HA/BG ratio was chosen since it exhibited better mechanical and biological performance in the study presented in Chapter 5. Flame spheroidization was used to spheroidise the glass powder in order to ensure flowability and spreadability of the powder feedstock. Spherical particle morphology [5], [21], [192], [193], [196], [215], [224], [225], [230] and a narrow size distribution with particle size ranging between 10 – 150 μm [5], [20], [225], [226], [230], [21], [191], [193]–[196], [215], [224] are considered optimal in terms of powder characteristics for SLS processing. That was the reason behind the selection of the powder characteristics for both HA and BG in this feasibility study.

Parts of this section are published as first-author and may contain replication from [1]

In the following section the characterisation of the powder feedstock in terms of physical properties, flowability and absorbance are presented. In addition, a summary of the printing process and results are presented, alongside information regarding the physicochemical properties of the printed parts.

6.1 Powder characterisation

The SEM images and particle size distribution analysis of the HA powder used during the SLS feasibility study is presented in Figure 6.1 and Figure 6.2, respectively. The HA particles are of spherical geometry (sphericity index: 0.94 ± 0.04) and exhibit an average particle size (D_{50}) of 62.2 μm. Additionally, they exhibit a rough surface, a typical trait of spray-dried HA powders comprising of smaller crystallites [227], [265]. Various non-optimal shapes in terms of flowability (e.g., doughnut, mushroom, etc.) can be achieved via the spray drying route, including hollow geometries [266]–[268]. The cross section of the HA particle revealed a solid geometry, as it can be seen in Figure 6.1.

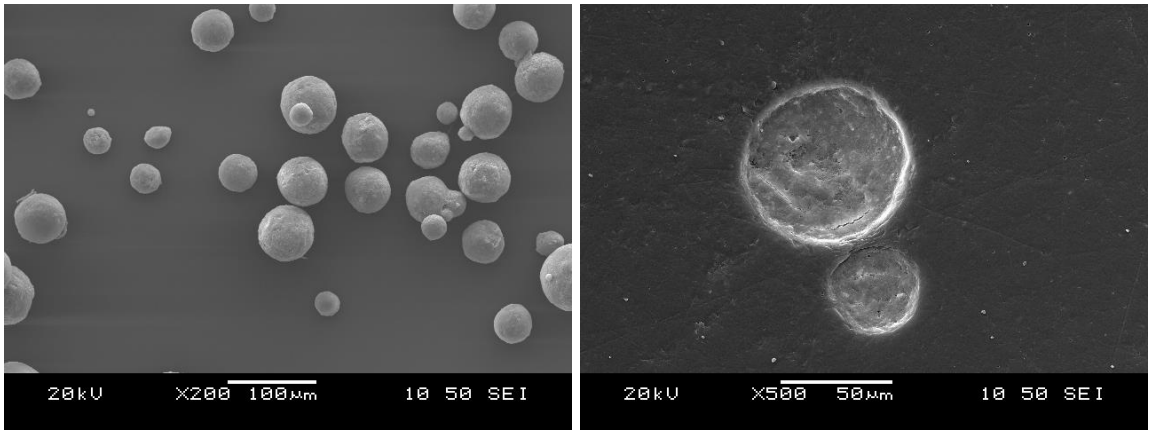

Figure 6.1: SEM micrographs of the spheroidised HA particles (left) and a cross section of the HA microspheres (right).

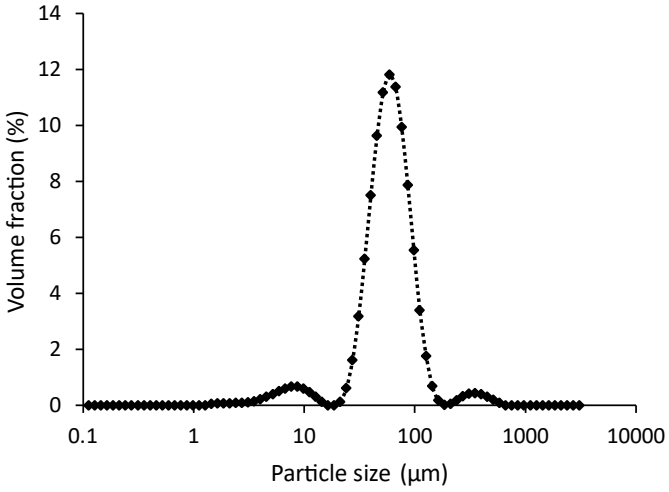

Figure 6.2: Particle size distribution of the spheroidised HA powder.

SEM images of the BG powder prior and post spheroidization particle size distribution analysis for both powders are presented in Figure 6.3 and Figure 6.4, respectively.

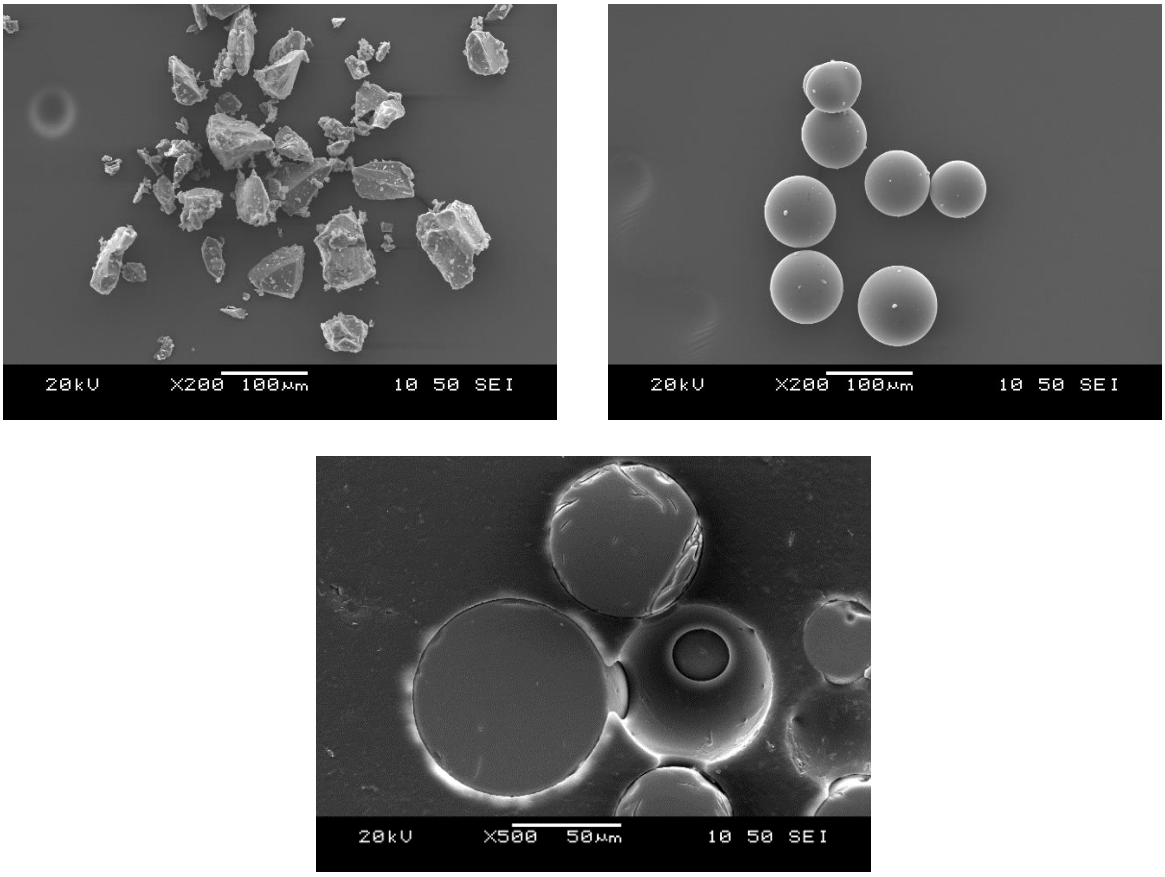

Figure 6.3: SEM micrographs of the pre-spheroidised BG particles (left), the spheroidised BG particles (right) and a cross section of the BG microspheres (bottom).

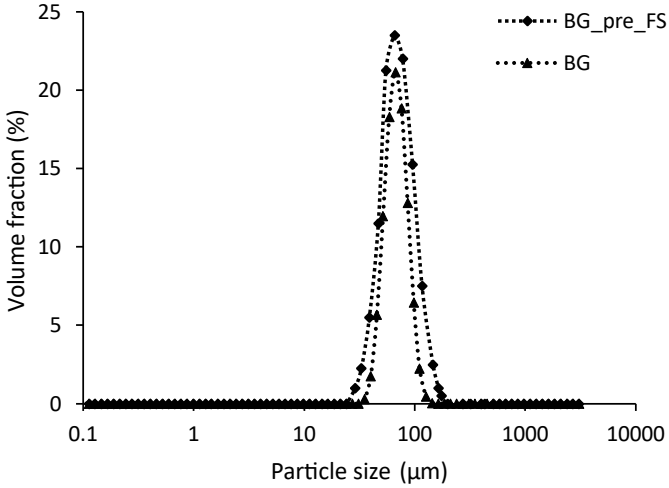

Figure 6.4: Particle size distribution of the pre-spheroidised and spheroidised BG powders.

The BG particles pre-spheroidisation are of irregular shape, exhibiting an average particle size (D_{50}) of 70.4 μm. Post-spheroidization, the geometry of the particles is spherical (sphericity index: 0.97 ± 0.04), exhibiting a similar particle size as their non-spheroidised counterparts (71.9 μm). The surface of the particles is smooth and the developed microspheres are solid as it can been seen in Figure 6.3.

Through the particle size analysis, it was shown that the spheroidisation process affected the size distribution of the processed BG powder. More specifically, the particle size remained almost identical to the one recorded pre-spheroidisation, however the particle size distribution became narrower as it can be seen in Figure 6.4. This is not uncommon [247] and it is favourable in terms of flowability [187], [225].

Lastly, it is worth mentioning that BG remained amorphous during flame spheroidisation, as it can be seen in the X-ray diffractogram presented in Figure 6.5. No crystallisation occurred during the process due to the small residence time and rapid quenching.

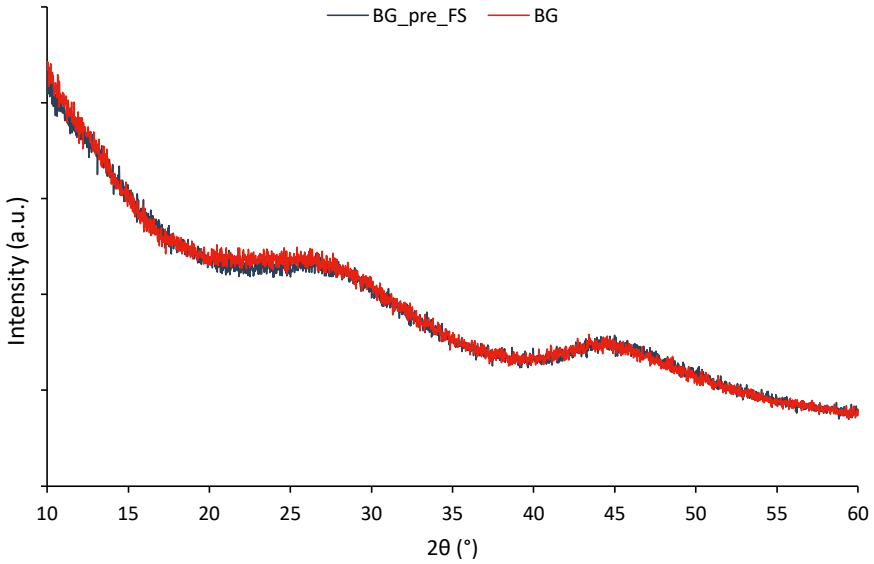

Figure 6.5: X-ray diffractograms of BG glasses pre and post spheroidisation.

6.2 Absorbance measurements

Ensuring adequate coupling between the laser source and the powder feedstock is of utmost importance during SLS processing [221], [225], [230], [231], [233]–[235]. In general, ceramics and glasses absorb energy much more efficiently when they are irradiated with CO_2 laser sources operating at 10.6 μm [186], [187], [269]. However, the majority of the powder bed fusion printers in the market are not suitable for processing ceramics [187]. They are either equipped with Nd:YAG or fibre laser sources operating at 1.06 μm, an optimal wavelength for processing metallic feedstocks but extremely inefficient for ceramics, or their overall specifications do not meet the requirements for this purpose [187]. More specifically, SLS equipment designed for polymer processing are equipped with CO_2 lasers, nevertheless they are not equipped to accommodate the extreme conditions required for ceramic processing (e.g., printing bed/chamber preheating temperatures > 1000 °C, suitable cooling rates, etc.) [187]. A comparison between the absorbance of various ceramic powders for both wavelengths is presented in Table 6.1.

Table 6.1: Absorbance of ceramic and glass powders at 1.06 μm and 10.6 μm wavelengths

Material	Nd-YAG (λ=1.06 μm)	CO_2 (λ= 10.6 μm)	Ref
ZnO	0.02	0.94	[233]
Al_2O_3	0.03	0.96	[233]
SiO_2	0.04	0.96	[233]
BaO	0.04	0.92	[233]
8YSZ	0.02	-	[187]
CuO	0.11	0.76	[233]
HA	0.03	-	[187]
TiC	0.82	0.46	[233]
SiC	0.78	0.66	[233]
45S5 - Bioglass	0.2	-	[270]
Typical soda lime silicate glass	0.2	-	[271]
Schott Borofloat® 33	0.07	-	[272]

Absorbance enhancers are usually blended with ceramic powders when processed with SLS printers equipped with 1.06 µm laser sources. That was the case in this feasibility study since processing the developed GR-HA feedstock would be impossible without the use of one. This was validated by the absorbance measurements recorded for HA, BG and the GR-HA blend consisting of 10 wt.% of BG, presented in Figure 6.6.

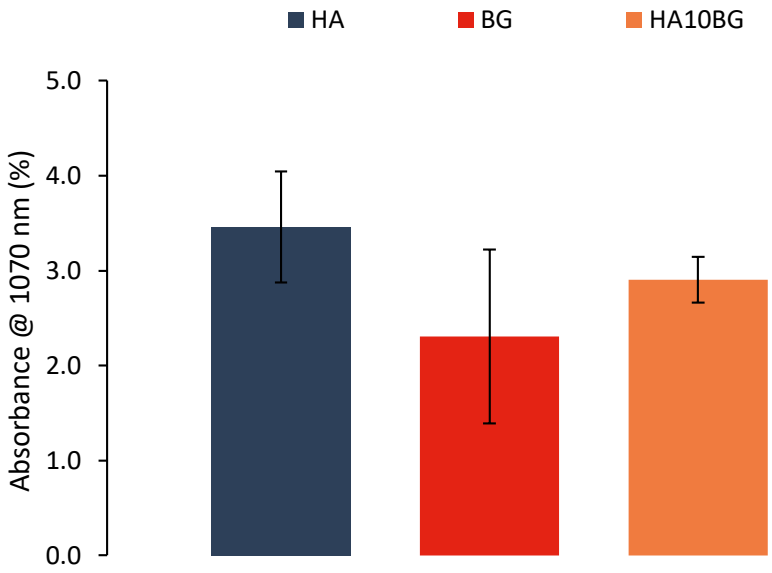

Figure 6.6: Absorbance of HA, BG and HA10BG powders at 1070 nm.

The energy absorbance was extremely low for all three of the tested powders, making the experimentation via SLS unpragmatic. Thus, graphite powder was used in order to enhance the energy absorption. The graphite powder morphology alongside the particle size distribution analysis of the same powder are presented in Figure 6.7.

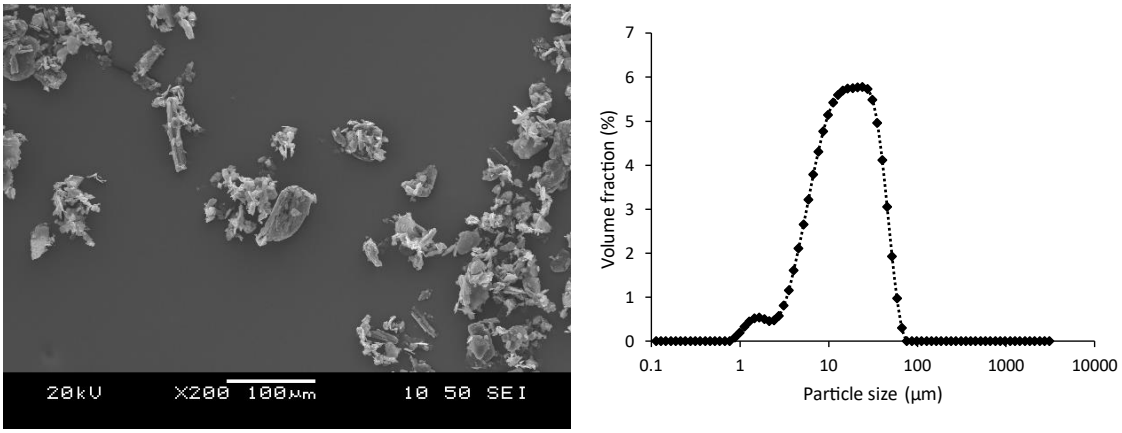

Figure 6.7: SEM micrograph of the graphite powder (left) and particle size analysis of the same powder (right).

The graphite particles are of irregular shape and exhibit an average particle size (D_{50}) of 16.3 µm. This powder profile is not optimal for SLS processing due to the smaller average particle size and the irregular geometry. A spherical graphite powder with similar powder characteristics would be a better option for this feasibility study. However, this was the sole viable option for enhancing absorbance at the time of experimentation.

10 wt.% of graphite was mixed with pure HA (hereafter HA10G) and the GR-HA blend (hereafter HA10BG10G). The absorbance measurements for pure graphite, HA10G and HA10BG10G are presented in Figure 6.8.

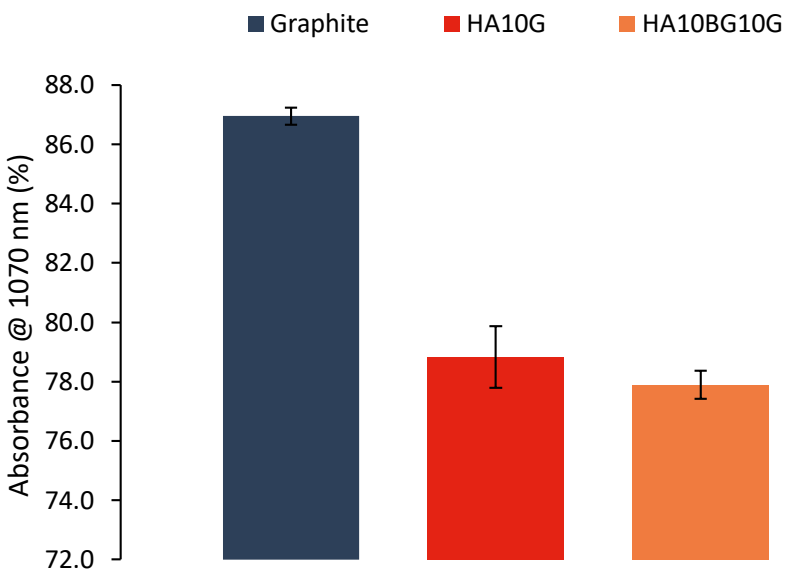

Figure 6.8: Absorbance of graphite, HA10G and HA10BG10G powders at 1070 nm.

The absorbance for both HA10G and HA10BG10G increased from approximately 3% to 79% and 78%, respectively. The slight hysteresis in absorbance between HA and BG that was recorded before blending with the graphite powder is present in the graphite-rich powder feedstocks, too. The absorbance measurements for all the tested powder feedstocks are presented in Table 6.2.

Table 6.2: Absorbance measurements of the powders studied in the SLS feasibility study

Description	Absorbance ± STD (%)
HA	3.5 ± 0.6
BG	2.3 ± 0.9
Graphite	86.9 ± 0.3
HA10G	78.8 ± 1.0
HA10BG	2.9 ± 0.2
HA10BG10G	77.9 ± 0.5

6.3 Flowability

A non-cohesive and free flowing powder feedstock is essential for achieving optimal printing results while processing via SLS. Powder flow characteristics are heavily influencing the printed parts' density and mechanical properties [5], [187], [273], [274]. In order to assess the aptitude of the developed powder feedstocks in terms of flowability, both static and dynamic powder flow behaviour metrics were investigated. More specifically, the angle of repose, Hausner ratio, compressibility index and average flow rate were assessed. The results are presented in Table 6.3 and Figure 6.9.

It is worth mentioning that there is no single technique that could provide a complete powder behaviour profile [273], [275]. For instance, the angle of repose, a commonly used flowability metric, can provide a general understanding of both static and dynamic features in terms of flowability [276]. On the other hand, the average flow rate, a dynamic metric, is able to simulate better the recoating process during SLS processing. Therefore, a holistic solution towards identifying the flow behaviour of any powder feedstock is potentially a combination of both types of measurements.

Table 6.3: Flowability metrics of HA, BG, HA10G, HA10BG and HA10BG10G

Description	Angle of repose ± STD (°)	Hausner ratio ± STD	Compressibility Index ± STD (%)	Average flow rate ± STD (g/s)
HA	24.9 ± 1.9	1.14 ± 0.01	11.95 ± 0.85	23.1 ± 0.6
BG	24.0 ± 1.6	-	-	58.2 ± 5.5
HA10G	33.4 ± 0.9	1.24 ± 0.01	19.08 ± 0.74	22.8 ± 1.0
HA10BG	23.7 ± 0.7	1.12 ± 0.01	11.01 ± 0.68	24.8 ± 0.6
HA10BG10G	33.5 ± 0.9	1.23 ± 0.02	18.79 ± 1.00	25.3 ± 0.7

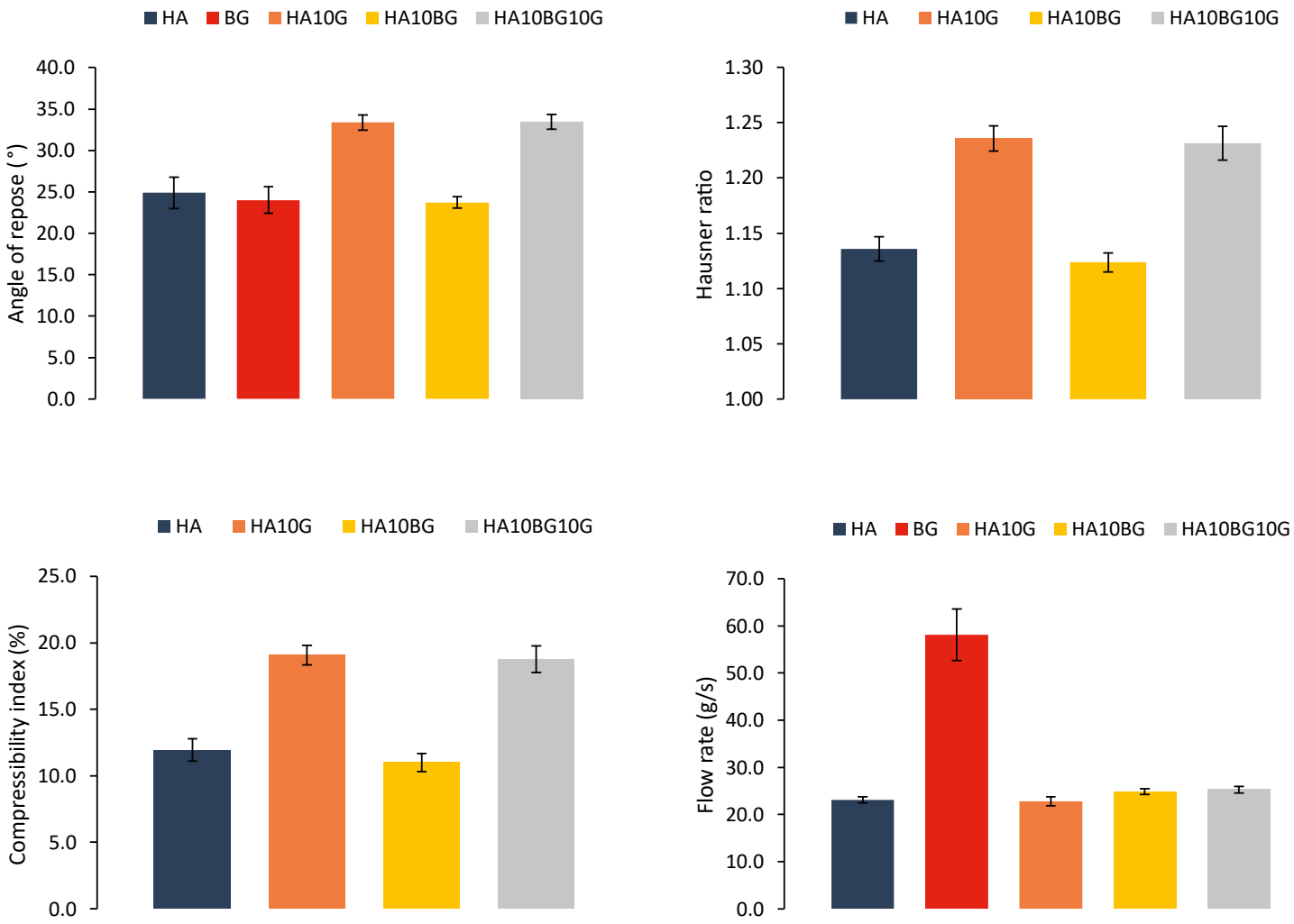

Figure 6.9: Angle of repose (upper left), Hausner ratio (upper right), compressibility index (lower left) and flow rate (lower right) measurements for the powders studied in the SLS feasibility study.

Both spheroidised powder feedstocks exhibited excellent flowability characteristics according to Carr's classification regarding the angle of repose [243]. The spheroidised glass powder performed slightly better than the calcium phosphate powder in this specific metric, with 25° and 24° being the values recorded for HA and BG, respectively. The GR-HA blend (i.e., HA10BG) slightly outperformed pure HA in the same test, a trend that can be attributed to the glass presence in the mix. The graphite-rich blends did not match the performance of their pure counterparts. More specifically, both tested powder feedstocks (i.e., HA10G and HA10BG10G) exhibited an angle of repose of 34°. This 36% increase can be attributed to the presence of irregular and fine graphite particles within the powder feedstocks, that hinders flowability in general. However, both HA10G and HA10BG10G are still potentially suitable for SLS processing since they classify under "Good" in the Carr classification [243].

Similar trends were observed for both Hausner ratio and compressibility index measurements. HA and HA10BG outperformed their graphite counterparts in both tests. More specifically, HA10G and HA10BG10G were classified as "Good" in terms of flowability as per Carr's classification. Whereas HA and HA10BG performed "Excellent" on the same scale. The glass presence has a positive effect on flowability, since slightly lower values are recorded for Hausner ratio and compressibility index compared to pure HA; a similar trend is observed for the graphite-rich blends. This could potentially be attributed to the smoother surface of the glass particles enhancing the total flowability of the powder feedstock. (BG powder was excluded from these measurements. The nature of the test posed a risk towards the structural integrity of the glass microspheres and the realisation of the SLS feasibility study)

In terms of flow rate measurements, a counter intuitive result was recorded. The graphite-rich blends exhibited slightly higher flow rates compared to pure HA and HA10BG. In this metric, the graphite content did not hinder the flow behaviour of the powder feedstocks, as previously seen with the angle of repose measurements. Bimodal distributions tend to hinder flowability since they usually increase the interparticle friction within the powder feedstocks [274]. Hence this mechanism cannot be the underlying cause regarding the slightly higher flow rates recorded for HA10G and HA10BG10G. This could potentially be attributed to fine graphite particles coating the rough surface of HA particles, lowering the interparticle friction within those feedstocks. Furthermore, the spheroidised glass powder exhibited the highest flow rate throughout the test group, a result that can potentially be attributed to the smooth surface of the glass particles.

To conclude, all tested powder feedstocks were potentially suitable for SLS processing in terms of flowability; both HA and BG powders performed excellently. The presence of graphite in HA10G and HA10BG10G influenced the flow behaviour in a negative manner since higher angle of repose, Hausner ratio and compressibility index values were recorded for the graphite containing powder feedstocks. However, they still classified under “Good” in the Carr classification regarding flowability.

6.4 SLS printing

Three different geometries were selected to be printed via SLS, utilising either pure HA or HA containing 10 wt.% of BG, HA10G and HA10BG10G, respectively. Two cylindrical designs exhibiting different heights where chosen in order to investigate the printability of the powder feedstocks with simple geometries and different number of layers. Additionally, a cylindrical scaffold was chosen in order to assess the printability with more complex geometries. It is worth mentioning that the printing profile used for both powder feedstocks was the same throughout this feasibility study. It was optimised for HA10G in a previous study by Navarrete-Segado et al. [240]. Due to time limitations in the usage of the SLS equipment during experimentation, the same profile was used for processing the glass containing powder feedstock. The different CAD models and panoramic views of the printing bed are presented in Figure 6.10.

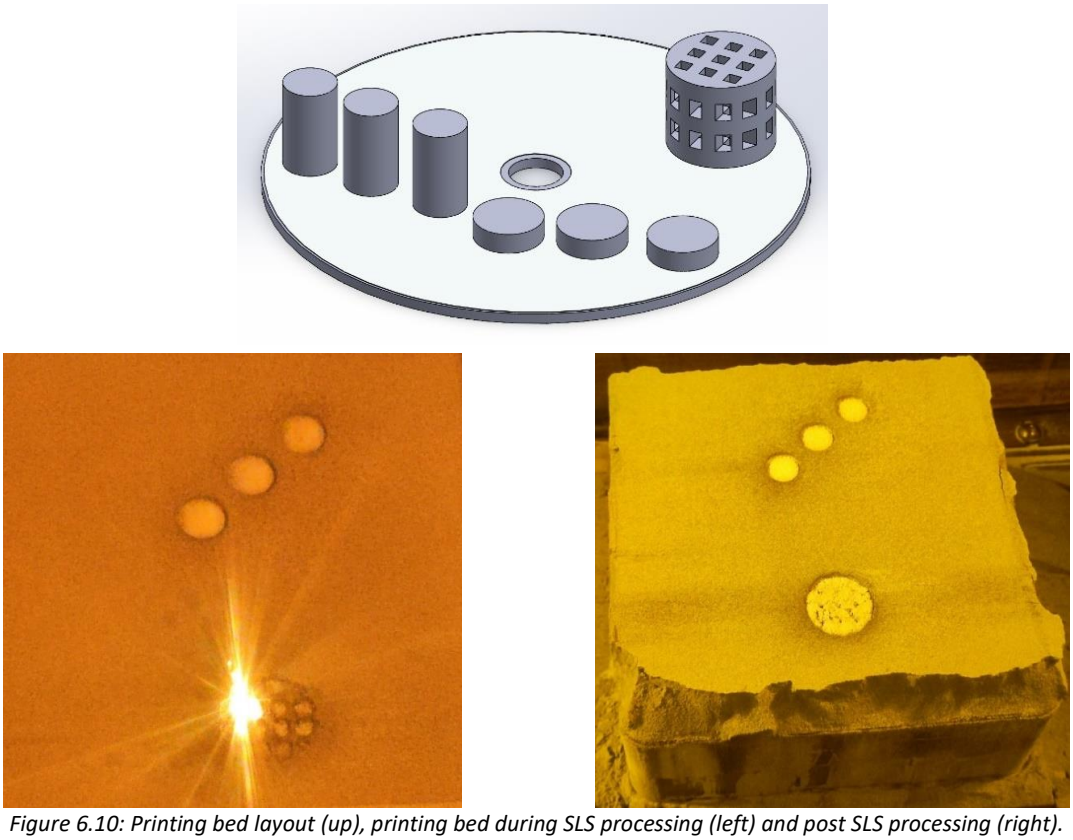

Figure 6.10: Printing bed layout (up), printing bed during SLS processing (left) and post SLS processing (right).

HA10G performance was not optimal in terms of SLS processability. All of the printed samples exhibited high levels of brittleness and only the tall cylinders were successfully retrieved from the printing bed. The remaining two designs lacked cohesion and compactness, breaking immediately upon any attempt of manually depowdering the printing bed and retrieval. This behaviour could potentially be attributed to different gradients of thermal conductivity upon processing. Most probably the energy input was not adequate due the proximity of the short cylinders to the printing bed and the open geometry of the scaffold. Based on the same speculation, a more even heat distribution throughout the volume of taller parts during processing, could be the reason behind the better fusion between each layer. The status of the printing bed post the depowdering step and the retrieved tall cylinders are presented in Figure 6.11.

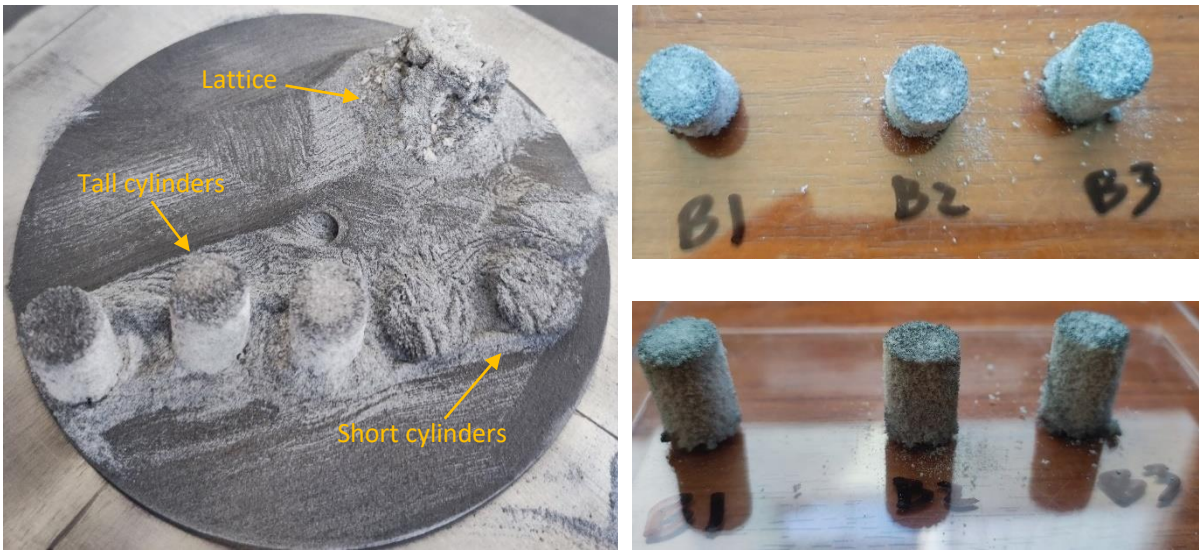

Figure 6.11: HA10G printed samples. Printing bed post the depowdering step (left), tall cylinder top (upper right) and side (lower right).

The glass containing powder feedstock exhibited better processability compared to HA10G since both the tall and the short cylinder design were printed successfully. (The scaffold design was not tested with HA10BG10G due to time constraints faced during experimentation) The printed samples still suffered from brittleness, however at a much lower extent. The task of

handling and retrieving them from the build plate was less complicated since they were more rigid compared to HA10G. This behaviour could be attributed to the glass content that potentially melted during sintering, acting as fusion agent for the HA particles within the powder feedstock. The same mechanism was most probably responsible for the darker look of HA10BG10G printed samples. Graphite particles were probably encapsulated within the glassy phase, alongside their HA counterparts. Additionally, balling was observed on the top side of these samples, a phenomenon driven by the Gibbs – Marangoni effect. During processing that involves a liquid phase, such as the glass component in this study, particles tend to agglomerate in ball-like structures in an attempt to reduce surface energy [18], [191], [201], [204]. It is a phenomenon that has been observed in SLS studies both in metallic [191], [205], [277] and ceramic [195], [201], [209], [278] powder feedstocks. Its occurrence is directly related to thermal gradients realised on the printing bed while processing and printing parameters such as hatch distance or layer thickness [18], [191], [204], [278]. Balling should be avoided during SLS processing since it introduces dimensional inaccuracies and unwanted roughness on the surface of the printed samples. This can be achieved with the the utilisation of a heated powder bed effectively minimising the thermal stresses during printing [204]. Additionally, optimised printing profiles can aid towards this direction and are usually identified through processing window studies [191], [204]. In the current study, this could have been prevented, either partially or fully, with the use of a preheated powder bed/chamber (an option that was not available with the utilised kit). Most probably, the glass content of the powder feedstock melted under the intense laser irradiation and then cooled down in a rapid manner, leading to the observed ball-like structures. This phenomenon could have been further minimised if an optimal printing profile was identified for the glass containing powder feedstock.

The printing bed post the depowdering step and the retrieved tall and short cylinders are presented in Figure 6.12.

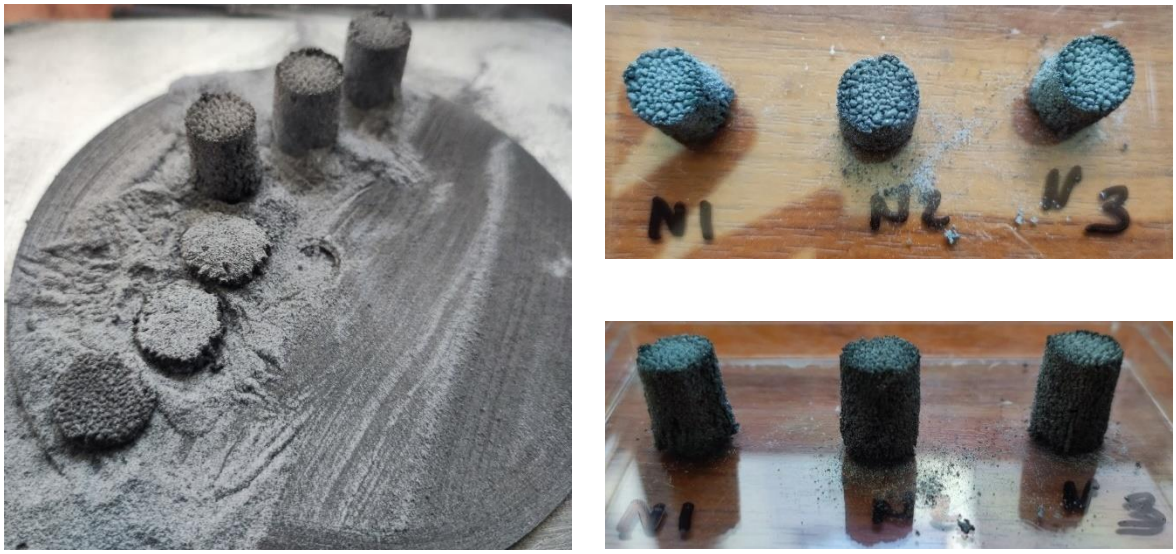

Figure 6.12: HA10BG10G printed samples. Printing bed post the depowdering step (left), tall cylinder top (upper right) and side (lower right).

Both pure HA and GR-HA printed samples underwent a heat treatment cycle at 1300 °C, the same as per the one described in Chapter 5, in order to assess any effects in terms of mechanical or chemical properties. Additionally, this post-processing step would ensure the removal of the graphite powder via pyrolysis. HA10G and HA10BG10G pre and post-sintering are presented Figure 6.13 and Figure 6.14, respectively. Both samples exhibit a darker hue before sintering that is directly linked to the amount of graphite present. Post thermal treatment, both samples seem to be graphite free since no dark areas are macroscopically visible. The pure HA sample (hereafter HA10G_S) is completely white while the GR-HA sample (hereafter HA10BG10G_S) is white combined with yellow discolorations throughout its volume. These discolorations could potentially be attributed to laser induced chemical reactions that took place during SLS processing. Due to the presence of oxygen and the high amount of graphite trapped within the glassy phase, it is possible that graphite reacted with oxygen in an exothermic reaction (i.e., combustion) [279], leaving behind the yellow

discolorations. Lastly, it is worth mentioning that during heat treatment, HA10G_S exhibited a mass loss of 1 wt.% whereas HA10BG10G_S lost 3 wt.% of its mass. This finding is directly connected with the darker hew of the sample (i.e., increased graphite content), that was pyrolysed at a higher extent compared to HA10G_S.

Figure 6.13: HA10G (left) and HA10BG10G (right) as-printed samples.

Figure 6.14: HA10G_S (left) and HA10BG10G_S (right) heat-treated samples.

Stereoscopic images were taken for both tested powder feedstocks, pre and post-processing, in order to assess the dimensional accuracy and surface morphology of the printed parts. Both sets of printed samples exhibited a fair amount of dimensional accuracy compared to the CAD model, considering the experimentation limitations (i.e., lack of preheated powder bed/chamber, optimised printing profile). The recorded differences diameter-wise were 10% and 14% for HA10G and HA10BG10G, respectively. The larger diameter difference for

HA10BG10G is probably related to the balling effect experienced while processing. A comparable difference was recorded in terms of length measurements for either powder feedstocks. HA10G samples were 7% smaller than the CAD model whereas HA10BG10G were 9% smaller. It is worth mentioning that GR-HA samples loaded with the same amount of glass content showed higher shrinkage rates compared to pure HA, as described in sub-section 5.4.

In terms of surface morphology HA10G samples exhibited smoother surface profiles compared to HA10BG10G, as it can be seen in Figure 6.15 and Figure 6.16, respectively. The height differences recorded on pure HA samples are much smaller compared to the GR-HA feedstock. This finding is directly related to the balling effect experienced during processing. Balling was not only present in the GR-HA printed samples but HA10G samples exhibited limited areas of molten HA that were shaped in a ball-like structure, as it can be seen in the magnified image.

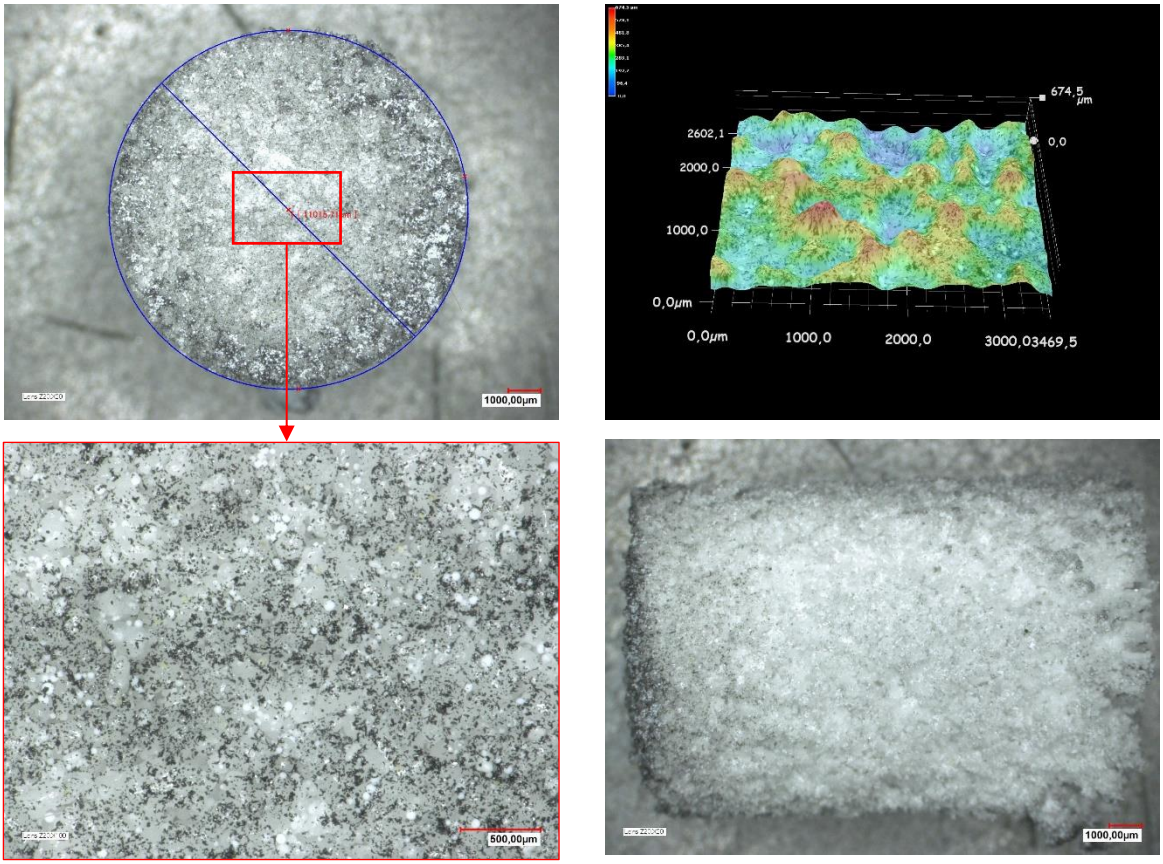

Figure 6.15: Stereoscopic images of HA10G: top view (upper left), top view detail (lower left), surface profilometry map (upper right), side view (lower right).

The extent of balling in the HA10BG10G samples is much more extensive, as previously described. The height differences on the surface almost double in size compared to HA10G creating a much rougher surface. Graphite particles are trapped at a higher extent either on or below the surface of HA10BG10G printed samples compared to HA10G. This finding explains the darker hue exhibited by the glass-rich samples. Additionally, pockets of graphite trapped within glass pockets are visible throughout the surface of the samples. Some of them are black however other exhibit a yellow tint. The latter could be indicative of the exothermic reaction that was described earlier and potentially explain the yellow hue of HA10BG10G_S.

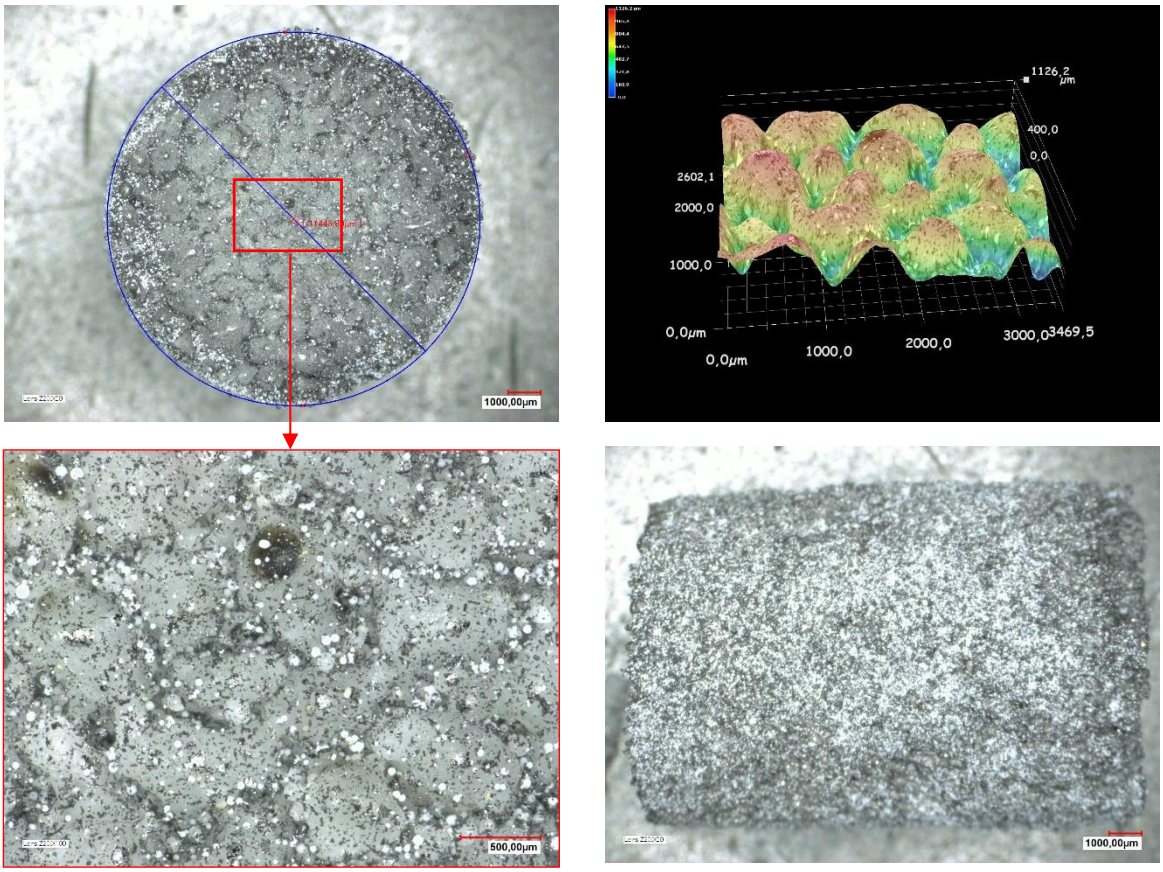

Figure 6.16: Stereoscopic images of HA10BG10G: top view (upper left), top view detail (lower left), surface profilometry map (upper right), side view (lower right).

After the heat treatment, both samples lost their dark hue due to the elimination of graphite via pyrolysis. HA10G_S is completely white while HA10BG10G_S exhibits a yellow tint, most probably related to a chemical reaction between the graphite and oxygen induced by the laser irradiation.

HA10G_S exhibited less brittleness compared to the as-printed samples, however they were still extremely fragile while handling. The surface of the sample did not exhibit any signs of graphite particles, as it can be seen in Figure 6.17. Additionally, extended solidified areas were observed compared to the as-printed samples. The heat treatment did not affect the areas exhibiting balling since they are still present on the surface of the sample. Furthermore, the

outer wall of the samples exhibits the same flaky consistency that was observed in the printed samples prior to the heat treatment.

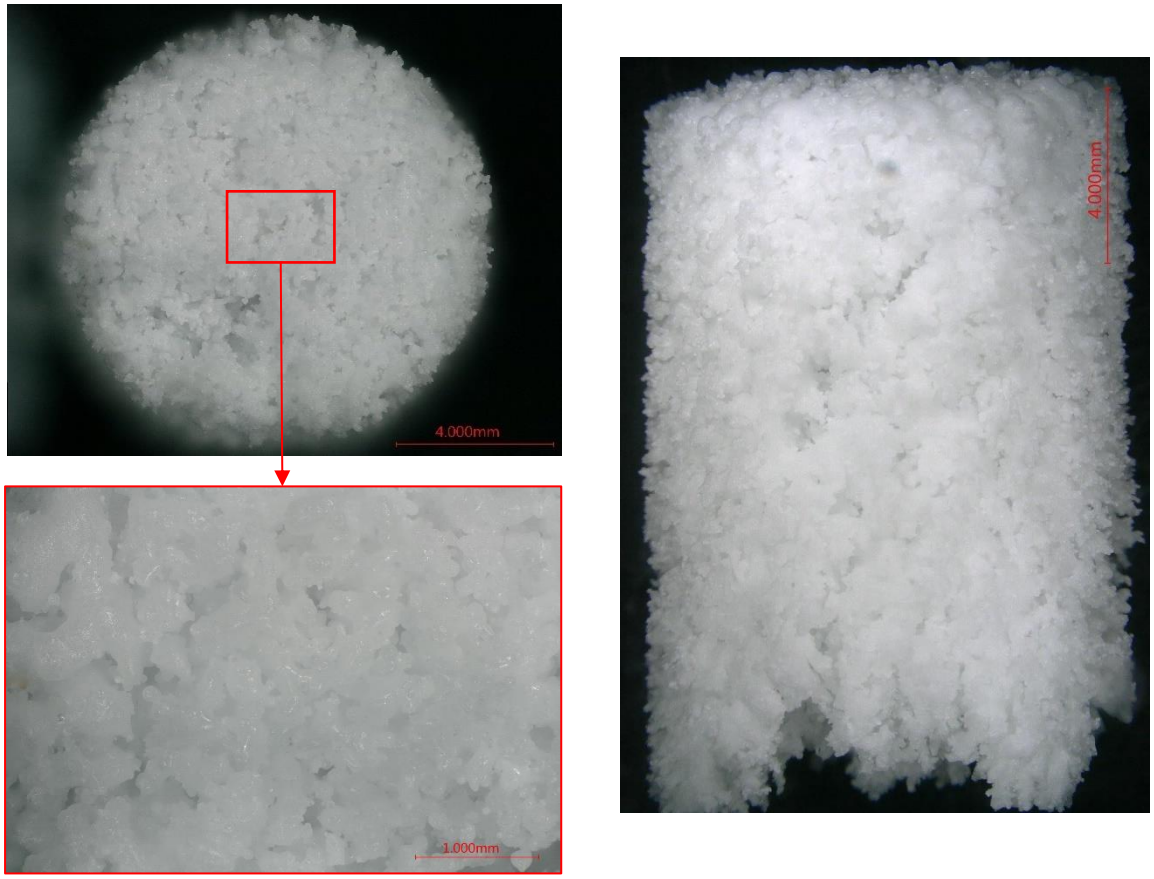

Figure 6.17: Stereoscopic images of HA10G_S: top view (upper left), top view detail (lower left), side view (right).

The heat treatment allowed the GR-HA samples to further solidify and eliminated any graphite content and pockets that were present in the as-printed samples, as it can be seen in Figure 6.18. The balling effect is still present on the surface of the sample and the outer walls exhibit a dendritic structure. This type of growth could potentially be driven or connected to the presence of glass and a similar mechanism to the Gibbs – Marangoni effect.

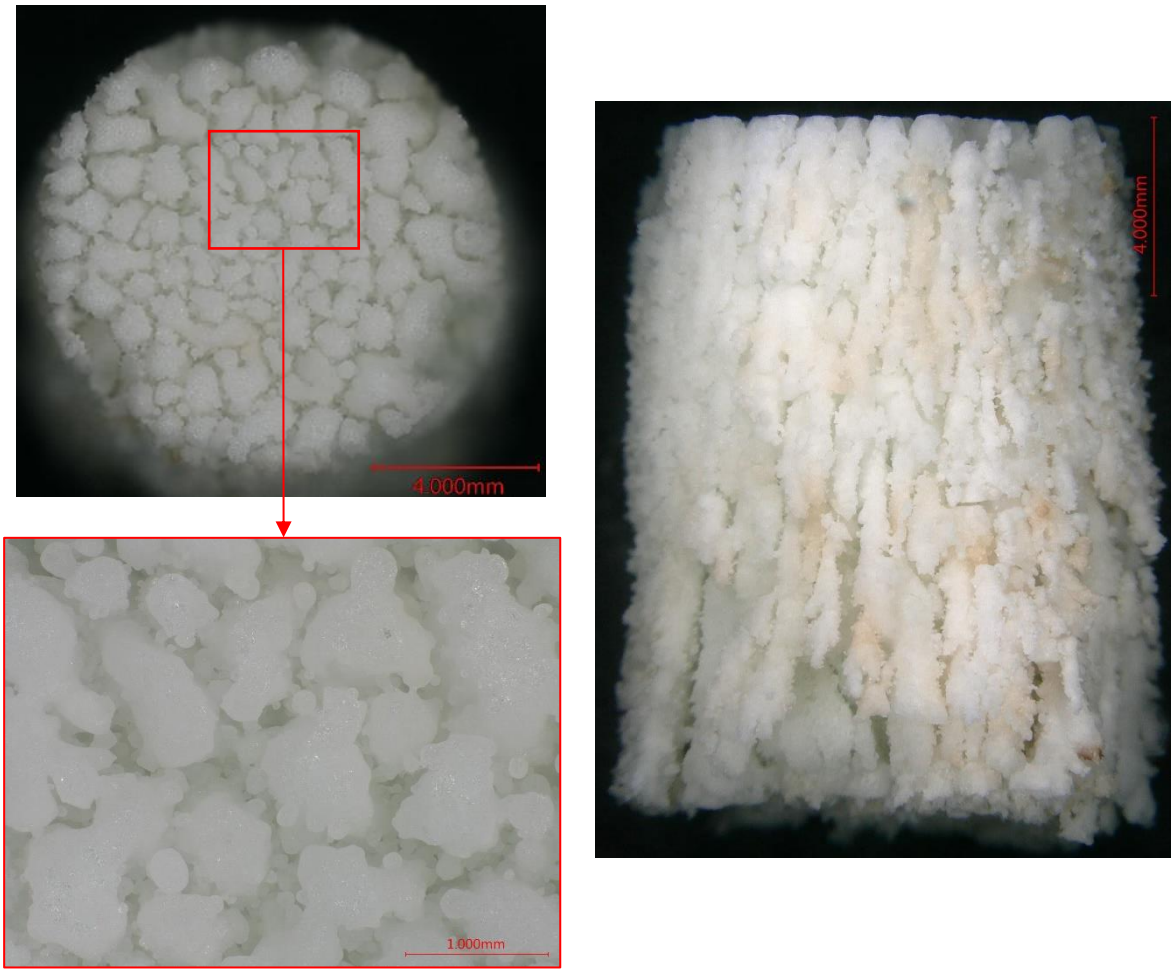

Figure 6.18: Stereoscopic images of HA10BG10G_S: top view (upper left), top view detail (lower left), side view (right).

In order to assess the chemical stability of the tested powder feedstocks, phase identification experiments were carried out throughout the SLS feasibility study. Figure 6.19 presents the diffractograms of all the initial powders prior to SLS printing. In terms of HA, all the diffraction peaks correspond to stoichiometric HA, as per JCPDS 00 009 0432; the same applies for graphite (JCPDS 75-1621). A distinct peak around 26.5° is observed for both HA10G and HA10BG10G and it corresponds to the graphite powder added to those powder blends.

As a result of SLS processing, additional phases were detected for both HA10G and HA10BG10G. More specifically, HA and traces of graphite are still present in HA10G, as it can be seen in Figure 6.20. However, tetracalcium phosphate (TTCP) and α-TCP were detected

alongside the initial components of the powder blend. This mixture is one of the stoichiometrically viable outcomes when processing HA at high temperatures, in an oxygen atmosphere [280]. Additionally, since the detected TCP phase is α-TCP, it is safe to assume that the processing temperature was at least 1200 °C [8]; similar behaviour was observed in a similar study by Navarrete-Segado et al. [240].

In the case of HA10BG10G, the same phases were detected however in miniscule quantities compared to HA10G. The TTCP peak is much broader and lower in intensity whereas the α-TCP peak is barely visible. This is a strong indication of the glass's performance as a prophylactic agent in terms of HA dehydroxylation. The same behaviour was observed in the traditionally manufactured samples, described in Chapter 5. Furthermore, the presence of graphite is more prominent in this sample, as it can be seen by the more distinct peak around 26.5°. This finding directly correlates to the darker hue exhibited by the glass-rich printed samples. It is worth mentioning, that no glass-related phases were introduced during SLS processing (with temperatures reaching at least 1200 °C). This is a strong indication of the thermal stability of the developed glass system even when processing with localised high energy density sources.

As expected both samples are graphite-free after the heat treatment cycle, since no distinct peak is observable around 26.5°, as it can be seen in Figure 6.20. In the case of HA10G_S, the HA peaks are sharper compared to the as-printed samples. In tandem, the TTCP and α-TCP peaks are broader and less prominent. This combination of findings provides a strong indication of a potential reverse phase transformation of TTCP and α-TCP to HA during the heat treatment. This behaviour has been previously documented by Liao et al. [281] during their study of thermal processing of HA in high temperatures under air. In the mentioned

study, HA powder was heated up to 1500 °C and then cooled at different temperatures with a cooling rate of 10°C/min. They identified a reverse phase transformation mechanism that drove TTCP and α-TCP to gradually transform to HA during cooling. The transformation ratio maximised with decreasing cooling temperature and 1100 °C was the threshold where the secondary phases would completely transform to HA. In the case of HA10BG10G_S, no other phases besides HA were detected. The heat treatment affected the GR-HA printed sample in a positive manner similar to pure HA. The miniscule quantities of TTCP and α-TCP detected in the as-printed samples reverted to HA.

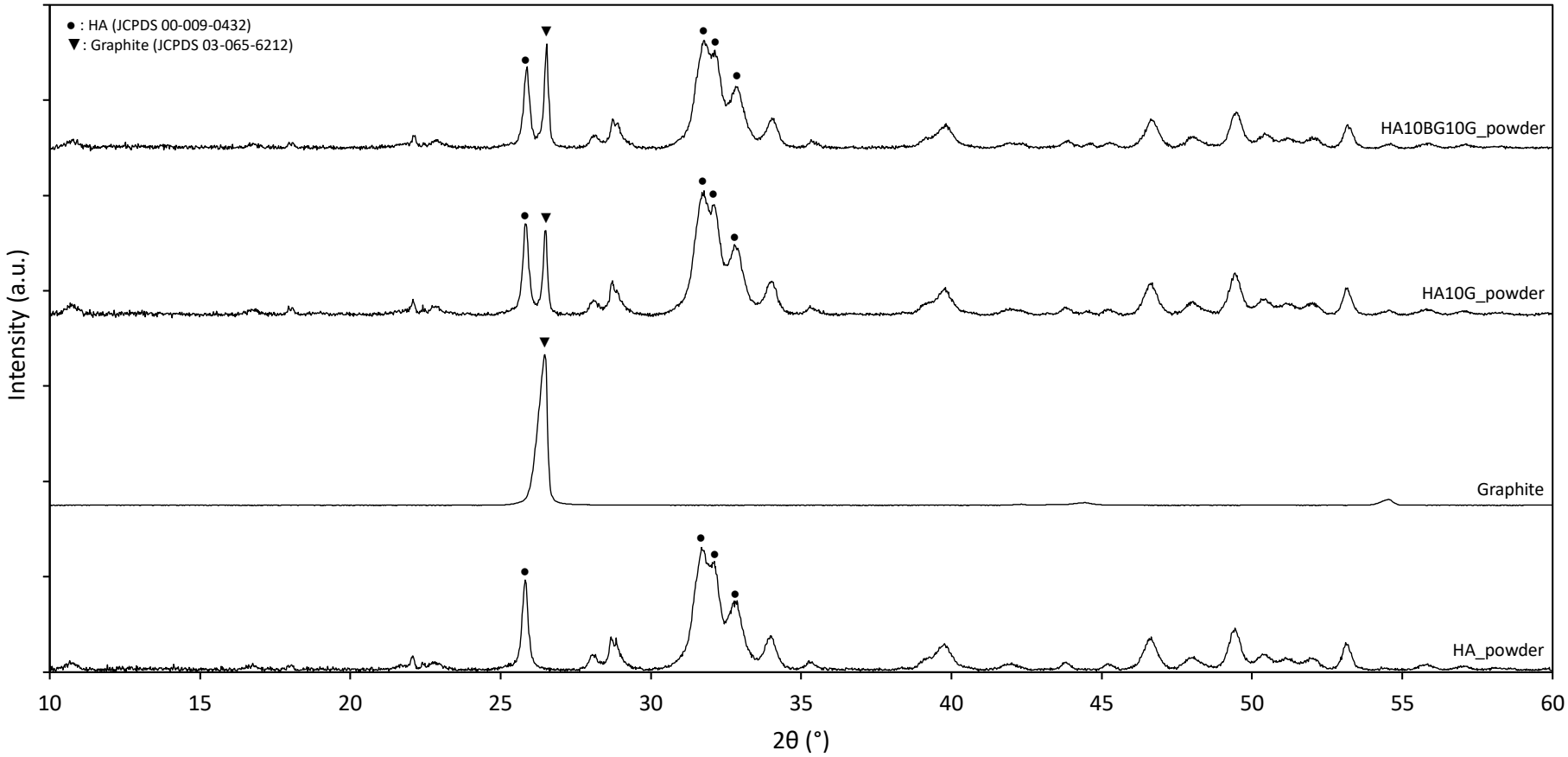

Figure 6.19: X-ray diffractograms of the initial powders and blends studied in the SLS feasibility study.

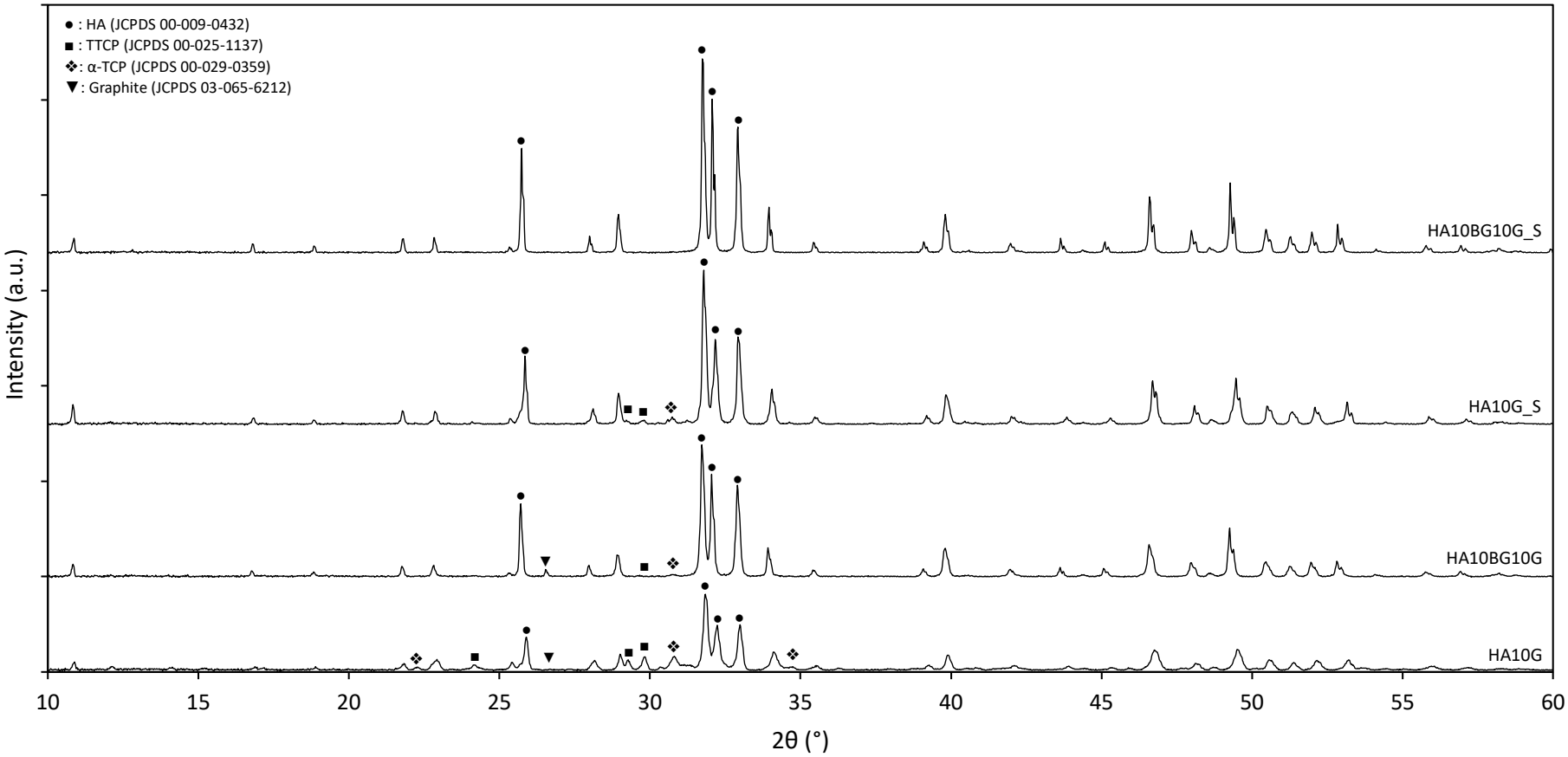

Figure 6.20: X-ray diffractograms of the as-printed (HA10G, HA10BG10G) and heat-treated samples (HA10G_S, HA10BG10G_S).

In order to quantify the phase composition in the as-printed and post-processed samples, Rietveld analysis was carried out. The results for all the tested specimens, including phase analysis and unit cell related values, can be found in Table 6.4.

Table 6.4: Rietveld analysis results of HA10G, HA10BG10G, HA10G_S and HA10BG10G_S

Description	a (Å)	b (Å)	c (Å)	Volume ($Å^3$)	HA	TTCP	α-TCP	Graphite
HA10G	9.395	9.395	6.884	526.22	60.0%	34.3%	4.1%	1.5%
HA10BG10G	9.410	9.410	6.922	530.72	68.5%	1.3%	0.5%	29.7%
HA10G_S	9.413	9.413	6.885	528.31	88.7%	10.2%	1.2%	0.0%
HA10BG10G_S	9.421	9.421	6.922	532.13	100.0%	0.0%	0.0%	0.0%

HA content in both as-printed samples ranges between 60 – 68% with HA10BG10G recording the highest value. However, in the case of HA10G the remaining 40% of its composition is comprising primarily from TTCP (34%) and smaller traces of α-TCP (4%) and graphite (1.5%). A completely different phase composition is recorded for HA10BG10G since TTCP and α-TCP phases accrue for a combined 2% while graphite completes the composition profile with the remaining 30%. The latter could be an overestimation from the Rietveld refinement analysis. The actual ratio of graphite within the composition could potentially be lower considering the HA/graphite peak intensity ratio in the recorded XRD data. Nevertheless, it is safe to assume that the chemical signature of the as-printed GR-HA samples produced through the Rietveld analysis is accurate since the two main components of the composition are predicted.

After the heat treatment, HA presence is more prominent in both samples. In the case of HA10G_S, HA covers almost 90% of the composition with TCCP (and miniscule quantities of α-TCP) accruing for the remaining 10%. No additional phases besides HA were recorded for HA10BG10G_S. The phase composition results for both the as-printed and post-processed samples are presented in Figure 6.21.

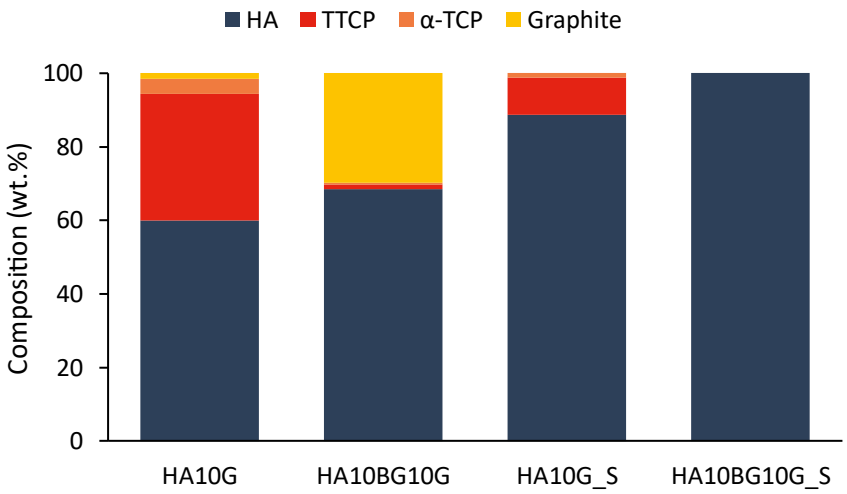

Figure 6.21: Composition map of HA10G, HA10BG10G, HA10G_S and HA10BG10G_S.

Variation of the a-axis, c-axis and unit cell volume parameters for both as-printed and heat-treated samples, are presented in Figure 6.22.

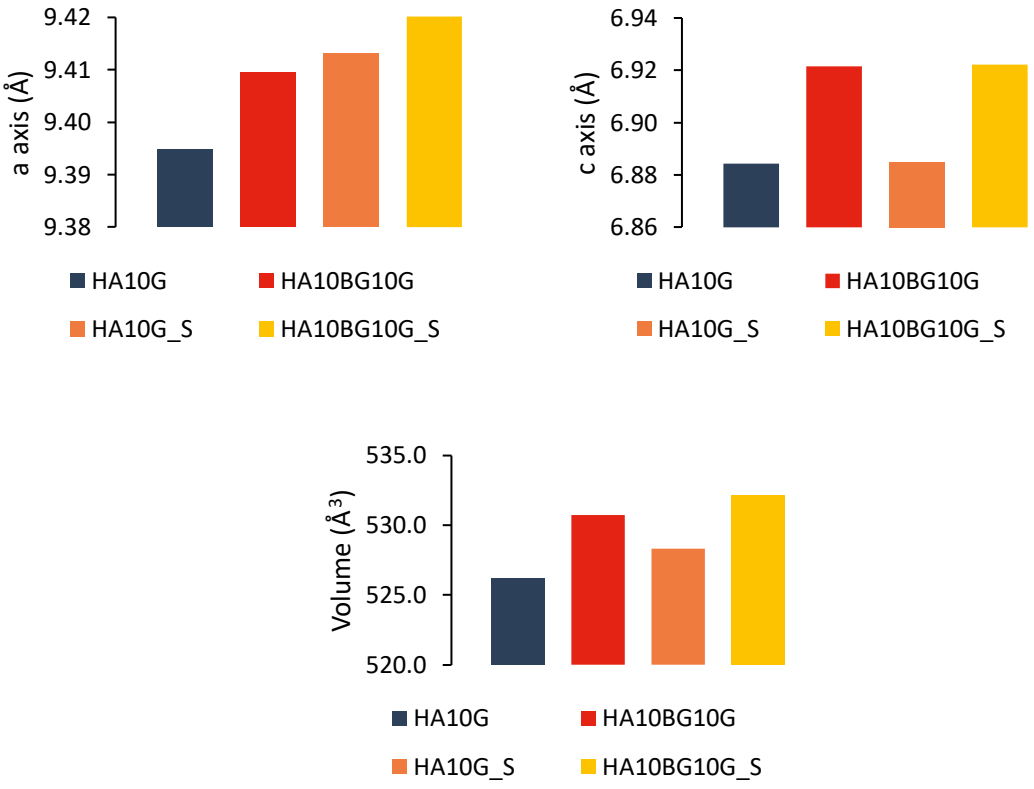

Figure 6.22: Unit cell lattice parameters of HA10G, HA10BG10G, HA10G_S and HA10BG10G_S.

An expansion of the a-axis is observed between HA10G and HA10BG10G which could potentially indicate ion exchange within the HA lattice. La ions exhibit a slightly larger ionic radius than Ca ions [254], hence such a replacement could justify the a-axis expansion. The same observations apply for the unit cell volume. The glass content does not seem to affect the c-axis of the unit cell, with HA10BG10G and HA10G exhibiting a similar c-axis value.

Post-processing significantly affected the unit cell parameters for both tested powder feedstocks. More specifically, the unit cell expanded both in the a and c-axis direction, after HA10G and HA10BG10G underwent the heat treatment cycle at 1300 °C. In the case of both HA10G_S and HA10BG10G_S, the c-axis expanded similarly compared to the as-printed samples. This finding is a strong indication that the glass presence was irrelevant to this expansion. The a-axis expansion for both tested samples does not exhibit the same behaviour as per the c-axis findings. It is dependent both on the sintering temperature and the glass content, with HA10BG10G_S exhibiting a larger a-axis compared to HA10G_S. This is an indication that the heat treatment was the sole driving mechanism behind the a-axis expansion of HA10G_S. In the case of HA10BG10G_S, the additional expansion can be attributed to ion exchange within the lattice.

Based on the XRD analysis it can be concluded that HA10BG10G exhibited better thermal stability during SLS processing compared to HA10G, since miniscule phase transformations were recorded for the glass-rich powder feedstock. On the contrary, HA10G was more susceptible to HA dehydroxylation phenomena that could be detrimental in tissue engineering applications in terms of biological and mechanical performance. Additionally, the post processing heat treatment cycle worked as expected in terms of graphite removal via pyrolysis since no traces were found in either of the tested powder feedstocks.

In order to assess the effect of heat treatment in terms of densification, µCT experiments were carried out. Unfortunately, testing either HA10G and HA10G_S was not feasible due to brittleness and difficulty in mounting them on top of the sample holder. The glass containing SLS processed samples, before and after heat treatment, were easier to handle since they were less fragile compared to their pure HA counterparts. The µCT scans for HA10BG10G and HA10BG10G_S are presented in Figure 6.23 and Figure 6.24, respectively.

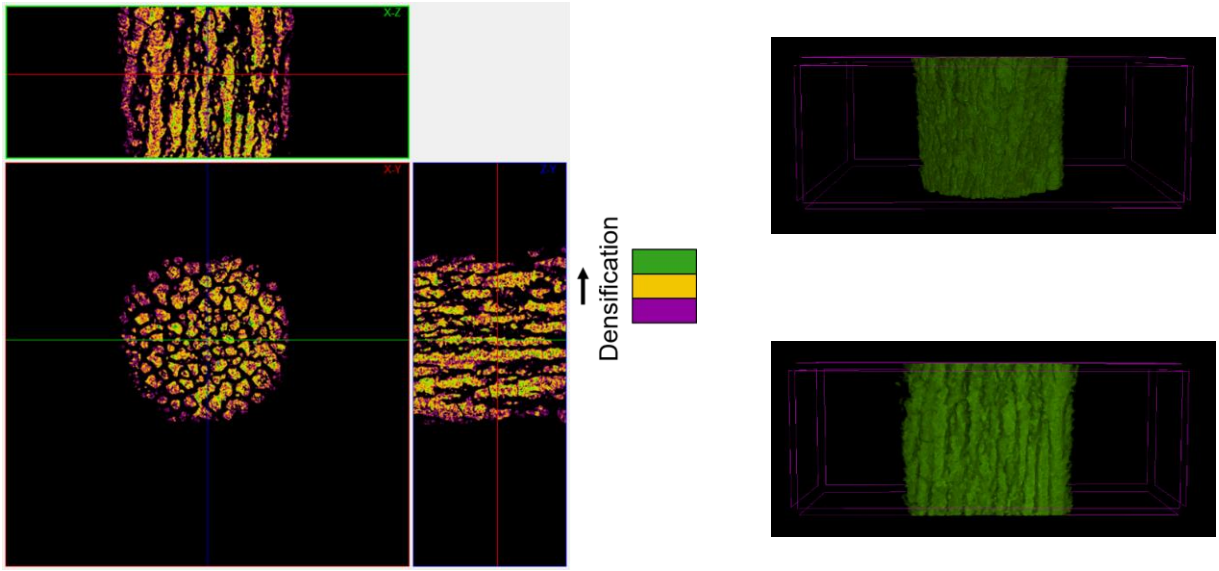

Figure 6.23: HA10BG10G: X-Z, X-Y and Z-Y cross sections (left), 3D volume reconstruction front (upper right) and X-Z cross section (lower right).

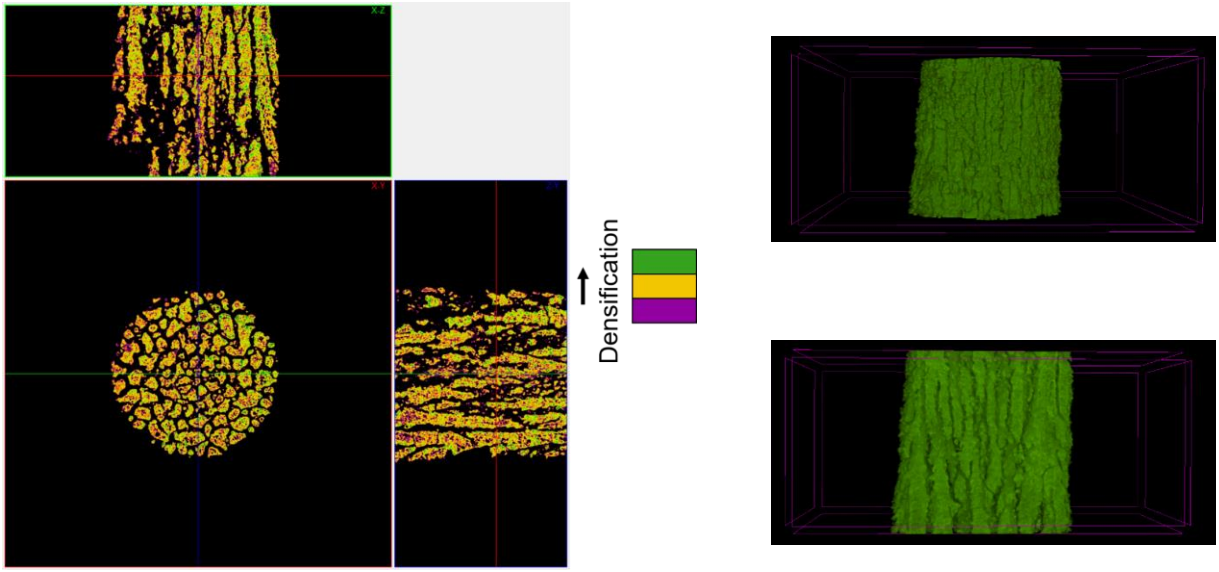

Figure 6.24: HA10BG10G_S: X-Z, X-Y and Z-Y cross sections (left), 3D volume reconstruction front (upper right) and X-Z cross section (lower right).

Comparing the as-printed sample to the heat-treated sample, it is obvious that sintering was beneficial towards densification. A larger densification gradient was observed for HA10BG10G compared to HA10BG10G_S, during this qualitative densification assessment. More specifically, the outer walls of the as-printed sample exhibit lower densification compared to its centre. On the contrary, minimal variation was observed on the densification of HA10BG10G_S throughout the volume of the sample. This could potentially be attributed to temperature gradients present during SLS processing that did not allow the perimeter of the sample to fuse properly. The thermal diffusivity was probably higher in the core of the sample and was attenuated when the laser scanning reached non-irradiated colder regions towards the outskirts of the cylinder. Similar findings were reported in various studies focusing on the simulation of the temperature field during SLS processing via discrete element method (DEM) [282]–[284]; a schematic representation of this phenomenon is presented in Figure 6.25 [282]. Additionally, the dendritic structures observed at the outer wall of HA10BG10G_S via optical microscopy, were verified by the μCT experiments. They are present both in the as-printed samples and the heat-treated ones, as it can be seen in Figure 6.23 and Figure 6.24.

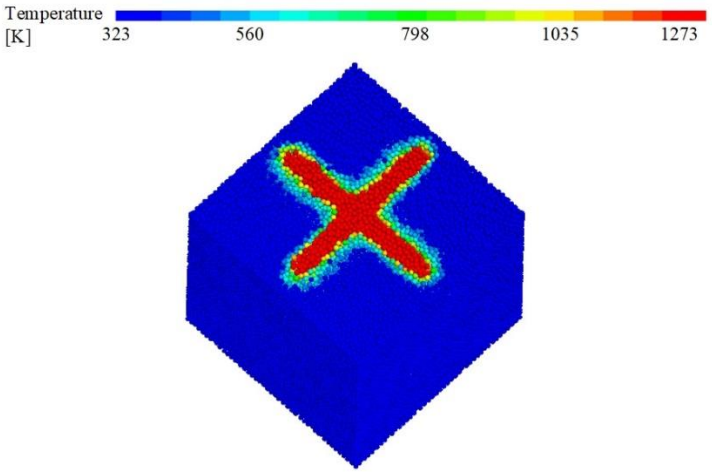

Figure 6.25: Temperature profile during SLS processing of a mini propeller blade [282].

Based on the µCT investigation it can be concluded that the heat treatment had a positive effect on HA10BG10G samples in terms of densification. Furthermore, a more uniform densification profile across the volume of the post-processed sample was observed compared to the as-printed specimen.

CHAPTER 7 – Conclusions, discussion and future work

Glass reinforced hydroxyapatite feedstocks provide an optimal framework for tissue engineering applications. The enhanced biological and mechanical performance of biomaterials comprising of HA and silicate or phosphate-based biomedical glasses has been established since the early 1990s. However, GR-HA formulations employing either of those family of glasses are usually prone to either crystallisation and/or phase transformation phenomena. These effects can prove to be detrimental in terms of a biomaterial's efficacy. Considerably fewer studies utilising borate-based glasses in GR-HA composites have been carried out besides their biocompatibility and enhanced thermal stability.

The overall aim of this work was to identify a novel GR-HA feedstock that would be resistant to crystallisation and HA thermal degradation, while being versatile in terms of processing via traditional means and SLS. So far preventing the development of such detrimental secondary phases in GR-HA biomaterials is either unattainable or requires complicated processing procedures. GR-HA SLS processing is currently at its infancy, with the limited studies on the topic facing similar phase transformation problems and/or processing issues both in terms of powder and scanning parameters optimization. Upon identifying the gaps in the literature, $50B_2O_3$-$20SiO_2$-$20Na_2O$-$(10-x)CaO$-xLa_2O_3 ($0 \leq x \leq 2.5$) was identified as a promising candidate for utilisation in a such novel GR-HA system.

7.1 Conclusions and discussion

This work focused on the development of a novel GR-HA feedstock, utilising the novel glass system, $50B_2O_3$-$20SiO_2$-$20Na_2O$-$(10-x)CaO$-xLa_2O_3 ($0 \leq x \leq 2.5$) both in a traditional and an SLS approach. The following conclusions were drawn:

- *The use of 10 wt.% of glass content mitigates the occurrence of thermal degradation phenomena, enhances densification and overall mechanical performance.*

HA dehydroxylation products were detected in GR-HA specimens containing ≤ 5wt.% of glass content, regardless of the lanthanum content. The main phase recorded was β-TCP that reverted to α-TCP at higher sintering temperatures. Thermal degradation was more severe with increasing sintering temperature but the maximum HA to TCP conversion never exceeded 27%, throughout the study. The presence of small quantities of β-TCP is not necessarily harmful in terms of bioactivity, since its solubility and dissolution rate can be favourable in biomedical systems. On the other hand, the higher dissolution rates of α-TCP could prove to be problematic. The underlying cause behind the presence of those phase transformations could be attributed to the glass reactivity when utilised in quantities equal to or less than 5 wt.%. Small glass additions act as heterogeneous nuclei sites or triggering points that promote such HA dehydroxylation phenomena. In the case of GR-HA composites employing 10 wt.% of glass content, no thermal degradation was observed which indicates that the glass presence mitigates HA decomposition. This can be attributed to even heat distribution during sintering with the glass acting as a liquid phase sintering aid.

This was further validated in the densification investigation via μCT, where samples containing 10 wt.% of glass content, exhibited higher densification rates compared to their 2.5 and 5.0 wt.% counterparts. Thermal degradation was identified as the underlying cause behind

this phenomenon. Both TCP phases exhibit a higher unit cell volume compared to HA, leading to an overall volume expansion that inhibits sintering and further densification. This mechanism was further investigated and it was identified that 8.0 wt.% is the threshold upon which the glass acts a sintering aid and minimises porosity.

Densification was instrumental in terms of enhancing microhardness since GR-HA specimens containing ≤ 5 wt.% of glass content exhibited lower microhardness values compared to pure HA samples. The porosity was the main driving mechanism behind the inferior mechanical performance recorded for these samples. On the contrary, composites employing 10 wt.% of glass content exhibited an increase in microhardness ranging from 10 – 31%. The overall higher microhardness values recorded for these samples compared to pure HA specimens, can be attributed to the glass' function acting as a liquid sintering aid.

- *The novel GR-HA powder feedstock is resistant to crystallisation and no glass-specific secondary phases were detected post sintering at temperatures up to 1300 °C.*

This finding is in line with the literature, validating the thermal stability of similar borate-based glass systems.

- *The GR-HA specimens did not exhibit any antimicrobial efficacy against either Gram positive or Gram negative bacteria.*

The attachment studies carried out with S. Epidermidis and P. Aeruginosa showed no signs of bacterial growth inhibition, in either case. This result directly correlates with the literature since neither non-doped borosilicate glasses nor La_2O_3 have been shown to exhibit any antimicrobial activity.

- *No cytotoxic behaviour was recorded during the SaoS-2 human osteosarcoma cell attachment studies.*

GR-HA samples containing 2.5 wt.% of glass loading, exhibited similar or slightly increased cell viability on days 1 and 4 compared to pure HA, regardless of their lanthanum content. Composite samples employing 10 wt.% of glass exhibited a similar response as per their 2.5 wt.% counterparts. The trend was reversed on day 7, where GR-HA samples containing 10 wt.% of glass content exhibited higher cell viability rates compared to pure HA and composites containing 2.5 wt.% of glass loading. Limited inhibition in terms of cell viability was observed in the case of samples containing 5 wt.% of glass loading. However, this can be attributed to the increased dissolution rates associated with the TCP phases present in those specimens, effectively decreasing the available surface area that could be utilised for cell attachment and proliferation. The morphological analysis of the attached cells upon the surface of the GR-HA samples, verified the quantitative MTT cell viability results. Cells attached on the surface of GR-HA samples containing 10 wt.% of glass content exhibited a flattened and elongated geometry, covering large areas of the substrate, indicating reduced cell stress. The samples showing a similar response but to a lesser extent were the one containing 2.5 wt.% of glass content, followed by their pure HA counterparts. In the case of composite specimens containing 5.0 wt.% of glass content, limited attachment and proliferation was observed.

- *There are indications that lanthanum oxide potentially enhances the overall mechanical and biological performance of GR-HA samples.*

The samples containing the highest amount of lanthanum oxide content within this study exhibited the best performance both in terms of microhardness and cell culture studies. Those findings directly correlate with the literature suggesting that lanthanum oxide is known to act

beneficially towards mechanical strengthening and enhanced biological performance. The incorporation of La ions within the HA matrix aids densification, leading to better mechanical properties, and enhances biological activities such as osteoblastic response.

- *The novel glass powder used in the SLS feasibility study ($50B_2O_3$-$20SiO_2$-$20Na_2O$-$7.5CaO$-$2.5La_2O_3$) was successfully subjected to spheroidisation via flame spraying, without suffering any adverse effects (e.g., crystallisation).*
- *The novel GR-HA feedstock containing 10 wt.% of $50B_2O_3$-$20SiO_2$-$20Na_2O$-$7.5CaO$-$2.5La_2O_3$ exhibited better SLS processability compared to pure HA.*

Two cylindrical designs exhibiting different heights where chosen in order to investigate the printability of either powder feedstock with simple geometries and different number of layers. The printing parameters used throughout the study (energy density: 96 J cm^{-3}, power: 36 W, scanning speed: 75 mm/s) were optimised solely for the pure HA powder due to time limitations during experimentation. Even with a non-optimised printing profile, the GR-HA feedstock exhibited similar, and in some cases even better, printability compared to pure HA during SLS processing. Both designs were printed successfully with the composite powder feedstock, whereas only the tall cylinders were retrieved from the building plate in the case of pure HA. The glass content acted as a fusing agent that allowed the composite samples to be more compact compared to their pure HA counterparts, which suffered from higher levels of brittleness. Balling was observed on the surface of both sets of samples, with the composite samples exhibiting increased surface roughness in comparison with HA printed specimens. This was attributed to the Gibbs – Marangoni effect and the non-optimal scanning parameters used for the glass containing powder feedstock. Both sets of printed samples exhibited a fair amount of dimensional accuracy compared to the CAD model. A diameter deviation of 10%

and 14% was recorded for pure HA and composite printed samples, respectively. Length-wise the composite specimens were 9% smaller compared to the nominal value, whereas the pure HA samples were 7% smaller.

SLS processability could have been further enhanced if the printing platform was equipped with a CO_2 laser source. A 10.6 μm laser source would potentially negate the need of using any absorbance enhancers, in this case graphite powder, since the laser-powder interaction would be more efficient. Furthermore, the lack of irregularly shaped, fine graphite particles within the tested powder feedstocks, would have a positive impact towards flowability, ergo enhancing processability even further. Controlling the environmental conditions during printing, an option not available during the realised SLS feasibility study, could aid processability, too. The utilisation of a preheated powder bed/chamber and control over heating/cooling rates would effectively limit printing defects (e.g., balling), via the minimisation of thermal gradients during processing.

- *The novel GR-HA feedstock containing 10 wt.% of $50B_2O_3$-$20SiO_2$-$20Na_2O$-$7.5CaO$-$2.5La_2O_3$ exhibited better thermal stability compared to pure HA during SLS processing.*

In terms of thermal stability, the GR-HA feedstock exhibited enhanced thermal stability compared its pure HA counterpart. More specifically, miniscule HA decomposition products, TTCP and α-TCP, were detected in the as-printed, glass-containing samples (i.e., < 2%). Additionally, no glass-related phases were introduced during SLS processing which is a strong indication regarding the thermal stability of the developed glass system even when localised high energy density sources are used. On the other hand, pure HA was much more susceptible to HA decomposition with TTCP and α-TCP accounting for almost 40% of the total composition. This can be attributed to the glass content acting as liquid sintering aid, preventing thermal

degradation during SLS processing, in a similar manner to the traditionally GR-HA manufactured samples.

- *Conventional heat treatment was beneficial towards removing any graphite content present in the as-printed samples via pyrolysis. The heat-treated samples exhibited enhanced densification while thermal degradation was partially reversed as a consequence of sintering, too.*

Post-processing via conventional sintering at 1300 °C, had a positive effect on both set of samples. Firstly, any graphite content trapped during SLS processing was successfully removed through pyrolysis, as expected. Additionally, the thermal degradation in the as-printed, pure HA samples was partially remedied via a reverse phase transformation of TTCP and α-TCP to HA; a decrease by 30% was recorded, with the secondary phases accruing for 10% of the total composition. Post processing had a similar effect on the composite printed samples; HA was the sole phase detected in GR-HA samples. Furthermore, similar findings as per the traditionally manufactured composite specimens were observed in terms of unit cell variations in the SLS processed composite samples. More specifically, the unit cell of the GR-HA samples exhibited an expansion compared to the unit cell pure HA specimens. This provides a strong indication of ionic exchange within the HA lattice, with La ions replacing the slightly smaller Ca ions. Lastly, a densification study was carried out to assess the effect of thermal treatment on the post-processed samples. This study focused solely on the composite specimens since pure HA samples were too brittle to handle even after sintering. A densification gradient propagating from the centre of the sample to the outer wall was identified in μCT images. This was attributed to thermal diffusivity attenuation during laser scanning that is common during SLS processing. The heat treatment minimised the

aforementioned densification gradient and had a positive effect in terms of total densification, too.

7.2 Future work

The development and optimisation of a novel GR-HA feedstock requires a thorough investigation for ensuring its suitability as a biomaterial. This includes testing both in terms of its physical properties as well as its biological performance. During the course of this study, a broad spectrum of different characterization techniques were employed in order to assess the suitability of the novel borate-based glass reinforced HA system. The results are definitely promising regarding its efficacy as a biomaterial but additional testing could complement and further validate those findings. More specifically:

- NMR and or X-ray cyclotron studies with the novel glass system could provide further insight on its structural characteristics.
- Investigating the replacement of lanthanum with other active elements used in biomedical research.
    - Lanthanides such as samarium or cerium could be tested due to their chemical affinity to lanthanum and their antimicrobial and bioactive properties.
    - More commonly used active elements in biomedical glasses such as silver or magnesium.
- Additional biological tests should be conducted in order to further characterise the biological performance of the developed GR-HA system.
    - Wettability studies could provide complementary information on the cell attachment and proliferation on the surface of the samples.
    - Dissolution studies in SBF testing both the glass and the GR-HA samples could provide further insight on bioactivity.

- In vitro cell culture studies using different osteoblastic cell lines, such as the MG63 cell line, in order to compare the results collected during this study.
- In vivo cell culture studies in order to investigate the biocompatibility in dynamic conditions.

The results from the SLS feasibility study were promising, since the novel GR-HA feedstock exhibited similar processability and enhanced thermal stability compared to pure HA. However, further investigation is required to fully assess the SLS printability of the composite powder feedstock. More specifically:

- A study utilising a similar SLS printing platform but equipped with environmental control hardware (e.g., preheated powder bed/chamber, suitable cooling rates, etc.)
- A study utilising an SLS printing platform that is equipped with a CO_2 laser source and environmental control hardware (e.g., preheated powder bed/chamber, suitable cooling rates, etc.).
- A parametric study should be carried out in order to investigate the effect of the glass content in terms of procesability and thermal degradation.
- A process window study should be conducted for every powder composition tested in order to identify the optimal printing parameters.
    - Studies focusing on direct SLS of borosilicate [285] or other glass systems [286]–[288], could provide initial insights on identifying suitable printing parameters and strategies (e.g., preheated powder bed temperature, heating/cooling rates, etc.).
- The usage of spherical graphite powder should be investigated.

- The printability of complex designs such as scaffolds and organic structures should be tested upon identification of the optimal printing profiles.
- The mechanical performance of the printed samples should be investigated.
- In vitro and vivo biological tests should be conducted in order to assess the biological performance of the printed samples.

References

[1] C. Softas, “Selective Laser Sintering of Hydroxyapatite-Based Materials for Tissue Engineering,” in *Additive Manufacturing in Biomedical Applications*, vol. 23, ASM International, 2022, pp. 92–105.

[2] R. Mala and A. S. Ruby Celsia, *Bioceramics in orthopaedics: A review*. Elsevier Ltd., 2018.

[3] R. Heimann, “Materials science of crystalline bioceramics: a review of basic properties and applications,” *Chiang Mai Univ. J.*, vol. 1, pp. 23–46, 2002.

[4] A. S. Brydone, D. Meek, and S. MacLaine, “Bone grafting, orthopaedic biomaterials, and the clinical need for bone engineering,” *Proc. Inst. Mech. Eng. Part H J. Eng. Med.*, vol. 224, no. 12, pp. 1329–1343, 2010, doi: 10.1243/09544119JEIM770.

[5] A. Tufail, F. Schmidt, and M. Maqbool, “Three-dimensional printing of hydroxyapatite,” in *Handbook of Ionic Substituted Hydroxyapatites*, no. i, Elsevier, 2020, pp. 355–381.

[6] H. E. Jazayeri *et al.*, “The cross-disciplinary emergence of 3D printed bioceramic scaffolds in orthopedic bioengineering,” *Ceram. Int.*, vol. 44, no. 1, pp. 1–9, 2018, doi: 10.1016/j.ceramint.2017.09.095.

[7] H. Ma, C. Feng, J. Chang, and C. Wu, “3D-printed bioceramic scaffolds: From bone tissue engineering to tumor therapy,” *Acta Biomater.*, vol. 79, pp. 37–59, 2018, doi: 10.1016/j.actbio.2018.08.026.

[8] N. Eliaz and N. Metoki, “Calcium phosphate bioceramics: A review of their history, structure, properties, coating technologies and biomedical applications,” *Materials (Basel).*, vol. 10, no. 4, 2017, doi: 10.3390/ma10040334.

[9] P. Feng, M. Niu, C. Gao, S. Peng, and C. Shuai, “A novel two-step sintering for nano-hydroxyapatite scaffolds for bone tissue engineering,” *Sci. Rep.*, vol. 4, no. 1, p. 5599, May 2014, doi: 10.1038/srep05599.

[10] Y. Chen, W. Li, C. Zhang, Z. Wu, and J. Liu, “Recent Developments of Biomaterials for Additive Manufacturing of Bone Scaffolds,” *Adv. Healthc. Mater.*, vol. 9, no. 23, p. 2000724, Dec. 2020, doi: 10.1002/adhm.202000724.

[11] D. C. Tancred, B. A. O. McCormack, and A. J. Carr, “A quantitative study of the sintering and mechanical properties of hydroxyapatite/phosphate glass composites,” *Biomaterials*, vol. 19, no. 19, pp. 1735–1743, 1998, doi: 10.1016/S0142-9612(98)00082-9.

[12] J. C. Knowles, S. Talal, and J. D. Santos, “Sintering effects in a glass reinforced hydroxyapatite,” *Biomaterials*, vol. 17, no. 14, pp. 1437–1442, Jul. 1996, doi: 10.1016/0142-9612(96)87287-5.

[13] G. Georgiou and J. C. Knowles, “Glass reinforced hydroxyapatite for hard tissue surgery - Part 1: Mechanical properties,” *Biomaterials*, vol. 22, no. 20, pp. 2811–2815, 2001, doi: 10.1016/S0142-9612(01)00025-4.

[14] D. E. Abulyazied, A. M. Alturki, and R. A. Youness, “Synthesis , Structural and Biomedical Characterization of Hydroxyapatite / Borosilicate Bioactive Glass Nanocomposites,” *J. Inorg. Organomet. Polym. Mater.*, vol. 31, no. 10, pp. 4077–4092, 2021, doi: 10.1007/s10904-021-02070-6.

[15] D. S. Morais *et al.*, “Samarium doped glass-reinforced hydroxyapatite with enhanced osteoblastic performance and antibacterial properties for bone tissue regeneration,” *J. Mater. Chem. B*, vol. 2, no. 35, pp. 5872–5881, 2014, doi: 10.1039/c4tb00484a.

[16] J. Coelho *et al.*, “Development and Characterization of Lanthanides Doped Hydroxyapatite Composites for Bone Tissue Application,” in *Current Trends on Glass and Ceramic Materials*, no. May 2014, J. Coelho, S. H. Nandyala, P. S. Gomes, M. P. Garcia, M. A. Lopes, M. H. Fernandes, and J. D. Santos, Eds. BENTHAM SCIENCE PUBLISHERS, 2013, pp. 87–115.

[17] Y. Hu and X. Miao, “Comparison of hydroxyapatite ceramics and hydroxyapatite/borosilicate glass composites prepared by slip casting,” *Ceram. Int.*, vol. 30, no. 7, pp. 1787–1791, 2004, doi: 10.1016/j.ceramint.2003.12.119.

[18] K. Lin, R. Sheikh, S. Romanazzo, and I. Roohani, “3D printing of bioceramic scaffolds-barriers to the clinical translation: From promise to reality, and future perspectives,” *Materials (Basel).*, vol. 12, no. 7, 2019, doi: 10.3390/ma12172660.

[19] V. Karageorgiou and D. Kaplan, “Porosity of 3D biomaterial scaffolds and osteogenesis,” *Biomaterials*, vol. 26, no. 27, pp. 5474–5491, 2005, doi: 10.1016/j.biomaterials.2005.02.002.

[20] A. Mazzoli, “Selective laser sintering in biomedical engineering,” *Med. Biol. Eng. Comput.*, vol. 51, no. 3, pp. 245–256, 2013, doi: 10.1007/s11517-012-1001-x.

[21] Z. Chen *et al.*, “3D printing of ceramics: A review,” *J. Eur. Ceram. Soc.*, vol. 39, no. 4, pp. 661–687, Apr. 2019, doi: 10.1016/j.jeurceramsoc.2018.11.013.

[22] A. Kumar, S. Kargozar, F. Baino, and S. S. Han, “Additive Manufacturing Methods for Producing Hydroxyapatite and Hydroxyapatite-Based Composite Scaffolds: A Review,” *Front. Mater.*, vol. 6, no. December, pp. 1–20, 2019, doi: 10.3389/fmats.2019.00313.

[23] R. D. Goodridge, K. W. Dalgarno, and D. J. Wood, “Indirect selective laser sintering of an apatite-mullite glass-ceramic for potential use in bone replacement applications,” *Proc. Inst. Mech. Eng. Part H J. Eng. Med.*, vol. 220, no. 1, pp. 57–68, 2006, doi: 10.1243/095441105X69051.

[24] J. C. Lorrison, R. D. Goodridge, K. W. Dalgarno, and D. J. Wood, “Selective Laser Sintering of Bioactive Glass-Ceramics,” *Proc. 13th Annu. Int. Solid Free. Fabr. Symp.*, no. January, pp. 1–8, 2002, doi: http://dx.doi.org/10.26153/tsw/3409.

[25] J. C. Lorrison, K. W. Dalgarno, and D. J. Wood, “Processing of an apatite-mullite glass-ceramic and an hydroxyapatite/ phosphate glass composite by selective laser sintering,” *J. Mater. Sci. Mater. Med.*, vol. 16, no. 8, pp. 775–781, 2005, doi: 10.1007/s10856-005-2616-3.

[26] L. Gremillard and S. Tadier, “Materials for hard tissue applications: An overview,” *Adv. Ceram. Biomater. Mater. Devices Challenges First Ed.*, pp. 3–20, 2017, doi: 10.1016/B978-0-08-100881-2.00001-4.

[27] L. L. Hench, “Bioceramics: From Concept to Clinic,” *J. Am. Ceram. Soc.*, vol. 74, no. 7, pp. 1487–1510, 1991, doi: 10.1111/j.1151-2916.1991.tb07132.x.

[28] J. Massera, “Bioactive glass-ceramics: From macro to nano,” in *Nanostructured Biomaterials for Regenerative Medicine*, Elsevier, 2020, pp. 275–292.

[29] J. Huang, X. Li, and Z. X. Guo, “Biomechanical and biochemical compatibility in innovative biomaterials,” *Biocompat. Perform. Med. Devices*, pp. 23–46, 2020, doi: 10.1016/b978-0-08-102643-4.00004-5.

[30] M. Arango-Ospina and A. R. Boccaccini, “Bioactive glasses and ceramics for tissue engineering,” in *Tissue Engineering Using Ceramics and Polymers*, 3rd ed., Elsevier, 2022, pp. 111–178.

[31] G. Kaur *et al.*, “Mechanical properties of bioactive glasses, ceramics, glass-ceramics and

composites: State-of-the-art review and future challenges," *Mater. Sci. Eng. C*, vol. 104, p. 109895, Nov. 2019, doi: 10.1016/j.msec.2019.109895.

[32] M. Šupová, "Substituted hydroxyapatites for biomedical applications: A review," *Ceram. Int.*, vol. 41, no. 8, pp. 9203–9231, 2015, doi: 10.1016/j.ceramint.2015.03.316.

[33] J. An, J. E. M. Teoh, R. Suntornnond, and C. K. Chua, "Design and 3D Printing of Scaffolds and Tissues," *Engineering*, vol. 1, no. 2, pp. 261–268, 2015, doi: 10.15302/J-ENG-2015061.

[34] A. Bandyopadhyay, S. Bose, and S. Das, "3D printing of biomaterials," *MRS Bull.*, vol. 40, no. 2, pp. 108–115, Feb. 2015, doi: 10.1557/mrs.2015.3.

[35] M. Vaezi and S. Yang, "Freeform fabrication of nanobiomaterials using 3D printing," in *Rapid Prototyping of Biomaterials*, Elsevier, 2014, pp. 16–74.

[36] R. H. Doremus, "Bioceramics," *J. Mater. Sci.*, vol. 27, no. 2, pp. 285–297, 1992, doi: 10.1007/BF00543915.

[37] J. Crush, A. Hussain, K. T. M. Seah, and W. S. Khan, "Bioactive Glass: Methods for Assessing Angiogenesis and Osteogenesis," *Front. Cell Dev. Biol.*, vol. 9, no. June, pp. 1–10, Jun. 2021, doi: 10.3389/fcell.2021.643781.

[38] L. L. Hench and E. Fielder, "Biological Gel-Glasses," in *Sol-Gel Technologies for Glass Producers and Users*, M. A. Aegerter and M. Mennig, Eds. Boston, MA: Springer US, 2004, pp. 153–156.

[39] S. V Dorozhkin, "Calcium Orthophosphates in Nature, Biology and Medicine," pp. 399–498, 2009, doi: 10.3390/ma2020399.

[40] J. E. Shelby, *Introduction to Glass Science and Technology*. Cambridge, UNITED KINGDOM: The Royal Society of Chemistry, 2005.

[41] A. K. Varshneya and J. C. Mauro, *Fundamentals of Inorganic Glasses*. San Diego, UNITED STATES: Elsevier, 2019.

[42] American Society for Testing and Materials (ASTM), "Standard Terminology of Glass and Glass Products," in *Book of Standards Volume: 15.02*, vol. 05, no. Reapproved, 2015.

[43] W. Bragg, "THE GLASSY STATE," in *Structural Chemistry of Glasses*, K. J. Rao, Ed. Elsevier, 2002, pp. 13–76.

[44] W. H. Zachariasen, "THE ATOMIC ARRANGEMENT IN GLASS," *J. Am. Chem. Soc.*, vol. 54, no. 10, pp. 3841–3851, Oct. 1932, doi: 10.1021/ja01349a006.

[45] T. Izumitani, *Optical glass*. New York: American Institute of Physics, 1986.

[46] F. Baino, "Bioactive glasses – When glass science and technology meet regenerative medicine," *Ceram. Int.*, vol. 44, no. 13, pp. 14953–14966, 2018, doi: 10.1016/j.ceramint.2018.05.180.

[47] D. Bellucci, A. Sola, and V. Cannillo, "Hydroxyapatite and tricalcium phosphate composites with bioactive glass as second phase: State of the art and current applications," *J. Biomed. Mater. Res. - Part A*, vol. 104, no. 4, pp. 1030–1056, 2016, doi: 10.1002/jbm.a.35619.

[48] D. Ege, K. Zheng, and A. R. Boccaccini, "Borate Bioactive Glasses (BBG): Bone Regeneration, Wound Healing Applications, and Future Directions," *ACS Appl. Bio Mater.*, vol. 5, no. 8, pp. 3608–3622, 2022, doi: 10.1021/acsabm.2c00384.

[49] H. Scholze, *Glass : Nature, Structure, and Properties*. New York, NY, UNITED STATES: Springer, 1991.

[50] E. Le Bourhis, *Glass: Mechanics and Technology: Second Edition*. Wiley, 2014.

[51] D. P. Birnie and M. D. Dyar, "Cooling rate calculations for silicate glasses," *J. Geophys. Res. Solid Earth*, vol. 91, no. B4, pp. 509–513, Mar. 1986, doi: 10.1029/JB091iB04p0D509.

[52] L. L. Hench, "The story of Bioglass®," *J. Mater. Sci. Mater. Med.*, vol. 17, no. 11, pp. 967–978, 2006, doi: 10.1007/s10856-006-0432-z.

[53] J. R. Jones, "Reprint of: Review of bioactive glass: From Hench to hybrids," *Acta Biomater.*, vol. 23, no. S, pp. S53–S82, 2015, doi: 10.1016/j.actbio.2015.07.019.

[54] T. Kasuga, "Unique Nature of Phosphate and Borate Bioactive Glasses," in *Phosphate and Borate Bioactive Glasses*, no. 11, The Royal Society of Chemistry, 2022, pp. 1–9.

[55] M. T. Islam, L. Macri-Pellizzeri, V. Sottile, and I. Ahmed, "Rapid conversion of highly porous borate glass microspheres into hydroxyapatite," *Biomater. Sci.*, vol. 9, no. 5, pp. 1826–1844, 2021, doi: 10.1039/d0bm01776k.

[56] V. Stanić, "Boron-Containing Bioactive Glasses for Bone Regeneration," in *Biomedical, Therapeutic and Clinical Applications of Bioactive Glasses*, Elsevier, 2019, pp. 219–249.

[57] M. Fabert *et al.*, "Crystallization and sintering of borosilicate bioactive glasses for application in tissue engineering," *J. Mater. Chem. B*, vol. 5, no. 23, pp. 4514–4525, 2017, doi: 10.1039/c7tb00106a.

[58] H. Fu *et al.*, "In vitro evaluation of borate-based bioactive glass scaffolds prepared by a polymer foam replication method," *Mater. Sci. Eng. C*, vol. 29, no. 7, pp. 2275–2281, Aug. 2009, doi: 10.1016/j.msec.2009.05.013.

[59] X. Liu *et al.*, "Bioactive borosilicate glass scaffolds: in vitro degradation and bioactivity behaviors," *J. Mater. Sci. Mater. Med.*, vol. 20, no. 6, pp. 1237–1243, Jun. 2009, doi: 10.1007/s10856-009-3691-7.

[60] U. Pantulap, M. Arango-Ospina, and A. R. Boccaccini, "Bioactive glasses incorporating less-common ions to improve biological and physical properties," *J. Mater. Sci. Mater. Med.*, vol. 33, no. 1, 2022, doi: 10.1007/s10856-021-06626-3.

[61] P. Balasubramanian, T. Büttner, V. Miguez Pacheco, and A. R. Boccaccini, "Boron-containing bioactive glasses in bone and soft tissue engineering," *J. Eur. Ceram. Soc.*, vol. 38, no. 3, pp. 855–869, 2018, doi: 10.1016/j.jeurceramsoc.2017.11.001.

[62] F. Westhauser *et al.*, "Selective and caspase-independent cytotoxicity of bioactive glasses towards giant cell tumor of bone derived neoplastic stromal cells but not to bone marrow derived stromal cells," *Biomaterials*, vol. 275, no. March, 2021, doi: 10.1016/j.biomaterials.2021.120977.

[63] E. O'Neill, G. Awale, L. Daneshmandi, O. Umerah, and K. W. H. Lo, "The roles of ions on bone regeneration," *Drug Discov. Today*, vol. 23, no. 4, pp. 879–890, 2018, doi: 10.1016/j.drudis.2018.01.049.

[64] S. Naseri, W. C. Lepry, and S. N. Nazhat, "Bioactive glasses in wound healing: Hope or hype?," *J. Mater. Chem. B*, vol. 5, no. 31, pp. 6167–6174, 2017, doi: 10.1039/c7tb01221g.

[65] S. D. Conzone and D. E. Day, "Preparation and properties of porous microspheres made from borate glass," *J. Biomed. Mater. Res. - Part A*, vol. 88, no. 2, pp. 531–542, 2009, doi: 10.1002/jbm.a.31883.

[66] L. Pătcaş, E. Vanea, M. Tămăşan, D. Eniu, and V. Simon, "Nanostructural changes induced by

thermal treatment of calcium-silicate glasses containing dysprosium and iron," *Optoelectron. Adv. Mater. Rapid Commun.*, vol. 8, no. 9–10, pp. 989–992, 2014.

[67] S. Huang, X. Kang, Z. Cheng, P. Ma, Y. Jia, and J. Lin, "Electrospinning preparation and drug delivery properties of Eu3+/Tb3+ doped mesoporous bioactive glass nanofibers," *J. Colloid Interface Sci.*, vol. 387, no. 1, pp. 285–291, 2012, doi: 10.1016/j.jcis.2012.08.004.

[68] M. Shi *et al.*, "Europium-doped mesoporous silica nanosphere as an immune-modulating osteogenesis/angiogenesis agent," *Biomaterials*, vol. 144, pp. 176–187, 2017, doi: 10.1016/j.biomaterials.2017.08.027.

[69] Y. Fan, P. Yang, S. Huang, J. Jiang, H. Lian, and J. Lin, "Luminescent and mesoporous europium-doped bioactive glasses (MBG) as a drug carrier," *J. Phys. Chem. C*, vol. 113, no. 18, pp. 7826–7830, 2009, doi: 10.1021/jp900515x.

[70] Y. Zhang, M. Hu, X. Wang, Z. Zhou, and Y. Liu, "Design and evaluation of europium containing mesoporous bioactive glass nanospheres: Doxorubicin release kinetics and inhibitory effect on osteosarcoma MG 63 cells," *Nanomaterials*, vol. 8, no. 11, 2018, doi: 10.3390/nano8110961.

[71] Y. Xue *et al.*, "Monodisperse photoluminescent and highly biocompatible bioactive glass nanoparticles for controlled drug delivery and cell imaging," *J. Mater. Chem. B*, vol. 3, no. 18, pp. 3831–3839, 2015, doi: 10.1039/c5tb00204d.

[72] T. Zambanini *et al.*, "Dissolution, bioactivity behavior, and cytotoxicity of rare earth-containing bioactive glasses (RE = Gd, Yb)," *Int. J. Appl. Ceram. Technol.*, vol. 16, no. 5, pp. 2028–2039, 2019, doi: 10.1111/ijac.13317.

[73] F. Liao, X. Y. Peng, F. Yang, Q. F. Ke, Z. H. Zhu, and Y. P. Guo, "Gadolinium-doped mesoporous calcium silicate/chitosan scaffolds enhanced bone regeneration ability," *Mater. Sci. Eng. C*, vol. 104, no. July, p. 109999, 2019, doi: 10.1016/j.msec.2019.109999.

[74] D. Y. Zhu *et al.*, "Gadolinium-doped bioglass scaffolds promote osteogenic differentiation of hBMSC via the Akt/GSK3β pathway and facilitate bone repair in vivo," *Int. J. Nanomedicine*, vol. 14, pp. 1085–1100, 2019, doi: 10.2147/IJN.S193576.

[75] R. Borges, J. F. Schneider, and J. Marchi, "Structural characterization of bioactive glasses containing rare earth elements (Gd and/or Yb)," *J. Mater. Sci.*, vol. 54, no. 17, pp. 11390–11399, 2019, doi: 10.1007/s10853-019-03715-1.

[76] K. Halubek-Gluchowska, D. Szymański, T. N. L. Tran, M. Ferrari, and A. Lukowiak, "Upconversion luminescence of silica–calcia nanoparticles co-doped with tm3+ and yb3+ ions," *Materials (Basel).*, vol. 14, no. 4, pp. 1–19, 2021, doi: 10.3390/ma14040937.

[77] G. P. Delpino *et al.*, "Sol-gel-derived 58S bioactive glass containing holmium aiming brachytherapy applications: A dissolution, bioactivity, and cytotoxicity study," *Mater. Sci. Eng. C*, vol. 119, no. June 2020, p. 111595, 2021, doi: 10.1016/j.msec.2020.111595.

[78] T. Zambanini *et al.*, "Holmium-containing bioactive glasses dispersed in poloxamer 407 hydrogel as a theragenerative composite for bone cancer treatment," *Materials (Basel).*, vol. 14, no. 6, 2021, doi: 10.3390/ma14061459.

[79] B. A. E. Ben-Arfa, S. Neto, I. M. Miranda Salvado, R. C. Pullar, and J. M. F. Ferreira, "Robocasting of Cu2+ & La3+ doped sol–gel glass scaffolds with greatly enhanced mechanical properties: Compressive strength up to 14 MPa," *Acta Biomater.*, vol. 87, pp. 265–272, 2019, doi: 10.1016/j.actbio.2019.01.048.

[80] B. A. E. Ben-Arfa, I. E. Palamá, I. M. Miranda Salvado, J. M. F. Ferreira, and R. C. Pullar,

"Cytotoxicity and bioactivity assessments for Cu2+ and La3+ doped high-silica sol-gel derived bioglasses: The complex interplay between additive ions revealed," *J. Biomed. Mater. Res. - Part A*, vol. 107, no. 12, pp. 2680–2693, 2019, doi: 10.1002/jbm.a.36772.

[81] E. El-Meliegy, M. M. Farag, A. M. El-Kady, M. S. Mohamed, H. K. Abdelhakim, and M. Moaness, "Evaluation of solubility and cytotoxicity of lanthanum-doped phosphate glasses nanoparticles for drug delivery applications," *J. Non. Cryst. Solids*, vol. 475, no. September, pp. 59–70, 2017, doi: 10.1016/j.jnoncrysol.2017.08.034.

[82] H. Jodati, B. Güner, Z. Evis, D. Keskin, and A. Tezcaner, "Synthesis and characterization of magnesium-lanthanum dual doped bioactive glasses," *Ceram. Int.*, vol. 46, no. 8, pp. 10503–10511, 2020, doi: 10.1016/j.ceramint.2020.01.050.

[83] R. A. Youness, M. A. Taha, M. Ibrahim, and A. El-Kheshen, "FTIR Spectral Characterization, Mechanical Properties and Antimicrobial Properties of La-Doped Phosphate-Based Bioactive Glasses," *Silicon*, vol. 10, no. 3, pp. 1151–1159, May 2018, doi: 10.1007/s12633-017-9587-0.

[84] M. Ershad, V. K. Vyas, S. Prasad, A. Ali, and R. Pyare, "Effect of Sm2O3 substitution on mechanical and biological properties of 45S5 bioactive glass," *J. Aust. Ceram. Soc.*, vol. 54, no. 4, pp. 621–630, 2018, doi: 10.1007/s41779-018-0190-7.

[85] A. Baranowska *et al.*, "Biological properties of rare-earth doped bioactive glass," in *Optical Fibers and Their Applications 2020*, 2020, vol. 11456, p. 1145604, doi: 10.1117/12.2566347.

[86] Y. Zhang, X. Wang, Y. Su, D. Chen, and W. Zhong, "A doxorubicin delivery system: Samarium/mesoporous bioactive glass/alginate composite microspheres," *Mater. Sci. Eng. C*, vol. 67, pp. 205–213, 2016, doi: 10.1016/j.msec.2016.05.019.

[87] A. Baranowska, J. R. Dąbrowski, M. Kochanowicz, and J. Dorosz, "Effect of biodegradation on spectroscopic properties of Sm3+ doped 45S5 bioglass," in *Photonics Applications in Astronomy, Communications, Industry, and High-Energy Physics Experiments 2018*, 2018, vol. 10808, p. 1080833, doi: 10.1117/12.2500274.

[88] X. Wang, Y. Zhang, C. Lin, and W. Zhong, "Sol-gel derived terbium-containing mesoporous bioactive glasses nanospheres: In vitro hydroxyapatite formation and drug delivery," *Colloids Surfaces B Biointerfaces*, vol. 160, pp. 406–415, 2017, doi: 10.1016/j.colsurfb.2017.09.051.

[89] A. M. Deliormanlı, B. Rahman, S. Oguzlar, and K. Ertekin, "Structural and luminescent properties of Er3+ and Tb3+-doped sol–gel-based bioactive glass powders and electrospun nanofibers," *J. Mater. Sci.*, vol. 56, no. 26, pp. 14487–14504, 2021, doi: 10.1007/s10853-021-06203-7.

[90] N. J. Thyparambil, L. C. Gutgesell, C. C. Hurley, L. E. Flowers, D. E. Day, and J. A. Semon, "Adult stem cell response to doped bioactive borate glass," *J. Mater. Sci. Mater. Med.*, vol. 31, no. 2, 2020, doi: 10.1007/s10856-019-6353-4.

[91] A. Arafat, S. A. Samad, J. J. Titman, A. L. Lewis, E. R. Barney, and I. Ahmed, "Yttrium doped phosphate-based glasses: Structural and degradation analyses," *Biomed. Glas.*, vol. 6, no. 1, pp. 34–49, 2020, doi: 10.1515/bglass-2020-0004.

[92] J. K. Christie, J. Malik, and A. Tilocca, "Bioactive glasses as potential radioisotope vectors for in situ cancer therapy: Investigating the structural effects of yttrium," *Phys. Chem. Chem. Phys.*, vol. 13, no. 39, pp. 17749–17755, 2011, doi: 10.1039/c1cp21764j.

[93] A. H. Tesfay *et al.*, "Control of dopant distribution in yttrium-doped bioactive glass for selective internal radiotherapy applications using spray pyrolysis," *Materials (Basel).*, vol. 12, no. 6, 2019, doi: 10.3390/ma12060986.

[94] R. Z. Legeros, “Biodegradation and Bioresorption of Calcium Phosphate Ceramics,” vol. 14, pp. 65–88, 1993, doi: 10.1016/0267-6605(93)90049-D.

[95] C. Shuai, P. Li, J. Liu, and S. Peng, “Optimization of TCP/HAP ratio for better properties of calcium phosphate scaffold via selective laser sintering,” *Mater. Charact.*, vol. 77, pp. 23–31, Mar. 2013, doi: 10.1016/j.matchar.2012.12.009.

[96] M. Alizadeh-Osgouei, Y. Li, and C. Wen, “A comprehensive review of biodegradable synthetic polymer-ceramic composites and their manufacture for biomedical applications,” *Bioact. Mater.*, vol. 4, no. 1, pp. 22–36, 2019, doi: 10.1016/j.bioactmat.2018.11.003.

[97] J. Li, B. Fartash, and L. Hermansson, “Hydroxyapatite—alumina composites and bone-bonding,” *Biomaterials*, vol. 16, no. 5, pp. 417–422, Jan. 1995, doi: 10.1016/0142-9612(95)98860-G.

[98] E. Champion, S. Gautier, and D. Bernache-Assollant, “Characterization of hot pressed Al2O3-platelet reinforced hydroxyapatite composites,” *J. Mater. Sci. Mater. Med.*, vol. 7, no. 2, pp. 125–130, Feb. 1996, doi: 10.1007/BF00058724.

[99] J. Li, L. Hermansson, and R. Soremark, “High-strength biofunctional zirconia: mechanical properties and static fatigue behaviour of zirconia-apatite composites,” *J. Mater. Sci. Mater. Med.*, vol. 4, no. 1, pp. 50–54, Jan. 1993, doi: 10.1007/BF00122977.

[100] M. Takagi, M. Mochida, N. Uchida, K. Saito, and K. Uematsu, “Filter cake forming and hot isostatic pressing for TZP-dispersed hydroxyapatite composite,” *J. Mater. Sci. Mater. Med.*, vol. 3, no. 3, pp. 199–203, May 1992, doi: 10.1007/BF00713450.

[101] J. D. Santos, J. C. Knowles, R. L. Reis, F. J. Monteiro, and G. W. Hastings, “Microstructural characterization of glass-reinforced hydroxyapatite composites,” *Biomaterials*, vol. 15, no. 1, pp. 5–10, Jan. 1994, doi: 10.1016/0142-9612(94)90188-0.

[102] F. N. Oktar and G. Göller, “Sintering effects on mechanical properties of glass-reinforced hydroxyapatite composites,” *Ceram. Int.*, vol. 28, no. 6, pp. 617–621, Jan. 2002, doi: 10.1016/S0272-8842(02)00017-2.

[103] M. A. Lopes, J. C. Knowles, and J. D. Santos, “Structural insights of glass-reinforced hydroxyapatite composites by Rietveld refinement,” *Biomaterials*, vol. 21, no. 18, pp. 1905–1910, 2000, doi: 10.1016/S0142-9612(00)00068-5.

[104] J. D. Santos, R. L. Reis, F. J. Monteiro, J. C. Knowles, and G. W. Hastings, “Liquid phase sintering of hydroxyapatite by phosphate and silicate glass additions: structure and properties of the composites,” *J. Mater. Sci. Mater. Med.*, vol. 6, no. 6, pp. 348–352, 1995, doi: 10.1007/BF00120303.

[105] J. C. Knowles and W. Bonfield, “Development of a glass reinforced hydroxyapatite with enhanced mechanical properties. The effect of glass composition on mechanical properties and its relationship to phase changes,” *J. Biomed. Mater. Res.*, vol. 27, no. 12, pp. 1591–1598, Dec. 1993, doi: 10.1002/jbm.820271217.

[106] M. A. Lopes, F. J. Monteiro, and J. D. Santos, “Glass-reinforced hydroxyapatite composites: Secondary phase proportions and densification effects on biaxial bending strength,” *J. Biomed. Mater. Res.*, vol. 48, no. 5, pp. 734–740, 1999, doi: 10.1002/(SICI)1097-4636(1999)48:5<734::AID-JBM20>3.0.CO;2-2.

[107] M. A. Lopes, F. J. Monteiro, and J. D. Santos, “Glass-reinforced hydroxyapatite composites: Fracture toughness and hardness dependence on microstructural characteristics,” *Biomaterials*, vol. 20, no. 21, pp. 2085–2090, 1999, doi: 10.1016/S0142-9612(99)00112-X.

[108] J. D. Santos, P. L. Silva, J. C. Knowles, S. Talal, and F. J. Monteiro, “Reinforcement of hydroxyapatite by adding P2O5-CaO glasses with Na2O, K2O and MgO,” *J. Mater. Sci. Mater. Med.*, vol. 7, no. 3, pp. 187–189, 1996, doi: 10.1007/BF00121259.

[109] M. A. Lopes, J. D. Santos, F. J. Monteiro, and J. C. Knowles, “Glass-reinforced hydroxyapatite: A comprehensive study of the effect of glass composition on the crystallography of the composite,” *J. Biomed. Mater. Res.*, vol. 39, no. 2, pp. 244–251, 1998, doi: 10.1002/(SICI)1097-4636(199802)39:2<244::AID-JBM11>3.0.CO;2-D.

[110] S. Kapoor and U. Batra, “Preparation and Bioactivity Evaluation of Bone like Hydroxyapatite - Bioglass Composite,” *Int. J. Mater. Metall. Eng.*, vol. 4, no. 1, pp. 37–41, 2010, [Online]. Available: https://publications.waset.org/2720/pdf.

[111] M. A. Lopes, F. J. Monteiro, J. D. Santos, A. P. Serro, and B. Saramago, “Hydrophobicity, surface tension, and zeta potential measurements of glass-reinforced hydroxyapatite composites,” *J. Biomed. Mater. Res.*, vol. 45, no. 4, pp. 370–375, Jun. 1999, doi: 10.1002/(SICI)1097-4636(19990615)45:4<370::AID-JBM12>3.0.CO;2-0.

[112] M. A. Lopes, R. F. Silva, F. J. Monteiro, and J. D. Santos, “Microstructural dependence of Young’s and shear moduli of P2O5 glass reinforced hydroxyapatite for biomedical applications,” *Biomaterials*, vol. 21, no. 7, pp. 749–754, 2000, doi: https://doi.org/10.1016/S0142-9612(99)00248-3.

[113] M. A. Lopes, J. C. Knowles, J. D. Santos, F. J. Monteiro, and I. Olsen, “Direct and indirect effects of P2O5 glass reinforced-hydroxyapatite composites on the growth and function of osteoblast-like cells,” *Biomaterials*, vol. 21, no. 11, pp. 1165–1172, 2000, doi: 10.1016/S0142-9612(00)00007-7.

[114] J. D. Santos, L. J. Jha, and F. J. Monteiro, “Surface modifications of glass-reinforced hydroxyapatite composites,” *Biomaterials*, vol. 16, no. 7, pp. 521–526, 1995, doi: 10.1016/0142-9612(95)91124-H.

[115] U. Batra and S. Kapoor, “Microstructural and In-Vitro Characterization of Glass-Reinforced Hydroxyapatite Composites,” *Int. J. Mater. Metall. Eng.*, vol. 4, no. 1, pp. 81–86, 2010, [Online]. Available: https://publications.waset.org/2747/pdf.

[116] A. C. Queiroz, J. D. Santos, R. Vilar, S. Eugénio, and F. J. Monteiro, “Laser surface modification of hydroxyapatite and glass-reinforced hydroxyapatite,” *Biomaterials*, vol. 25, no. 19, pp. 4607–4614, 2004, doi: 10.1016/j.biomaterials.2003.11.054.

[117] G. Georgiou, J. C. Knowles, J. E. Barralet, Y. M. Kong, and H. E. Kim, “The effect of hot pressing on the physical properties of glass reinforced hydroxyapatite,” *J. Mater. Sci. Mater. Med.*, vol. 15, no. 6, pp. 705–710, 2004, doi: 10.1023/B:JMSM.0000030213.70979.5e.

[118] G. Goller, H. Demirkiran, F. N. Oktar, and E. Demirkesen, “Processing and characterization of bioglass reinforced hydroxyapatite composites,” *Ceram. Int.*, vol. 29, no. 6, pp. 721–724, 2003, doi: 10.1016/S0272-8842(02)00223-7.

[119] D. Bellucci, V. Cannillo, and A. Sola, “A new highly bioactive composite for bone tissue repair,” *Int. J. Appl. Ceram. Technol.*, vol. 9, no. 3, pp. 455–467, 2012, doi: 10.1111/j.1744-7402.2011.02641.x.

[120] D. C. Tancred, A. J. Carr, and B. A. O. McCormack, “The sintering and mechanical behavior of hydroxyapatite with bioglass additions,” *J. Mater. Sci. Mater. Med.*, vol. 12, no. 1, pp. 81–93, 2001, doi: 10.1023/A:1026773522934.

[121] A. C. Silva, A. H. Aparecida, and F. J. C. Braga, “Dispersed hydroxyapatite bioglass 45S5

composites: Comparative evaluation of the use of bovine bone and synthetic hydroxyapatite," *Mater. Sci. Forum*, vol. 727–728, no. May 2015, pp. 1147–1152, 2012, doi: 10.4028/www.scientific.net/MSF.727-728.1147.

[122] D. Bellucci, A. Sola, V. Cannillo, and V. Vignolese, "Low Temperature Sintering of Innovative Bioactive Glasses," *J. Am. Ceram. Soc.*, vol. 95, pp. 1313–1319, 2012, doi: 10.1111/j.1551-2916.2012.05100.x.

[123] D. Bellucci, V. Cannillo, and A. Sola, "Calcium and potassium addition to facilitate the sintering of bioactive glasses," *Mater. Lett.*, vol. 65, no. 12, pp. 1825–1827, 2011, doi: 10.1016/j.matlet.2011.03.060.

[124] D. Bellucci, V. Cannillo, and A. Sola, "A new potassium-based bioactive glass : Sintering behaviour and possible applications for bioceramic scaffolds," *Ceram. Int.*, vol. 37, no. 1, pp. 145–157, 2011, doi: 10.1016/j.ceramint.2010.08.020.

[125] D. Bellucci, A. Sola, R. Salvatori, A. Anesi, L. Chiarini, and V. Cannillo, "Sol – gel derived bioactive glasses with low tendency to crystallize : Synthesis , post-sintering bioactivity and possible application for the production of porous scaffolds," *Mater. Sci. Eng. C*, vol. 43, pp. 573–586, 2014, doi: 10.1016/j.msec.2014.07.037.

[126] D. Bellucci, A. Sola, M. Gazzarri, F. Chiellini, and V. Cannillo, "A new hydroxyapatite-based biocomposite for bone replacement," *Mater. Sci. Eng. C*, vol. 33, no. 3, pp. 1091–1101, 2013, doi: 10.1016/j.msec.2012.11.038.

[127] D. Bellucci, A. Anesi, R. Salvatori, L. Chiarini, and V. Cannillo, "A comparative in vivo evaluation of bioactive glasses and bioactive glass-based composites for bone tissue repair," *Mater. Sci. Eng. C*, vol. 79, pp. 286–295, 2017, doi: 10.1016/j.msec.2017.05.062.

[128] D. Bellucci, A. Sola, and V. Cannillo, "Bioactive glass-based composites for the production of dense sintered bodies and porous scaffolds," *Mater. Sci. Eng. C*, vol. 33, no. 4, pp. 2138–2151, 2013, doi: 10.1016/j.msec.2013.01.029.

[129] A. Saranti, I. Koutselas, and M. A. Karakassides, "Bioactive glasses in the system CaO-B2O3-P2O5: Preparation, structural study and in vitro evaluation," *J. Non. Cryst. Solids*, vol. 352, no. 5, pp. 390–398, 2006, doi: 10.1016/j.jnoncrysol.2006.01.042.

[130] L. A. Ivanchenko, "Sintering of different hydroxyapatite powders and low-melting sodium borosilicate glass," *Powder Metall. Met. Ceram.*, vol. 51, no. 3–4, pp. 165–171, 2012, doi: 10.1007/s11106-012-9412-7.

[131] L. A. Ivanchenko, T. I. Fal'kovskaya, N. D. Pinchuk, O. V. Lavrent'eva, and I. A. Lagunova, "Preparation and properties of hydroxyapatite strengthened with a glass phase," *Powder Metall. Met. Ceram.*, vol. 42, no. 1, pp. 54–59, 2003, doi: 10.1023/A:1023947216937.

[132] V. V. Skorokhod *et al.*, "Porosity and bioactivity of hydroxyapatite-glass composites," *Funct. Mater.*, vol. 13, no. 2, pp. 260–264, 2006.

[133] O. Vasylkiv *et al.*, "Morphology and properties of new porous biocomposites based on biogenic hydroxyapatite and synthetic calcium phosphates," *Funct. Mater.*, vol. 14, no. 4, pp. 430–435, Apr. 2007.

[134] O. Gunduz, Z. Ahmad, N. Ekren, S. Agathopoulos, S. Salman, and F. Oktar, "Reinforcing of Biologically Derived Apatite with Commercial Inert Glass," *J. Thermoplast. Compos. Mater.*, vol. 22, no. 4, pp. 407–419, 2009, doi: 10.1177/0892705709105974.

[135] N. Demirkol, F. Oktar, and E. Kayali, "Influence of Commercial Inert Glass Addition on the

Mechanical Properties of Commercial Synthetic Hydroxyapatite," *Acta Phys. Pol. Ser. a*, vol. 123, no. 2, pp. 427–429, 2013, doi: 10.12693/APhysPolA.123.427.

[136] R. A. Youness, M. A. Taha, A. A. El-kheshen, and M. Ibrahim, "Influence of the addition of carbonated hydroxyapatite and selenium dioxide on mechanical properties and in vitro bioactivity of borosilicate inert glass," *Ceram. Int.*, vol. 44, no. 17, pp. 20677–20685, 2018, doi: 10.1016/j.ceramint.2018.08.061.

[137] A. M. Alturki, D. E. Abulyazied, M. A. Taha, and H. M. A. Rasha, "A Study to Evaluate the Bioactivity Behavior and Electrical Properties of Hydroxyapatite/Ag2O - Borosilicate Glass Nanocomposites for Biomedical Applications," *J. Inorg. Organomet. Polym. Mater.*, vol. 32, no. 1, pp. 169–179, 2022, doi: 10.1007/s10904-021-02100-3.

[138] S. J. Kalita, S. Bose, H. L. Hosick, and A. Bandyopadhyay, "CaO–P2O5–Na2O-based sintering additives for hydroxyapatite (HAp) ceramics," *Biomaterials*, vol. 25, no. 12, pp. 2331–2339, May 2004, doi: 10.1016/j.biomaterials.2003.09.012.

[139] H. Demirkiran, A. Mohandas, M. Dohi, A. Fuentes, K. Nguyen, and P. Aswath, "Bioactivity and mineralization of hydroxyapatite with bioglass as sintering aid and bioceramics with Na3Ca6(PO4)5 and Ca5(PO4)2SiO4 in a silicate matrix," *Mater. Sci. Eng. C*, vol. 30, no. 2, pp. 263–272, 2010, doi: 10.1016/j.msec.2009.10.011.

[140] E. J. Lee, H. E. Kim, and H. W. Kim, "Production of hydroxyapatite/bioactive glass biomedical composites by the hot-pressing technique," *J. Am. Ceram. Soc.*, vol. 89, no. 11, pp. 3593–3596, 2006, doi: 10.1111/j.1551-2916.2006.01276.x.

[141] Z. Yazdanpanah, M. E. Bahrololoom, and B. Hashemi, "Evaluating morphology and mechanical properties of glass-reinforced natural hydroxyapatite composites," *J. Mech. Behav. Biomed. Mater.*, vol. 41, pp. 36–42, 2015, doi: 10.1016/j.jmbbm.2014.09.021.

[142] T. Kokubo, "Bioactive glass ceramics: properties and applications," *Biomaterials*, vol. 12, no. 2, pp. 155–163, Mar. 1991, doi: 10.1016/0142-9612(91)90194-F.

[143] T. Kokubo and H. Takadama, "How useful is SBF in predicting in vivo bone bioactivity?," *Biomaterials*, vol. 27, pp. 2907–2915, 2006, doi: 10.1016/j.biomaterials.2006.01.017.

[144] M. Bohner and J. Lemaitre, "Biomaterials Can bioactivity be tested in vitro with SBF solution?," *Biomaterials*, vol. 30, no. 12, pp. 2175–2179, 2009, doi: 10.1016/j.biomaterials.2009.01.008.

[145] S. Kotani *et al.*, "Bone bonding mechanism of beta-tricalcium phosphate," *J. Biomed. Mater. Res.*, vol. 25, no. 10, pp. 1303–1315, Oct. 1991, doi: 10.1002/jbm.820251010.

[146] R. Xin, Y. Leng, J. Chen, and Q. Zhang, "A comparative study of calcium phosphate formation on bioceramics in vitro and in vivo," vol. 26, pp. 6477–6486, 2005, doi: 10.1016/j.biomaterials.2005.04.028.

[147] K. Anselme, "Osteoblast adhesion on biomaterials," *Biomaterials*, vol. 21, no. 7, pp. 667–681, Apr. 2000, doi: 10.1016/S0142-9612(99)00242-2.

[148] C. J. Wilson, R. E. Clegg, D. I. Leavesley, and M. Pearcy, "Mediation of Biomaterial – Cell Interactions by Adsorbed Proteins: A Review," no. June 2014, 2005, doi: 10.1089/ten.2005.11.1.

[149] M. A. Lopes, J. C. Knowles, L. Kuru, J. D. Santos, F. J. Monteiro, and I. Olsen, "Flow cytometry for assessing biocompatibility," in *Journal of Biomedical Materials Research*, 1998, vol. 41, no. 4, pp. 649–656, doi: 10.1002/(SICI)1097-4636(19980915)41:4<649::AID-JBM17>3.0.CO;2-9.

[150] V. Salih, G. Georgiou, J. C. Knowles, and I. Olsen, “Glass reinforced hydroxyapatite for hard tissue surgery - Part II: In vitro evaluation of bone cell growth and function,” *Biomaterials*, vol. 22, no. 20, pp. 2817–2824, 2001, doi: 10.1016/S0142-9612(01)00026-6.

[151] M. . Ferraz, J. . Knowles, I. Olsen, F. . Monteiro, and J. . Santos, “Flow cytometry analysis of the effects of pre-immersion on the biocompatibility of glass-reinforced hydroxyapatite plasma-sprayed coatings,” *Biomaterials*, vol. 21, no. 8, pp. 813–820, Apr. 2000, doi: 10.1016/S0142-9612(99)00249-5.

[152] M. P. Ferraz, M. H. Fernandes, A. Trigo Cabral, J. D. Santos, and F. J. Monteiro, “In vitro growth and differentiation of osteoblast-like human bone marrow cells on glass reinforced hydroxyapatite plasma-sprayed coatings,” *J. Mater. Sci. Mater. Med.*, vol. 10, no. 9, pp. 567–576, 1999, doi: 10.1023/A:1008924516146.

[153] M. P. Ferraz, J. C. Knowles, I. Olsen, F. J. Monteiro, and J. D. Santos, “Flow cytometry analysis of effects of glass on response of osteosarcoma cells to plasma-sprayed hydroxyapatite/CaO-P2O5 coatings,” *J. Biomed. Mater. Res.*, vol. 47, no. 4, pp. 603–611, Dec. 1999, doi: 10.1002/(SICI)1097-4636(19991215)47:4<603::AID-JBM18>3.0.CO;2-6.

[154] J. D. Santos, M. Vasconcelos, R. L. Reis, A. Afonso, F. J. Monteiro, and G. W. Hastings, “Glass Reinforced Hydroxyapatite Composites: Physical Properties and Preliminary Histological Studies in Rabbits,” in *Bioceramics*, Ö. H. Andersson, R.-P. Happonen, and A. Yli-Urpo, Eds. Oxford: Elsevier, 1994, pp. 243–248.

[155] Y. Du *et al.*, “Selective laser sintering scaffold with hierarchical architecture and gradient composition for osteochondral repair in rabbits,” *Biomaterials*, vol. 137, pp. 37–48, 2017, doi: 10.1016/j.biomaterials.2017.05.021.

[156] A. Afonso, J. D. Santos, M. Vasconcelos, R. Branco, and J. Cavalheiro, “Granules of osteopatite and glass-reinforced hydroxyapatite implanted in rabbit tibiae,” *J. Mater. Sci. Mater. Med.*, vol. 7, no. 8, pp. 507–510, 1996, doi: 10.1007/BF00705433.

[157] M. A. Lopes *et al.*, “Push-out testing and histological evaluation of glass reinforced hydroxyapatite composites implanted in the tibia of rabbits,” *J. Biomed. Mater. Res.*, vol. 54, no. 4, pp. 463–469, 2001, doi: 10.1002/1097-4636(20010315)54:4<463::AID-JBM10>3.0.CO;2-Y.

[158] J. Santos, G. W. Hastings, and J. Knowles, “Sintered hydroxyapatite compositions and method for the preparation thereof,” WO 00/068164, 1999.

[159] M. H. Fernandes, R. Caram, N. Sooraj Hussain, A. C. Mauricio, and J. D. Santos, “Bonelike® Graft for Regenerative Bone Applications,” in *Surgical Tools and Medical Devices*, W. Ahmed and M. J. Jackson, Eds. Cham: Springer International Publishing, 2016, pp. 409–437.

[160] L. M. Atayde, P. P. Cortez, A. Afonso, M. Santos, A. C. Maurício, and J. D. Santos, “Morphology effect of bioglass-reinforced hydroxyapatite (Bonelike ®) on osteoregeneration,” *J. Biomed. Mater. Res. Part B Appl. Biomater.*, vol. 103, no. 2, pp. 292–304, Feb. 2015, doi: 10.1002/jbm.b.33195.

[161] J. V. Lobato *et al.*, “Assessment of Bonelike® graft with a resorbable matrix using an animal model,” *Thin Solid Films*, vol. 515, no. 1, pp. 362–367, Sep. 2006, doi: 10.1016/j.tsf.2005.12.153.

[162] I. D. Xynos, A. J. Edgar, L. D. K. Buttery, L. L. Hench, and J. M. Polak, “Gene-expression profiling of human osteoblasts following treatment with the ionic products of Bioglass® 45S5 dissolution,” *J. Biomed. Mater. Res.*, vol. 55, no. 2, pp. 151–157, May 2001, doi:

10.1002/1097-4636(200105)55:2<151::AID-JBM1001>3.0.CO;2-D.

[163] I. D. Xynos, A. J. Edgar, L. D. K. Buttery, L. L. Hench, and J. M. Polak, “Ionic Products of Bioactive Glass Dissolution Increase Proliferation of Human Osteoblasts and Induce Insulin-like Growth Factor II mRNA Expression and Protein Synthesis,” vol. 465, pp. 461–465, 2000, doi: 10.1006/bbrc.2000.3503.

[164] G. J. M. M. Stevens, “Gene activation by bioactive glasses,” no. October 2005, pp. 997–1002, 2006, doi: 10.1007/s10856-006-0435-9.

[165] P. Valerio, M. M. Pereira, A. M. Goes, and M. F. Leite, “The effect of ionic products from bioactive glass dissolution on osteoblast proliferation and collagen production,” vol. 25, pp. 2941–2948, 2004, doi: 10.1016/j.biomaterials.2003.09.086.

[166] L. L. Hench, “Genetic design of bioactive glass,” vol. 29, pp. 1257–1265, 2009, doi: 10.1016/j.jeurceramsoc.2008.08.002.

[167] I. Allan, H. Newman, and M. Wilson, “Antibacterial activity of particulate Bioglass® against supra- and subgingival bacteria,” *Biomaterials*, vol. 22, no. 12, pp. 1683–1687, Jun. 2001, doi: 10.1016/S0142-9612(00)00330-6.

[168] I. Allan, M. Wilson, and H. Newman, “Particulate Bioglass ® reduces the viability of bacterial biofilms formed on its surface in an in vitro model,” *Clin. Oral Implants Res.*, vol. 13, no. 1, pp. 53–58, Feb. 2002, doi: 10.1034/j.1600-0501.2002.130106.x.

[169] A. Leu, S. M. Stieger, P. Dayton, K. W. Ferrara, and J. K. Leach, “Angiogenic Response to Bioactive Glass Promotes Bone Healing in an Irradiated Calvarial Defect,” *Tissue Eng. Part A*, vol. 15, no. 4, pp. 877–885, Apr. 2009, doi: 10.1089/ten.tea.2008.0018.

[170] A. A. Gorustovich, J. A. Roether, and A. R. Boccaccini, “Effect of Bioactive Glasses on Angiogenesis: A Review of In Vitro and In Vivo Evidences,” *Tissue Eng. Part B Rev.*, vol. 16, no. 2, pp. 199–207, 2010, doi: 10.1089/ten.teb.2009.0416.

[171] R. M. Day, “Bioactive Glass Stimulates the Secretion of Angiogenic Growth Factors and Angiogenesis in Vitro,” *Tissue Eng.*, vol. 11, no. 5–6, pp. 768–777, 2005, doi: 10.1089/ten.2005.11.768.

[172] H. Demirkiran, Y. Hu, L. Zuin, N. Appathurai, and P. B. Aswath, “XANES analysis of calcium and sodium phosphates and silicates and hydroxyapatite – Bioglass ® 45S5 co-sintered bioceramics,” *Mater. Sci. Eng. C*, vol. 31, no. 2, pp. 134–143, 2011, doi: 10.1016/j.msec.2010.08.009.

[173] X. Chatzistavrou, K. Chrissafis, E. Kontonasaki, T. Zorba, P. Koidis, and K. M. Paraskevopoulos, “Sintered Hydroxyapatite / Bioactive Glass Composites: Thermal Analysis and Bioactivity,” in *Bioceramics 18*, 2006, vol. 309, pp. 167–170, doi: 10.4028/www.scientific.net/KEM.309-311.167.

[174] S. Padilla, J. Román, S. Sánchez-Salcedo, and M. Vallet-Regí, “Hydroxyapatite/SiO2–CaO–P2O5 glass materials: In vitro bioactivity and biocompatibility,” *Acta Biomater.*, vol. 2, no. 3, pp. 331–342, 2006, doi: https://doi.org/10.1016/j.actbio.2006.01.006.

[175] S. Padilla, S. Sánchez-Salcedo, and M. Vallet-Regí, “Bioactive and biocompatible pieces of HA/sol-gel glass mixtures obtained by the gel-casting method,” *J. Biomed. Mater. Res. Part A*, vol. 75A, no. 1, pp. 63–72, Oct. 2005, doi: 10.1002/jbm.a.30405.

[176] M. Vallet-Regí, A. Rámila, S. Padilla, and B. Muñoz, “Bioactive glasses as accelerators of apatite bioactivity,” *J. Biomed. Mater. Res. Part A*, vol. 66A, no. 3, pp. 580–585, Sep. 2003, doi:

10.1002/jbm.a.10576.

[177] A. Rámila, S. Padilla, B. Muñoz, and M. Vallet-Regí, “A New Hydroxyapatite/Glass Biphasic Material: In Vitro Bioactivity,” *Chem. Mater.*, vol. 14, no. 6, pp. 2439–2443, Jun. 2002, doi: 10.1021/cm011165p.

[178] C. V Ragel, M. Vallet-Regí, and L. M. Rodríguez-Lorenzo, “Preparation and in vitro bioactivity of hydroxyapatite/solgel glass biphasic material,” *Biomaterials*, vol. 23, no. 8, pp. 1865–1872, 2002, doi: https://doi.org/10.1016/S0142-9612(01)00313-1.

[179] N. Pinchuk, O. Parkhomey, and O. Sych, “In Vitro Investigation of Bioactive Glass-Ceramic Composites Based on Biogenic Hydroxyapatite or Synthetic Calcium Phosphates.,” *Nanoscale Res. Lett.*, vol. 12, no. 1, p. 111, Dec. 2017, doi: 10.1186/s11671-017-1895-1.

[180] D. S. Morais *et al.*, “Novel cerium doped glass-reinforced hydroxyapatite with antibacterial and osteoconductive properties for bone tissue regeneration,” *Biomed. Mater.*, vol. 10, no. 5, p. 055008, Sep. 2015, doi: 10.1088/1748-6041/10/5/055008.

[181] J. N. Dinoro *et al.*, “Laser Sintering Approaches for Bone Tissue Engineering,” *Polymers*, vol. 14, no. 12. pp. 1–29, 2022, doi: 10.3390/polym14122336.

[182] M. Brooks, “The day the world became 3D,” *New Sci.*, vol. 232, no. 3096, pp. 40–41, Oct. 2016, doi: 10.1016/S0262-4079(16)31941-8.

[183] Hybrid Manufacturing Technologies, “7 Families of Additive Manufacturing.” http://www.hybridmanutech.com/resources.

[184] S. Bose, S. Vahabzadeh, and A. Bandyopadhyay, “Bone tissue engineering using 3D printing,” *Mater. Today*, vol. 16, no. 12, pp. 496–504, 2013, doi: 10.1016/j.mattod.2013.11.017.

[185] J. J. Beaman and C. R. Deckard, “Selective Laser Sinterng With Assisted Powder Handlng,” *Google Patents*, no. 19, p. 17, 1990, [Online]. Available: https://patents.google.com/patent/US4938816A/en%0Ahttps://patentimages.storage.googleapis.com/bf/cb/03/4cbcb828f78e25/US4938816.pdf.

[186] N. Travitzky *et al.*, “Additive manufacturing of ceramic-based materials,” *Adv. Eng. Mater.*, vol. 16, no. 6, pp. 729–754, 2014, doi: 10.1002/adem.201400097.

[187] D. Grossin *et al.*, “A review of additive manufacturing of ceramics by powder bed selective laser processing (sintering / melting): Calcium phosphate, silicon carbide, zirconia, alumina, and their composites,” *Open Ceram.*, vol. 5, no. October 2020, p. 100073, Mar. 2021, doi: 10.1016/j.oceram.2021.100073.

[188] K. Dalgarno and T. Stewart, “Production tooling for polymer moulding using the RapidSteel process,” *Rapid Prototyp. J.*, vol. 7, no. 3, pp. 173–179, 2001, doi: 10.1108/13552540110395600.

[189] T. D. Stewart, K. W. Dalgarno, and T. H. C. Childs, “Strength of the DTM RapidSteelTM 1.0 material,” *Mater. Des.*, vol. 20, no. 2–3, pp. 133–138, Jun. 1999, doi: 10.1016/S0261-3069(99)00019-9.

[190] J. Doval and K. Winter, “Reinventing Metal Additive Technology,” 2019. https://uk.3dsystems.com/blog/2019/2019-07/reinventing-metal-additive-technology (accessed Jan. 10, 2021).

[191] S. F. S. Shirazi *et al.*, “A review on powder-based additive manufacturing for tissue engineering: Selective laser sintering and inkjet 3D printing,” *Sci. Technol. Adv. Mater.*, vol. 16, no. 3, pp. 1–20, Jun. 2015, doi: 10.1088/1468-6996/16/3/033502.

[192] F. Chen, J.-M. Wu, H.-Q. Wu, Y. Chen, C.-H. Li, and Y.-S. Shi, “Microstructure and mechanical properties of 3Y-TZP dental ceramics fabricated by selective laser sintering combined with cold isostatic pressing,” *Int. J. Light. Mater. Manuf.*, vol. 1, no. 4, pp. 239–245, 2018, doi: 10.1016/j.ijlmm.2018.09.002.

[193] K. Shahzad, J. Deckers, S. Boury, B. Neirinck, J. P. Kruth, and J. Vleugels, “Preparation and indirect selective laser sintering of alumina/PA microspheres,” *Ceram. Int.*, vol. 38, no. 2, pp. 1241–1247, 2012, doi: 10.1016/j.ceramint.2011.08.055.

[194] A. P. Moreno Madrid, S. M. Vrech, M. A. Sanchez, and A. P. Rodriguez, “Advances in additive manufacturing for bone tissue engineering scaffolds,” *Mater. Sci. Eng. C*, vol. 100, no. March 2018, pp. 631–644, Jul. 2019, doi: 10.1016/j.msec.2019.03.037.

[195] R. Z. Liu *et al.*, “Effects of B 4 C addition on the microstructure and properties of porous alumina ceramics fabricated by direct selective laser sintering,” *Ceram. Int.*, vol. 44, no. 16, pp. 19678–19685, 2018, doi: 10.1016/j.ceramint.2018.07.220.

[196] S. Lohfeld and P. E. McHugh, “Laser Sintering for the Fabrication of Tissue Engineering Scaffolds,” in *Methods in Molecular Biology*, vol. 868, no. 1, M. A. K. Liebschner, Ed. Totowa, NJ: Humana Press, 2012, pp. 303–310.

[197] S. Eosoly, D. Brabazon, S. Lohfeld, and L. Looney, “Selective laser sintering of hydroxyapatite/poly-ε-caprolactone scaffolds,” *Acta Biomater.*, vol. 6, no. 7, pp. 2511–2517, 2010, doi: 10.1016/j.actbio.2009.07.018.

[198] J. Deckers, J. Vleugels, and J. P. Kruth, “Additive manufacturing of ceramics: A review,” *J. Ceram. Sci. Technol.*, vol. 5, no. 4, pp. 245–260, 2014, doi: 10.4416/JCST2014-00032.

[199] FM1418, “Selective laser sintering,” *CC BY-SA 4.0 <https://creativecommons.org/licenses/by-sa/4.0>, via Wikimedia Commons, Modifications: “(brown state)” , “ (green state)” “Levelling” text removed. “Scanning layer” text added, Dark grey color added*, 2020. https://commons.wikimedia.org/wiki/File:SelectiveLaserSintering.svg (accessed Sep. 09, 2021).

[200] ISO/ASTM International, “Standard Terminology for Additive Manufacturing – General Principles – Terminology. ISO/ASTM 52900:2015,” 2015.

[201] J. P. Deckers, K. Shahzad, L. Cardon, M. Rombouts, J. Vleugels, and J. P. Kruth, “Shaping ceramics through indirect selective laser sintering,” *Rapid Prototyp. J.*, vol. 22, no. 3, pp. 544–558, 2016, doi: 10.1108/RPJ-10-2014-0143.

[202] J. P. Kruth, G. Levy, F. Klocke, and T. H. C. Childs, “Consolidation phenomena in laser and powder-bed based layered manufacturing,” *CIRP Ann. - Manuf. Technol.*, vol. 56, no. 2, pp. 730–759, 2007, doi: 10.1016/j.cirp.2007.10.004.

[203] M. Schmidt *et al.*, “Laser based additive manufacturing in industry and academia,” *CIRP Ann.*, vol. 66, no. 2, pp. 561–583, 2017, doi: 10.1016/j.cirp.2017.05.011.

[204] S. L. Sing *et al.*, “Direct selective laser sintering and melting of ceramics: A review,” *Rapid Prototyp. J.*, vol. 23, no. 3, pp. 611–623, 2017, doi: 10.1108/RPJ-11-2015-0178.

[205] J. P. Kruth, P. Mercelis, L. Froyen, and M. Rombouts, “Binding Mechanisms in Selective Laser Sintering and Selective Laser Melting,” in *International Solid Freeform Fabrication Symposium*, 2004, pp. 44–59, doi: http://dx.doi.org/10.26153/tsw/5707.

[206] L. Papadakis, D. Chantzis, and K. Salonitis, “On the energy efficiency of pre-heating methods in SLM/SLS processes,” *Int. J. Adv. Manuf. Technol.*, vol. 95, no. 1–4, pp. 1325–1338, 2018, doi:

10.1007/s00170-017-1287-9.

[207] Z. Yang, X. Liu, Z. Zhang, S. Li, and Q. Fang, “Analysis of preheating temperature field characteristics in selective laser sintering,” *Adv. Mech. Eng.*, vol. 14, no. 1, pp. 1–14, 2022, doi: 10.1177/16878140211072397.

[208] S. Kumar, “Selective laser sintering: A qualitative and objective approach,” *JOM*, vol. 55, no. 10, pp. 43–47, Oct. 2003, doi: 10.1007/s11837-003-0175-y.

[209] K. H. Tan, C. K. Chua, K. F. Leong, M. W. Naing, and C. M. Cheah, “Fabrication and characterization of three-dimensional poly(ether-ether-ketone)/-hydroxyapatite biocomposite scaffolds using laser sintering,” *Proc. Inst. Mech. Eng. Part H J. Eng. Med.*, vol. 219, no. 3, pp. 183–194, Mar. 2005, doi: 10.1243/095441105X9345.

[210] L. J. Tan, W. Zhu, and K. Zhou, “Recent Progress on Polymer Materials for Additive Manufacturing,” *Adv. Funct. Mater.*, vol. 30, no. 43, pp. 1–54, 2020, doi: 10.1002/adfm.202003062.

[211] R. Gmeiner *et al.*, “Additive manufacturing of bioactive glasses and silicate bioceramics,” *J. Ceram. Sci. Technol.*, vol. 6, no. 2, pp. 75–86, 2015, doi: 10.4416/JCST2015-00001.

[212] H. Yves-Christian, W. Jan, M. Wilhelm, W. Konrad, and P. Reinhart, “Net shaped high performance oxide ceramic parts by selective laser melting,” *Phys. Procedia*, vol. 5, pp. 587–594, 2010, doi: 10.1016/j.phpro.2010.08.086.

[213] L. C. Hwa, S. Rajoo, A. M. Noor, N. Ahmad, and M. B. Uday, “Recent advances in 3D printing of porous ceramics: A review,” *Curr. Opin. Solid State Mater. Sci.*, vol. 21, no. 6, pp. 323–347, Dec. 2017, doi: 10.1016/J.COSSMS.2017.08.002.

[214] J. Wilkes, Y. Hagedorn, W. Meiners, and K. Wissenbach, “Additive manufacturing of ZrO2 - Al2O3 ceramic components by selective laser melting,” *Rapid Prototyp. J.*, vol. 19, no. 1, pp. 51–57, Jan. 2013, doi: 10.1108/13552541311292736.

[215] T. D. Ngo, A. Kashani, G. Imbalzano, K. T. Q. Nguyen, and D. Hui, “Additive manufacturing (3D printing): A review of materials, methods, applications and challenges,” *Compos. Part B Eng.*, vol. 143, pp. 172–196, Jun. 2018, doi: 10.1016/j.compositesb.2018.02.012.

[216] F.-H. Liu, “Synthesis of biomedical composite scaffolds by laser sintering: Mechanical properties and in vitro bioactivity evaluation,” *Appl. Surf. Sci.*, vol. 297, pp. 1–8, Apr. 2014, doi: 10.1016/j.apsusc.2013.12.130.

[217] S. Duan *et al.*, “Microstructure Evolution and Mechanical Properties Improvement in Liquid-Phase-Sintered Hydroxyapatite by Laser Sintering,” *Materials (Basel).*, vol. 8, no. 3, pp. 1162–1175, Mar. 2015, doi: 10.3390/ma8031162.

[218] A. Zocca, P. Colombo, C. M. Gomes, and J. Günster, “Additive Manufacturing of Ceramics: Issues, Potentialities, and Opportunities,” *J. Am. Ceram. Soc.*, vol. 98, no. 7, pp. 1983–2001, Jul. 2015, doi: 10.1111/jace.13700.

[219] Y. Lakhdar, C. Tuck, J. Binner, A. Terry, and R. Goodridge, “Additive manufacturing of advanced ceramic materials,” *Prog. Mater. Sci.*, vol. 116, no. October 2019, p. 100736, 2021, doi: 10.1016/j.pmatsci.2020.100736.

[220] R. Galante, C. G. Figueiredo-Pina, and A. P. Serro, “Additive manufacturing of ceramics for dental applications: A review,” *Dent. Mater.*, vol. 35, no. 6, pp. 825–846, Jun. 2019, doi: 10.1016/j.dental.2019.02.026.

[221] M. Savalani, L. Hao, and R. A. Harris, “Evaluation of CO2 and Nd:YAG lasers for the selective

laser sintering of HAPEX," *Proc. Inst. Mech. Eng. Part B J. Eng. Manuf.*, vol. 220, no. 2, pp. 171–182, 2006, doi: 10.1243/095440505X32986.

[222] K. . Tan *et al.*, "Scaffold development using selective laser sintering of polyetheretherketone–hydroxyapatite biocomposite blends," *Biomaterials*, vol. 24, no. 18, pp. 3115–3123, Aug. 2003, doi: 10.1016/S0142-9612(03)00131-5.

[223] R. P. Padilla, "Selective Laser Melting of Silica Glass Powders," Aalto University, 2018.

[224] B. Duan and M. Wang, "Selective laser sintering and its application in biomedical engineering," *MRS Bull.*, vol. 36, no. 12, pp. 998–1005, Dec. 2011, doi: 10.1557/mrs.2011.270.

[225] L. Ferrage, G. Bertrand, P. Lenormand, D. Grossin, and B. Ben-Nissan, "A review of the additive manufacturing (3DP) of bioceramics: Alumina, zirconia (PSZ) and hydroxyapatite," *J. Aust. Ceram. Soc.*, vol. 53, no. 1, pp. 11–20, 2017, doi: 10.1007/s41779-016-0003-9.

[226] K. F. Leong, C. K. Chua, W. S. Gui, and Verani, "Building Porous Biopolymeric Microstructures for Controlled Drug Delivery Devices Using Selective Laser Sintering," *Int. J. Adv. Manuf. Technol.*, vol. 31, no. 5–6, pp. 483–489, Nov. 2006, doi: 10.1007/s00170-005-0217-4.

[227] S. W. K. Kweh, K. A. Khor, and P. Cheang, "Production and characterization of hydroxyapatite (HA) powders," *J. Mater. Process. Technol.*, vol. 89–90, pp. 373–377, 1999, doi: 10.1016/S0924-0136(99)00061-8.

[228] M. Bohner, S. Tadier, N. van Garderen, A. de Gasparo, N. Döbelin, and G. Baroud, "Synthesis of spherical calcium phosphate particles for dental and orthopedic applications," *Biomatter*, vol. 3, no. 2, 2013, doi: 10.4161/biom.25103.

[229] S. H. Riza, S. H. Masood, R. A. R. Rashid, and S. Chandra, "Selective laser sintering in biomedical manufacturing," in *Metallic Biomaterials Processing and Medical Device Manufacturing*, Elsevier, 2020, pp. 193–233.

[230] A. Awad, F. Fina, A. Goyanes, S. Gaisford, and A. W. Basit, "3D printing: Principles and pharmaceutical applications of selective laser sintering," *Int. J. Pharm.*, vol. 586, no. June, p. 119594, 2020, doi: 10.1016/j.ijpharm.2020.119594.

[231] H. Lee, C. H. J. Lim, M. J. Low, N. Tham, V. M. Murukeshan, and Y. J. Kim, "Lasers in additive manufacturing: A review," *Int. J. Precis. Eng. Manuf. - Green Technol.*, vol. 4, no. 3, pp. 307–322, 2017, doi: 10.1007/s40684-017-0037-7.

[232] F. Klocke and C. Ader, "DIRECT LASER SINTERING OF CERAMICS," in *International Solid Freeform Fabrication Symposium*, 2003, pp. 447–455, doi: http://dx.doi.org/10.26153/tsw/5605.

[233] N. K. Tolochko, Y. V. Khlopkov, S. E. Mozzharov, M. B. Ignatiev, T. Laoui, and V. I. Titov, "Absorptance of powder materials suitable for laser sintering," *Rapid Prototyp. J.*, vol. 6, no. 3, pp. 155–161, Sep. 2000, doi: 10.1108/13552540010337029.

[234] K. W. Dalgarno and C. S. Wright, "Approaches to Processing Metals and Ceramis Through the Laser Scanning of Powder Beds-A Review," *Powder Metall. Prog.*, vol. 1, no. 1, pp. 70–79, 2001.

[235] S. C. Ligon, R. Liska, J. Stampfl, M. Gurr, and R. Mülhaupt, "Polymers for 3D Printing and Customized Additive Manufacturing," *Chem. Rev.*, vol. 117, no. 15, pp. 10212–10290, 2017, doi: 10.1021/acs.chemrev.7b00074.

[236] Y. Shi, T. Pan, W. Zhu, C. Yan, and Z. Xia, "Artificial bone scaffolds of coral imitation prepared by selective laser sintering," *J. Mech. Behav. Biomed. Mater.*, vol. 104, no. January, p. 103664,

2020, doi: 10.1016/j.jmbbm.2020.103664.

[237] C. Shuai, P. Feng, C. Cao, and S. Peng, “Processing and Characterization of Laser Sintered Hydroxyapatite Scaffold for Tissue Engineering,” *Biotechnol. Bioprocess Eng.*, vol. 18, pp. 520–527, 2013, doi: 10.1007/s12257-012-0508-1.

[238] G. Brunello *et al.*, “Powder-based 3D printing for bone tissue engineering,” *Biotechnol. Adv.*, vol. 34, no. 5, pp. 740–753, 2016, doi: 10.1016/j.biotechadv.2016.03.009.

[239] C. Shuai, C. Gao, Y. Nie, H. Hu, Y. Zhou, and S. Peng, “Structure and properties of nano-hydroxypatite scaffolds for bone tissue engineering with a selective laser sintering system,” *Nanotechnology*, vol. 22, no. 28, p. 285703, Jul. 2011, doi: 10.1088/0957-4484/22/28/285703.

[240] P. Navarrete-Segado, C. Frances, M. Tourbin, C. Tenailleau, B. Duployer, and D. Grossin, “Powder bed selective laser process (sintering/melting) applied to tailored calcium phosphate-based powders,” *Addit. Manuf.*, vol. 50, no. September 2021, p. 102542, 2022, doi: 10.1016/j.addma.2021.102542.

[241] H. Zeng *et al.*, “Indirect selective laser sintering-printed microporous biphasic calcium phosphate scaffold promotes endogenous bone regeneration via activation of ERK1/2 signaling,” *Biofabrication*, vol. 12, no. 2, 2020, doi: 10.1088/1758-5090/ab78ed.

[242] Mettler-Toledo GmbH, “Density Kit for Analytical Balances.” p. 20, 2020, [Online]. Available: https://www.mt.com/dam/P5/labtec/13_Accessories/Density_determination/03_Documentation/RM_DensityKit_advanced-standard_EN.pdf.

[243] R. L. Carr, “EVALUATING FLOW PROPERTIES OF SOLIDS,” *Chem. Eng.*, vol. 72, pp. 163–168, 1965.

[244] K. M. Z. Hossain, U. Patel, and I. Ahmed, “Development of microspheres for biomedical applications: a review,” *Prog. Biomater.*, vol. 4, no. 1, pp. 1–19, 2015, doi: 10.1007/s40204-014-0033-8.

[245] N. J. Lakhkar *et al.*, “Titanium phosphate glass microspheres for bone tissue engineering,” *Acta Biomater.*, vol. 8, no. 11, pp. 4181–4190, 2012, doi: 10.1016/j.actbio.2012.07.023.

[246] K. M. Z. Hossain *et al.*, “Porous calcium phosphate glass microspheres for orthobiologic applications,” *Acta Biomater.*, vol. 72, pp. 396–406, 2018, doi: 10.1016/j.actbio.2018.03.040.

[247] K. A. Khor and P. Cheang, “Characterization of thermal sprayed hydroxyapatite powders and coatings,” *J. Therm. Spray Technol.*, vol. 3, no. 1, pp. 45–50, 1994, doi: 10.1007/BF02648998.

[248] P. Cheang and K. A. Khor, “Thermal spraying of hydroxyapatite (HA) coatings: Effects of powder feedstock,” *J. Mater. Process. Technol.*, vol. 48, no. 1–4, pp. 429–436, Jan. 1995, doi: 10.1016/0924-0136(94)01679-U.

[249] K. A. Khor and P. Cheang, “Plasma sprayed hydroxyapatite(HA) coatings produced with flame spheroidised powders,” *J. Mater. Process. Technol.*, vol. 63, no. 1–3, pp. 271–276, 1997, doi: 10.1016/S0924-0136(96)02634-9.

[250] K. A. Khor, P. Cheang, and Y. Wang, “Plasma Spraying of Combustion Flame Spheroidized Hydroxyapatite (HA) Powders,” *J. Therm. Spray Technol.*, vol. 7, no. 2, pp. 254–260, 1998, doi: 10.1361/105996398770351007.

[251] K. Annapurna and S. Buddhudu, “Characterization of fluorophosphate optical glasses,” *J. Solid State Chem.*, vol. 93, no. 2, pp. 454–460, Aug. 1991, doi: 10.1016/0022-4596(91)90319-D.

[252] L. S. Ravangave and G. N. Devde, “Structure and Physical Properties of 59B2O3–10Na2O–(30 −

x)CdO–xZnO–1CuO (0 ≤ x ≤ 30) Glass System," in *Advances in Glass Science and Technology*, InTech, 2018.

[253] G. Pal Singh, P. Kaur, S. Kaur, and D. P. Singh, "Gamma ray effect on the covalent behaviour of the CeO2–BaO–B2O3 glasses," *Phys. B Condens. Matter*, vol. 450, no. December 2017, pp. 106–110, Oct. 2014, doi: 10.1016/j.physb.2014.05.017.

[254] R. D. Shannon, "Revised effective ionic radii and systematic studies of interatomic distances in halides and chalcogenides," *Acta Crystallogr. Sect. A*, vol. 32, no. 5, pp. 751–767, Sep. 1976, doi: 10.1107/S0567739476001551.

[255] V. Y. Ganvir and R. S. Gedam, "Effect of La2O3 addition on structural and electrical properties of sodium borosilicate glasses," *Mater. Res. Express*, vol. 4, no. 3, 2017, doi: 10.1088/2053-1591/aa66e4.

[256] M. F. Faznny, M. K. Halimah, and M. N. Azlan, "Effect Of Lanthanum Oxide On Optical Properties Of Zinc Borotellurite Glass System," *J. Optoelectron. Biomed. Mater.*, vol. 8, no. April-June, pp. 49–59, 2016.

[257] C. Rey, C. Combes, C. Drouet, and D. Grossin, "Bioactive Ceramics: Physical Chemistry," in *Comprehensive Biomaterials*, vol. 1, Elsevier, 2011, pp. 187–221.

[258] F. H. Chung, "Quantitative interpretation of X-ray diffraction patterns of mixtures. II. Adiabatic principle of X-ray diffraction analysis of mixtures," *J. Appl. Crystallogr.*, vol. 7, no. 6, pp. 526–531, Dec. 1974, doi: 10.1107/S0021889874010387.

[259] R. Surana and R. Suryanarayanan, "Quantitation of crystallinity in substantially amorphous pharmaceuticals and study of crystallization kinetics by X-ray powder diffractometry," *Powder Diffr.*, vol. 15, no. 1, pp. 2–6, 2000, doi: DOI: 10.1017/S0885715600010757.

[260] S. R. Byrn, G. Zografi, and X. S. Chen, *Solid State Properties of Pharmaceutical Materials*. Hoboken: John Wiley & Sons, Inc., 2017.

[261] J. A. Newman, P. D. Schmitt, S. J. Toth, F. Deng, S. Zhang, and G. J. Simpson, "Parts per Million Powder X-ray Diffraction," *Anal. Chem.*, vol. 87, no. 21, pp. 10950–10955, 2015, doi: 10.1021/acs.analchem.5b02758.

[262] A. Slósarczyk and J. Białoskórski, "Hardness and fracture toughness of dense calcium-phosphate-based materials.," *J. Mater. Sci. Mater. Med.*, vol. 9, no. 2, pp. 103–108, Feb. 1998, doi: 10.1023/a:1008803232685.

[263] C. R. Gautam, S. Kumar, V. K. Mishra, and S. Biradar, "Synthesis, structural and 3-D architecture of lanthanum oxide added hydroxyapatite composites for bone implant applications: Enhanced microstructural and mechanical properties," *Ceram. Int.*, vol. 43, no. 16, pp. 14114–14121, 2017, doi: 10.1016/j.ceramint.2017.07.150.

[264] D. G. Guo, A. H. Wang, Y. Han, and K. W. Xu, "Characterization, physicochemical properties and biocompatibility of La-incorporated apatites," *Acta Biomater.*, vol. 5, no. 9, pp. 3512–3523, 2009, doi: 10.1016/j.actbio.2009.05.026.

[265] N. Patel, I. R. Gibson, S. Ke, S. M. Best, and W. Bonfield, "Calcining influence on the powder properties of hydroxyapatite," *J. Mater. Sci. Mater. Med.*, vol. 12, no. 2, pp. 181–188, 2001, doi: 10.1023/A:1008986430940.

[266] A. B. D. Nandiyanto and K. Okuyama, "Progress in developing spray-drying methods for the production of controlled morphology particles: From the nanometer to submicrometer size ranges," *Adv. Powder Technol.*, vol. 22, no. 1, pp. 1–19, 2011, doi: 10.1016/j.apt.2010.09.011.

[267] P. Luo and T. G. Nieh, “Preparing hydroxyapatite powders with controlled morphology,” *Biomaterials*, vol. 17, no. 20, pp. 1959–1964, Oct. 1996, doi: 10.1016/0142-9612(96)00019-1.

[268] P. Navarrete-Segado, C. Frances, D. Grossin, and M. Tourbin, “Tailoring hydroxyapatite microspheres by spray-drying for powder bed fusion feedstock,” *Powder Technol.*, vol. 398, p. 117116, 2022, doi: 10.1016/j.powtec.2022.117116.

[269] C. Shi, M. Ermold, G. Oulundsen, and L. Newman, “CO2 and CO laser comparison of glass and ceramic processing,” in *High-Power Laser Materials Processing: Applications, Diagnostics, and Systems VIII*, 2019, vol. 10911, p. 109110M, doi: 10.1117/12.2516966.

[270] A. Hoppe, “Bioactive Glass Derived Scaffolds with Therapeutic Ion Releasing Capability for Bone Tissue Engineering,” University of Erlangen-Nuremberg, 2014.

[271] S. M. Karazi, I. U. Ahad, and K. Y. Benyounis, “Laser Micromachining for Transparent Materials,” in *Reference Module in Materials Science and Materials Engineering*, Elsevier, 2017.

[272] ABRISA Technologies, “Specialty Glass Materials Products & Specifications.” pp. 1–35, 2014, [Online]. Available: https://abrisatechnologies.com/media/Glass-Materials-Brochure.pdf.

[273] A. B. Spierings, M. Voegtlin, T. Bauer, and K. Wegener, “Powder flowability characterisation methodology for powder-bed-based metal additive manufacturing,” *Prog. Addit. Manuf.*, vol. 1, no. 1–2, pp. 9–20, Jun. 2016, doi: 10.1007/s40964-015-0001-4.

[274] L. C. Capozzi, A. Sivo, and E. Bassini, “Powder spreading and spreadability in the additive manufacturing of metallic materials: A critical review,” *J. Mater. Process. Technol.*, vol. 308, no. March, p. 117706, 2022, doi: 10.1016/j.jmatprotec.2022.117706.

[275] M. Krantz, H. Zhang, and J. Zhu, “Characterization of powder flow: Static and dynamic testing,” *Powder Technol.*, vol. 194, no. 3, pp. 239–245, Sep. 2009, doi: 10.1016/j.powtec.2009.05.001.

[276] C. Rey, O. Marsan, C. Combes, C. Drouet, D. Grossin, and S. Sarda, “Characterization of Calcium Phosphates Using Vibrational Spectroscopies,” in *Advances in Calcium Phosphate Biomaterials*, B. Ben-Nissan, Ed. Berlin, Heidelberg: Springer Berlin Heidelberg, 2014, pp. 229–266.

[277] D. Gu and Y. Shen, “Balling phenomena in direct laser sintering of stainless steel powder : Metallurgical mechanisms and control methods,” *Mater. Des.*, vol. 30, no. 8, pp. 2903–2910, 2009, doi: 10.1016/j.matdes.2009.01.013.

[278] S. XiaoHui *et al.*, “Selective laser sintering of aliphatic-polycarbonate/hydroxyapatite composite scaffolds for medical applications,” *Int. J. Adv. Manuf. Technol.*, vol. 81, no. 1–4, pp. 15–25, 2015, doi: 10.1007/s00170-015-7135-x.

[279] Y. Wang, M. Zhang, S. Chang, S. Li, and X. Huang, “Laser-induced ignition and combustion behavior of individual graphite microparticles in a micro-combustor,” *Processes*, vol. 8, no. 11, pp. 1–13, 2020, doi: 10.3390/pr8111493.

[280] K. Tõnsuaadu, K. A. Gross, L. Pluduma, and M. Veiderma, “A review on the thermal stability of calcium apatites,” *J. Therm. Anal. Calorim.*, vol. 110, no. 2, pp. 647–659, 2012, doi: 10.1007/s10973-011-1877-y.

[281] C. J. Liao, F. H. Lin, K. S. Chen, and J. S. Sun, “Thermal decomposition and reconstitution of hydroxyapatite in air atmosphere,” *Biomaterials*, vol. 20, no. 19, pp. 1807–1813, 1999, doi: 10.1016/S0142-9612(99)00076-9.

[282] Q. He, X. Ao, H. Xia, J. Liu, C. Yang, and C. Ren, “Modeling and simulation of the temperature field of selective laser sintering,” *J. Phys. Conf. Ser.*, vol. 1885, no. 3, 2021, doi: 10.1088/1742-6596/1885/3/032073.

[283] H. Xin, W. C. Sun, and J. Fish, “Discrete element simulations of powder-bed sintering-based additive manufacturing,” *Int. J. Mech. Sci.*, vol. 149, no. November 2017, pp. 373–392, 2018, doi: 10.1016/j.ijmecsci.2017.11.028.

[284] O. D. Quintana-Ruiz and E. M. B. Campello, “Discrete element modeling of selective laser sintering additive manufacturing processes,” *Comput. Methods Appl. Mech. Eng.*, vol. 410, p. 115994, 2023, doi: 10.1016/j.cma.2023.115994.

[285] F. Klocke, A. McClung, and C. Ader, “Direct laser sintering of borosilicate glass,” in *International Solid Freeform Fabrication Symposium*, 2004, pp. 214–219.

[286] M. Fateri and A. Gebhardt, “Selective Laser Melting of soda-lime glass powder,” *Int. J. Appl. Ceram. Technol.*, vol. 12, no. 1, pp. 53–61, 2015, doi: 10.1111/ijac.12338.

[287] R. S. Khmyrov, S. N. Grigoriev, A. A. Okunkova, and A. V. Gusarov, “On the possibility of selective laser melting of quartz glass,” *Phys. Procedia*, vol. 56, no. C, pp. 345–356, 2014, doi: 10.1016/j.phpro.2014.08.117.

[288] K. C. Datsiou, F. Spirrett, I. Ashcroft, M. Magallanes, S. Christie, and R. Goodridge, “Laser powder bed fusion of soda lime silica glass: Optimisation of processing parameters and evaluation of part properties,” *Addit. Manuf.*, vol. 39, no. September 2020, p. 101880, 2021, doi: 10.1016/j.addma.2021.101880.